

# ADVANCED STEEL CONSTRUCTION

*An International Journal*

Volume 19 Number 4

December 2023

## CONTENTS

### Technical Papers

Investigation on Lateral Behavior of Corrugated Steel Plate Shear Walls with Openings or Slits  
En-Feng Deng, Yu-Han Wang, Dou-Dou Si, Zhe Zhang and Guang-Cao Zhang

Investigating Fatigue Mechanisms and Crack Growth in 20mntib Steel High-Strength Bolts: An Experimental and Simulation Study  
Jin-Feng Jiao, Li-Xuan Fan, Yong Liu, Hong-Gang Lei and Qi Guo

Shear Behaviour of Demountable Connections with Bolts and Headed Studs  
Isidora Jakovljević, Milan Spremić and Zlatko Marković

Behaviours of Steel-Concrete Composite Beams at Low Temperatures: Materials and Structures  
Jia-Bao Yan, Er-Cong Kang and Jian Xie

Inversion Method of Uncertain Parameters for Truss Structures Based on Graph Neural Networks  
Zhang-Qi Wang, Zhe Zheng, Jun-Wei MengXiang and Wen-Qiang Jiang

An Experimental Study on Seismic Performance of Steel Composite Beam-Column Rigid Joint and Buckling Restrained Knee-Braced Joint  
Feng Xu, Zhe Yuan, Na Liu, Zhen-Xing Li, Lian-Guang Jia and Wei Xu

A Review of Direct Fastening Steel Jacket for Strengthening of Reinforced Concrete Columns  
Zhi-Wei Shan, R.K.L. Su, D.T.W. Looi and Li-Jie Chen

Deep Learning Damage Identification Method for Steel-Frame Bracing Structures Using Time-Frequency Analysis and Convolutional Neural Networks  
Xiao-Jian Han, Qi-Bin Cheng and Ling-Kun Chen

Conformation and Static Performance Analysis of Pentagonal Three-Four Strut Hybrid Open-Type Cable Dome  
Hui Lv, De-Wang Liu, Shi-Lin Dong and Yan-Fen Zhong

Second-Order Analysis of Beam-Columns by Machine Learning-Based Structural Analysis Through Physics-Informed Neural Networks  
Liang Chen, Hao-Yi Zhang, Si-Wei Liu and Siu-Lai Chan

Copyright © 2023 by :

The Hong Kong Institute of Steel Construction

Website: <http://www.jkisc.org>

ISSN 1816-112X

Science Citation Index Expanded, Materials Science Citation Index and ISI Alerting

Cover: A steel bridge in Kuching, Sarawak, Malaysia. Photo ©Lili Yao-Peng

e-copy of IJASC is free to download at "www.ascjournal.com" in internet and mobile apps.

ADVANCED STEEL CONSTRUCTION

VOL.19, NO.4 (2023)

# ADVANCED STEEL CONSTRUCTION

*an International Journal*

ISSN 1816-112X

Volume 19 Number 4

December 2023



## Editors-in-Chief

**S.L. Chan**, The Hong Kong Polytechnic University, Hong Kong, China

**W.F. Chen**, University of Hawaii at Manoa, USA

**R. Zandonini**, Trento University, Italy



ISSN 1816-112X

Science Citation Index Expanded,  
Materials Science Citation Index  
and ISI Alerting

#### EDITORS-IN-CHIEF

**Asian Pacific, African  
and organizing Editor**  
S.L. Chan  
*The Hong Kong Polyt. Univ.,  
Hong Kong, China*

**American Editor**  
W.F. Chen  
*Univ. of Hawaii at Manoa, USA*

**European Editor**  
R. Zandonini  
*Trento Univ., Italy*

#### ASSOCIATE EDITORS

Y.P. Liu  
*The Hong Kong Polyt. Univ., Hong Kong, China*

S.W. Liu  
*The Hong Kong Polyt. Univ., Hong Kong, China*

#### INTERNATIONAL EDITORIAL BOARD

F.G. Albermani  
*Central Queensland Univ., Australia*

I. Burgess  
*Univ. of Sheffield, UK*

F.S.K. Bijlaard  
*Delft Univ. of Technology, The Netherlands*

R. Bjorhovde  
*The Bjorhovde Group, USA*

M.A. Bradford  
*The Univ. of New South Wales, Australia*

D. Camotim  
*Technical Univ. of Lisbon, Portugal*

C.M. Chan  
*Hong Kong Univ. of Science & Technology, Hong Kong, China*

T.H.T. Chan  
*Queensland Univ. of Technology, Australia*

T.M. Chan  
*The Hong Kong Polyt. Univ., Hong Kong, China*

Z.H. Chen  
*Tianjin Univ., China*

S.P. Chiew  
*Nanyang Technological Univ., Singapore*

W.K. Chow  
*The Hong Kong Polyt. Univ., Hong Kong, China*

G.G. Deierlein  
*Stanford Univ., California, USA*

L. Dezi  
*Univ. of Ancona, Italy*

D. Dubina  
*The Politehnica Univ. of Timisoara, Romania*

R. Greiner  
*Technical Univ. of Graz, Austria*

L. Gardner  
*Imperial College of Science, Technology and Medicine, UK*

Y. Goto  
*Nagoya Institute of Technology, Japan*

L.H. Han  
*Tsinghua Univ. China*

S. Herion  
*University of Karlsruhe, Germany*

G.W.M. Ho  
*Ove Arup & Partners Hong Kong Ltd., Hong Kong,  
China*

B.A. Izzuddin  
*Imperial College of Science, Technology and  
Medicine, UK*

J.P. Jaspart  
*Univ. of Liege, Belgium*

S. A. Jayachandran  
*IIT Madras, Chennai, India*

S.E. Kim  
*Sejong Univ., South Korea*

S. Kitipornchai  
*The Univ., of Queensland, Australia*

D. Lam  
*Univ. of Bradford, UK*

H.F. Lam  
*City Univ. of Hong Kong, Hong Kong, China*

G.C. Li  
*Shenyang Jianzhu Univ., China*

G.Q. Li  
*Tongji Univ., China*

J.Y.R. Liew  
*National Univ. of Singapore, Singapore*

E.M. Lui  
*Syracuse Univ., USA*

Y.L. Mo  
*Univ. of Houston, USA*

J.P. Muzeau  
*CUST, Clermont Ferrand, France*

D.A. Nethercot  
*Imperial College of Science, Technology and  
Medicine, UK*

Y.Q. Ni  
*The Hong Kong Polyt. Univ., Hong Kong, China*

D.J. Oehlers  
*The Univ. of Adelaide, Australia*

J.L. Peng  
*Yunlin Uni. of Science & Technology, Taiwan, China*

K. Rasmussen  
*The Univ. of Sydney, Australia*

J.M. Rotter  
*The Univ. of Edinburgh, UK*

C. Scawthorn  
*Scawthorn Porter Associates, USA*

P. Schaumann  
*Univ. of Hannover, Germany*

Y.J. Shi  
*Tsinghua Univ., China*

G.P. Shu  
*Southeast Univ. China*

L. Simões da Silva  
*Department of Civil Engineering, University of  
Coimbra, Portugal*

J.G. Teng  
*The Hong Kong Polyt. Univ., Hong Kong, China*

G.S. Tong  
*Zhejiang Univ., China*

K.C. Tsai  
*National Taiwan Univ., Taiwan, China*

C.M. Uang  
*Univ. of California, USA*

B. Uy  
*University of Western Sydney, Australia*

M. Veljkovic  
*Univ. of Lulea, Sweden*

F. Wald  
*Czech Technical Univ. in Prague, Czech*

Y.C. Wang  
*The Univ. of Manchester, UK*

Y.L. Xu  
*The Hong Kong Polyt. Univ., Hong Kong, China*

D. White  
*Georgia Institute of Technology, USA*

E. Yamaguchi  
*Kyushu Institute of Technology, Japan*

Y.B. Yang  
*National Taiwan Univ., Taiwan, China*

Y.Y. Yang  
*China Academy of Building Research, Beijing, China*

B. Young  
*The Univ. of Hong Kong, Hong Kong, China*

X.L. Zhao  
*Monash Univ., Australia*

X.H. Zhou  
*Chongqing University, China*

Z.H. Zhou  
*The Hong Kong Polyt. Univ., Hong Kong, China*

S.Y. Zhu  
*The Hong Kong Polyt. Univ., Hong Kong, China*

R.D. Ziemian  
*Bucknell Univ., USA*

## General Information

### *Advanced Steel Construction, an international journal*

#### Aims and scope

The International Journal of Advanced Steel Construction provides a platform for the publication and rapid dissemination of original and up-to-date research and technological developments in steel construction, design and analysis. Scope of research papers published in this journal includes but is not limited to theoretical and experimental research on elements, assemblages, systems, material, design philosophy and codification, standards, fabrication, projects of innovative nature and computer techniques. The journal is specifically tailored to channel the exchange of technological know-how between researchers and practitioners. Contributions from all aspects related to the recent developments of advanced steel construction are welcome.

**Disclaimer.** No responsibility is assumed for any injury and / or damage to persons or property as a matter of products liability, negligence or otherwise, or from any use or operation of any methods, products, instructions or ideas contained in the material herein.

**Subscription inquiries and change of address.** Address all subscription inquiries and correspondence to Member Records, IJASC. Notify an address change as soon as possible. All communications should include both old and new addresses with zip codes and be accompanied by a mailing label from a recent issue. Allow six weeks for all changes to become effective.

**The Hong Kong Institute of Steel Construction**

HKISC

c/o Department of Civil and Environmental Engineering,  
The Hong Kong Polytechnic University,  
Hung Hom, Kowloon, Hong Kong, China.

Tel: 852- 2766 6047 Fax: 852- 2334 6389

Email: [ceslchan@polyu.edu.hk](mailto:ceslchan@polyu.edu.hk) Website: <http://www.hkisc.org/>

**ISSN 1816-112X**

**Science Citation Index Expanded, Materials Science Citation Index and ISI Alerting**

**Copyright © 2023 by:**

**The Hong Kong Institute of Steel Construction.**



ISSN 1816-112X

Science Citation Index Expanded,  
Materials Science Citation Index and  
ISI Alerting

## EDITORS-IN-CHIEF

### Asian Pacific, African and organizing Editor

S.L. Chan

*The Hong Kong Polyt. Univ.,  
Hong Kong, China  
Email: ceslchan@polyu.edu.hk*

### American Editor

W.F. Chen

*Univ. of Hawaii at Manoa, USA  
Email: waifah@hawaii.edu*

### European Editor

R. Zandonini

*Trento Univ., Italy  
Email: riccardo.zandonini@ing.unitn.it*

# Advanced Steel Construction

*an international journal*

VOLUME 19 NUMBER 4

December 2023

## Technical Papers

Investigation on Lateral Behavior of Corrugated Steel Plate Shear Walls with 321  
Openings or Slits

*En-Feng Deng \*, Yu-Han Wang, Dou-Dou Si, Zhe Zhang and Guang-Cao Zhang*

Investigating Fatigue Mechanisms and Crack Growth in 20mntib Steel 329  
High-Strength Bolts: An Experimental and Simulation Study

*Jin-Feng Jiao, Li-Xuan Fan, Yong Liu, Hong-Gang Lei and Qi Guo \**

Shear Behaviour of Demountable Connections with Bolts and Headed Studs 341

*Isidora Jakovljević \*, Milan Spremić and Zlatko Marković*

Behaviours of Steel-Concrete Composite Beams at Low Temperatures: Materials 353  
and Structures

*Jia-Bao Yan, Er-Cong Kang \* and Jian Xie \**

Inversion Method of Uncertain Parameters for Truss Structures Based on Graph 366  
Neural Networks

*Zhang-Qi Wang, Zhe Zheng, Jun-Wei MengXiang and Wen-Qiang Jiang \**

An Experimental Study on Seismic Performance of Steel Composite 375  
Beam-Column Rigid Joint and Buckling Restrained Knee-Braced Joint

*Feng Xu \*, Zhe Yuan, Na Liu, Zhen-Xing Li, Lian-Guang Jia and Wei Xu*

A Review of Direct Fastening Steel Jacket for Strengthening of Reinforced 383  
Concrete Columns

*Zhi-Wei Shan, R.K.L. Su \*, D.T.W. Looi and Li-Jie Chen*

Deep Learning Damage Identification Method for Steel-Frame Bracing Structures 389  
Using Time-Frequency Analysis and Convolutional Neural Networks

*Xiao-Jian Han, Qi-Bin Cheng and Ling-Kun Chen \**

Conformation and Static Performance Analysis of Pentagonal Three-Four Strut 403  
Hybrid Open-Type Cable Dome

*Hui Lv \*, De-Wang Liu, Shi-Lin Dong and Yan-Fen Zhong*

Second-Order Analysis of Beam-Columns by Machine Learning-Based Structural 411  
Analysis Through Physics-Informed Neural Networks

*Liang Chen, Hao-Yi Zhang, Si-Wei Liu \* and Siu-Lai Chan*





# INVESTIGATION ON LATERAL BEHAVIOR OF CORRUGATED STEEL PLATE SHEAR WALLS WITH OPENINGS OR SLITS

En-Feng Deng <sup>1,\*</sup>, Yu-Han Wang <sup>1</sup>, Dou-Dou Si <sup>2</sup>, Zhe Zhang <sup>1</sup> and Guang-Cao Zhang <sup>1</sup>

<sup>1</sup> School of Water Conservancy and Civil Engineering, Zhengzhou University, Zhengzhou 450001, China

<sup>2</sup> School of Civil Engineering, Tongji University, Shanghai 200092, China

\* (Corresponding author: E-mail: dengenfeng@zzu.edu.cn)

## ABSTRACT

In place of traditional on-site construction, modular steel construction (MSC) is an excellent alternative and it is gaining popularity. The innovative construction method possesses higher construction speed and quality by moving large proportion of the building to be manufactured in the factory, which is favorable to environmental protection. Schools, hotels, and apartments have widely adopted modular steel construction as its convenience for transportation. This paper mainly focused on the lateral behavior of corrugated steel plate shear walls (CSPSWs) with openings or slits in container-like modular steel construction. A 3D finite element model (FEM) was established and validated against the test results. The failure process of the CSPSWs with opening was revealed and discussed. Further, theoretical deduction was carried out to predict the initial lateral stiffness of CSPSWs with opening and the proposed formulas agreed well with the test and simulation results. In addition, parametric analysis was performed to reveal the lateral behavior of CSPSWs with vertical slits based on the verified FEM. It indicated that the layer and location of the vertical slit have prominent influence on the initial stiffness and ultimate load of CSPSWs. Meanwhile, in order to investigate the effect of opening location on the initial stiffness of CSPSWs with openings, a parametric study was conducted and the reasonable location of the opening was recommended. The present study provides useful design guidelines for the design of CSPSWs, which is beneficial to promoting the application of modular steel construction.

## ARTICLE HISTORY

Received: 12 January 2023  
Revised: 12 April 2023  
Accepted: 10 May 2023

## KEYWORDS

Modular steel construction;  
CSPSW;  
Vertical slits;  
Opening;  
Finite element analysis;  
Design consideration

Copyright © 2023 by The Hong Kong Institute of Steel Construction. All rights reserved.

## 1. Introduction

Modular construction, or off-site prefabricated volumetric construction, is increasingly used for hotels, schools and hospitals, which can be modularized manufactured [1][2]. A permanent modular structure is made up by the module unit prefabricated in the factory and assembled together on the construction site after transportation [3]. The main technical highlights of the innovative construction method include higher efficiency, better quality and less resource wastage. Therefore, modular construction is of particular interest across the construction industry and academia [4][5].

Lawson et al. [6], Kim and Lee [7] have conducted case studies of modular construction, indicating the superiority of modular construction. Liew et al. [8][9] proposed the prefabricated prefinished volumetric construction (PPVC) and introduced its potential practice. The lightweight concrete with different strength grades was filled in the square hollow section (SHS) to satisfy the varied load bearing requirements for columns in different layers. A review of modular building structures was presented by Lacey et al. [10]. The structural form, construction material as well as the existing inter-module connections were summarized. Among the various types of modular construction, the container-like modular steel construction has been widely employed attributable to its convenience for transportation and connecting. The nonstandard container can be transformed and finished for building function, shown as Fig. 1. The dimensions of the module units are generally in the range of 3–5m in width, 10–20m in length, and 3–4m in height. The corrugated steel plates are usually served as the surface enclosures of the module. It is necessary to decorate the corrugated steel plates with thermal insulation material to realize the building function. Meanwhile, corrugated steel plate has been proven to be an favourable lateral-force resisting component compared to steel plate shear walls (SPSWs) [11][12].

For investigating the seismic mechanism of corrugated steel plate shear walls (CSPSWs), a series of studies have been carried out. Giriunas et al. [13] found that the surface corrugated steel plates were important lateral load-resisting components for containers by numerical simulation. The strengthening effect of sidewalls cannot be ignored. Corrugated steel shear walls performed better than unstiffened steel plate shear walls (SPSWs) according to the cyclic tests conducted by Fereshteh et al. [14]. Deng et al. [15] investigated the initial stiffness of CSPSWs in modular steel construction through numerical and theoretical studies. The practical design formulas on initial stiffness of CSPSWs were derived. Yu and Chen [16] studied the stiffness strengthening effect of corrugated sidewalls in container-like modules. The initial stiffness and a simplified numerical model of CSPSWs were presented.

Finite element analysis and cyclic tests were conducted on two kinds of steel plate shear walls with non-uniform spacing slits by Lu et al [17]. It indicated that the steel plate shear wall can dissipate more energy through the development of plasticity in the strip between the slits. In addition, Lu et al. [18] conducted finite element analysis of self-centering steel plate shear walls with slits under cyclic loading, and the numerical results agreed well with the test ones. Wang et al. [19] designed an innovative modular panel with slits on steel plate shear walls, and a series of tests under cyclic load were taken to reveal its seismic characteristic. Meanwhile, considering the necessity of openings to install windows or doors for realization of building function in MSC, Ding et al. [20] conducted cyclic tests on CSPSWs with openings in modular construction. It indicated that the seismic characteristic of CSPSWs was evidently influenced owing to the opening. The initial stiffness of CSPSWs reduced rapidly as the increasing of the area of the opening. Farzampour and Laman [21] compared the mechanical behavior of CSPSWs and SPSWs with and without openings through a series of numerical studies. Given the extensive researches available on seismic performance of CSPSWs, the excellent seismic performance of CSPSWs has been verified. However, the related research on seismic behavior of CSPSWs with openings is inadequate, and few research has been focused on the lateral behavior of CSPSWs with slits.

The main focus of this paper was on the lateral performance of CSPSWs with openings or slits. Detailed finite element models (FEM) were developed firstly and verified by the previous tests conducted by the authors. In addition, the theoretical model of CSPSWs with openings was developed and the initial stiffness of CSPSWs with openings was deduced and validated. Then, the influence of the vertical slits and openings on the initial stiffness of CSPSWs was investigated through a series of parametric studies. The influence of layer of the slit, location of the slit and location of the opening was revealed. The reasonable location of the opening and design recommendation on the vertical slit were proposed, providing useful design guidelines for CSPSWs with openings or slits in modular construction.



Fig. 1 CSPSWs with openings in modular construction



## 2. General of the test and finite element modelling

### 2.1. General of the test

Four full-scale CSPSWs specimens with openings labeled as CSPSWO1–CSPSWO4 were tested by Ding et al. [20]. Table 1 shows the geometric and material characteristics of the specimens. Specimen CSPSWO1 and CSPSWO3 were designed with window opening and CSPSWO2 and CSPSWO4 were designed with door opening. The constructional columns were utilized to reinforce the edges of the opening. Fig. 2(a) shows the test device. The specimen was fixed by two hinged supports to simulate the connection between the individual modules and tested under cyclic horizontal displacement. Lateral-restraint apparatus was adopted to prevent the global twist of the specimen during the test. The seismic performance test results reported by Ding et al. [20] was used to validate the developed FEM in the following section.

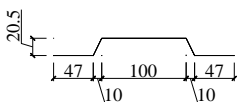
### 2.2. Development of the FEM

The FEM was established based on the universal software ABAQUS (Version 6.13) [22]. The established FEM is illustrated in Fig. 2(b). The FEM consists of the outer frame and the infill corrugated steel plate. The constructional columns are tied to the adjacent frame beam or frame column. The four-node shell element S4R with reduced integration is adopted to simulate the frame beam, frame column, constructional column and the infill corrugated steel plate with a mesh size of 40mm. Similarly, each infill plate is tied to the adjacent beam or column. In this way, each infill plate and the outer frame can be meshed independently using the structured meshing method. This meshing strategy is useful to avoid the irregular elements and obtain satisfactory computing efficiency. The bilinear kinematic hardening model and Von-Mise yielding criterion available in the ABAQUS metal plasticity library are employed in the FEM. The elastic modulus, yield strength, and ultimate strength are accordance with the test results, as given in Table 1. The hardening modulus equals to 0.01 times of the elastic modulus and the Poisson's ratio is set to 0.3. The bottoms of the two modular columns are pin-constrained to be consistent with the test setup. Meanwhile, the webs of the ceiling beam are restrained from out-of-plane lateral displacement, simulating the lateral restraint apparatus, as shown in Fig. 2(b).

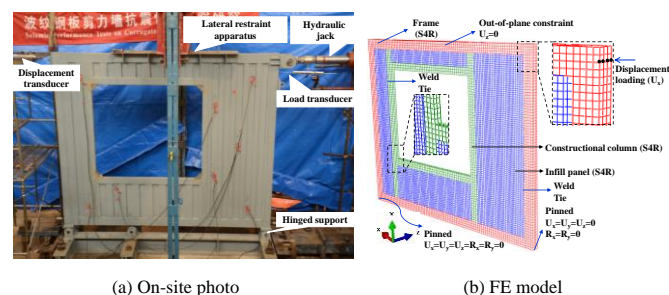
In order to simulate the initial imperfection of the infill corrugated steel plate, linear elastic eigenvalue buckling analysis was primarily performed using the subspace iteration method available in ABAQUS to extract the buckling modes. Global buckling occurred in the first buckling mode for all the four specimens, as shown in Fig.3. The geometric imperfection amplitude was set to be  $H/200$  of the first buckling mode, where  $H$  was the height of specimen [23][24]. Then, the cyclic displacement load the same as the test was applied at one end of the ceiling beam to simulate the cyclic load. The ABAQUS/implicit module was used to solve the response of the FEM.

**Table 1**

The geometric and material properties of the CSPSW specimens with openings

Specimen	$t$ (mm)	Opening		Section of the specimen (mm)	$E$ (GPa)	$f_y$ (MPa)	$f_u$ (MPa)
		Size $l \times h$ (mm)	Function				
CSPSWO1	1.70	1000×1600	Window		195	388	511
CSPSWO2	1.58	1000×2290	Door				
CSPSWO3	1.68	1800×1600	Window				
CSPSWO4	1.70	1800×2290	Door				
				corrugated steel plate			
				□150×100×6			
				frame beam/	195	394	504
				frame column			

Note:  $t$ : measured thickness of the corrugated steel plate;  $l$ : length of the opening;  $h$ : height of the opening;  $E$ : elastic modulus;  $f_y$ : yield strength;  $f_u$ : ultimate tensile strength.



**Fig. 2** Test setup and FEM for CSPSWs with openings

### 2.3. Validation and discussion

A comparison of the hysteretic curve and the skeleton curve between the test results and finite element analysis (FEA) is shown in Fig. 4. Generally, the FEA agrees well with the test results. In addition, the comparisons between the initial stiffness ( $K_0$ ) and ultimate load ( $F_u$ ) of the specimens are listed in Table 2. The positive loading is signed as “+”, while the negative loading is signed as “-”. As shown in Fig. 2(a), the push (from right to left) applied on the specimen is defined as positive loading and the pull (from left to right) is defined as negative loading.

All the specimens failed in three stages: the elastic stage, the yield stage, and the failure stage. The FEA almost coincides with the test results in the elastic stage. The comparisons in Table 2 indicate that the FEM overestimated the initial stiffness ( $K_0$ ) of the specimens averagely with FEA-to-test ratios ranging from 1.01 to 1.25 with a mean value of 1.16 and coefficient of variation (COV) of 0.07. The overestimation may be caused by the difference of boundary conditions between the test setup and FEM. The out-of-plane displacement of the web of the ceiling beam is restrained ideally in the FEM. However, a gap with a width of 10mm is necessary between the lateral restraint apparatus and the specimen for the convenience of installation, as shown in Fig. 2(a). The gap may result in slight global twist of the specimen in the positive loading, leading to the lower  $K_0$  of the test results, especially in the positive direction. The FEM also simulates well of the test results in the yield development stage. The FEA-to-test ratio of the ultimate load ( $F_u$ ) ranges from 0.99 to 1.09 with a mean value of 1.02 and COV of 0.05. In the failure stage, the fracture of the infill panel and the constructional column develops and aggravates rapidly as the accumulation of damage. The damage is particularly concentrated in the corner regions of the opening, as shown in Fig. 5. The fracture of the constructional column and infill panel results in the decline of the load-bearing capacity in the failure stage. However, the fracture is not considered in the FEM, leading to the higher load of FEA than the test results, as shown in Fig. 4.

The comparisons of failure mode between test results and FEA are shown in Fig. 5. It indicates that the FEM predicts well the failure mode of the specimens, including the global buckling of the infill panel and the local buckling of the constructional columns in the corners of the opening.

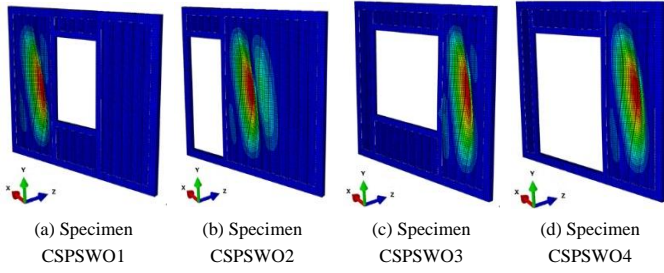


Fig. 3 First buckling mode of CSPSWs with openings

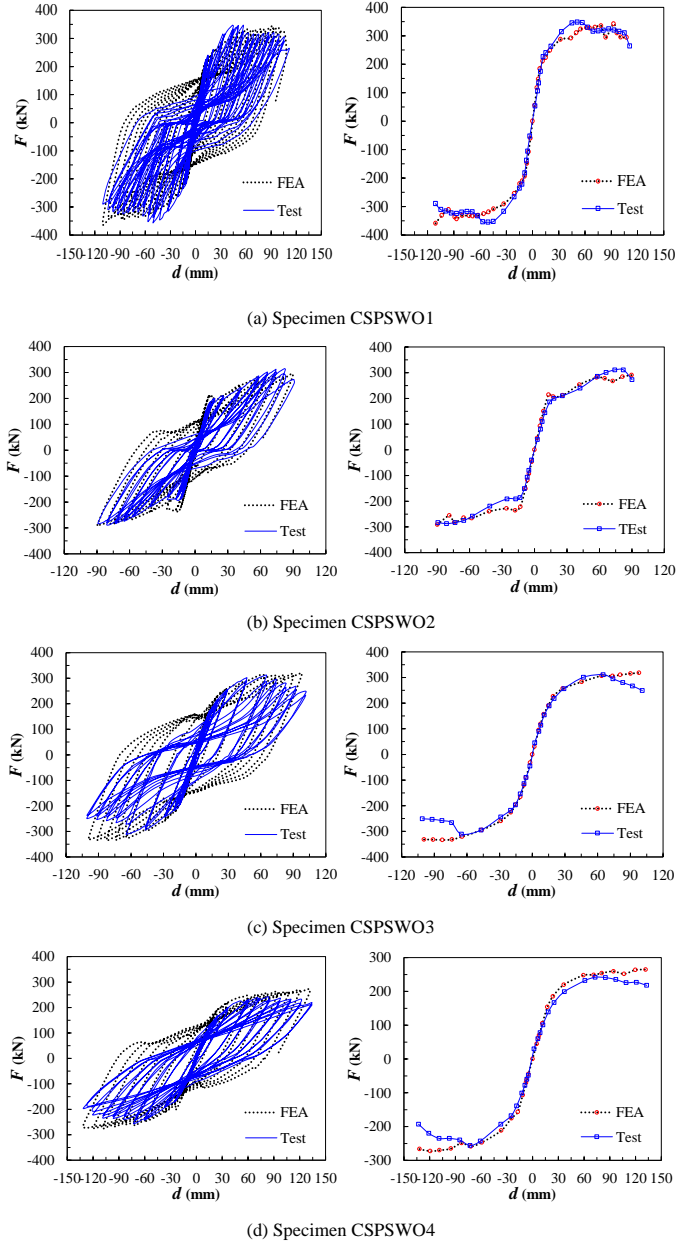


Fig. 4 Comparisons of hysteretic and skeleton curves between test and FEA

The above comparisons and discussion verify the reliability of the FEM, which can be used for further analysis. The failure process of the four specimens is shown in Fig. 6. It is found that the damage mainly exists in the corner regions of the openings due to stress concentration, as the increasing of the inter-story drift ratio. Local buckling and fracture occur in the constructional column in the corner regions, indicating the consistence of FEA and test results. The failure inter-story drifts of CSPSWO1~CSPSWO4 are 0.0389rad, 0.0315rad, 0.0354rad and 0.0467rad, respectively. Specimen CSPSWO2 performs the worst deformation capacity. The door opening locates in the corner of the outer frame, as shown in Fig. 5(b). The stress concentration in the corners of the opening leads to the undesired fracture of the weld between the frame beam and the frame column. The specimen loses load-bearing capacity due to the fracture and performs the worst deformation capacity and ductility. As a result, the opening should be located off the diagonal tension field of the infill panel.

Table 2

Validation of the FEM by comparisons of characteristic values between test and FEA

Specimen	Loading direction	$K_0$ (kN/mm)			$F_u$ (kN)		
		Test	FEA	FEA/Test	Test	FEA	FEA/Test
CSPSWO1	+	20.4	25.4	1.25	347	342	0.99
	—	21.2	25.4	1.20	356	360	1.01
CSPSWO2	+	13.3	16.3	1.23	315	291	0.92
	—	16.1	16.3	1.01	291	291	1.00
CSPSWO3	+	12.6	14.7	1.17	313	318	1.02
	—	12.3	14.7	1.20	312	333	1.07
CSPSWO4	+	6.80	7.80	1.15	242	265	1.09
	—	7.10	7.80	1.10	256	273	1.07
Mean	-	-	-	1.16	-	-	1.02
COV	-	-	-	0.07	-	-	0.05

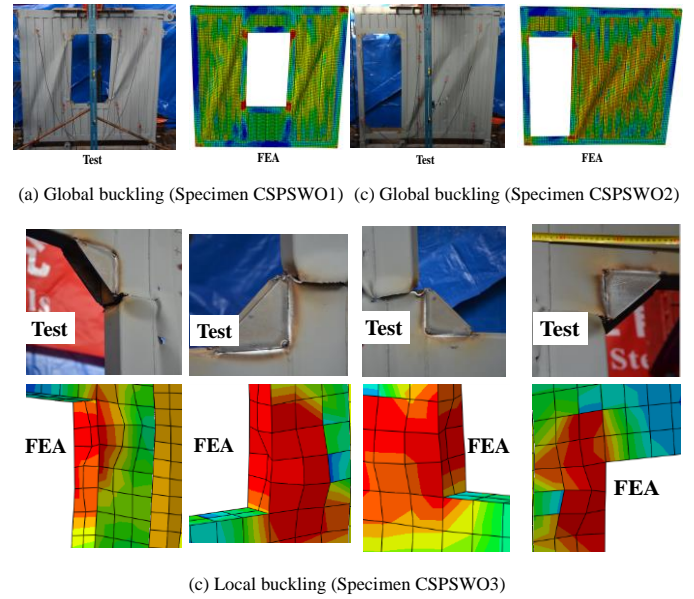


Fig. 5 Comparisons of failure mode between test and FEA

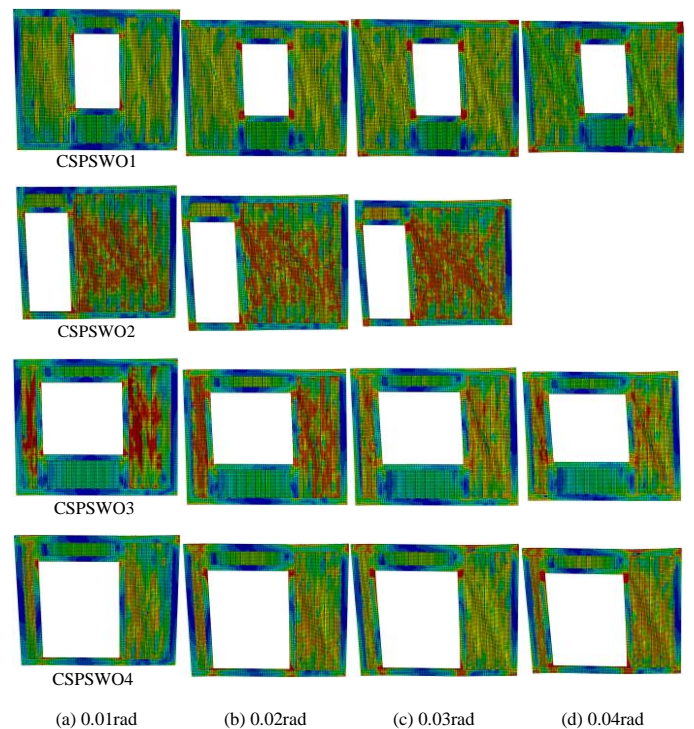


Fig. 6 Failure process of the CSPSW specimens with openings



### 3. Theoretical modelling of CSPSWs with openings

#### 3.1. General

The initial stiffness of the infill panel ( $K_w$ ) was derived by Deng et al. [15] as following:

$$K_w = \frac{\gamma}{\frac{H_e^3}{12E \cdot I_z} + \frac{3.12 \cdot H_e}{E \cdot \eta \cdot L_e \cdot t}} \quad (1)$$

where, the thickness and the elastic modulus of the infill panel are denoted by  $t$  and  $E$ , respectively; the effective length and height of the panel are described by  $L_e$  and  $H_e$ , respectively;  $\eta$  indicates the shape factor of the section; as a result of elastic buckling and geometrical imperfections, the initial stiffness is reduced and it is described by  $\gamma$ , based on the following equation.

$$\gamma = 0.014 \ln(L_e / H_e) - 0.118 \ln(\lambda) + 1.24 \quad (2)$$

where,  $\lambda$  represents the relative height-to-thickness ratio of the infill panel, which can be expressed as Eq. (3).  $f_y$  denotes the yield strength of the infill panel.

$$\lambda = \frac{H_e}{t \cdot \sqrt{\frac{235}{f_y}}} \quad (3)$$

Shape factor is a measure of the ratio between the unfolding length and the net length of the corrugated steel plate and it is denoted by  $\eta$ .

$$\eta = \frac{a+d+c}{a+b+c} \quad (4)$$

where,  $a$ ,  $b$ ,  $c$  and  $d$  denote the geometrical parameters, as shown in Fig. 7.

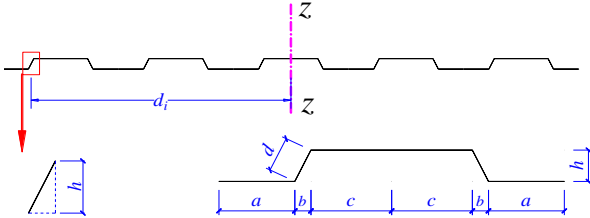


Fig. 7 Cross section characteristics of the corrugated steel plate

The mechanical model of CSPSWs with openings under horizontal force  $f$  was shown in Fig. 8. The infill panel was divided into several regions along the edges of the opening. Each region was equivalent to a spring with elastic stiffness equals to the corresponding corrugated steel plate. The initial stiffness of the spring  $K_{ij}$  can be determined by Eq. (1), where  $K_{ij}$  denotes initial stiffness of the  $i$ th row  $j$ th column region. Taking the window opening in Fig. 8(a) for example, the following equation can be obtained according to the compatibility of deformation.

$$\frac{f}{K_{00}} = \frac{f}{K_1} + \frac{\alpha_{21} \cdot f}{K_{21}} + \frac{f}{K_3} \quad (5)$$

$$\frac{f}{K_{00}} = \frac{f}{K_1} + \frac{\alpha_{22} \cdot f}{K_{22}} + \frac{f}{K_3} \quad (6)$$

where,  $K_{00}$  denotes the initial stiffness of the infill panel with opening;  $\alpha_{21}$  and  $\alpha_{22}$  denote the distribution coefficient of horizontal force in the 2nd layer;  $K_1$  and  $K_3$  denote the initial stiffness of the 1st and 3rd layers, which can be determined by the following equations.

$$K_1 = K_{11} + K_{12} + K_{13} \quad (7)$$

$$K_3 = K_{31} + K_{32} + K_{33} \quad (8)$$

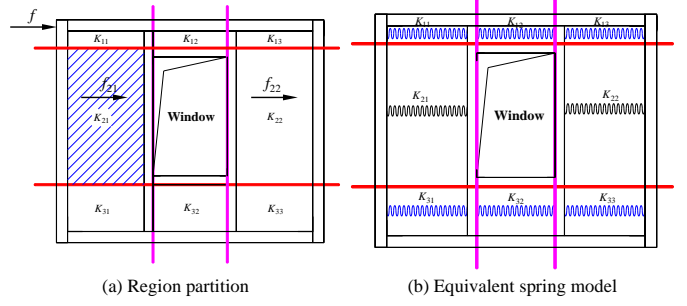


Fig. 8 Mechanical model of CSPSWs with openings

The horizontal force in the 2nd layer was distributed proportionally to the stiffness of the region, yielding the following equations.

$$\alpha_{21} + \alpha_{22} = 1 \quad (9)$$

$$\frac{\alpha_{21}}{K_{21}} = \frac{\alpha_{22}}{K_{22}} \quad (10)$$

Substituting Eqs. (7) ~ (10) into Eq. (5) yields the initial stiffness of the infill panel with openings, as expressed in Eq. (11).

$$K_{00} = \frac{1}{\frac{1}{K_{11} + K_{11} + K_{11}} + \frac{1}{K_{21} + K_{22}} + \frac{1}{K_{31} + K_{32} + K_{33}}} \quad (11)$$

Similarly, Eq. (11) can be generalized as Eq. (12) to calculate the initial stiffness of the infill panel with arbitrary openings.

$$K_{00} = \frac{1}{\sum_{j=1}^n \frac{1}{\sum_{i=1}^m K_{ij}}} \quad (12)$$

where,  $m$  and  $n$  denote the column number and row number of the region after partition.

Considering the contribution of the outer frame to the initial stiffness of CSPSWs with openings, the following equation can be given to predict the initial stiffness of the CSPSWs with openings ( $K_0$ ).

$$K_0 = \frac{1}{\frac{H^3}{6E_1 I_1} (3\phi^2 - 3\phi + 1) + \frac{LH^2 \phi^2}{12E_2 I_2} + \frac{(1-\phi)^2 H^2 L}{12E_3 I_3}} + \frac{1}{\sum_{j=1}^n \frac{1}{\sum_{i=1}^m K_{ij}}} \quad (13)$$

#### 3.2. Verification of the theoretical modelling

In this section, the accuracy of the theoretical derivation was validated by comparing the theoretical values with the test and numerical results. The tests conducted by Ding et al. [15] were adopted and the developed FEM in Section 2 was used to provide more validating datas. Fig 9 and Table 3 provide comparisons between theoretical values ( $K_0$ ) and the related test and numerical results. The specimens used for finite element analysis (FEA) were labeled by the specimen number and the thickness of the infill panel. For example, specimen CSPSWO1-0.8 means the thickness of the infill corrugated steel plate is 0.8mm and the other geometric dimensions are the same as Specimen CSPSWO1.

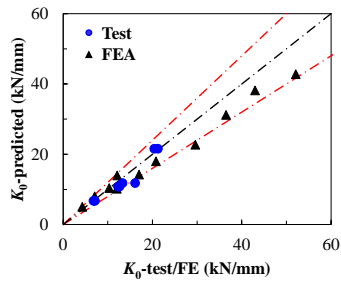
The comparisons indicated that Eq. (13) was effective to predict the initial stiffness of CSPSW with openings. In terms of  $K_0$ -to-test and  $K_0$ -to-FE ratios, the mean value was 0.93 and the coefficient of variation was 0.13. As discussed in Section 2.2, the space between the lateral restraint apparatus and specimens

in the test led to the lower stiffness in the positive direction than the negative direction. Therefore, the  $K_0$ -to-test ratio was averagely higher in the positive direction than that of the negative direction. These validations verify that Eq. (13) derived in this paper is reasonable to predict the initial stiffness of CSPSWs with openings, which will be analysed in depth in the following section.

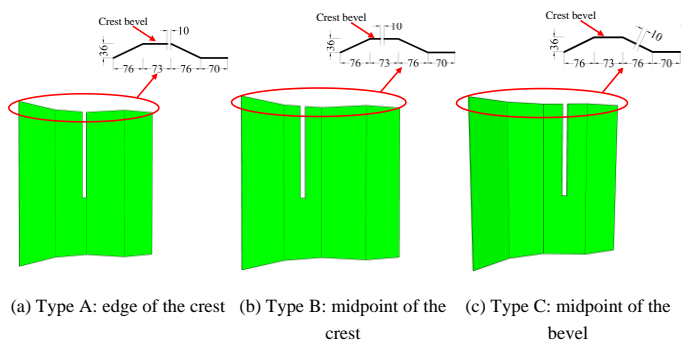
**Table 3**

Validation of the theoretical formulas against the test results and FEA

Specimen		$L \times H$ (m×m)	$l \times h$ (m×m)	Test (kN/mm)	$K_0$ (kN/mm)	$K_0/\text{Test}$
CSPSWO1	+	3.6×3.0	1.00×1.60	20.4	21.6	1.06
	−	3.6×3.0	1.00×1.60	21.2	21.6	1.02
CSPSWO2	+	3.6×3.0	1.00×2.29	13.3	11.8	0.89
	−	3.6×3.0	1.00×2.29	16.1	11.8	0.73
CSPSWO3	+	3.6×3.0	1.80×1.60	12.6	10.8	0.86
	−	3.6×3.0	1.80×1.60	12.3	10.8	0.88
CSPSWO4	+	3.6×3.0	1.80×2.29	6.80	6.76	0.99
	−	3.6×3.0	1.80×2.29	7.10	6.76	0.95
Specimen		$L \times H$ (m×m)	$l \times h$ (m×m)	FEA (kN/mm)	$K_0$ (kN/mm)	$K_0/\text{FEA}$
CSPSWO1-0.8		3.6×3.0	1.00×1.60	12.1	14.0	1.15
CSPSWO1-2.4		3.6×3.0	1.00×1.60	36.5	31.2	0.85
CSPSWO1-3.2		3.6×3.0	1.00×1.60	52.1	42.8	0.82
CSPSWO2-0.8		3.6×3.0	1.00×2.29	10.3	10.4	1.00
CSPSWO2-2.4		3.6×3.0	1.00×2.29	43.0	38.2	0.89
CSPSWO2-3.2		3.6×3.0	1.00×2.29	61.8	51.1	0.83
CSPSWO3-0.8		3.6×3.0	1.80×1.60	7.08	8.03	1.13
CSPSWO3-2.4		3.6×3.0	1.80×1.60	20.8	18.0	0.87
CSPSWO3-3.2		3.6×3.0	1.80×1.60	29.6	22.7	0.77
CSPSWO4-0.8		3.6×3.0	1.80×2.29	4.27	5.05	1.18
CSPSWO4-2.4		3.6×3.0	1.80×2.29	12.0	10.2	0.85
CSPSWO4-3.2		3.6×3.0	1.80×2.29	17.0	14.2	0.84
Mean		-	-	-	-	0.93
COV		-	-	-	-	0.13

**Fig. 9** Validation of the theoretical formulas

#### 4. Parametric analysis on CSPSWs with vertical slits

**Fig. 10** Different locations of the vertical slits

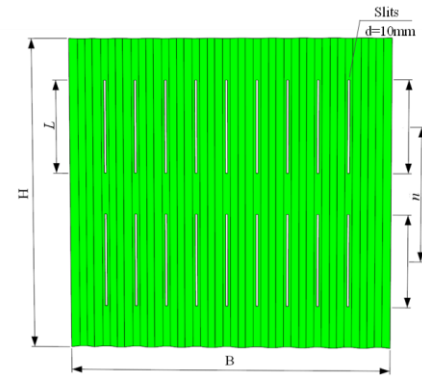
In this section, the verified FEM was used to analyse the factors influencing the lateral behaviour of CSPSWs with vertical slits. The considered parameters include thickness of the infill panel, the location and layer of the slits. The detailed dimensions of the models in parametric study and FEA results were listed in Table 4. It should be mentioned that the spacing of each slit is 295mm and the width of the slit was 10mm. The different locations of the vertical slits are shown in Fig. 10. Fig. 11 shows CSPSWs models with different layers of vertical slits.

**Table 4**

Parameters and analysis results of CSPSWs with slits

Specimen	Slit	$n$	Location of the vertical slits	$t$ (mm)	$L$ (mm)	$P_u$ (kN)	$K_0$ (kN/mm)
SW-1	Yes	1	B	2.0	3000	85.41	11.16
SW-2	Yes	1	C	2.0	3000	66.96	6.83
SW-3	Yes	1	B	3.0	3000	144.97	16.60
SW-4	Yes	1	C	3.0	3000	177.35	9.54
SW-5	Yes	1	B	4.0	3000	247.82	21.55
SW-6	Yes	1	C	4.0	3000	221.44	12.87
SW-7	Yes	1	B	5.0	3000	337.24	26.32
SW-8	Yes	1	C	5.0	3000	273.40	15.57
SW-9	Yes	1	B	6.0	3000	418.06	30.82
SW-10	Yes	1	C	6.0	3000	321.42	18.38
SW-11	Yes	1	B	8.0	3000	509.34	38.74
SW-12	Yes	1	B	8.0	3000	429.34	23.75
SW-13	Yes	1	B	6.0	3000	504.59	36.87
SW-14	Yes	2	B	6.0	1500	842.27	71.80
SW-15	Yes	3	B	6.0	1000	1036.78	92.38
SW-16	Yes	1	A	6.0	3000	466.90	34.20
SW-17	Yes	2	A	6.0	1500	760.60	68.58
SW-18	Yes	3	A	6.0	1000	934.47	90.44
SW-19	Yes	1	C	6.0	3000	467.38	23.78
SW-20	Yes	2	C	6.0	1500	740.63	47.83
SW-21	Yes	3	C	6.0	1000	910.62	69.58
SW-22	No	—	—	4.0	—	486.41	76.01
SW-23	No	—	—	6.0	—	576.70	89.59

Note:  $n$ : number of the layers of the slits;  $t$ : thickness of the corrugated steel plate;  $L$ : length of the slits.

**Fig. 11** Details of CSPSWs

##### 4.1. Influence of the vertical slit

Fig. 12 and Fig. 13 showed the first buckling mode of the CSPSWs with and without slits with two different thickness of the corrugated steel plate. It can be found out that global buckling occurred for the specimens without slit, i.e., Specimen SW-22 and Specimen SW-23. However, local buckling occurred for



the wall limbs between the slits for the specimens with slits. This finding suggested that the vertical slits changed the load bearing mechanism of CSPSWs. Local buckling occurred for the specimen with slits, which was favorable to dissipate energy under earthquake.

The load-displacement curves of Specimen SW-5, SW-6 and SW-22 were displayed by Fig. 14. As shown in Fig.14, before the lateral displacement reaches 9.8mm, Specimen SW-22 which is without slits behaves almost in an elastic manner and global buckling can be observed. With the temporary occurrence of the “negative stiffness”, the decrease of load-displacement curve can be observed correspondingly. With the increasing of displacement, tension strip develops after drifts of 10.3mm and the load bearing capacity begins to increase. Different from Specimen SW-22, shear yielding occurred for Specimen SW-5 and SW-6 which were with slits. Each specimen failed due to tension field development, fracture propagation, local buckling and fracture of the infill panel. The elastic stage, the yielding development stage and the failure stage occurred in sequence during the damage process. The results indicate that the initial stiffness and ultimate load of the CSPSWs were significantly reduced due to the slits. Specifically, the initial stiffness and ultimate load of Specimen SW-22 is 96.3% and 252.7% higher than Specimen SW-5 and those of Specimen SW-6 is 119.7% and 490.6% lower than Specimen SW-22. However, the ductility of CSPSWs with slits was improved due to the fact that the failure mode of CSPSWs changed from global buckling to shear yielding.

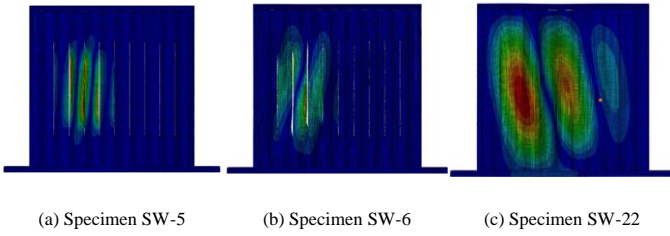


Fig. 12 First buckling mode of CSPSWs with and without slits ( $t=4.0\text{mm}$ )

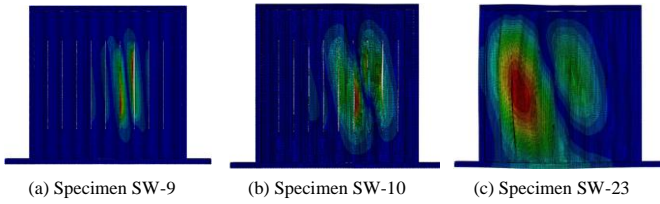


Fig. 13 First buckling mode model of CSPSWs with and without slits ( $t=6.0\text{mm}$ )

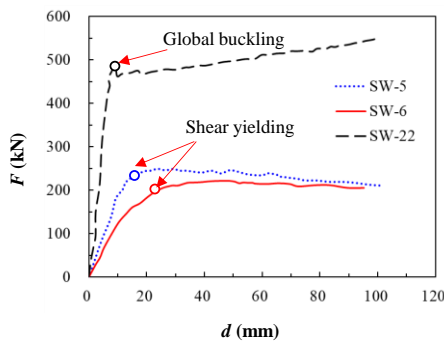


Fig. 14 Influence of vertical slits on lateral load-displacement curve of CSPSWs

#### 4.2. Influence of layers of the vertical slit

Fig. 15 shows the first buckling model of Specimens SW-13 to SW-21. Local buckling can be found for the Specimens with one layer of vertical slit. With the increasing of layers of the vertical slit, the first buckling model of the specimen was close to global buckling, resulting in larger plastic area of the infill panel. This finding suggested that increasing layers of the vertical slit may increase the energy dissipation capacity of CSPSWs. Meanwhile, the buckling mode of the specimens with three layers of vertical slits was similar to the CSPSWs without slits. Therefore, it can be concluded that increasing the layers of the slit can improve the integrity and mechanical property of CSPSWs.

Fig. 16 shows the load-displacement curves of Specimen SW-13 to SW-21. As shown in the picture, both of the initial stiffness and ultimate load of the specimen improved with the increasing of the layers of the vertical slit. The initial stiffness of specimens with three layer slits SW-18 and SW-15 are 100.1% and 105.5% higher than specimens with one layer slits SW-16 and SW-13. Moreover, the initial stiffness of specimen SW-16 and SW-13 are 164.4% and 150.6% lower than those of Specimens SW-18 and SW-15. Comparing with Specimen SW-19, the initial stiffness and ultimate load of Specimen SW-21 increase by 192.6% and 94.7%, respectively. It indicated that the lateral behavior of CSPSWs was obviously affected by the layer of the slit. It is suggested to increase the layer of slit to improve the lateral behavior of CSPSWs with slits.

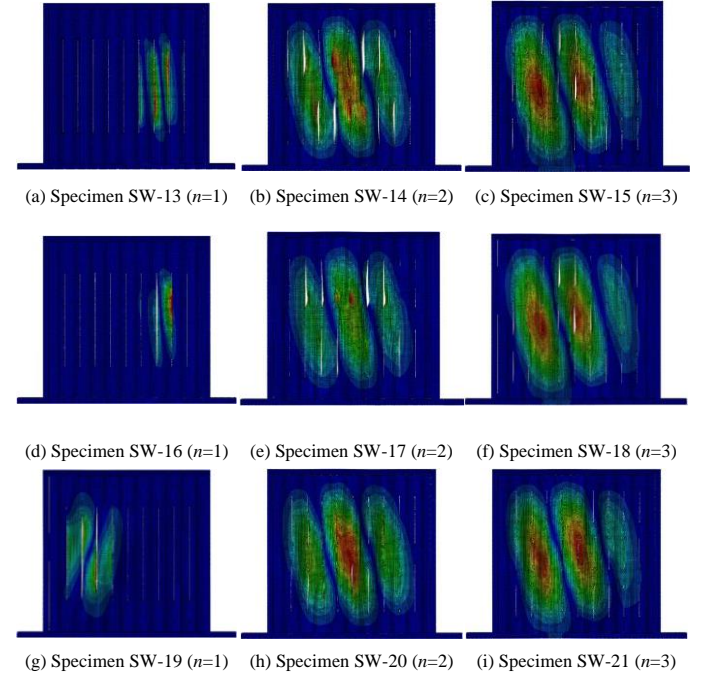


Fig. 15 First buckling model of Specimens with different layers of the vertical slit

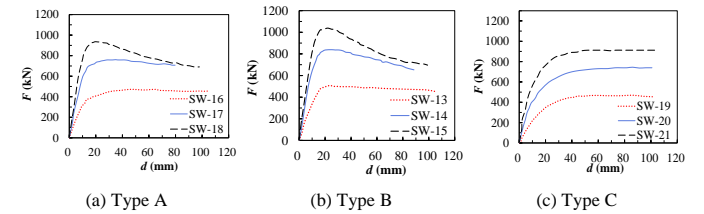


Fig. 16 Influence of layers of vertical slits on lateral load-displacement curve of CSPSWs

#### 4.3. Influence of location of the vertical slits

Fig. 17 showed the load-displacement curves of specimens with different location of the slit. It can be seen that Specimens SW-13, SW-14, SW-15 performed better than other specimens with the same layer of vertical slit. With the increasing of the displacement, the curves of Specimen SW-13 to SW-15 whose slits are on the crest occur the descent stage. Meanwhile, the curves of Specimen SW-19 to SW-21 occur ascending stage and tend to be stable. It can be concluded from Table 4 that it is better to set the slit at the midpoint of the crest to obtain higher initial stiffness and load bearing capacity. Furthermore, the difference can be more obvious with the increasing of the layer of the slits.

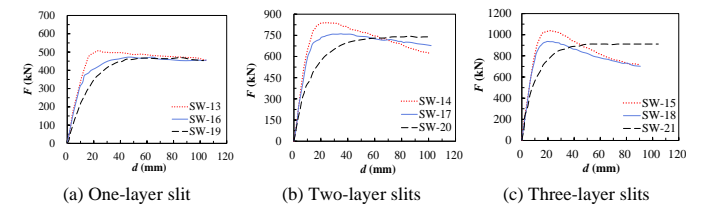


Fig. 17 Load-displacement curve of Specimens with different location of slits

### 5. Parametric analysis on CSPSWs with openings

Conventionally, the vertical position of the opening is determined by the building function. The bottom edge of the window is set to a fixed value and the bottom edge of the door is required to fall on the ground. Therefore, only the horizontal position of the opening was considered and discussed. The axes of the opening are displayed in Fig. 18. Each specimen is divided into seven parts along the horizontal direction averagely. Specimens CSPSWO1~CSPSWO4 were used for analysis. Each specimen with different thickness ( $t$ ) and different height of the crest of the corrugated steel plate ( $h$ ) was analyzed and discussed to provide a better understanding on how the location of the opening affects the specimens and to explore the proper design recommendation. The influence of the location of the opening on initial stiffness of CSPSWs with openings is shown in Fig. 19.

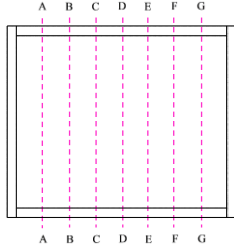


Fig. 18 The axes of the opening for parametric analysis

It is indicated that the location of the opening influence the initial stiffness of CSPSW significantly, as shown in Fig. 19. The specimens have the least initial stiffness when the opening is located in the middle of the specimen, i.e., the axis of the opening is D. On the contrary, the specimens have the largest initial stiffness when the opening is located in the edges of the specimen, i.e., the axis of the opening is A or G. It can be concluded that it is the most unfavorable to locate the opening in the middle of the specimen. The influence of the location of the opening is especially obvious with higher  $t$  and  $h$ . Take Specimen CSPSWO1 as an example, the initial stiffness of the specimen is 119.5kN/mm and 68.5kN/mm when the axis of the opening is A and D, respectively, with the thickness of the infill panel is fixed to 4mm. The initial stiffness of the specimen is 1.74 times higher with the opening in the edge than in the middle. The initial stiffness of the specimen is 56.2kN/mm and 31.9kN/mm when the axis of the opening is A and D, respectively, with the height of the crest of the corrugated steel plate is fixed to 80mm. The initial stiffness of the specimen is 1.76 times higher with the opening in the edge than in the middle. Therefore, it is recommended to locate the opening close to the edges of the specimen to alleviate the weakening of the opening on the initial stiffness of CSPSWs. As discussed in Section 2.2, it is recommended that the opening should not be placed at the end of the diagonal tension field to ensure the deformation capacity and ductility of the specimen. Therefore, the location of the opening is recommended as shown in Fig. 20.

## 6. Conclusions

This paper investigated the lateral behavior of CSPSWs with openings or slits in modular steel construction numerically and theoretically. A finite element model was developed and the numerical results are consistent to the test results, which verifies the reliability of the FEM. The failure process of the specimens was revealed and evaluated. In addition, CSPSWs were studied parametrically for initial stiffness and ultimate load considering parameters related to the vertical slit and the opening. The influence of the vertical slit or openings on lateral behavior of CSPSWs was revealed and discussed in detail. The design consideration of the openings and slits was recommended based on the present study. Following are the main conclusions.

- (1) CSPSWs with openings is simulated using the developed FEM, including the initial stiffness, ultimate shear capacity, and failure mode.
- (2) Stress concentration exists in the corner regions of the opening. It is recommended that the opening should be located off the end of the diagonal tension field to guarantee the deformation capacity and ductility of the specimen.
- (3) Compared with the CSPSWs without slits, the ultimate load and initial stiffness of CSPSWs with slits are reduced significantly. Meanwhile, the failure mode of the CSPSWs with slits changed from global buckling to shear yielding.
- (4) The initial stiffness and ultimate load of CSPSWs improved with the increasing of the layer of slits. It is better to set the slit at the midpoint of the crest to obtain higher initial stiffness and load bearing capacity.
- (5) The location of the opening impacts the initial stiffness of CSPSWs obviously. The opening is suggested to be located at the edge of the specimen to obtain higher initial stiffness.

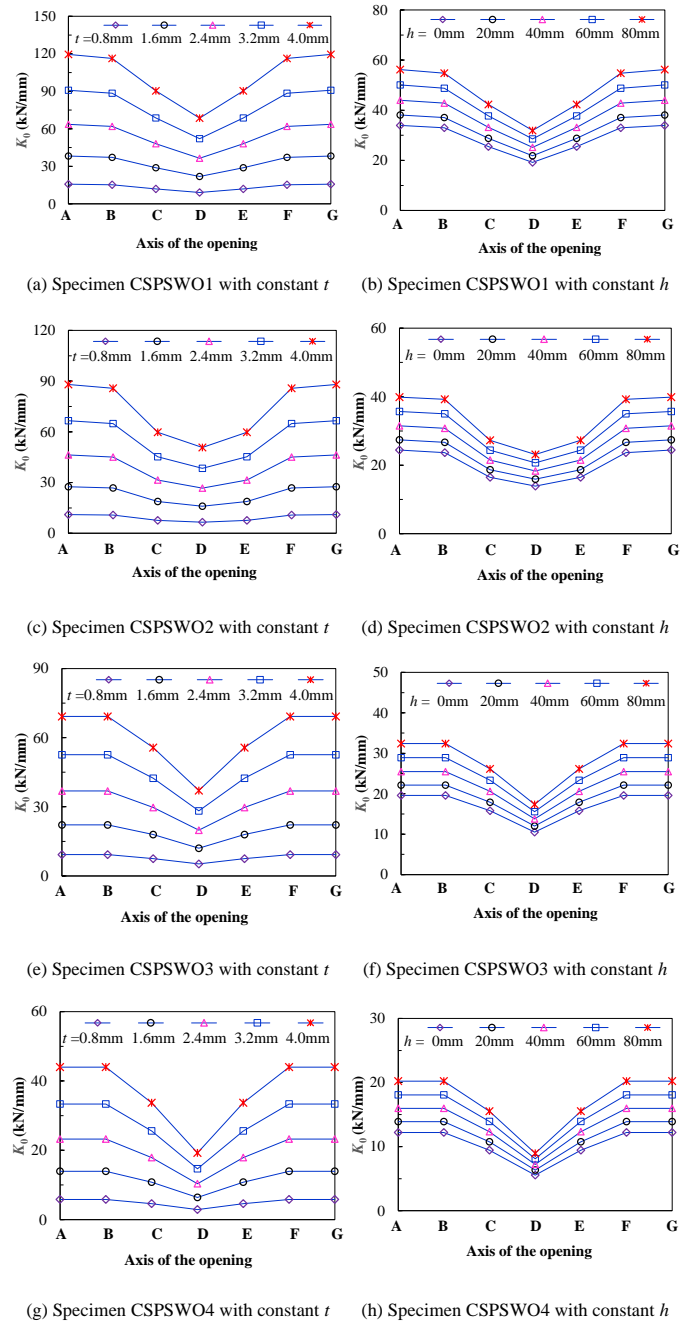


Fig. 19 Influence of the location of the opening on initial stiffness of CSPSWs

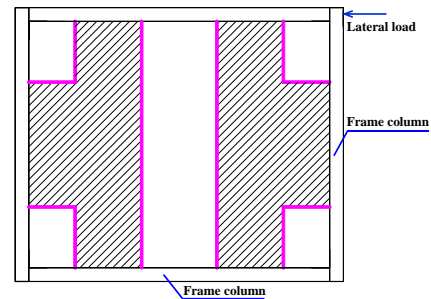


Fig. 20 Suggested location for opening (hatched)

## Acknowledgements

The reported research work was sponsored by the National Natural Science Foundation of China (Grant Nos. 52378206 and 51908511), Young Talent Lifting Project of Henan Province (No. 2023HYTP015) and the Program for Innovative Research Team (in Science and Technology) in University of Henan Province (Grant No. 23IRTSTHN006).

## References

- [1] Li, G.Q., Cao K., Lu, Y. EFFECTIVE LENGTH FACTOR OF COLUMNS IN NON-SWAY MODULAR STEEL BUILDINGS, *Adv. Steel Con*, 2017, 13(4): 412-426.
- [2] Liu, H.B., Zhou, Y. and Chen, Z.U. STRUCTURAL PERFORMANCE AND DESIGN METHOD OF NEW MORTISE-TENON FULL STEEL-TUBE SCAFFOLD, *Adv. Steel Con*, 2018, 14(2), 291-307.
- [3] Park K.S., Moon J., Lee S.S., Bae K.W. and Charles W.R. Embedded steel column-to-foundation connection for a modular structural system. *Eng Struct*, 2016, 110: 244-257.
- [4] Sanches R, Mercan O, Roberts B. Experimental investigations of vertical posttensioned connection for modular steel structures. *Eng Struct*, 2018, 175: 776-789.
- [5] Deng E.F., Zong L., Ding Y., Zhang Z., Zhang J.F., Shi F.W., Cai L.M., Gao S.C. Seismic performance of mid-to-high rise modular steel construction - A critical review. *Thin Wall Struct*, 2020, 155: 106924.
- [6] Lawson RM, Ray O and Chris G. *Design in Modular Construction*. CRC Press, Boca Raton, FL, 2014.
- [7] Kim J.Y., Lee J.K. A basic study on the application of modular construction, *J Korean Hou Asso*, 2014, 25(4): 39-46.
- [8] Liew J.Y.R., Dai Z. and Chua Y.S. Steel concrete composite systems for modular construction of high-rise buildings. *Proceedings of the 12th International Conference on Advances in Steel-Concrete Composite Structures*, 2018, València, Spain, June.
- [9] Liew J.Y.R., Dai Z. and Wang Y. Prefabricated prefinished volumetric construction in high-rise buildings. *Proceedings of the 11th Pacific Structural Steel Conference*, 2016, Shanghai, China, October.
- [10] Lacey A.W., Chen W.S., Hao H., Bi K.M. Structural response of modular buildings—an overview. *J Build Eng*, 2018, 16: 45-56.
- [11] Cao, Q., Huang, J.Y. Experimental study and numerical simulation of corrugated steel plate shear walls subjected to cyclic loads. *Thin Wall Struct*, 2018, 123: 306-317.
- [12] Qiu, J., Zhao, Q.H., Wang, ZY. Lateral behavior of trapezoidally corrugated wall plates in steel plate shear walls, Part 1: Elastic buckling. *Thin Wall Struct*, 2022, 174: 109104.
- [13] Giriunas K., Sezen H. and Dupaux R.B. Evaluation, modelling, and analysis of shipping container building structures. *Eng Struct*, 2012, 43: 48-57.
- [14] Fereshteh E, Massood M, Abolhassan V. Experimental study on cyclic behavior of trapezoidally corrugated steel shear walls. *Eng Struct*, 2013, 48: 750-762.
- [15] Deng E.F., Zong L., Ding Y. Numerical and analytical study on initial stiffness of corrugated steel plate shear walls in modular construction. *Steel Compos Struct*, 2019, 32(3): 347-359.
- [16] Yu Y.J., Chen Z.H. Rigidity of corrugated plate sidewalls and its effect on the modular structural design. *Eng Struct*, 2018, 175: 191-200.
- [17] Lu, J.Y., Qiao, X.D., Liao, J.. Experimental study and numerical simulation on steel plate shear walls with non-uniform spacing slits. *Interna J Steel Struct*, 2016, 16(4): 1373-1380.
- [18] Lu, J.Y., Zhang H.Y., Yu S. Study on seismic behaviors of self-centering steel plate shear walls with slits. *J Constr Steel Res*, 2021, 185: 106878.
- [19] Wang W., Kong J.H., Zhang Y.F. Seismic Behavior of Self-Centering Modular Panel with Slit Steel Plate Shear Walls: Experimental Testing. *J Struct Eng*, 2018, 144(1): 04017179.
- [20] Ding Y., Deng E.F., Zong L., Dai X.M., Lou N., Chen Y. Cyclic tests on corrugated steel plate shear walls with openings in modularized-construction. *J Constr Steel Res*, 2017, 138: 675-691.
- [21] Farzampour A., Laman J.A. Behavior prediction of corrugated steel plate shear walls with openings, *J Constr Steel Res*, 2015, 114: 258-268.
- [22] ABAQUS (2013), User manual Version 6.13. DS SIMULIA Corp, Providence, RI, USA.
- [23] Bahrebar M., Kabir M.Z., Zirakian T., Hajsadeghi M., Lim J.P.B. Structural performance assessment of trapezoidally-corrugated and centrally-perforated plate shear walls, 2016, *J Constr Steel Res*, 122: 584-594.
- [24] Eurocode (2003), *Design of Steel Structures. Part 1.5: Plated Structural elements*, European Committee for Standardization; Brussels, Belgium.



# INVESTIGATING FATIGUE MECHANISMS AND CRACK GROWTH IN 20MNTiB STEEL HIGH-STRENGTH BOLTS: AN EXPERIMENTAL AND SIMULATION STUDY

Jin-Feng Jiao<sup>1,2</sup>, Li-Xuan Fan<sup>2</sup>, Yong Liu<sup>3</sup>, Hong-Gang Lei<sup>2</sup> and Qi Guo<sup>2,\*</sup>

<sup>1</sup> Department of Architecture, Lyuliang University, Lyuliang, Shanxi Province, China

<sup>2</sup> College of Civil Engineering, Taiyuan University of Technology, Taiyuan, Shanxi Province, China

<sup>3</sup> Shandong Electric Power Engineering Consulting Institute Corp., Ltd, Jinan, Shandong Province, China

\* (Corresponding author: E-mail: guoqi\_tony@163.com)

## ABSTRACT

In this paper, axial-tensile, constant-amplitude fatigue experiments are performed on M24 high-strength bolts with grade 8.8 fabricated from 20MnTiB steel with a stress ratio ( $R$ ) of 0.3, and their crack development is simulated. The stress range-fatigue life ( $S-N$ ) curve is derived by using the experimental results. The fatigue mechanism is then investigated through strain and fractographic analyses. Moreover, the extended finite element method (XFEM) is applied for assessing the fatigue crack propagation behavior of the high-strength bolts. The findings reveal that the 20MnTiB steel bolt exhibits a threshold fatigue strength of 140.77 MPa at two million loading cycles, which is 1.68 times greater than the corresponding value for 35K steel bolts at the same stress ratio. The bolt's stable deformation stage constitutes 87% of its total fatigue life. The XFEM is capable of accurately predicting the fatigue crack propagation trajectory and the lifespan of the high-strength bolts. Our analysis indicates that the crack initially propagates predominantly along the bolt's circumferential direction, accounting for 85% of the overall crack propagation life, before transitioning to unstable growth and experiencing an exponential increase in length.

## ARTICLE HISTORY

Received: 9 December 2022  
Revised: 10 May 2023  
Accepted: 11 May 2023

## KEYWORDS

High-strength bolt;  
Constant-amplitude fatigue;  
Fatigue fracture propagation;  
Extended finite element method (XFEM);  
Stress intensity factor (SIF)

Copyright © 2023 by The Hong Kong Institute of Steel Construction. All rights reserved.

## 1. Introduction

High-strength bolts play a crucial role in securing prefabricated steel structures and are extensively employed in offshore wind turbines and grid structures [1-3]. Despite their resilience, bolts are exposed to cyclic loads throughout their service life. Although they may not fail instantly under such loading conditions, the progressive accumulation of fatigue damage ultimately compromises their mechanical properties, leading to engineering failures [4]. Consequently, the fatigue behavior of bolts warrants investigation.

Numerous studies have been conducted to explore the fatigue properties of high-strength bolts, including research by Yang et al. [3,5], Qiu et al. [6], Jiao et al. [7,8], Liu et al. [9], Tizani et al. [10], and Schumann and Rasmus [11]. These works focused on factors influencing bolt fatigue properties, such as geometry, types, and surface heat treatment. Jiang et al. [12] introduced a method to calculate the critical loosening load of bolted connections under lateral loading. The wealth of fatigue test data obtained has enhanced the understanding of high-strength bolt fatigue properties. As a result, Bartsch and Feldmann [13] recommended adopting the fatigue classification in EC 3-1-9 after reviewing approximately 573 groups of experimental fatigue data on high-strength bolts with varying constructional details.

Furthermore, the fracture surface retains essential information about the bolt's fatigue process, recording a wealth of specific fatigue data. Consequently, fractography analysis can be employed to study the fatigue failure process [14]. Maljaars and Euler [15] and Lochan et al. [16] reported that bolts subjected to tensile force frequently fractured at the first engaged thread due to stress concentration caused by the thread shape. Kaushik and Anup [17] argued that fiber trajectories and microscopic fracture texture micro-flows could indicate the crack growth path. Liu et al. [18] also determined the fatigue crack growth rate through fractography analysis using scanning electron microscopy (SEM).

The advancement of finite element modeling has led to an increasing number of researchers adopting this technique to uncover the fatigue failure mechanisms of components. Wang et al. [19], for example, demonstrated that the drilling position significantly influenced the peak stress on the hole edge using finite element analysis. Fang et al. [20] simulated crack propagation direction and path in a perforated plate using Abaqus, with results closely aligning with experimental data. In another study, Gu et al. [21] calculated the stress intensity factor (SIF) of cold-formed, circular, hollow-section (CFCHS), T-type, welded joints using Ansys software and developed a method for assessing the fatigue life of such joints. The extended finite element method (XFEM) is the most prevalent technique for investigating fatigue crack propagation issues. Researchers such as Shi et al. [22], Malekan et al. [23], and Shu et al. [24] found that XFEM could accurately predict fracture location, crack propagation path, fatigue fracture morphology, and fatigue life of standard

specimens. Additionally, Samai et al. [25], Bergara et al. [26], and Ngoula et al. [27] employed XFEM to examine fatigue crack growth in connection plates with varying joints, aero-engine blades, and cruciform welded joints, respectively. Pandey et al. [28] simulated the fatigue life of compact tension (CT) specimens and turbine disks composed of different materials using continuum damage mechanics and XFEM. Lin and Smith [29] predicted the fatigue crack propagation life of cracked slabs, while Yang and Kuang [30] and Kumar and Prakash [31] analyzed the effects of thread angle, mesh size, and crack size on the SIF of bolts using XFEM. These analyses achieved satisfactory prediction accuracy.

In summary, previous research has conducted numerous experiments on factors affecting the fatigue properties of bolts. Furthermore, the material composition of a bolt significantly influences its fatigue behavior [32]. Consequently, stress range-fatigue life ( $S-N$ ) data derived from tests on bolts made of different materials can offer valuable insights for accurately predicting their fatigue life. However, the study of fatigue crack propagation in high-strength bolts remains limited.

This paper examines the constant-amplitude fatigue properties of 20MnTiB steel high-strength bolts at a stress ratio ( $R$ ) of 0.3. An  $S-N$  curve is constructed based on the test data. The results are then compared with existing research data on the fatigue properties of 35K steel high-strength bolts to determine the impact of material properties on bolt fatigue behavior. The fatigue fracture process and characteristics of the fatigue-fractured surfaces are analyzed using strain analysis and fractographic analysis. Furthermore, the crack propagation process of the bolts is modeled using XFEM, and the SIF at the crack front and the crack characteristics at different propagation stages are discussed. Finally, the crack propagation law and fracture mechanism of high-strength bolts are investigated.

## 2. Experimental

### 2.1. Preparation of specimens

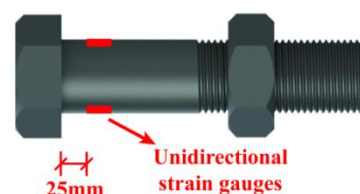


Fig. 1 Specimen design

The fatigue test was carried out on grade 8.8 M24 high-strength bolts made from 20MnTiB steel, a material frequently used in engineering applications. The rod was ground 25 mm away from the bolt head to attach a strain gauge, which monitored changes in the bolt rod's strain during the test and ensured the correct application of tightening torque, as depicted in Fig. 1.

## 2.2. Fundamental mechanical properties

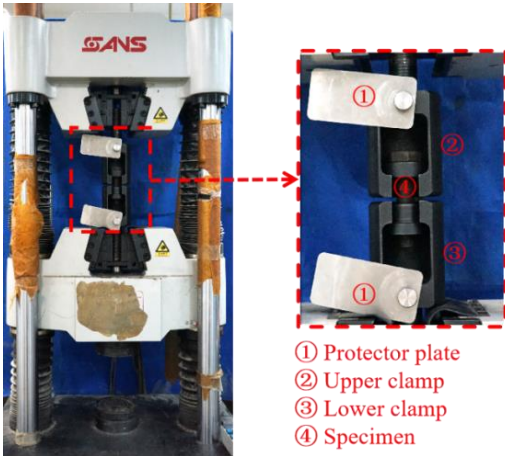


Fig. 2 Electrohydraulic servo universal testing machine

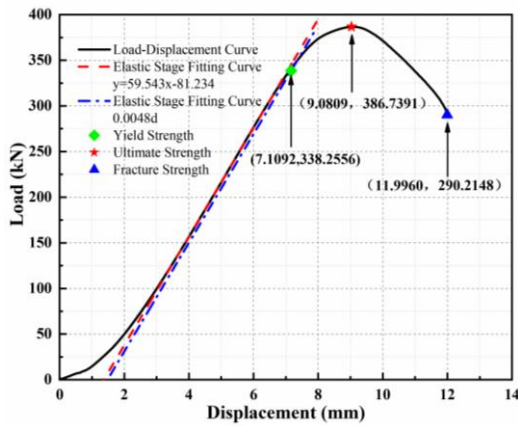


Fig. 3 Load-displacement curve

The static test was employed for determining the bolts' mechanical properties, design a suitable loading system for the fatigue experiments, and provide a constitutive relationship for subsequent finite element analysis. In accordance with ISO 898-1:2013 standard [33], three specimens were randomly chosen for testing. An electrohydraulic servo universal testing machine performed the tensile test using force control (Fig. 2), with a loading rate of 2.7 kN/s.

The test data were processed, and load-displacement curves were generated. Fig. 3 illustrates the load-displacement curve for one specimen. Elastic modulus ( $E$ ), yield strength ( $f_y$ ), and ultimate strength ( $f_u$ ) were calculated for the three specimens after fracture, and the average values were taken, as presented in Table 1.

Table 1

Mechanical attributes of the high-strength bolt

Test results	Mechanical properties		
	$E$ (MPa)	$f_y$ (MPa)	$f_u$ (MPa)
20MnTiB	$2.66 \times 10^5$	780.30	861.80

## 2.3. Constant-amplitude fatigue testing

Considering the three structural classifications of bolts in relevant specifications [34,35,36,37], the fatigue strength of the base metals in bolted end-plate connections is the highest for 2 million loading cycles, followed by the shear fatigue of the bolt. The tensile fatigue strength of the bolt is the lowest, with a difference of over 50% compared to the other two. This suggests that bolt fatigue under tension is disadvantageous, and this section investigates the constant-amplitude fatigue properties of high-strength bolts subjected to axial tension.

### 2.3.1. Fatigue testing system

Given the experimental conditions and referring to the standard static tensile testing device [33] and previous related studies [7,8], a simplified loading device for axial-tensile fatigue experiments was designed and installed in the MTS testing machine (Figs. 4a and 4b).

To ensure sufficient stiffness and stability, the thickness of the clamp base plate was set at 25 mm, and stiffening ribs were welded to both sides of the device. Additionally, the loading device was aligned so that the bolt only experienced axially tensile loads during testing. A torque wrench pretensioned the bolt while monitoring the strain to guarantee proper pretensioning application (Fig. 4c).

The fatigue test began after completing the above procedures. Throughout the test, the strain changes on the bolt were recorded every 30 minutes to estimate crack growth. The fatigue test concluded when the bolt failed.

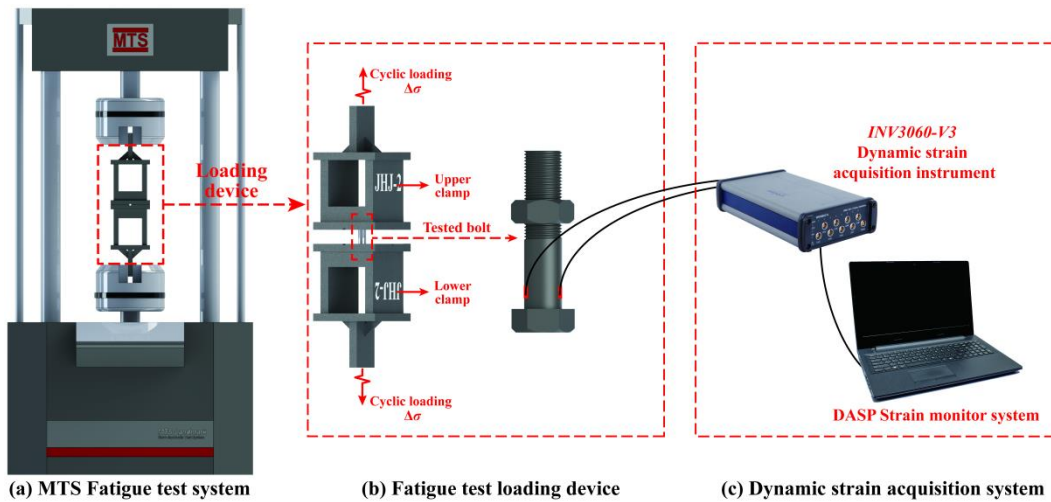


Fig. 4 Fatigue testing setup

### 2.3.2. Loading scheme

The stress level in the fatigue test primarily consists of two numerical indicators: minimum stress ( $\sigma_{min}$ ) and maximum stress ( $\sigma_{max}$ ). With a fixed stress ratio ( $R$ ), the stress level can be represented by the stress range ( $\Delta\sigma$ ). The stress

level of the loading scheme corresponding to the bolt was calculated based on its effective cross-sectional area.

The present research explored the fatigue characteristics of high-strength bolts at an  $R$  value of 0.3. A sinusoidal wave with a frequency of 7 Hz was

employed to apply the fatigue load. The stress range ( $\Delta\sigma$ ) varied from 180 to 280 MPa in order to investigate the bolts' fatigue behavior under elevated stress levels. Prior to the fatigue test, a pretensioning torque ( $T$ ) given by Eq. (3) was applied to the bolt to simulate its actual stress state.

$$R = \sigma_{\min} / \sigma_{\max} \quad (1)$$

$$\Delta\sigma = \sigma_{\max} - \sigma_{\min} \quad (2)$$

**Table 2**

The loading scheme and fatigue test results of the bolt with an  $R$  of 0.3

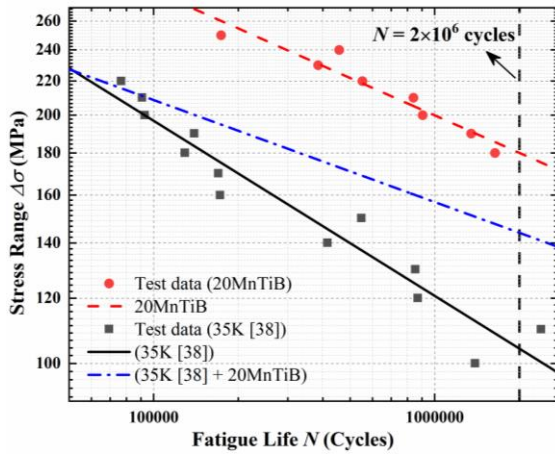
Specimen	$\sigma_{\max}$ , (MPa)	$\sigma_{\min}$ , (MPa)	$\Delta\sigma$ , (MPa)	$T$ , (N·m)	Fatigue life, $N$ , ( $\times 10^4$ )
S-01	257.14	77.14	180	330	163.83
S-02	271.43	81.43	190	440	134.41
S-03	285.71	85.71	200	350	90.64
S-04	300.00	90.00	210	270	83.97
S-05	314.29	94.29	220	370	55.29
S-06	328.57	98.57	230	270	38.47
S-07	342.86	102.86	240	370	45.72
S-08	357.14	107.14	250	370	17.37

### 3. Results

All bolts underwent fatigue fractures, with their fatigue lives presented in Table 2.

#### 3.1. $S$ - $N$ curves

Fig. 5 illustrates the double logarithmic regression analysis relating stress range ( $\Delta\sigma$ ) to fatigue loading cycles ( $N$ ). All test results are uniformly distributed near the fitting line, with a 95% confidence level. A negative correlation exists between  $\Delta\sigma$  and  $N$ .



**Fig. 5** The double logarithmic regression curve of the stress range versus the fatigue loading cycles

**Table 3**

$S$ - $N$  curve and fatigue strength comparison for high-strength bolts fabricated from distinct materials

Test data	$S$ - $N$ curves	Correlation coefficient ( $R^2$ )	$[\Delta\sigma]_{2 \times 10^6}$	$[\Delta\sigma]_{2 \times 10^6} / f_u$
20MnTiB steel	$\lg(\Delta\sigma) = -0.151 \cdot \lg N + 3.205 \pm 0.107$	0.918	140.77 MPa	0.18
35K steel [38]	$\lg(\Delta\sigma) = -0.212 \cdot \lg N + 3.356 \pm 0.095$	0.933	83.83 MPa	0.14
35K steel [38] + 20MnTiB steel	$\lg(\Delta\sigma) = -0.124 \cdot \lg N + 2.938 \pm 0.276$	0.251	76.36 MPa	—

#### 3.2. Analysis of dynamic strain

The strain data are closely associated with the local shape of the component and can depict the stress redistribution near the sensor. The local component damage is intuitively characterized, and the curve trend can qualitatively assess the crack growth process. The strain data gathered on the bolt rod are illustrated

$$T = K \cdot F \cdot d_0 \quad (3)$$

where  $K$  represents the tightening torque coefficient related to surface treatment,  $F$  denotes the pretensioning force, and  $d_0$  represents the high-strength bolt's nominal diameter, which equals 24 mm. Table 2 displays the loading scheme for this test.

The  $S$ - $N$  curve for the 35K steel high-strength bolt [38] is also displayed at the same  $R$  value. Additionally, Fig. 5 includes another curve that fits data for both 35K [38] and 20MnTiB steel bolts, enabling a comparison of the fatigue properties between M24 high-strength bolts made from 20MnTiB and 35K steel. The fatigue characteristics of the 35K steel bolt are less favorable compared to those of the 20MnTiB steel bolt at the same stress range, indicating that material properties have an impact on the bolt's fatigue life.

Table 3 shows the fatigue properties of bolts made of 20MnTiB and 35K steel. Both curves modeling the 20MnTiB and 35K steel [38] bolts exhibit a relatively high goodness of fit. When the number of loading cycles reaches  $2 \times 10^6$ , the fatigue strength of the 20MnTiB steel bolt is 1.68 times greater than that of the 35K steel bolt. This is because fatigue properties are associated with the yield strength to ultimate strength ratio of the material: a higher ratio facilitates stress redistribution of the material at the notch or thread root [39]. The yield strength to ultimate strength ratio of the 20MnTiB and 35K steel bolts is 0.91 and 0.75 [38], respectively, with the former being 1.21 times higher than the latter, resulting in superior fatigue properties for the 20MnTiB steel bolt.

Moreover, the fatigue strength at  $2 \times 10^6$  loading cycles to yield strength ratio, obtained from the static test for the 20MnTiB and 35K steel bolts, is only 0.18 and 0.14, respectively. This indicates that high-strength bolts may experience fatigue fractures under cyclic stress levels significantly below their yield strength [16], warranting attention.

Nonetheless, the correlation coefficient of the  $S$ - $N$  curve obtained by fitting the test data on the 35K [38] and 20MnTiB steel bolts together decreases to 0.251, rendering this curve unrepresentative. This suggests that material properties considerably impact fatigue life. Thus, incorporating a correction factor into the  $S$ - $N$  curve assists in obtaining the actual fatigue strength of the bolts, serving as a reference for engineering design practice.

in Fig. 6, with the points representing the average strain amplitude at each time.



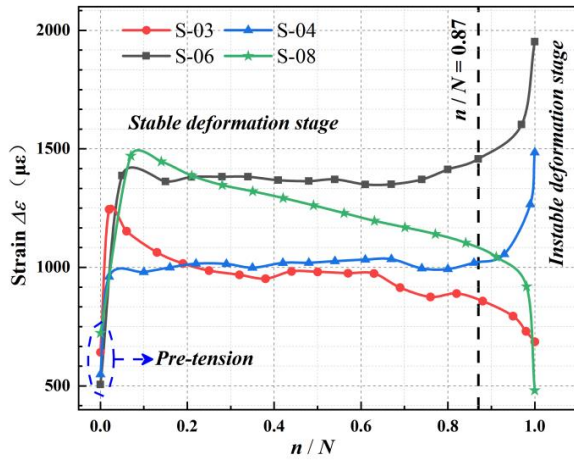


Fig. 6 The association between strain and fatigue loading cycles of the test specimens

Fig. 6 reveals that the deformation of the bolt can be categorized into stable and unstable phases. The strain does not increase from zero due to the application of the pretensioning force before the fatigue test. After the fatigue load is applied, the mean strain amplitude experiences significant changes. Subsequently, as the test progresses, the average strain remains nearly constant, and the fatigue crack expands consistently during this period. This phase constitutes the primary part (i.e., 87%) of the fatigue life and is the stable propagation life of fatigue cracks. The subsequent phase is the variable deformation stage. Due to the sufficient accumulation of fatigue damage in the previous stage, the bolt undergoes rapid deformation, and the fatigue crack grows inconsistently; thus, fracture occurs swiftly. The crack origin location can be inferred from the strain variation, that is, the crack begins near the gauge with the strain gradually decreasing. This is because the crack initiation and opening contribute to the eccentricity of the initial axial tension and the reduction of the load on the crack side, subsequently decreasing the average strain. Conversely, the strain of the opposite gauge exhibits a rising trend due to the increase in the eccentric load.

### 3.3. Fractographic examination

Fractographic analysis is an essential method to investigate the fatigue fracture of components. This section inspects the macroscopic fracture morphology characteristics of the high-strength bolts and then analyzes their microscopic fracture morphology and roughness of the fracture surface using SEM and 3-D morphology scanning, as displayed in Figs. 7 and 8, to deduce their fracture mechanisms at different stress levels.

#### 3.3.1. Macroscopic fracture

Fig.9 shows that all specimen fractures occur at the root of the first or second engaged thread of the bolt. This is due to the significant stress concentration caused by the cross-sectional variation at the bolt thread.



Fig. 7 The scanning electron microscope



Fig. 8 The Keyence VK-X1000 3D noncontact morphology scanner

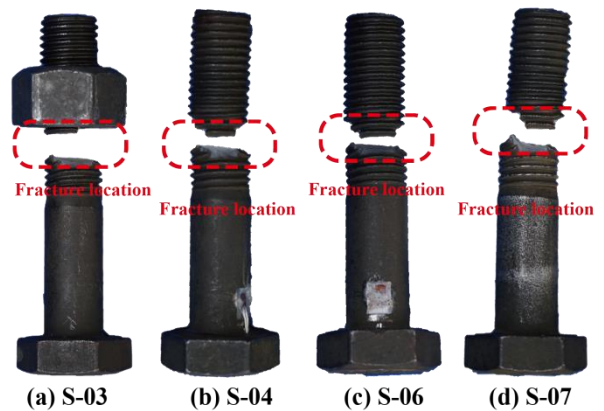


Fig. 9 The failure fracture position of the high-strength bolts

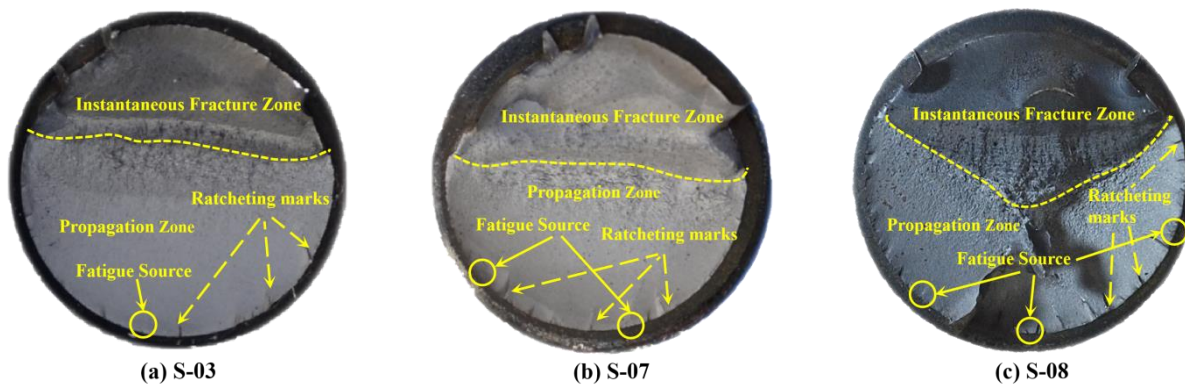


Fig. 10 Macroscopic fracture morphology of the high-strength bolts

Fig. 10 displays three representative specimens, specifically S-03, S-07, and S-08, taken as examples to show the detailed fatigue fracture features. The fracture can be categorized into three areas: the fatigue origin, the crack growth

zone, and the instantaneous fracture zone. It is observed that all fatigue origins form on the surface of the specimens, and the fatigue fractures display features of multiple crack initiation, as indicated by the ratcheting marks. These marks

result from the nucleation and connection of multiple cracks at different points, forming steps on the fracture surface. The steps extending from the origin zone grow more significantly in the growth zone, and noticeable radial streaks form. The crack growth zone occupies most of the fracture area, which is rougher and darker than the previous zone. The sudden fracture area exhibits the roughest texture, and a noticeable shear lip can be observed. Because the bolt is notched, the stress concentration on the outer surface is significant, and the crack growth rate on both sides is higher than that in the middle; thus, the crack front is a convex arc.

Upon examining the macroscopic fracture morphology of the cross sections of the high-strength bolts, it becomes evident that an elevated stress level can augment the quantity of ratcheting marks on the fracture surface. This suggests the potential presence of multiple crack sources on the fracture surface, resulting in a complex fracture morphology. The quantitative analysis of the fractures across all specimens demonstrates that the crack growth portion constitutes 55%–75% of the total surface area ( $A$ ), signifying that it forms the primary fatigue life. This portion exhibits a negative relationship with the stress level. In particular, a higher stress level hastens the crack propagation rate, meaning that fewer fatigue loading cycles are needed for the same length of crack propagation; thus, the area of the propagation zone diminishes, as depicted in Fig. 11.

Additionally, the swift expansion of the crack leads to a rapid decline in the effective cross-sectional area of the load-bearing capacity, causing the bolt to be incapable of withstanding high stress. Consequently, the bolt fails more rapidly, resulting in pronounced tear marks and a highly irregular surface in the instantaneous fracture zone.

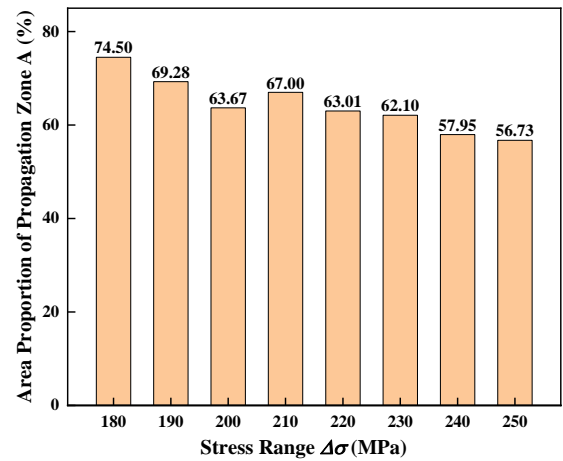


Fig. 11 The bar graph of the area proportion of the propagation zone versus the stress range

### 3.3.2. Microscopic fracture

Figs. 12–14 display the two-dimensional representations of the microscopic fracture morphology of the characteristic high-strength bolts subjected to high-cycle fatigue loading.

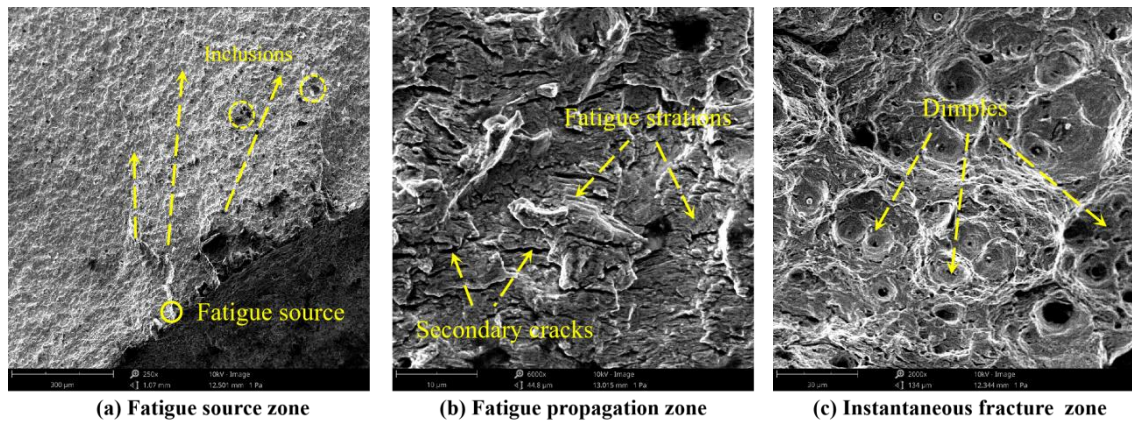


Fig. 12 Microscopic fracture analysis of specimen S-03

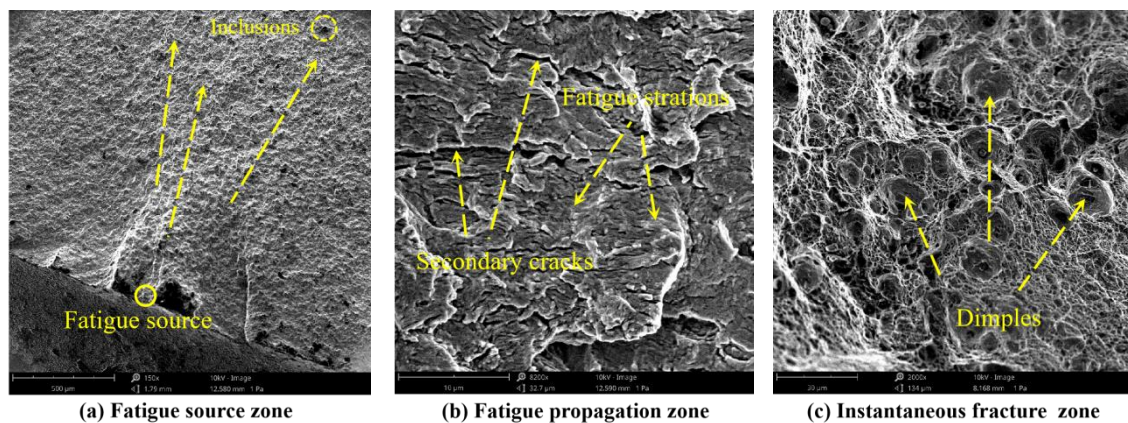


Fig. 13 Microscopic fracture analysis of specimen S-07



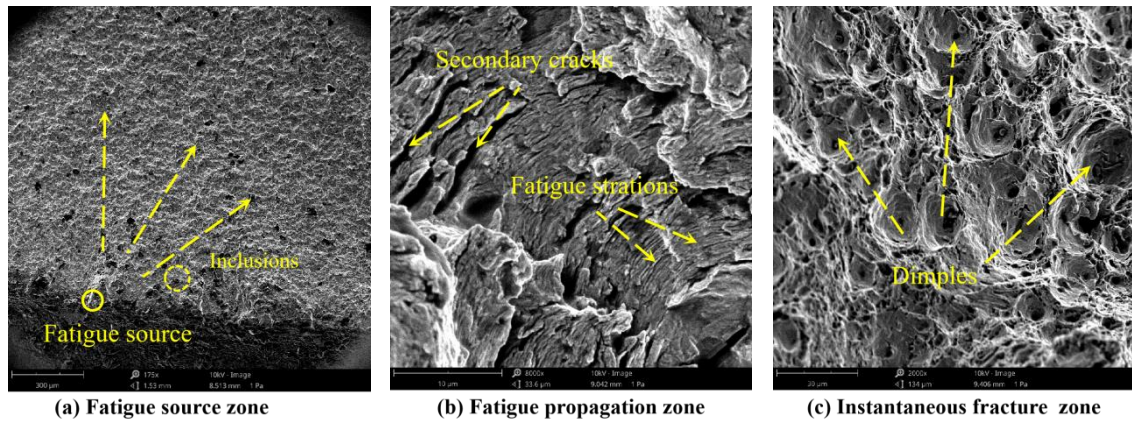


Fig. 14 Microscopic fracture analysis of specimen S-08

Cracks initiate in the fatigue source and develop further, with numerous radial rays present on the fracture surface. In this region, black specks are visible, which represent inclusions during fabrication, contributing to a reduction in the cross-sectional area's strength, as illustrated in Figs. 12(a), 13(a), and 14(a). The images also reveal that an increase in stress level results in more pronounced ratcheting marks and a higher density of radial rays, primarily due to heightened stress concentration at the bolt thread.

The conspicuous bright fatigue striation is a distinguishing feature in the fatigue propagation zone. This striation consists of a series of nearly parallel stripes with minor band bending in a wave-like pattern, perpendicular to the local crack propagation direction. Additionally, secondary cracks can be observed in this area, running parallel to the fatigue striations. These cracks exhibit a discontinuous distribution and a depth notably greater than that of the fatigue striations.

A comparison of Fig. 12(b), Fig. 13(b), and Fig. 14(b) indicates that a higher stress level results in larger spacing between fatigue striations. This suggests that elevated stress levels promote damage accumulation at the crack tip and an

increased crack propagation rate; in other words, crack propagation values rise for the same loading cycles, and fatigue striation spacing expands. Consequently, this area displays a reduced reflective capacity, yielding a darker color. Moreover, the quantity and size of secondary cracks increase, correlating with the stress state at the crack front: a higher stress level corresponds to a more pronounced stress concentration.

The surface in the instantaneous fracture zone is the most uneven and coarse among the three regions. Some dimples, whose diameter and depth depend on the material properties and loading scheme, can be observed in this area. These dimples are either elliptical or circular, suggesting they form under tension. Their formation mechanism involves microscopic cavities within metals undergoing nucleation, growth, and accumulation until a plastic fracture occurs due to an axial load perpendicular to the fracture plane.

A comparison of Fig. 12(c), Fig. 13(c), and Fig. 14(c) reveals that dimples exhibit larger diameters and greater depths at higher stress levels, as increased stress accelerates pore nucleation and growth.

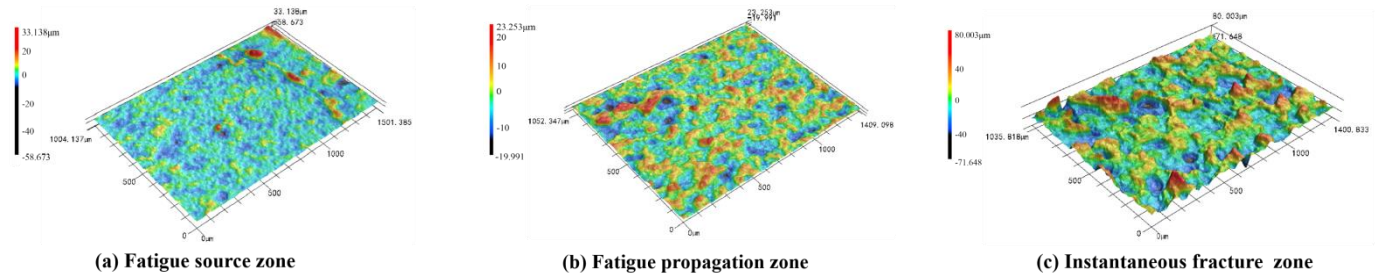


Fig. 15 3-D surface morphology of specimen S-03

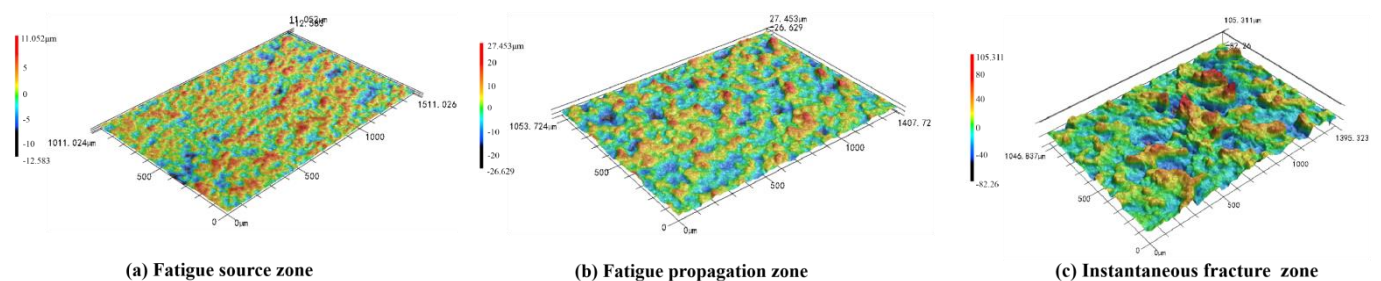


Fig. 16 3-D surface morphology of specimen S-07

Figs. 15 and 16 present two representative specimens, S-03 and S-07, as examples to illustrate the roughness of various zones. They indicate that as the crack propagates, the surface's concave and convex features intensify. It is apparent that the fracture surface is relatively smooth in the fatigue source zone, while a "topographic relief" characteristic emerges in the propagation zone. In the instantaneous fracture zone, the surface morphology exhibits greater fluctuations, interspersed with "ditches" and "gullies."

Fig. 17 demonstrates that the roughness at an identical position on the fracture surface is directly proportional to the stress level, as higher stress levels facilitate crack nucleation, resulting in a greater number of cracks and more convoluted and intricate crack propagation paths. Consequently, the fracture surface becomes rougher.



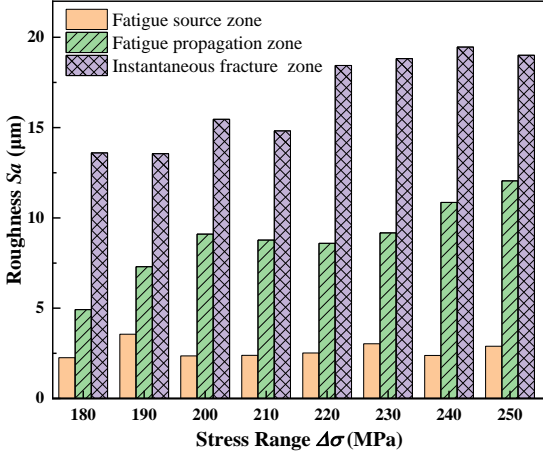


Fig. 17 Variation in roughness of different zones with the stress range

#### 4. Finite element modeling of fatigue crack propagation in high-strength bolt

A finite element model is established employing the XFEM introduced by Abaqus software to examine the fatigue crack growth process of the 20MnTiB steel high-strength bolts. According to the test results and the existing research, the critical parameters are determined: the initial position of the crack, the crack shape, the initial size of the crack, the crack growth criterion, the material constant, the crack growth increment, and the cycle termination conditions. Then, the SIF at the bolt crack front is calculated. The fatigue crack growth process and fatigue life of the high-strength bolt are also predicted based on fracture mechanics. These findings can promote research on the fatigue crack propagation law and fracture mechanism of high-strength bolts.

##### 4.1. XFEM validation

To confirm the accuracy of XFEM in calculating the SIF, a rectangular block with a crack is used as an example for calculating the stress intensity factor at the crack front. The dimensions of the rectangular block model are assigned: height, width, thickness, and crack length of 200, 100, 10, and 25 mm, respectively. A tensile stress ( $\sigma$ ) of 25 MPa is applied to the model's upper and lower ends. The model's element type is C3D8R, with a global size of approximately 3.0 mm. The mesh size influences the SIF calculation accuracy; hence, the mesh size at the crack front is refined locally to examine its effect on

Table 4

The calculation results of the SIF under different mesh sizes.

XFEM	Mesh size (mm)						Theoretical calculations of SIF, $K_I$ ( $MPa \cdot mm^{1/2}$ )
	0.1	0.2	0.5	0.8	1.0	1.2	
$K_I$ ( $MPa \cdot mm^{1/2}$ )	338.80	339.67	340.10	340.27	340.17	342.47	333.28
Difference (%)	1.66%	1.92%	2.05%	2.10%	2.17%	2.70%	

The difference between SIF values calculated using XFEM and the theoretical method is within 3.00%, validating the accuracy of  $K(I)$  determined by XFEM. Considering the model's computational accuracy and efficiency, the mesh size of the refinement region is set at 0.5 mm for subsequent analyses.

##### 4.2. Extended finite element model of high-strength bolt

The bolt thread angle has a negligible effect on stress concentration and the SIF when less than  $4^\circ$  [31]. Thus, to enhance calculation efficiency, the thread angle for the bolt is disregarded, as depicted in Fig. 19.

The material properties introduced into the model include yield strength and ultimate strength of 780.30 and 861.80 MPa, respectively. Young's modulus and Poisson's ratio of the model are set at  $2.66 \times 10^5$  MPa and 0.3, respectively.

Two analysis steps, 1 and 2, are established to calculate the  $K_{I,min}$  and  $K_{I,max}$  of the bolt under minimum and maximum loads, respectively.

Fig. 19 presents the loading and boundary conditions of the model. Two reference points, RP-1 and RP-2, are positioned on the upper and lower surfaces of the model, respectively, and are coupled with the two surfaces. The axial load is applied to the model at point RP-1, while a fixed boundary condition ( $U_X = U_Y = U_Z = U_{RX} = U_{RY} = U_{RZ} = 0$ ) is assigned at point RP-2. Table 5 displays the model's loading scheme.

the SIF, with refinement mesh sizes ranging from 0.1 to 1.2 mm. Fig. 18 illustrates the impacts of the mesh size in the refinement area and the integral path on the SIF simulation outcomes. Decreasing the mesh size improves the simulation results' accuracy. Additionally, the SIF exhibits significant fluctuations with a small integral path but stabilizes from the sixth integral path onwards, in line with the theory that the integral value is path-independent, as demonstrated in Fig. 18. Consequently, the average value of the SIF on the 7th, 9th, and 10th paths is used for subsequent analyses.

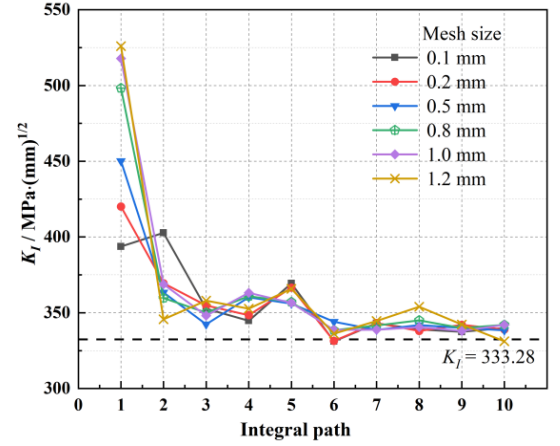


Fig. 18 Variation in stress intensity factor with integral path at different mesh sizes

The theoretical expression of the SIF for this example is derived as follows [40]:

$$K_I = F\left(\frac{a}{b}\right) \sigma \sqrt{\pi a} \quad (4)$$

$$\text{where } F\left(\frac{b}{a}\right) = \frac{1 + 2\left(\frac{b}{a}\right)}{1 - \left(\frac{a}{b}\right)^{3/2}} \left[ 1.1200 - 3.682\chi\left(\frac{b}{a}\right) + 11.954\chi\left(\frac{b}{a}\right)^2 - 25.852\chi\left(\frac{b}{a}\right)^3 + 33.097\chi\left(\frac{b}{a}\right)^4 - 22.442\chi\left(\frac{b}{a}\right)^5 + 6.178\chi\left(\frac{b}{a}\right)^6 \right], \text{ and}$$

$K_I$  is calculated at 332.46  $MPa \cdot mm^{1/2}$  using Eq. (4).

Table 4 compares the XFEM results with the theoretical calculations.

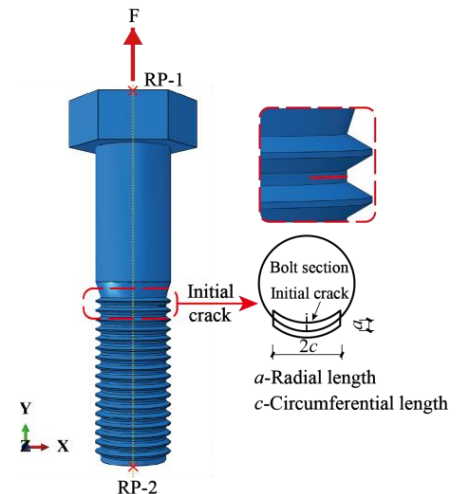
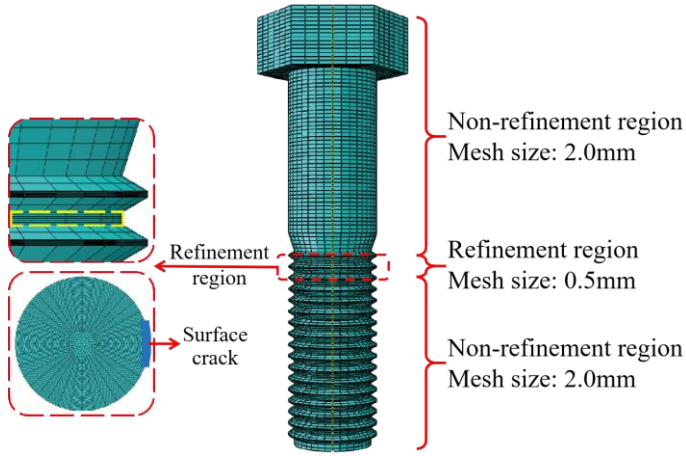


Fig. 19 Bolt model with a surface crack in the thread root region

**Table 5**

Loading scheme for simulating the fatigue crack propagation process

Model	$F$ , (kN)		$\sigma$ , (MPa)		$\Delta\sigma$ , (MPa)	$T$ , (N·m)	$R$
	$F_{max}$	$F_{min}$	$\sigma_{max}$	$\sigma_{min}$			
M-1	80.69	21.21	228.57	65.57	160		
M-2	85.73	25.72	242.86	72.86	170	360	0.3
M-3	90.77	27.23	257.14	77.14	180		

**Fig. 20** The meshed model of the bolt

The model's element type is C3D8R, with a global size of approximately 2.0 mm. The first two threads' mesh is refined to a size of 0.5 mm, as shown in Fig. 20.

Fatigue test results and prior studies [8,15,16,26] indicate that fatigue cracks are prone to appear at the root of the first or second meshed thread of the high-strength bolt, so a sharp initial crack is introduced. The crack front

shape is assumed to be a fan ring based on fractographic analysis and model convergence, as depicted in Fig. 19.

#### 4.3. Fatigue crack propagation modeling

##### 4.3.1. Crack propagation criteria and material parameters

Fracture mechanics is utilized to investigate crack propagation in this section. The Paris formula [41] is the most widely used crack growth criterion, reflecting the crack growth rate in different stages by selecting appropriate material constants.

$$\frac{da}{dN} = C(\Delta K_I^a)^m \quad (5)$$

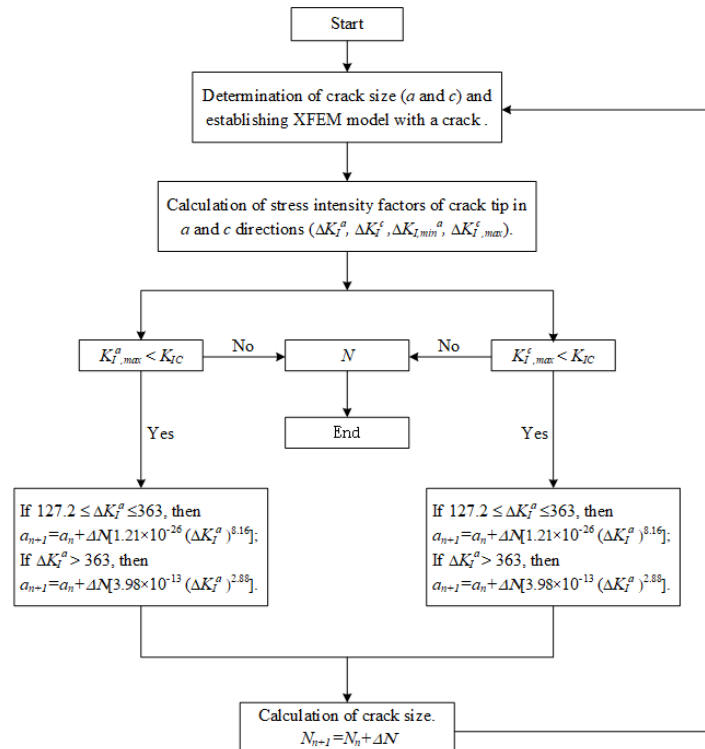
$$\frac{da}{dN} = C(\Delta K_I^c)^m \quad (6)$$

where  $a$  and  $c$  represent the circumferential and radial length of the crack, respectively,  $N$  denotes the number of loading cycles,  $C$  and  $m$  are material constants,  $\Delta K_I^a = K_{I,max}^a - K_{I,min}^a$ , and  $\Delta K_I^c = K_{I,max}^c - K_{I,min}^c$ . The values of  $C$  and  $m$ , the threshold value ( $\Delta K_{th}$ ), and the fracture toughness ( $K_{IC}$ ) in different propagation stages are determined by the recommended values of Eurocode [43], as listed in Table 6.

**Table 6**

Recommended material constants for fatigue crack growth [45].

$R$	Stage I		Stage II		Threshold value, $\Delta K_{th}$ , (MPa·(mm) <sup>1/2</sup> )	Boundary of stage I and stage II, $\Delta K_I$ , (MPa·(mm) <sup>1/2</sup> )	Fracture toughness, $K_{IC}$ , (MPa·(mm) <sup>1/2</sup> )
	$C$	$m$	$C$	$m$			
0.3	$1.21 \times 10^{-26}$	8.16	$3.98 \times 10^{-13}$	2.88	127.20	363.00	3475.00

**Fig. 21** Flow chart for iterative simulation of the fatigue crack propagation process [44]

#### 4.3.2. Modeling process

Hirt and Fisher [43] inferred that a circle with a radius of 1.016 mm could represent the initial crack size, and the precision of the magnetic particle flaw detection method, typically used for detecting surface cracks, was approximately 1 mm. Consequently, the initial crack's circumferential length (twice  $c$ ) is set at 1 mm, and the radial length ( $a$ ) is assumed to be 0.5 mm. Next, a suitable increment of loading cycles ( $\Delta N$ ) is selected to ensure that the increase in  $a$  or  $c$  is more than one mesh size (0.5 mm). The fatigue life is predicted by calculating  $a$  and  $c$  incrementally until the cycle termination

conditions are met.

Fig. 21 displays the flow chart for the iterative simulation of the fatigue crack propagation process. The crack is presumed not to propagate when  $\Delta K_I \leq 127.2 \text{ MPa} \cdot (\text{mm})^{1/2}$ .

#### 4.3.3. Modeling results

Tables 7–9 present the iterative results of crack propagation at different stress ranges.

**Table 7**  
Iterative calculation results of crack propagation at  $\Delta\sigma$  of 160 MPa

Crack size (mm)		Fatigue life, $N$ , ( $\times 10^4$ )	$\Delta K_I$ (MPa $\cdot$ (mm) $^{1/2}$ )		$K_{max}$ (MPa $\cdot$ (mm) $^{1/2}$ )	
$a$	$c$		$\Delta K_I^a$	$\Delta K_I^c$	$K_{I,max}^a$	$K_{I,max}^c$
0.5	0.5	0	261.40	399.70	621.03	945.10
0.5	1.1	5	118.57	406.30	243.75	736.67
0.5	1.8	10	203.14	305.80	482.08	705.58
0.6	2.3	30	318.80	368.24	695.96	909.14
0.8	2.8	35	376.44	368.28	830.54	823.44
1.3	3.3	40	403.13	373.04	863.03	832.38
1.9	3.8	45	519.48	431.25	1010.86	1003.96
3.2	4.6	50	874.12	477.06	1789.24	1542.95
5.6	5.0	52	1717.53	1324.81	3316.30	3049.33
6.4	5.4	52.1 (Fatigue failure)	3430.28	2229.06	5652.93	3578.97

**Table 8**  
Iterative calculation results of crack propagation at  $\Delta\sigma$  of 170 MPa

Crack size (mm)		Fatigue life, $N$ , ( $\times 10^4$ )	$\Delta K_I$ (MPa $\cdot$ (mm) $^{1/2}$ )		$K_{max}$ (MPa $\cdot$ (mm) $^{1/2}$ )	
$a$	$c$		$\Delta K_I^a$	$\Delta K_I^c$	$K_{I,max}^a$	$K_{I,max}^c$
0.5	0.5	0	278.10	428.17	651.50	994.47
0.6	1.3	5	106.17	533.35	272.95	750.18
0.6	2.7	10	264.23	343.33	626.08	789.38
0.6	3.3	20	325.42	371.18	620.03	840.78
0.8	3.8	25	328.60	471.63	715.38	982.81
1.0	4.8	30	483.71	442.56	943.38	876.05
2.1	5.6	35	822.81	836.05	1335.17	1622.20
3.1	6.6	36	1081.52	1181.66	1891.62	2102.88
3.7	7.5	36.3	1384.26	1493.86	3008.30	3293.34
4.1	7.7	37 (Fatigue failure)	2860.44	2770.41	4951.78	4533.09

**Table 9**  
Iterative calculation results of crack propagation at  $\Delta\sigma$  of 180 MPa

Crack size (mm)		Fatigue life, $N$ , ( $\times 10^4$ )	$\Delta K_I$ (MPa $\cdot$ (mm) $^{1/2}$ )		$K_{max}$ (MPa $\cdot$ (mm) $^{1/2}$ )	
$a$	$c$		$\Delta K_I^a$	$\Delta K_I^c$	$K_{I,max}^a$	$K_{I,max}^c$
0.5	0.5	0	296.58	461.17	676.82	1037.87
0.6	1.4	5	155.88	415.60	299.20	837.07
0.6	2.1	10	318.01	315.43	711.09	676.92
1.2	2.7	30	547.68	693.04	1240.72	1322.35
1.8	3.9	32	605.46	550.21	1148.93	1126.80
3.1	4.9	35	1264.46	1135.10	2147.14	1979.31
4.4	5.9	35.4	1792.18	717.53	3269.36	3149.89
5.4	5.9	35.5 (Fatigue failure)	2938.93	4182.75	4523.64	6580.71



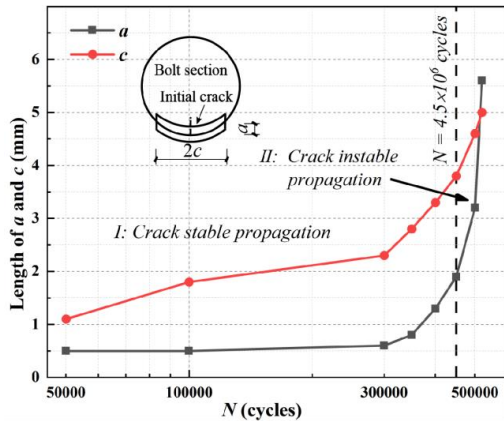
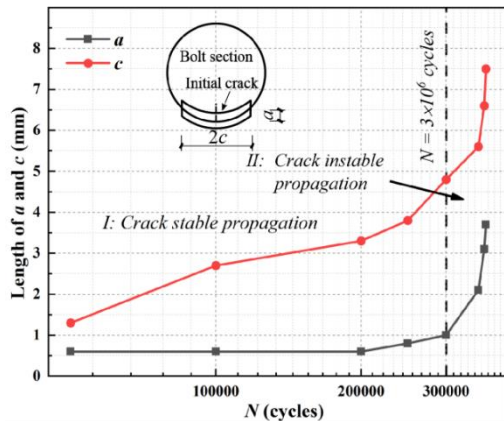
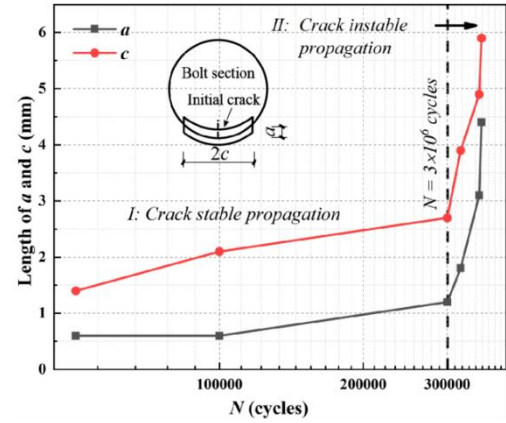
**Table 10**Comparison of simulated fatigue life of high-strength bolts with values fitted by the  $S-N$  curves at various stress ranges

Model	Stress range, $\Delta\sigma$ , (MPa)	Fatigue life, $N_f$ ( $\times 10^4$ )		$N_s/N_f$
		Simulated values, $N_s$	Values fitted by the $S-N$ curves, $N_f$	
M-1	160	52.00	59.19	0.88
M-2	170	36.30	57.62	0.63
M-3	180	35.40	56.19	0.63
Average value				0.71

Table 10 compares the simulated fatigue life of high-strength bolts with values determined by the  $S-N$  curves. The simulated fatigue life is 0.88, 0.63, and 0.63 times the fitted value at stress ranges of 160, 170, and 180 MPa, respectively, yielding an average value of 0.71, which is acceptable. These findings suggest that the numerical simulation of fatigue crack propagation devised in this study can accurately predict the fatigue life of high-strength bolts. Additionally, the differences can be attributed to the simulation results disregarding the crack initiation life, that is, the fatigue life from microscopic defects to macroscopically detectable cracks. Furthermore, the parameters employed in the crack propagation simulation are based on the conservative recommended values of Eurocode, ensuring sufficient safety.

## 5. Discussion

Fig. 22 illustrates the changes in crack length in both circumferential and radial directions concerning the loading cycles at different stress ranges during fatigue failure.

(a)  $\Delta\sigma = 160$  MPa(b)  $\Delta\sigma = 170$  MPa(c)  $\Delta\sigma = 180$  MPa**Fig. 22** The association between crack length and oading cycles at various stress ranges

Two distinct crack propagation phases are identified in the curves based on the crack length alteration: stable phase (I) and unstable phase (II). In phase I, the crack mainly expands slowly in the circumferential direction and exhibits a reduced growth rate in the radial direction. This phase encompasses 85% of the crack propagation life, which aligns well with the  $\Delta\epsilon-n/N$  curve analysis outcomes from the tests, thus validating the feasibility of using XFEM for simulating crack propagation progress. In phase II, the crack growth rate substantially increases in both directions, the crack length expands exponentially, and the propagation rate in the radial direction surpasses that in the other direction. These features are consistent with the bolt fracture morphology derived from the fatigue test: a crescent in the fatigue source area and nearly a semicircle in the propagation area.

Fig. 22 reveals that augmenting the stress range accelerates the crack growth rate in both directions, causing the high-strength bolt to fail under a reduced number of loading cycles. This occurs because crack propagation is strongly related to the stress field intensity at the crack front. An increased load amplifies the stress at this point, supplying the necessary stress for rapid material separation; hence, the crack extends swiftly.

The aforementioned analysis indicates that a swiftly enlarges in phase II, which is more favorable for load eccentricity, subsequently raising the stress on the effective section and consequently diminishing the bolt fatigue life in this phase. Consequently, the following section concentrates on the evolution of  $a$  during the fatigue failure process.

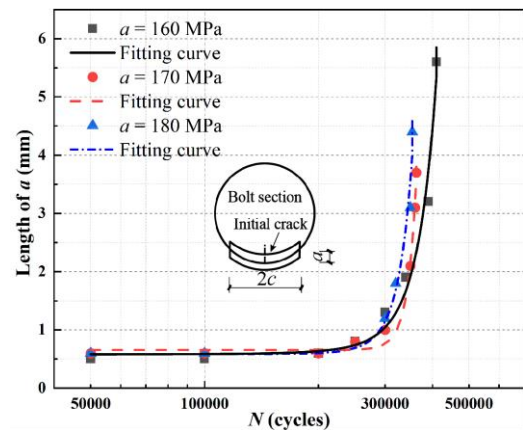
**Fig. 23** The changes in  $a$  with loading cycles at different stress ranges

Fig. 23 demonstrates the changes in  $a$  in relation to the loading cycle number at various stress ranges:  $a$  starts to slowly grow with an increase in  $N$ . An elevated stress level quickens the fatigue damage accumulation rate, so  $a$  starts to rise at lower loading cycles:  $a$   $\Delta\sigma$  of 160, 170, and 180 MPa results in loading cycles of  $3.00 \times 10^5$ ,  $2.00 \times 10^5$ , and  $1.00 \times 10^5$ , respectively. In the later stages of crack propagation, an increase in the stress range produces larger crack increments under the same number of loading cycles.

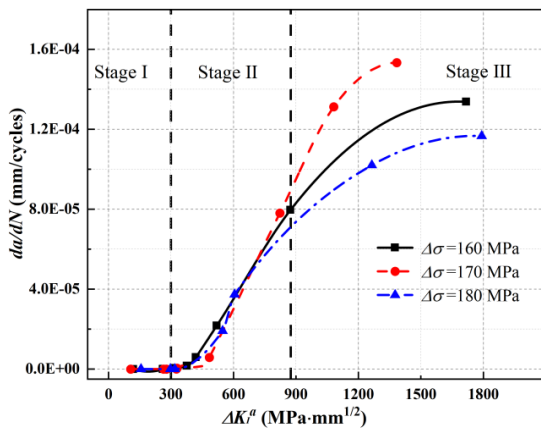
The equation for calculating the changes in  $a$  concerning  $N$  is derived from curve fitting. The correlation coefficients ( $R^2$ ) of the fitted curves all surpass 0.9, signifying that the fitted outcomes are optimal, as presented in Table 11.

**Table 11**

The fitted results of the  $a$ - $N$  curves

$\Delta\sigma$ (MPa)	Fitted equation	Correlation coefficient ( $R^2$ )
160	$a = 8.322 \cdot 10^{-5} \cdot e^{N/47488.130} + 0.601$	0.979
170	$a = 1.909 \cdot 10^{-8} \cdot e^{N/19250.079} + 0.655$	0.989
180	$a = 2.426 \cdot 10^{-5} \cdot e^{N/29848.439} + 0.586$	0.970

Additionally, in fracture mechanics, the stress intensity factor is a crucial parameter governing the crack growth rate ( $da/dN$ ). Therefore, we plot the variation of  $da/dN$  with  $\Delta K_I$  to characterize the fatigue crack propagation, as shown in Fig. 24.



**Fig. 24** The variation of  $da/dN$  with  $\Delta K_I$  at various stress ranges

The curves can be divided into three stages based on the crack growth rate: stages I, II, and III. In stage I,  $da/dN$  is less than  $10^{-10}$  mm/cycle, indicating that the crack does not grow in this stage. In stage II,  $da/dN$  typically ranges from  $10^{-9}$  to  $10^{-5}$  mm/cycle, a linear relationship exists between  $da/dN$  and  $\Delta K_I$ , and a higher stress range corresponds to an increased crack propagation rate under the same  $\Delta K_I$ . In stage III,  $da/dN$  is greater than  $10^{-5}$  mm/cycle, and the crack size expands rapidly, leading to a swift fracture of the high-strength bolt. As a result, the contribution of stage III to the crack propagation life is generally disregarded. Fig. 24 indicates that stage III deviates from the commonly used  $da/dN$ - $\Delta K_I$  curve, which can be attributed to the fact that the standard  $da/dN$ - $\Delta K_I$  curve is derived from standard specimens with uniform thickness, whereas the bolts' thickness and surface shape change during crack propagation.

## 6. Conclusions

Axial-tensile constant-amplitude fatigue tests were carried out on M24 high-strength 20MnTiB steel bolts with a stress ratio of 0.3 in this study. The fatigue characteristics and failure mechanisms of the high-strength bolt was analyzed through regression analysis, strain analysis, and fracture surface analysis. Furthermore, the finite element method grounded in fracture mechanics was employed for examining the fatigue crack growth of the high-strength bolts, seeking to comprehend their fatigue crack propagation principles and elucidating the fracture mechanisms. The following conclusions were derived from the tests and numerical investigations:

- The  $S$ - $N$  curve for the 20MnTiB steel high-strength bolt with an  $R$  value of 0.3 was established, revealing a threshold fatigue strength of 140.77 MPa at  $2 \times 10^6$  loading cycles, which was 1.68 times greater than the fatigue life of the 35K steel bolt. This result demonstrated the superior fatigue performance of the former. Integrating a correction factor into the

$S$ - $N$  curve was recommended to address the impact of material properties on the fatigue life of the bolt.

- Strain analysis indicated that the stable deformation stage constituted 87% of the high-strength bolt's fatigue life, and the strain variation of the specimen could be employed to roughly estimate the crack source location. The strain was reduced on the crack initiation side.
- A model for predicting the high-strength bolts' fatigue life was developed using XFEM and fracture mechanics, enabling the investigation of their fatigue crack propagation progression, albeit with a minor deviation.
- The law governing crack growth in the circumferential and radial directions was determined, and the fatigue crack growth mechanism of the bolt was clarified by simulating crack propagation. During the stable crack propagation stage, the crack primarily advanced along the bolt's circumferential direction, accounting for 85% of the crack propagation life, in accordance with the  $\Delta\epsilon$ - $n/N$  curve analysis results from the tests. In the unstable crack propagation stage, the crack length grew exponentially, and the radial growth rate exceeded the growth rate in the other direction. An increased stress range elevated the SIF at the crack front, promoting rapid crack expansion and consequently reducing the fatigue life of the high-strength bolt.

## Acknowledgments

The research was financially supported by the National Natural Science Foundation of China [Grant No. 52278198] and the Fundamental Research Program in Shanxi Province, China [Grant No. 202203021211184].

## References

- Mehmanparast, A., Lotfian, S. and Vipin, S.P., "A review of challenges and opportunities associated with bolted flange connections in the offshore wind industry", *Metals*, 10(6), 732, 2020.
- Weijtjens, W., Stang, A., Devriendt, C. and Schaumann, P., "Bolted ring flanges in offshore-wind support structures - in-situ validation of load-transfer behavior", *Journal of Constructional Steel Research*, 176, 106361, 2021.
- Yang, X., Lei, H.G. and Chen, Y.F., "Constant amplitude fatigue test research on M20 high-strength bolts in grid structure with bolt-sphere joints", *Advances in Structural Engineering*, 20(10), 1466-1475, 2016.
- Si Q, Ding Y, Zong L, and Liu H, "Mechanical properties and simulation method of structural steel after high cycle fatigue damage", *Advanced steel construction*, 19(1), 70-76, 2023.
- Yang, X. and Lei, H.G., "Constant amplitude fatigue test of high strength bolts in grid structures with bolt-sphere joints", *Steel and Composite Structures*, 25(5), 571-579, 2017.
- Qiu, B., Yang, X., Zhou, Z.C. and Lei, H.G., "Experimental study on fatigue performance of M30 high-strength bolts in bolted spherical joints of grid structures", *Engineering structures*, 205, 110123, 2020.
- Jiao, J.F., Jia, P.P., Liu, Y., Liu, J.Q. and Lei, H.G., "Experimental study on constant amplitude fatigue of M24 high-strength bolts under critical stress ratio", *Journal of Taiyuan University of Technology*, 50(06), 749-755, 2019. (in Chinese)
- Jiao, J.F., L. Z.X., Guo, Q., Liu, Y. and Lei, H.G., "Constant-amplitude fatigue behavior of M24 high-strength bolt of end-plate flange connection", *Structures*, 34, 2041-2053, 2021.
- Liu, Y.Z., Chen, J., Zhang, X.F. and Tan, D., "Fatigue behavior of blind bolts under tensile cyclic loads", *Journal of Constructional Steel Research*, 148, 16-27, 2018.
- Tizani, W., Norashidah, Abd Rahman, N. and Pitrakos, T., "Fatigue life of an anchored blind-bolt loaded in tension", *Journal of Constructional Steel Research*, 93, 1-8, 2014.
- Schaumann, P. and Rasmus, E., "Ermüdung sehr großer hv-schraubengarnituren", *Stahlbau*, 85(9), 604-611, 2016.
- Jiang, W.Q., Mo, Z., Yang, L.Q., Liu, J.L. and Niu, Z.B., "Theoretical study on early stage self-loosening of bolted joint in lattice transmission tower under transverse load", *Advanced steel construction*, 18(2), 574-584, 2022.
- Bartsch, H. and Feldmann, Markus., "Reassessment of fatigue detail categories of bolts and rods according to EC 3-1-9", *Journal of Constructional Steel Research*, 180, 106588, 2021.
- Li, Z.H., Han, K., Chen, T., Yang, H.S., Liu, P. and Lu, Y.H., "Fatigue life prediction of nuclear reactor main bolt based on temperature effect and size effect", *International Journal of Fatigue*, 152, 106443, 2021.
- Maljaars, J. and Euler, M., "Fatigue  $S$ - $N$  curves of bolts and bolted connections for application in civil engineering structures", *International Journal of Fatigue*, 151, 106355, 2021.
- Lochan, S., Mehmanparast, A. and Wintle, J., "A review of fatigue performance of bolted connections in offshore wind turbines", *Procedia Structural Integrity*, 17, 276-283, 2019.
- Kaushik, V. and Anup, G., "Experimental and numerical investigation of mode-i & mode-ii fatigue crack growth in unidirectional composites using xiga-czm approach", *International Journal of Fatigue*, 134, 105461, 2020.
- Liu, H., Hu, D.Y., Wang, P.Q., Wang, X., Jin, S. A. and Gu, Y.X., "Experimental and numerical investigations on the influence of cold expansion on low cycle fatigue life of bolt holes in aeroengine superalloy disk at elevated temperature", *International Journal of Fatigue*, 132, 105390, 2020.
- Wang, Y.X., Ji, B.H., Fu, Z.Q. and Yao, Y., "Fatigue repairing craftsmanship of deck-to-vertical stiffener weld in the steel bridge deck", *Advanced steel construction*, 15(3), 232-241, 2019.
- Fang L, Fu Z.Q., Ji B.H., and Kainuma S., "Propagation mode and characteristics of fatigue cracks in steel bridge deck after drilling ahead of the crack tip", *Advanced steel construction*, 18(2), 544-551, 2022.
- Gu M, Tong LW, Zhao XL, and Zhang YF., "Numerical analysis of fatigue behavior of welded cfcfs t-joints", *Advanced steel construction*, 10(4), 476-497, 2015.
- Shi, J. X., Chopp, D., Lua, J., Sukumar, N. and Belytschko, T., "Abaqus implementation of extended finite element method using a level set representation for three-dimensional fatigue crack growth and life predictions", *Engineering Fracture Mechanics*, 77(14), 2840-2863, 2010.
- Malekan, M., Khosravi, A. and St-Pierre, L., "An Abaqus plug-in to simulate fatigue crack

- growth", *Engineering with Computers*, 38(4), 2991-3005, 2021.
- [24] Shu, Y.X., Li, Y.Z., Duan, M. and Yang, F., "An X-FEM approach for simulation of 3-D multiple fatigue cracks and application to double surface crack problems", *International Journal of Mechanical Sciences*, 130, 331-349, 2017.
- [25] Samaei, M., Zehsaz, M. and Chakherlou, T. N., "Experimental and numerical study of fatigue crack growth of aluminum alloy 2024-T3 single lap simple bolted and hybrid (adhesive/bolted) joints", *Engineering Failure Analysis*, 59, 253-268, 2016.
- [26] Bergara, A., Dorado J.L., Martín-Meizoso, A. and Martínez-Esnaola, J.M., "Fatigue crack propagation at aeronautic engine vane guides using the extended finite element method (XFEM)", *Mechanics of Advanced Materials and Structures*, 28(8), 861-873, 2021.
- [27] Ngoula, D.T., Beier, H.T. and Vormwald, M., "Fatigue crack growth in cruciform welded joints: Influence of residual stresses and of the weld toe geometry", *International Journal of Fatigue*, 101, 253-262, 2017.
- [28] Pandey, V.B., Singh, I.V., Mishra, B.K. Ahmad, S., Rao, A.V. and Kumar, V., "A new framework based on continuum damage mechanics and xfem for high cycle fatigue crack growth simulations", *Engineering Fracture Mechanics*, 206, 172-200, 2019.
- [29] Lin, X.B. and Smith, R.A., "Finite element modeling of fatigue crack growth of surface cracked plates: Part III: stress intensity factor and fatigue crack growth life", *Engineering Fracture Mechanics*, 63(5), 541-556, 1999.
- [30] Yang, F.P. and Kuang, P.J., "Fatigue crack growth for a surface crack in a round bar under multi-axial loading condition", *Fatigue Fract. Eng. Mater. Struct.*, 28(11), 963-70, 2005.
- [31] Kumar, S.S. and Prakash, R.V., "Effect of helix angle on the stress intensity factor of a cracked threaded bolt", *Journal of Pressure Vessel Technology- Trans. ASME*, 135(2), 12, 2013.
- [32] Sharda, L., Mehmanparast, A. and Wintle, J., "A review of fatigue performance of bolted connections in offshore wind turbines" [A], *The 3rd International Conference on Structural Integrity[C]*, *Procedia Structural Integrity*, 276-283, 2019.
- [33] ISO 898-1: 2013, Mechanical properties of fasteners made of carbon steel and alloy steel — Part 1: Bolts, screws, and studs with specified property classes — Coarse thread and fine pitch thread. International Organization for Standardization, 2013.
- [34] GB 50017-2017, Standard for design of steel structures. Ministry of Housing and Urban-Rural Development of the People's Republic of China, Beijing, People's Republic of China, 2017. (in Chinese)
- [35] BS EN 1993-1-9:2005, Eurocode 3: Design of Steel Structures. Part 1-9: Fatigue, European Committee for Standardization; Brussels, Belgium, 2005.
- [36] ANSI/AISC 360-16, Specification for Structural Steel Buildings, American Institute of Steel Construction, AISC Committee; Chicago, Illinois, USA, 2016.
- [37] BS 7608:1993, Code of practice for fatigue design and assessment of steel structures, British Standards Institution; London, UK, 1993.
- [38] Zhan, B., Liu, Y., Shang, W.N., Zhang, J.L. and Jiao J.F., "Experimental research on constant-amplitude fatigue characteristics of 8.8 grade M24 high-strength bolts", *Ind Constr*, 50(09), 122-127, 2020. (in Chinese)
- [39] Munn, B.S. and Li, K., Investigation into the effect of thread root condition on the high cycle fatigue performance of a metric threaded fastener [C]. ASME 2010 Pressure Vessels and Piping Division/K-PVP Conference. 2010.
- [40] Fett, T., Stress intensity factors, t-stresses, weight functions [M]. Karlsruhe: Universitätsverlag Karlsruhe, 2008.
- [41] Paris, P. and Erdogan, F., "A critical analysis of crack propagation laws", *Journal of Basic Engineering*, 85 (4), 528-533, 1963.
- [42] BS 7910:2013+A1:2015, Guide to methods for assessing the acceptability of flaws in metallic structures, British Standards Institution; London, UK, 2013.
- [43] Hirt, M.A. and Fisher, J.W., "Fatigue crack growth in welded beams", *Engineering Fracture Mechanics*, 5(2), 415-429, 1973.
- [44] Duan, H.C., "Numerical simulation and theoretical analysis of fatigue crack growth of steel pipe-welded hollow spherical joints", Ph.D. Dissertation, Taiyuan: Taiyuan University of Technology, 2019. (in Chinese)



# SHEAR BEHAVIOUR OF DEMOUNTABLE CONNECTIONS WITH BOLTS AND HEADED STUDS

Isidora Jakovljević \*, Milan Spremić and Zlatko Marković

University of Belgrade, Faculty of Civil Engineering, Belgrade, Republic of Serbia

\* (Corresponding author: E-mail: isidora@imk.grf.bg.ac.rs)

## ABSTRACT

Following the trend of sustainable development and structure reuse, many novel solutions related to demountable shear connectors for application in steel-concrete composite beams have been proposed in recent years. This paper provides a further contribution to the research field by proposing a demountable connection with bolts and welded headed studs. The transfer of shear force between a steel flange and a composite concrete slab cast in an open trough profiled steel sheeting is indirect, passing through a steel plate or angles. The proposed solution enables convenient dismantling and reuse of both the composite slab and the steel profile. The experimental investigation included push-out tests, performed to assess the connection shear behaviour, determine resistance and ductility, and identify failure modes. Various configurations of the demountable connection were analysed, including connections with continuous and discontinuous slabs over the support. The response of the suggested demountable solution was compared to the corresponding non-demountable shear connection with headed studs. According to experimental investigation, finite element models were developed, and their accuracy was validated by comparing numerical predictions with experimental results. Parametric studies were conducted using numerical models to evaluate the effects of key parameters on the connection performance, such as plate and angle thickness, stirrup reinforcement position, and transverse distance between a headed stud and slab edge. Directions for design were proposed taking into account the results obtained.

## ARTICLE HISTORY

Received: 20 December 2022  
Revised: 15 May 2023  
Accepted: 16 May 2023

## KEYWORDS

Reusability;  
Shear connection;  
Steel-concrete composite beam;  
Profiled steel sheeting;  
Push-out test;  
Finite element analysis

Copyright © 2023 by The Hong Kong Institute of Steel Construction. All rights reserved.

## 1. Introduction

Steel-concrete composite floor systems are widely used in construction, usually by casting concrete on profiled steel sheeting and installing welded headed studs as shear connectors between a steel profile and a concrete slab. However, this traditional method does not allow for demounting of the structure. The current trend of sustainable development encourages the application of principles of circular economy in construction, including the reuse of structural elements. If the proper design is applied to steel-concrete composite buildings, entire structures may be easily demounted and then relocated and reused. It has been shown that demountable steel-concrete systems lead to the lowest emissions and the highest savings of resources in most of the analysed environmental impact categories compared to other floor systems with composite and precast solid concrete slabs [1].

To develop demountable steel-concrete composite floor systems, bolted connectors are commonly applied instead of welded headed studs. Experimental investigation of bolted shear connections in steel-concrete composite beams started in the 1960s, mainly focusing on friction-grip bolts [2–4]. However, intensive research into bolted connectors in building and bridge design has continued over the past few decades with many different solutions being proposed [5,6]. The available database of experimental results on the behaviour of friction-grip bolts in solid concrete slabs has been expanded by several research groups [7–10]. Kwon et al. [7,11] compared the behaviour of friction-grip bolts, double nut bolts and adhesive anchors, whereas Pavlović et al. [12] focused on single nut bolts. Application of blind bolts in composite beams has been studied [13–16] and compared with the response of welded headed studs. Dai et al. [17] proposed threading a body of a headed stud, adding a nut and using these connectors in steel-concrete composite beams. Another suggested approach consists of a coupler system that connects two bolts: one embedded in a concrete slab and another passing through a steel flange [18]. Comparison between the response of friction-grip bolts and bolts with a coupler system with and without injected resin was made by Kozma et al. [19]. Certain sophisticated solutions have been proposed recently as locking-nut and friction-based shear connectors [20–22], which should be mounted in conical holes cut in a beam flange. Also, a system made of T-bolts and clamps was experimentally investigated [23]. Though most of the research has been focused on demountable shear connections in solid concrete slabs, some studies have investigated the behaviour of bolted shear connectors in composite slabs with profiled steel sheeting [19,24–26].

A considerable number of papers published in recent years have given rise to the promotion of demountable solutions in steel-concrete composite construction. However, design rules for the implementation of bolted connections in steel-concrete composite floors are still lacking in many design codes, including Eurocode 4 [27]. Specific provisions for the design of demountable beams with

bolted shear connectors have been recently summarised in the technical guidance publication by Coelho et al. [28].

This paper presents a contribution to the field of demountable steel-concrete composite floors by proposing a system consisting of two types of connectors: welded headed studs and bolts. The proposed connection has been created with the idea of implementing welded headed studs as connectors characterised by good mechanical performance, but also with a view to enabling reuse of the floor structure in the second life cycle. Besides the primary application in newly-designed demountable structures, the proposed connection may be implemented during reconstruction work by replacing the old concrete slabs with demountable composite steel-concrete slabs [29]. Both headed studs and bolts are broadly available products, which do not require additional supporting components when implemented in the proposed connection, which is considered an advantage of the suggested solution.

The developed connection is applicable in composite concrete slabs cast in open trough profiled steel sheeting. Welded headed studs are installed in concrete ribs, whereas bolts are placed in-between ribs. Two possible solutions may be applied depending on the chosen construction method, as shown in Fig. 1: (1) composite slab continuous over the steel beam (Fig. 1a); (2) composite slab discontinuous over the beam (Fig. 1b). To achieve demountability of the shear connection with a continuous slab given in Fig. 1a, an additional plate placed between the concrete slab and the steel profile is required. Headed studs are welded to the plate, connecting the concrete slab and the plate, whereas the bolts' role is to connect the plate with the upper flange of a steel profile. In the case of a discontinuous concrete slab presented in Fig. 1b, a pair of angles, which headed studs are welded to, is used. The connection between angles and the steel beam is accomplished by bolts, while the connection between angles and concrete slabs is established with the use of welded headed studs. In both cases shown in Fig. 1a and 1b, a longitudinal shear force transfer is indirect, passing through two shear planes: "concrete slab-plate/angle" and "plate/angle-steel profile".

With the removal of bolts on the contact between the steel flange and the plate or angles, the system is divided into two parts: a composite concrete slab and a steel beam, which both may be relocated and reused. Of note, bolts are entirely removed during deconstruction, and therefore, they are not affected during transportation to another location.

In order to exploit the proposed system, connection behaviour should be defined and directions for design provided. The diameter and height of headed studs, and bolt diameter and grade should be adequately selected to enable the sufficient shear performance of the connection and enable demountability and reusability of the system during the life cycles of a structure. Moreover, several other parameters need to be appropriately selected to result in a satisfactory response of the shear connection in terms of resistance and ductility:

- the thickness of the steel plate in connections with continuous slabs over the support, and the thickness of the steel angle in connections with discontinuous slabs over the support,
- the transverse distance between the headed studs and concrete slab edge in connections with discontinuous slabs over the support,
- the local stirrup reinforcement around headed studs in connections with discontinuous slabs over the support.

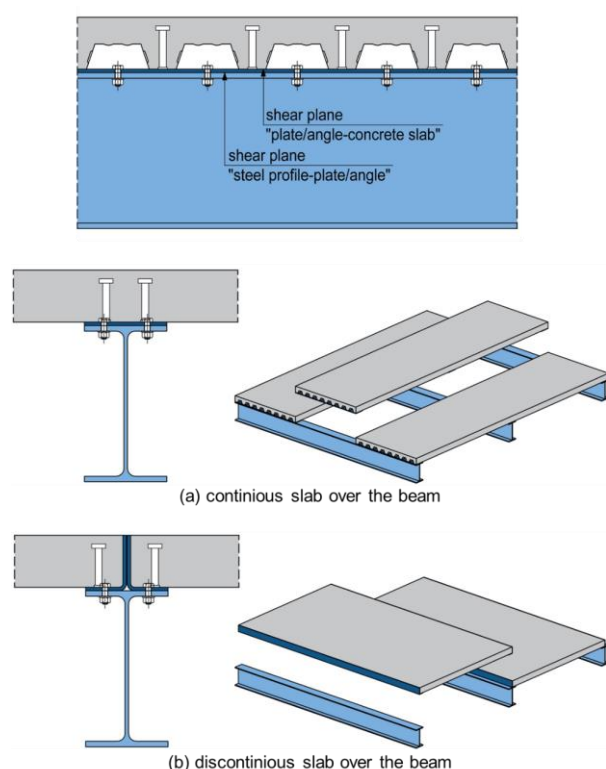


Fig. 1 Demountable connection layout

The aim of this paper is to present a solution for demountable shear connection with welded headed studs and bolts. The experimental investigation has been conducted through push-out tests to describe the shear connection performance and to identify failure modes. Various configurations of the demountable shear connection have been investigated, and results have been compared to the response of the corresponding non-demountable connection. In addition, finite element numerical models have been developed, verified against experimental results and used for further analysis of the connection response. Parametric studies have been conducted to determine and quantify the effects of key parameters on connection behaviour, such as plate and angle thickness, stirrup reinforcement position, and transverse distance between a headed stud and slab edge. In the end, recommendations for the design of the demountable shear connection have been proposed.

## 2. Experimental study

### 2.1. Push-out test specimens

The behaviour of the demountable shear connection with welded headed studs and bolts has been investigated through experimental testing of three configurations of the proposed system. Different connection configurations were made to study the influence of slab discontinuity over the support and the effects of stirrup reinforcement around headed studs. Alongside these, the equivalent non-demountable connection with welded headed studs has been tested and used for comparison.

The experimental work covers nine push-out tests in total, divided into the following series:

- Series S (2 specimens) – non-demountable steel-concrete composite connection with welded headed studs installed in a composite concrete slab with an open trough profiled steel sheeting (Fig. 2a);
- Series D (3 specimens) – demountable steel-concrete composite connection with welded headed studs and bolts applied in a composite slab with an open trough profiled sheeting; headed studs are welded to the steel plate, with bolts connecting the plate and the flange of a steel profile (Fig. 2b);

- Series DL (2 specimens) – demountable connection with bolts and welded headed studs, but contrary to series D, the concrete slab is discontinuous over the steel profile with a pair of angles applied instead of the steel plate (Fig. 2c);
- Series DLU (2 specimens) – connection identical to the series DL with the difference of the added stirrup U-bars passing around headed studs (Fig. 2d).

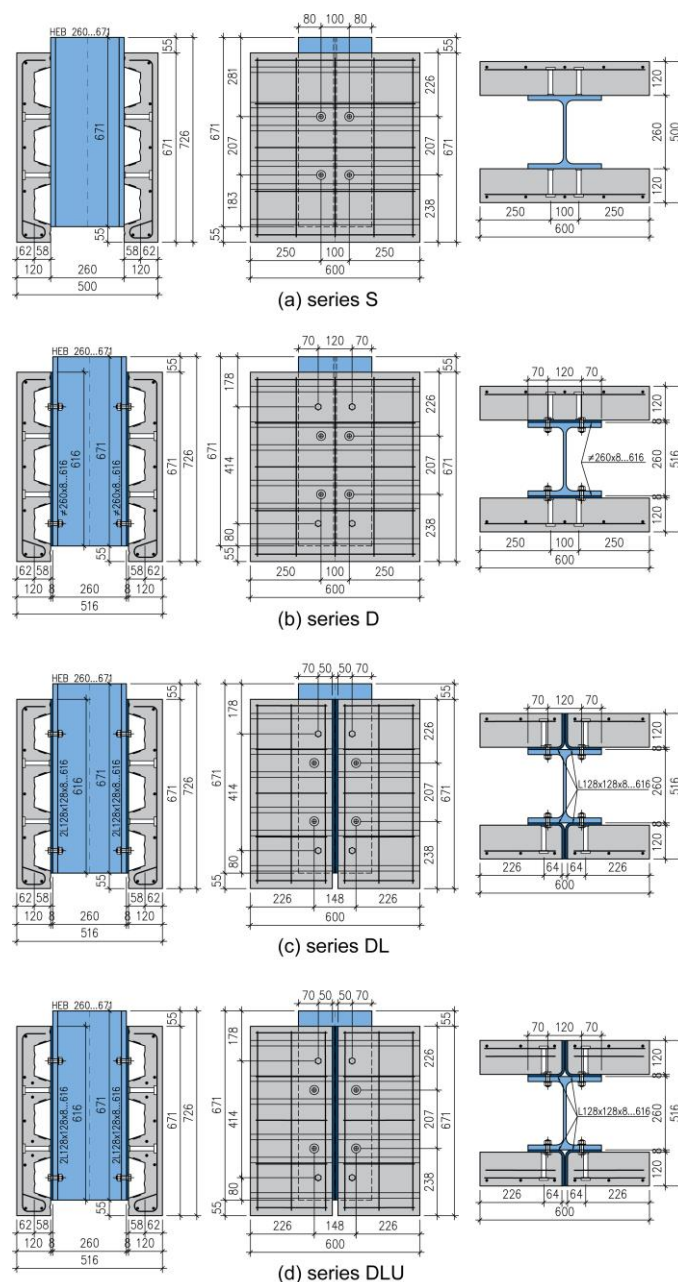


Fig. 2 Configuration of push-out specimens

A summary of the specimen properties and varied parameters is illustrated in Table 1. Demountable shear connections with continuous and discontinuous slabs over the beam are examined through series D and DL. Series DLU is used to determine the influence of the stirrup reinforcement around headed studs in connections with a discontinuous slab over the support. Series S, the non-demountable solution commonly used in building construction, is tested as a control series for comparison with the proposed demountable connections.

**Table 1**  
Summary of the push-out tests

Series	Headed studs	Bolts	Plate/angle thickness	Slab	Remark
S		/	/	continuous	/
D	$d = 16 \text{ mm}$	M12	8 mm	discontinuous	/
DL	$h_{sc} = 100 \text{ mm}$	8.8	8 mm	discontinuous	/
DLU					U-bars $\varnothing 8 \text{ mm}$

All specimens were made with Cofraplus 60 profiled steel sheeting [30]. Each specimen consisted of eight Ø16 mm headed studs. A headed stud height of 100 mm and an overall concrete slab depth of 120 mm were kept constant in all tests. Headed studs were welded to the steel profile flange and the steel plate, and afterwards profiled steel sheeting with pre-punched holes was placed.

Bolt diameter M12 and grade 8.8 were chosen to keep bolt resistance higher than that of the headed stud achieving thereby similar behaviour of demountable and non-demountable connections. The characteristic resistance of welded headed studs in the selected profiled steel sheeting was calculated according to EN 1994-1-1 [27] as 29.16 kN, assuming a concrete class C30/37. The characteristic resistance of bolts was obtained according to EN 1993-1-8 [31] as 43.43 kN. Given the ratio between the two values is 0.67, failure of welded headed studs is expected, whereas it is presumed that the bolt deformation remains in the elastic domain.

In specimens with continuous concrete slabs over the steel profile, a distance between headed studs was set to 100 mm (Fig. 2a, 2b) to satisfy detailing requirements given in EN 1994-1-1 [27]. At the same time, headed studs in discontinuous slabs were placed at a distance of  $4d = 64$  mm in the transverse direction from the concrete slab edge (Fig. 2c, 2d), where  $d$  is the diameter of the headed stud. The adopted length is smaller than the  $6d$ , which is required according to EN 1994-1-1 [27] as the minimum stud-to-slab edge distance. However, by choosing a shorter distance, it is possible to keep a headed stud right above a steel flange. The effects of the adopted stud-to-edge distance on the connection damage are discussed further in the study.

The bolt position was chosen according to the predefined hole position for HEB 260 profile. Bolt holes cut in the profile flange, plates and angles had a 13 mm diameter.

The thickness of the steel plate which headed studs were welded to should be appropriately adopted to avoid deformation of the bolt holes and the plate beneath headed studs. According to EN 1994-1-1 [27], the ratio between the headed stud diameter and the thickness of the part which the stud is welded to should be less than 2.5; in other words, the thickness should be greater than  $0.4d$ . In the case of the tested connection, as the limiting value of  $0.4d$  equals 6.4 mm, the plate thickness was rounded up and set to 8 mm. The same thickness was selected for angles, which were made of the plate by cutting and cold forming the material. Bearing resistance at bolt holes for an 8 mm thick plate is greater than bolt shear resistance; therefore, it is not considered critical. The validity of the adopted 8 mm thickness is examined throughout the study, and the potential application of a smaller 6 mm plate thickness is later numerically analysed.

A recess in the concrete slab base, marked as optional according to EN 1994-1-1, Annex B [27], was avoided during fabrication to accomplish easier specimen preparation. According to some research results, the absence of recess is not expected to influence the experimental results [32,33]. A slab width of  $b = 600$  mm was adopted to satisfy the condition  $b > e_1 + 2 h_{sc} / \tan(25^\circ)$  [34], where  $e_1$  is the transverse spacing between the studs inside the rib and  $h_{sc}$  is the height of the stud. Therefore, it was intended to fully include a concrete cone that develops during a failure of headed studs in push-out tests.

One layer of Ø8 mm reinforcement was placed in the top zone of the slab. Longitudinal bars were bent on one side forming a hook to reinforce the supporting rib of the concrete slab, as suggested by some authors [24,25]. Stirrup bars applied in specimens of the series DLU were formed in a U-shape to pass around the headed stud. The U-bar diameter was adopted as  $0.5d = 8$  mm. U-bars were placed at the level of the top surface of profiled steel sheeting and oriented in the transverse direction, according to Fig. 3.

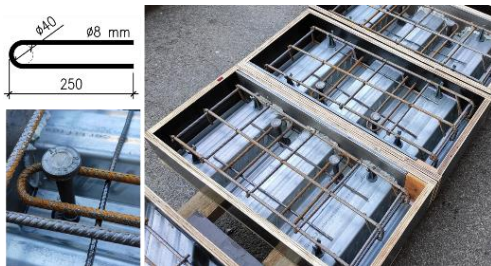


Fig. 3 U-bar geometry and specimens with stirrups before concrete casting

Concrete with a maximum aggregate size of 16 mm was used to satisfy the EN 1994-1-1 [27] requirement considering the relations between nominal aggregate size and connection geometry. To minimise initial shrinkage cracks, specimens were kept moist during the first three days after concrete casting, and assembled for push-out testing 28 days later. Demountable specimens were assembled by connecting concrete slabs and steel profiles with bolts. Nuts were

tightened to achieve firm contact between steel flange and plate, without the application of pretension force.

## 2.2. Test set-up and measurement procedure

Push-out tests were conducted following instructions given in EN 1994-1-1, Annex B [27]. Concrete slabs were placed on a layer of fresh gypsum to accomplish good contact with the support. According to recommendations given in the DISCO report [30], no transverse loading was applied as the ratio between the stud and rib height was greater than 1.56.

The test set-up for non-demountable and demountable specimens is shown in Fig. 4. For specimens from the series S, a total of eight displacement transducers were installed: four for measuring the horizontal separation between the concrete slab and steel profile (H1–H4 in Fig. 4a) and four for measuring the vertical slip between the concrete slab and steel profile (V1–V4 in Fig. 4a). For specimens from the series D, DL and DLU, 12 displacement transducers were installed: four for measuring the horizontal separation between the concrete slab and steel profile (H1–H4 in Fig. 4b), four for measuring the vertical slip between the concrete slab and steel profile (V1–V4 in Fig. 4b) and four for measuring the vertical slip between the concrete slab and steel plate/angle (V5–V8 in Fig. 4b). In this way, recorded data on the slip of demountable specimens includes not only displacement between the concrete slab and steel profile but also the slip in two shear planes: “steel plate/angle-concrete slab” and “steel profile-steel plate/angle”.

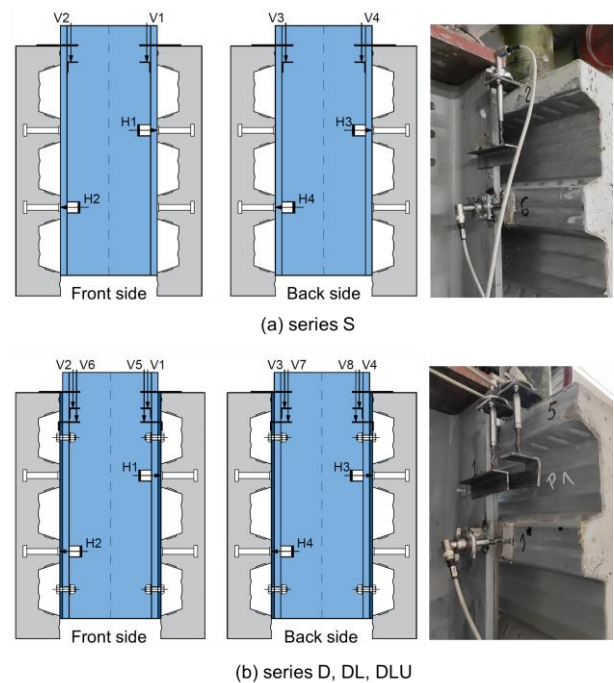


Fig. 4 Test set-up

Vertical displacements were measured on the top of the specimen. To measure the horizontal separation between the concrete slab and steel profile, profiled steel sheeting was locally cut on the rib as close as possible to headed studs, and a glass plate was glued to the concrete to accomplish a smooth surface for sensor movement.

The exception from the previously listed measured values was made in the case of the specimen DLU-01, where two additional displacement transducers for measuring the lateral horizontal separation between two segments of a discontinuous slab were used. Sensors were placed on the top of the specimen. However, it was observed that this displacement remained negligible during the experiment (less than 0.5 mm), and it was not measured in further testing.

The applied force was measured by a load cell with a capacity of 1000 kN placed on the top [35]. The loading regime was adopted according to EN 1994-1-1, Annex B [27]. After the application of 25 loading cycles, further loading was applied in one step, with a tendency that failure does not appear in less than 15 minutes. Data was recorded until the load dropped to 20% below the maximum load.

## 2.3. Experimental testing of material

For steel components of the push-out specimens, material properties such



as steel yield strength, ultimate strength and modulus of elasticity were obtained through standardised tensile tests by defining stress-strain curves for each material. A statistical evaluation was conducted according to the requirements given in Annex D of EN 1990 [36]. The adopted geometry of steel coupons were compliant with EN ISO 6892-1 requirements [37]. The testing procedure was conducted as a strain control, applying the uniform displacement rate of 0.1 mm/min up to 1% strain and setting the displacement rate of 2.2 mm/min afterwards [38]. A digital extensometer was used for measuring strains, and the gauge length was  $L_0 = 50$  mm. The only exception made was during testing coupons taken from bolts where the application of a digital extensometer during testing was not possible due to the small size of coupons; therefore, for measuring strains, two strain gauges glued around coupon diameter were used.

The obtained stress-strain curves and geometries of coupons taken from profiled steel sheeting, plate, profile flange, headed studs and bolts are shown in Fig. 5. Considering that angles were formed from the plates, no coupons from angles were taken. Material properties of all steel components are summarised in Table 2.

Material properties of concrete were examined on concrete cubes  $150 \times 150 \times 150$  mm. Concrete compressive strength  $f_{c,cube}$  was measured at the time of specimen push-out testing. The average value of the concrete compressive strength corresponding to each push-out specimen is given in Table 3 (Section 2.4).

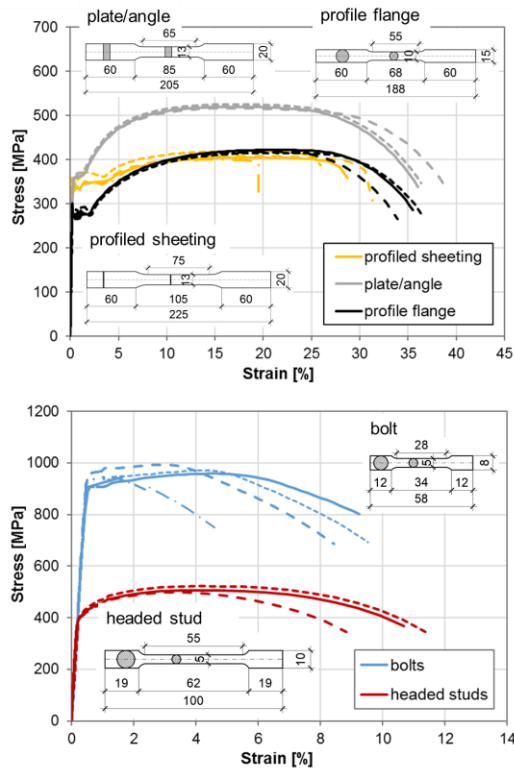


Fig. 5 Stress-strain curves

Table 2

Material properties of steel components

Element	Yield strength		Ultimate strength		Modulus of elasticity	Strain at ultimate strength
	Mean	CoV	Mean	CoV		
	$f_y$ [MPa]	[%]	$f_u$ [MPa]	[%]		
Profile flange	297.3	5.08	418.6	0.77	197.7	20.72
Plate/angle	357.1	0.85	520.7	0.84	200.7	17.06
Profiled sheeting	347.7	4.06	408.2	1.92	194.5	17.35
Headed stud	421.0	1.43	509.0	2.37	200.0	3.90
Bolt	928.9	2.64	966.5	2.14	204.0	-

## 2.4. Push-out test results and discussion

### 2.4.1. Failure modes

After push-out testing, specimens were demounted and failure modes were observed. Each test resulted in concrete failure, as shown in Fig. 6. The failure

modes of demountable D specimens and non-demountable S specimens are equivalent, indicating the concrete pull-out failure, which is manifested through the development of concrete cones. Concrete failure of a discontinuous concrete slab of specimen DL agrees with the failure form of the continuous slab of specimen D. DLU specimens reinforced with U-bars also feature concrete cone failure, as detected on the right side of the specimen presented in Fig. 6d. However, the left side of the DLU specimen, shown in Fig. 6d, indicates the separation of the entire concrete ribs from the rest of the concrete slab.

Specimens with discontinuous slabs over the beam did not exhibit longitudinal concrete splitting between a headed stud and a slab edge, though the applied stud-to-edge distance had been set to  $4d$ , which is smaller than the required  $6d$  according to EN 1994-1-1 [27]. It might be assumed that the vertical angle leg reinforces the edge and contributes to the prevention of splitting failure.

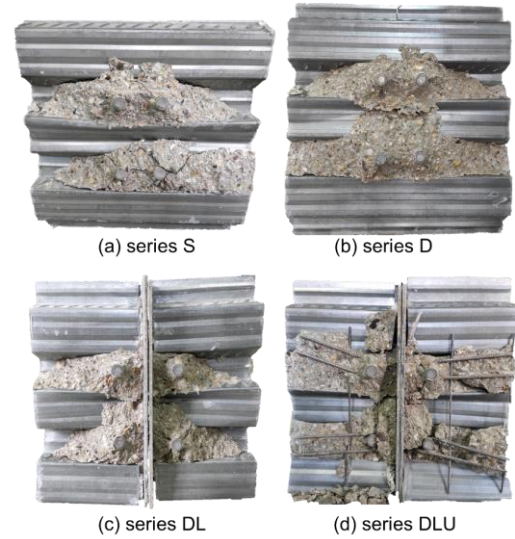


Fig. 6 Failure forms of specimens.

After removing the surrounding concrete, a certain deformation of welded headed studs was observed in the form of a single curvature along the stud height, but the deformation was not significant. No rupture of headed studs occurred in any of the conducted push-out tests. Deformation of the plate and angles was not detected, implying that plate bending on the contact with headed studs did not appear for the selected thickness.

To demonstrate reassembling of a demountable shear connection, bolts were dismantled after testing. Easy bolt removal proved the demountability of the proposed shear connection. As plastic deformation was not observed in bolts, it could be assumed that these connectors had an elastic response during the experiment, as it was intended. Also, no deformation of the steel material around bolt holes occurred in the steel plate and angles, nor the steel profile.

### 2.4.2. Load-slip curves

Load-slip curves obtained during push-out testing of non-demountable and demountable specimens are presented in Fig. 7 and 8, respectively. For demountable specimens, load-slip curves are given for the overall slip between the concrete slab and steel profile and the slip in the “steel plate/angle-concrete slab” plane. Ultimate load, stiffness at serviceability loads, slip and transverse separation between a concrete slab and a steel profile are summarised in Table 3. For demountable specimens, the slip is also presented for the shear plane on the contact between the steel plate/angles and the concrete slab. In addition, the average values of concrete compressive strength  $f_{c,cube}$ , obtained at the time of specimen push-out testing, are listed in Table 3. The characteristic load is calculated according to statistical evaluation procedures given in Annex D of EN 1990 [36] and the alternative method provided in Annex B of EN 1994-1-1 [27], which defines characteristic resistance as the minimum failure load reduced by 10%. Stiffness at serviceability loads is obtained per headed stud connector, i.e. bolt, at the load of  $0.7P_{ult,exp}$ . The slip capacity is obtained according to Annex B of EN 1994-1-1 [27] as the maximum slip in the post-ultimate domain corresponding to 90% of the failure load.

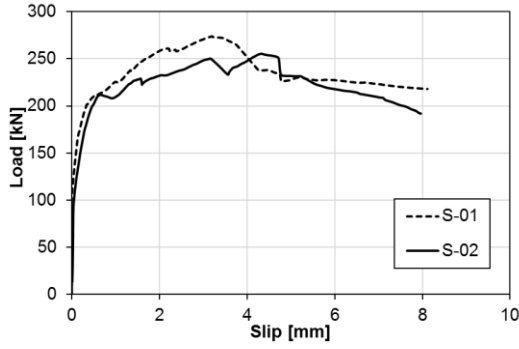
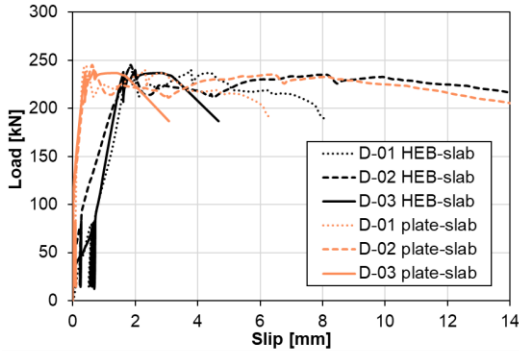
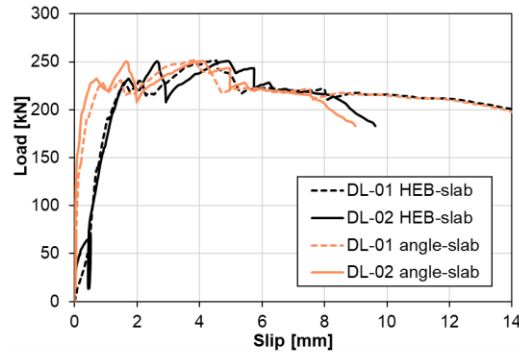


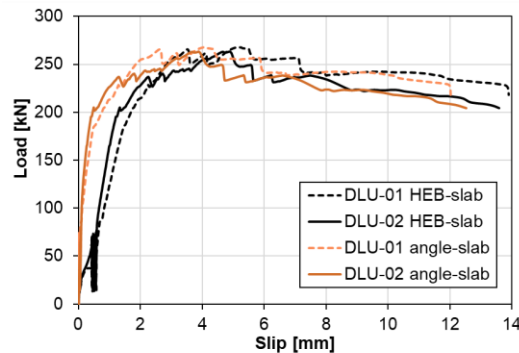
Fig. 7 Load-slip curves for non-demountable specimens



(a) series D



(b) series DL



(c) series DLU

Fig. 8 Load-slip curves for demountable specimens

## (a) Ultimate load

The measured ultimate loads of the tested connections are in the range of 240 to 274 kN. Comparisons of the ultimate loads of the series S, D, DL and DLU are given in Table 4. As in all push-out tests, concrete failure occurred and no rupture in bolts nor headed studs appeared, the experimental ultimate load for each specimen,  $P_{ult,exp}$ , is normalised with concrete compressive strength to compare load capacities of different test series. For normalisation on the concrete strength of the series S of 35 MPa, the following relation is applied [33]:

$$P_{ult,exp,nor} = P_{ult,exp} \left( \frac{35 \text{ MPa}}{f_{cm}} \right)^{2/3} \quad (1)$$

where  $f_{cm}$  is the concrete cylinder compressive strength, calculated by multiplying the concrete cube strength by 0.8. Correlation between specimens' resistance is shown through the ratio  $P_{ult,exp,nor}/\bar{P}_{ult,exp,nor,S}$ , where  $\bar{P}_{ult,exp,nor,S}$  is the mean value of the normalised ultimate load obtained for series S.

By accounting for the variation present between ultimate loads of specimens from the same series, no significant dissimilarities in the load capacity of the analysed shear connections were noted. Discontinuity of the composite slab over the support does not significantly affect the resistance of the shear connection for the set distance between a headed stud and slab edge of  $4d$ , as observed when comparing results shown for series D and DL. The implementation of U-bars in series DLU influences the increase of the peak load by approximately 5% compared with the DL specimens without stirrup reinforcement. A match between average ultimate loads obtained for series S and DLU indicates that the developed solution for a demountable shear connection with bolts and headed studs corresponds well, at the point of shear capacity, to the non-demountable connection with welded headed studs. Further review of the adopted design of demountable connections is conducted within the numerical parametric studies.

## (b) Stiffness and ductility

According to the presented load-slip curves, all demountable specimens feature initial slip at the beginning of loading, as observed in Fig. 8. However, this initial slip is not present in the shear plane "steel plate/angle-concrete slab" of demountable specimens, neither is it present for non-demountable specimens (Fig. 7). The initial slip of demountable specimens is the result of bolt movement inside the holes. As no pretension force was applied during bolt mounting, bolt slip inside the hole starts at the early loading stage before applying loading cycles. The measured initial slip due to bolt displacement has values in the range of 0.25–0.70 mm, depending on the exact bolt position inside the holes released during specimen mounting. As a result of the initial bolt slip inside the holes, the average stiffness per stud connector is in the range of 18–22 kN/mm for demountable specimens, which is less than the stiffness of the corresponding non-demountable connection (75 kN/mm).

After the initial slip of bolts inside the holes, the further behaviour of demountable specimens is in agreement with the behaviour of non-demountable specimens. In this stage, the slip of headed studs in the shear plane "steel plate/angle-concrete slab" starts, and gradually becomes the dominant component in the overall connection slip. Similar behaviour was observed for all demountable specimens.

According to the obtained data shown in Table 3, it is noticed that most of the demountable specimens feature larger slip at 90% of the ultimate load than non-demountable specimens. Slip in the shear plane "steel plate/angle-concrete slab" corresponding to 90% of the maximum load is less than the overall slip of demountable connections and closer to the slip of non-demountable specimens. The slip at load  $0.9P_{ult,exp}$  is below 6 mm for both S specimens, meaning that connectors cannot be classified as ductile, whereas two out of three tested demountable D specimens have slip capacity larger than 6 mm. It is noted, though, that the overall slip of the demountable connection contains the initial bolt slip. At demountable specimens with discontinuous slabs over the support, a larger slip capacity is observed in connections with the applied U-bars (more than 6 mm) than in connections without this reinforcement (less than 6 mm), indicating that stirrups placed around headed studs may increase ductility of the connection.

## 3. Numerical analysis

## 3.1. Development of finite element models

Numerical analysis including geometrical and material nonlinearities was conducted in finite element software Abaqus [39]. For modelling of push-out tests, the explicit solver was used, simulating the quasi-static analysis.

For the development of finite element models, all components of specimens tested in push-out tests were considered: headed studs, bolts, concrete slabs, profiled steel sheeting, steel profile, plate/angles and reinforcement bars. In addition, a supporting plate which the concrete slab was laid on was created. Components were modelled as solid parts, with two exceptions: profiled steel sheeting was modelled as a shell part, and reinforcement bars were modelled as truss parts.

**Table 3**  
Summary of push-out test results

Series	Specimen	Concrete cube compressive strength	Ultimate load	Stiffness	Transverse separation at $P_{ult,exp}$	Max. slip at $0.9P_{ult,exp}$	
						Total slip: steel profile-concrete slab	Slip in shear plane: steel plate/angle-concrete slab
		$f_{c,cube}$ [MPa]	$P_{ult,exp}$ [kN]	$k_{sc}$ [kN/mm]	[mm]	$\delta_{sk}$ [mm]	$\delta_{sk,ps}$ [mm]
S	S-01	43.7	274.0	80	0.36	4.09	
	S-02	43.7	255.1	70	0.59	5.30	
	Mean		264.6	75			
	St. deviation		13.36				
	CoV [%]		5.05				
	Characteristic		$-^{(1)} / 229.6^{(2)}$			3.68 <sup>(2)</sup>	
D	D-01	43.1	244.0	24	0.28	6.68	5.43
	D-02	43.1	245.0	21	0.84	13.06	-
	D-03	43.1	239.5	18	0.24	3.73	2.20
	Mean		242.8	21			
	St. deviation		2.93				
	CoV [%]		1.21				
	Characteristic		233.0 <sup>(1)</sup> /215.6 <sup>(2)</sup>			3.36 <sup>(2)</sup>	1.98 <sup>(2)</sup>
DL	DL-01	46.6	251.3	23	0.29	5.16	4.57
	DL-02	46.6	250.6	20	0.68	5.75	4.97
	Mean		251.0	22			
	St. deviation		0.49				
	CoV [%]		0.20				
	Characteristic		$-^{(1)} / 225.5^{(2)}$			4.64 <sup>(2)</sup>	4.11 <sup>(2)</sup>
DLU	DLU-01	46.6	267.8	15	0.67	10.66	9.25
	DLU-02	46.6	263.0	21	0.75	7.67	6.74
	Mean		265.4	18			
	St. deviation		3.39				
	CoV [%]		1.28				
	Characteristic		$-^{(1)} / 236.7^{(2)}$			6.90 <sup>(2)</sup>	6.07 <sup>(2)</sup>

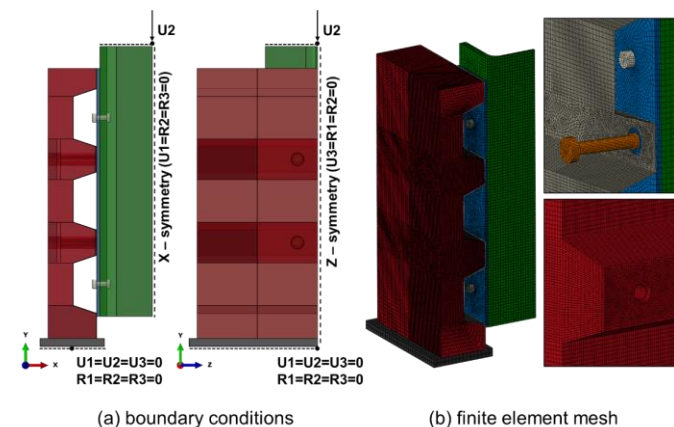
\*<sup>(1)</sup> according to EN 1990 [36], <sup>(2)</sup> according to EN 1994-1-1 [27]

**Table 4**  
Comparison of test series

Series	Specimen	Concrete cylinder compressive strength	Ultimate load	Normalised ultimate load*	Mean value of the normalised ultimate load	Ratio	
						$P_{ult,exp,nor} / \bar{P}_{ult,exp,nor,S}$	$\bar{P}_{ult,exp,nor} / \bar{P}_{ult,exp,nor,S}$
		$f_{cm}$ [MPa]	$P_{ult,exp}$ [kN]	$P_{ult,exp,nor}$ [kN]	$\bar{P}_{ult,exp,nor}$ [kN]		
S	S-01	35.0	274.0	274.2	264.8	1.04	1.00
	S-02	35.0	255.1	255.3		0.96	
D	D-01	34.5	244.0	246.4	245.3	0.93	0.93
	D-02	34.5	245.0	247.5		0.93	
	D-03	34.5	239.5	241.9		0.91	
DL	DL-01	37.3	251.3	240.9	240.6	0.91	0.91
	DL-02	37.3	250.6	240.3		0.91	
DLU	DLU-01	37.3	267.8	256.8	254.5	0.97	0.96
	DLU-02	37.3	263.0	252.2		0.95	

\*normalised with  $f_{cm} = 35$  MPa

Double vertical symmetry conditions were applied to models, as presented in Fig. 9a. All points at the top surface of the steel cross-section were constrained to the reference point to which vertical loading was applied. Nodes at the bottom surface of the supporting plate were also constrained to the reference point setting the fully fixed boundary condition.



**Fig. 9** Finite element models

For connecting headed studs with the surface to which they were welded (steel profile, plate or angles), the tie constraint was used, while for setting proper contact conditions between reinforcement bars and the concrete slab, the embedded constraint was applied. For the other contacts between parts, surface-to-surface contact was assigned, applying “hard” contact in the normal direction and setting different friction coefficients in the tangential direction:

- concrete slab-supporting plate 0.45,
- concrete slab-headed stud 0.45,
- concrete slab-profiled sheeting 0.45,
- concrete slab-steel profile/plate/angle 0.30,
- between steel parts 0.20.

Loading was applied as a controlled displacement, using the smooth step amplitude function. The duration of the experiment was set to 1000 s, whereas the mass scaling method was applied with a time increment of 0.003 s.

The complexity of the numerical model and large zones in the concrete slab where cracks propagate influenced a large total number of finite elements (up to 878 757), necessary for simulating a proper model response. Hence, a reduction in computing time was essential. As efficient elements at the point of the computing time, 8-node linear hexahedron elements with reduced integration C3D8R were applied to solid parts, and 4-node linear quadrilateral elements with reduced integration S4R were applied to shell parts [40]. For meshing truss parts, 2-node linear elements T3D2 were used. The optimum size of finite elements on different parts was adopted according to the mesh convergence study. The smallest size of elements was applied to headed studs



and surrounding concrete (2 mm), whereas the largest elements were assigned to the periphery regions of the model where the development of cracks and failure were not expected (10 mm), as shown in Fig. 9b.

Material models applied in the numerical analysis were based on the experimental testing of the material. To describe the material behaviour of the steel components in the elastic domain, the measured modulus of elasticity and Poisson's ratio of 0.3 were set. True stress-strain curves [39] obtained from experimental stress-strain curves of coupon testing were used to define material response in the plastic domain, as presented in Fig. 10. Since damage of steel components did not occur during experimental push-out tests, ductile and shear damage material models were not considered in the numerical analysis.

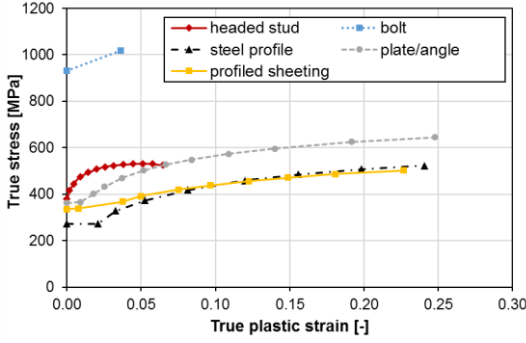


Fig. 10 True stress-strain curves for steel components

Since reinforcement bars were not tested in tensile tests, the material model for reinforcement was adopted as a bilinear model, according to EN 1992-1-1 [41]. The modulus of elasticity was defined with yield strength set to 500 MPa. A top branch of the stress-strain curve was assumed to be horizontal. The adopted approximations are justified by the fact that stress in bars does not exceed 130 MPa during simulations, as shown in Fig. 19.

As the failure of all push-out specimens was the failure of concrete, it was essential for numerical modelling to apply the material model for concrete which provides good predictions of the behaviour of concrete slab cast in open trough profiled steel sheeting. Although several approaches for defining the Concrete Damage Plasticity model were considered, the best results were obtained by applying the model proposed by Pavlović [12]. For describing concrete behaviour in the elastic domain, the modulus of elasticity and Poisson's ratio of 0.2 were applied. For defining compressive response in the plastic domain, the concrete stress-strain relation was described by the curve given in EN 1992-1-1 [41] and appropriate sinusoidal and linear function extensions, according to Fig. 11. EN 1992-1-1 provides the following equation for describing the concrete stress-strain relation for strains up to  $\epsilon_{cu1}$  (points A–D in Fig. 11):

$$\sigma_c(\epsilon_c) = f_{cm} \frac{k\eta - \eta^2}{1 + (k-2)\eta}, \quad \epsilon_c \leq \epsilon_{cu1} \quad (1)$$

where:

$$\eta = \frac{\epsilon_c}{\epsilon_{c1}} \quad (2)$$

$$k = 1.05 \epsilon_{c1} \frac{E_{cm}}{f_{cm}} \quad (3)$$

$\epsilon_{c1}$  is a compressive strain in the concrete at the peak stress  $f_{cm}$ , and  $\epsilon_{cu1} = \epsilon_{cuD}$  is the ultimate compressive strain of concrete. According to EN 1992-1-1 [41], values of strains  $\epsilon_{c1}$  and  $\epsilon_{cu1}$  are defined as functions of the concrete compressive strength.

For high strains beyond  $\epsilon_{cu1}$ , the following equation proposed by Pavlović [12] was implemented, including the sinusoidal part (points D–E in Fig. 11) and linear part (points E–F in Fig. 11):

$$\sigma_c(\epsilon_c) = \begin{cases} f_{cm} \left[ \frac{1}{\beta} - \frac{\sin(\mu^{\alpha_{ID}} - \alpha_{IE} \pi/2)}{\beta \sin(\alpha_{IE} \pi/2)} + \frac{\mu}{\alpha} \right], & \epsilon_{cuD} < \epsilon_c \leq \epsilon_{cuE} \\ [f_{cuE}(\epsilon_{cuF} - \epsilon_c) + f_{cuF}(\epsilon_c - \epsilon_{cuE})] / (\epsilon_{cuF} - \epsilon_{cuE}), & \epsilon_c > \epsilon_{cuE} \end{cases} \quad (4)$$

where:

$$\mu = \frac{\epsilon_c - \epsilon_{cuD}}{\epsilon_{cuE} - \epsilon_{cuD}} \quad (5)$$

$$\beta = \frac{f_{cm}}{f_{cuD}} \quad (6)$$

$$\alpha = \frac{f_{cm}}{f_{cuE}} \quad (7)$$

$\alpha_{ID}$  and  $\alpha_{IE}$  are factors that influence the shape of the sinusoidal function,  $f_{cuE}$  and  $f_{cuF}$  are compressive stresses at the points E and F, according to Fig. 11,  $\epsilon_{cuD}$ ,  $\epsilon_{cuE}$  and  $\epsilon_{cuF}$  are compressive strains at points D, E and F, respectively, according to Fig. 11.

As the applied material model is flexible at the point of adopting the exact shape of the sinusoidal function and stress and strain values at points E and F, parameters were calibrated to match experimental results and keep the curve smooth. The adopted values of parameters are:  $\alpha = 8$ ,  $\alpha_{ID} = 0.50$ ,  $\alpha_{IE} = 0.60$ ,  $\epsilon_{cuE} = 0.05$ ,  $\epsilon_{cuF} = 0.20$ , and  $f_{cuF} = 0.40$  MPa.

Concrete compression damage was described using the compressive damage variable  $D_c$ , derived from the uniaxial stress-strain curve and described by the following equation:

$$D_c = 1 - \frac{f_{cm}}{\sigma_c} \quad (8)$$

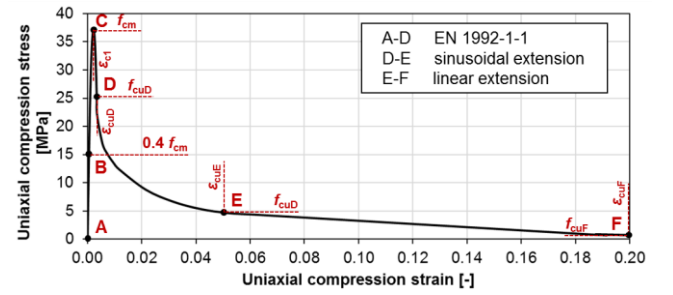


Fig. 11 Stress-strain curve for concrete behaviour in compression ( $f_{cm} = 37.3$  MPa)

Concrete behaviour in tension was described by linear stress-strain relation in the elastic domain up to concrete tensile strength  $f_{ctm}$ , whereas sinusoidal function was used for describing tension softening until the stress  $f_{ctm}/20$  [12]. Concrete tension damage was described similarly as concrete compression damage using the tensile damage variable  $D_t$ , according to the relation:

$$D_t = 1 - \frac{f_{ctm}}{\sigma_t} \quad (9)$$

The dilation angle required for defining the Concrete Damage Plasticity model was adopted as  $38^\circ$ , as performed in several other studies [33,42]. Other parameters were set according to recommendations given in the software user manual [39]: flow potential eccentricity as 0.1, the ratio of equibiaxial-to-uniaxial compressive strength as 1.16, and parameter  $K$ , which represents the ratio of the second stress invariant on the tensile meridian to that on the compressive meridian, as 0.67.

### 3.2. Validation of numerical results

To validate developed finite element models, their behaviour was compared with the behaviour of the experimental specimens by analysing the load-slip response, deformation of connectors and failure modes. Load-slip curves obtained by finite element analysis are compared with experimental load-slip curves in Fig. 12. Good agreement is accomplished between the load-slip response of experimental push-out specimens and corresponding finite element models. The mean values of ultimate loads obtained by experimental testing and the ultimate loads obtained through numerical simulations are compared in Table 5. The maximum relative difference in results is 5%.

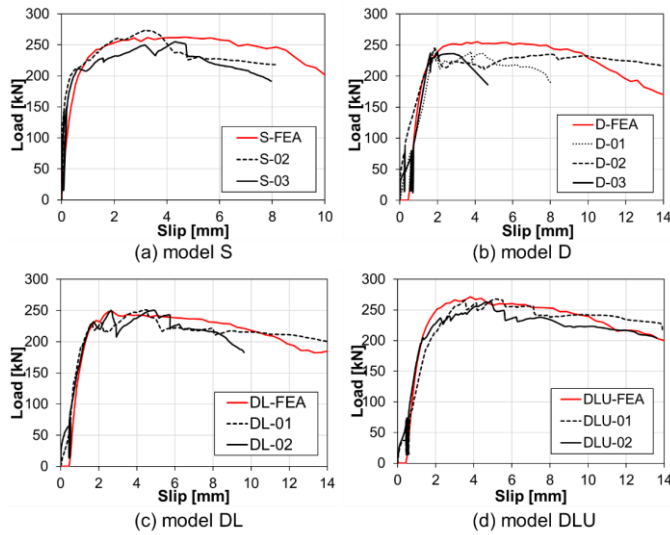
The behaviour of numerical models corresponds to the behaviour of push-out test specimens observed during experimental testing. Deformed shapes and stress in bolts and headed studs of model D are presented in Fig. 13. The slip of bolts is pronounced at the beginning of loading. After bolt-to-hole clearances are voided, headed studs start slipping. At the total connection slip of 2 mm and 6 mm, the slip of bolts remains almost the same (0.82 mm and 0.87 mm, respectively), whereas the slip of headed studs increases (from 1.22 mm to 5.13 mm). The increase of the stress in headed studs is noticed along with a deformation increase. The concentration of stress above the material yield strength in the stud shank just above the weld collar influences the development of a plastic hinge. Another concentration of stress occurs at the top half of the stud shank, although the hinge is not completely formed across the stud cross-section. The deformed shape of a headed stud in the form of a single curvature along stud height corresponds to the one observed during experimental testing. The highest stress in bolts is below the material yield strength. Changes in the

stress in bolts are minor at the connection slip of 2 mm and 6 mm, and the bolt deformation remains insignificant, as noticed during experimental testing. A similar connection behaviour is detected in other demountable models, DL and DLU.

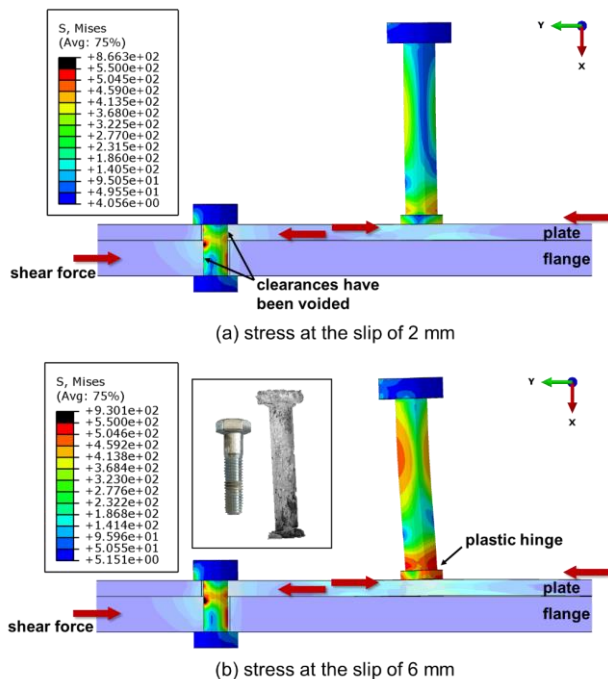
Developed numerical models are able to predict the actual failure modes of push-out test specimens. Crack patterns in concrete slabs of different models presented in Fig. 14 indicate the development of concrete cones and final pull-out failure. Concrete cones of presented connections have slightly different edge slopes, from 23° to 27°. Numerical models also showed the concrete damage occurring in front of the headed studs, indicating rib punching due to the narrow width of the ribs.

**Table 5**  
Comparison of the experimental and numerical ultimate loads

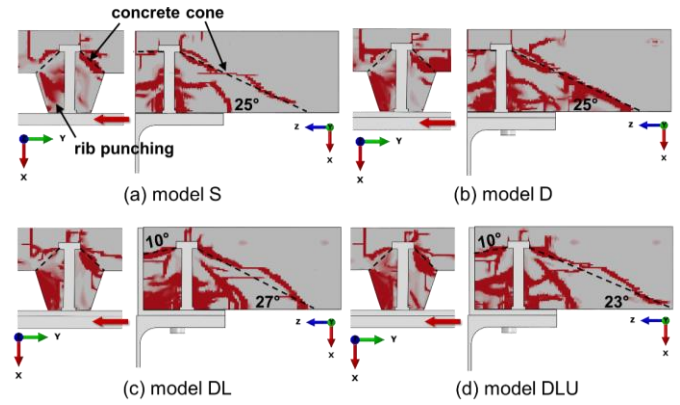
Series	Concrete compressive strength $f_{cm}$ [MPa]	Ultimate load		Ratio FEA/EXP
		EXP $\bar{P}_{ult,exp}$ [kN]	FEA $P_{ult,fea}$ [kN]	
S	35.0	264.6	262.5	0.99
D	34.5	242.8	255.3	1.05
DL	37.3	251.0	248.2	0.99
DLU	37.3	265.4	271.6	1.02



**Fig. 12** Comparison of the experimental and numerical load-slip curves



**Fig. 13** Headed studs and bolts at the connection slip of 2 mm and 6 mm



**Fig. 14** Concrete crack patterns

#### 4. Parametric studies

Based on the validated numerical models simulating push-out tests, parametric studies were performed to evaluate the effects of key parameters on the demountable shear connection response. Tested parameters included the plate and angle thickness, the distance between the headed stud and slab edge, and the stirrup position along the stud height.

##### 4.1. Effect of the plate and angle thickness

Effects of the plate and angle thickness on the connection response were studied on the demountable models D and DLU, varying the dimension in the range from 4 mm to 10 mm. Load-slip curves presented in Fig. 15 (curves are presented without the initial bolt slip) and a comparison of ultimate loads given in Table 6 indicate that the responses of models with the plate thickness of 8 mm and 10 mm do not differ. On the other hand, a decrease of the plate thickness below 8 mm induces a drop in the connection shear resistance, notably pronounced in the case of the plate thickness of 4 mm. A drop in the shear resistance when angle thickness is reduced from 8 mm to 6 mm (9%) is more pronounced than a drop in the shear resistance when the plate thickness is reduced to the same value (4%).

Plate deformation in the area near welded headed studs was analysed to explain the obtained results. Out-of-plane deformation at the slip of 6 mm is shown in Fig. 16. An increase in the plate deformation with a decrease in the plate thickness is present. For the plate thickness of 4 mm, the maximum deformation is 1.75 mm, whereas for the plate thickness of 10 mm, it is 0.25 mm and cannot be visually noticed. Deformation of the plate induces a certain rotation of the stud connector which results in lower resistance to shear.

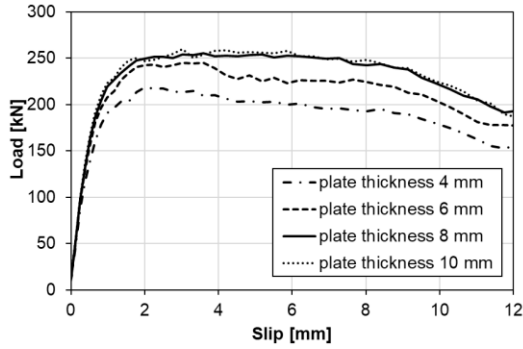
In order to minimise the plate deformation, additional models were developed with an added pair of bolts between two pairs of headed studs in the longitudinal direction. It was tested if the additional bolts may fix the plate to the profile flange and increase the plate stiffness. However, results showed that the plate deformation had a strictly local character and consequently, the implementation of the additional bolts did not affect the connection response. The deflection of the plate with the added bolts was negligibly smaller in comparison with the corresponding basic model. In terms of ultimate loads, relevant differences in the response of the two models were not noticed for any of the applied plate thicknesses, as presented in Table 7. Results validate the application of bolts in two times larger longitudinal spacing than headed studs, leading to savings in material consumption and construction time.

According to Fig. 15, for both plate and angle, the optimum thickness is 8 mm for the applied 16 mm diameter headed stud. Results are in agreement with the rules given in EN 1994-1-1 [27] regarding the relationship between the headed stud diameter and the thickness of the part to which the stud is welded, requiring the part thickness greater than  $0.4d$ , where  $d$  is the stud shank diameter. In order to confirm if the same applies in the general case, 12 additional numerical models of demountable connections with continuous slabs over the support were developed with varied diameters of headed studs (16, 19 and 22 mm), stud heights (100 and 125 mm) and concrete classes (C20/25–C50/60). In each model, bolt diameter was chosen to keep the ratio between the headed stud and bolt resistance lower than 0.70, whereas plate thickness was adopted as greater than  $0.4d$ . Additional models of non-demountable connections were formed as well. A comparison of obtained ultimate loads of corresponding demountable and non-demountable connections is illustrated in Table 8. A strong match between the ultimate loads of demountable and non-demountable models confirms the validity of the proposed demountable connection design with a plate thickness greater than  $0.4d$ .

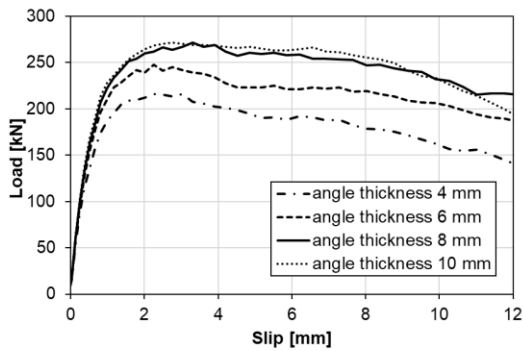
**Table 6**

Ultimate loads for varied plate and angle thickness

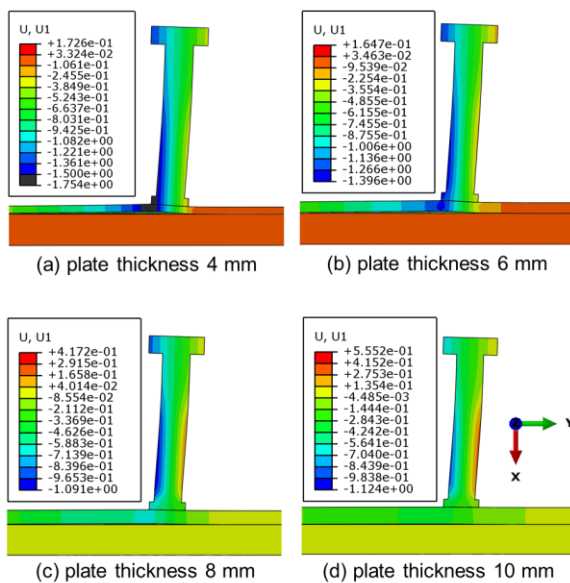
No.	Plate/angle thickness	D (continuous slab above the support)			DLU (discontinuous slab above the support)		
		Concrete strength	Ultimate load	Ratio	Concrete strength	Ultimate load	Ratio
		$f_{cm}$ [MPa]	$P_{ult,fea}$ [kN]	$P_{ult,fea(i)}/P_{ult,fea(3)}$	$f_{cm}$ [MPa]	$P_{ult,fea}$ [kN]	$P_{ult,fea(i)}/P_{ult,fea(3)}$
(1)	4	34.5	218.7	0.86	37.3	216.2	0.80
(2)	6	34.5	245.4	0.96	37.3	247.5	0.91
(3)	8	34.5	255.3	-	37.3	271.6	-
(4)	10	34.5	259.7	1.02	37.3	271.3	1.00



(a) model D



(b) model DL

**Fig. 15** Load-slip curves for varied plate thickness and angle thickness**Fig. 16** Plate deformation at the slip of 6 mm**Table 7**

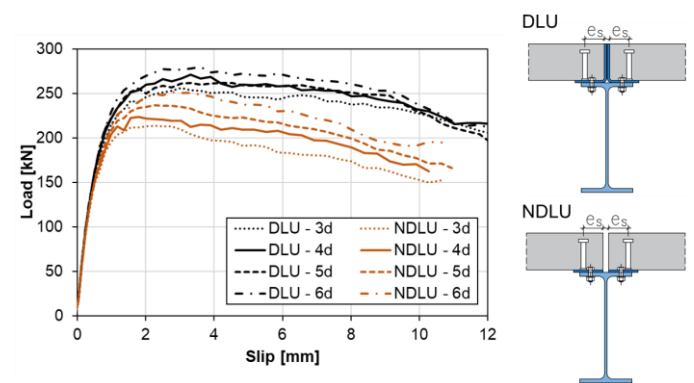
Ultimate loads for models with two and three bolts in the longitudinal direction

Plate thickness	Concrete strength	Ultimate load		
		Two bolts in the long. direction	Three bolts in the long. direction	Ratio
		$P_{ult,fea,2b}$ [kN]	$P_{ult,fea,3b}$ [kN]	$P_{ult,fea,3b}/P_{ult,fea,2b}$
4	34.5	218.7	219.8	1.01
6	34.5	245.4	248.5	1.01
8	34.5	255.3	257.4	1.01
10	34.5	259.7	267.7	1.03

#### 4.2. Effect of the stud-to-edge distance

In connections with discontinuous slabs over the support, the distance between the headed stud and slab edge in the lateral direction is an important parameter that should be carefully adopted in design. Although EN 1994-1-1 [27] requires the minimum stud-to-edge distance of  $6d$  in the general case, experimental results proved that the developed demountable connection with the stud-to-edge distance of  $4d$  has equal resistance to the non-demountable connection with a continuous slab over the beam. The effect of the stud-to-edge distance is assessed through parametric analysis by varying the distance in the range from  $3d$  to  $6d$  in the model DLU. The parametric study also covered demountable connections with discontinuous slabs without the vertical angle leg on the slab edge (models labelled as NDLU in Fig. 17) to determine if the presence of a steel angle contributes to the connection resistance.

Load-slip curves shown in Fig. 17 exhibit distinct differences present between models with and without vertical angle legs, indicating that the steel element on the slab edge plays an important role in the shear connection response. The connection with angles and stud-to-edge distance of  $3d$  has almost the same resistance as the connection without angles, with stud-to-edge distance of  $6d$ . However, the latter one is characterised by almost two times smaller slip capacity.

**Fig. 17** Load-slip curves for varied stud-to-edge distance

Comparisons between ultimate loads for chosen different slab-to-edge distances and models with and without angles are given in Table 9. An increase in the ultimate load with the increase in the slab-to-edge distance is more pronounced when the slab edge is without the angle than when angles are applied. The shear resistance of the models with angles is 11–21% higher compared to the models without angles. The increase in the ultimate load when angles are applied is more distinct for smaller slab-to-edge distances.



**Table 8**

Comparison of the resistance of demountable and non-demountable shear connections

Stud diameter	Stud height	Slab depth	Bolt diameter	Plate thickness	Concrete class	Concrete strength	Ultimate load per connector		Ratio
							Demountable connection	Non-demountable connection	
$d$ [mm]	$h_{sc}$ [mm]	$h$ [mm]	$d_b$ [mm]	$t_p$ [mm]	-	$f_{cm}$ [MPa]	$P_{ult,fea,D}$ [kN]	$P_{ult,fea,S}$ [kN]	$P_{ult,fea,D} / P_{ult,fea,S}$
16	100	120	12	8	C20/25	28.0	29.98	30.91	0.97
16	100	120	12	8	C30/37	38.0	34.51	34.91	0.99
16	100	120	12	8	C40/50	48.0	37.71	38.01	0.99
16	100	120	12	8	C50/60	58.0	40.26	40.66	0.99
19	125	150	16	8	C20/25	28.0	43.51	42.15	1.03
19	125	150	16	8	C30/37	38.0	49.76	47.61	1.05
19	125	150	16	8	C40/50	48.0	53.16	52.53	1.01
19	125	150	16	8	C50/60	58.0	57.13	56.15	1.02
22	125	150	16	10	C20/25	28.0	53.28	54.61	0.98
22	125	150	16	10	C30/37	38.0	61.65	62.71	0.98
22	125	150	16	10	C40/50	48.0	66.65	66.89	1.00
22	125	150	16	10	C50/60	58.0	70.68	69.99	1.01
Mean									1.00
Coefficient of variation [%]									2.28
Correlation coefficient									0.997

**Table 9**

Ultimate loads for varied stud-to-edge distance

No.	Distance between the headed stud and slab edge	Concrete strength	DLU (with angle)		NDLU (without angle)		Ratio
			Ultimate load	Ratio	Ultimate load	Ratio	
			$P_{ult,fea,DLU}$ [kN]	$P_{ult,fea,DLU(i)} / P_{ult,fea,DLU(2)}$	$P_{ult,fea,NDLU}$ [kN]	$P_{ult,fea,NDLU(i)} / P_{ult,fea,NDLU(2)}$	
	$e_s$ [-]	$f_{cm}$ [MPa]					$P_{ult,fea,DLU} / P_{ult,fea,NDLU}$
(1)	$3d$	37.3	256.5	0.94	213.5	0.95	1.20
(2)	$4d$	37.3	271.6	-	224.2	-	1.21
(3)	$5d$	37.3	262.1	0.97	237.0	1.06	1.11
(4)	$6d$	37.3	280.0	1.03	251.9	1.12	1.11

**Table 10**

Comparison of the resistance of demountable shear connections with continuous and discontinuous slabs

Stud diameter	Stud height	Slab depth	Bolt diameter	Angle thickness	U-bar diameter	Distance between the headed stud and angle		Concrete strength	Ultimate load per connector		Ratio
									Discontinuous slab over the beam	Continuous slab over the beam	
$d$ [mm]	$h_{sc}$ [mm]	$h$ [mm]	$d_b$ [mm]	$t_p$ [mm]	$\varnothing$ [mm]	$e_s$ [-]	$e_s$ [mm]	$f_{cm}$ [MPa]	$P_{ult,fea,DLU}$ [kN]	$P_{ult,fea,D}$ [kN]	$P_{ult,fea,DLU}/P_{ult,fea,D}$
16	100	120	12	8	8	3 <i>d</i>	48	28.0	26.98	29.98	0.90
16	100	120	12	8	8	3 <i>d</i>	48	38.0	31.98	34.51	0.93
16	100	120	12	8	8	3 <i>d</i>	48	48.0	35.69	37.71	0.95
16	100	120	12	8	8	3 <i>d</i>	48	58.0	38.55	40.26	0.96
16	100	120	12	8	8	4 <i>d</i>	64	28.0	29.61	29.98	0.99
16	100	120	12	8	8	4 <i>d</i>	64	38.0	34.03	34.51	0.99
16	100	120	12	8	8	4 <i>d</i>	64	48.0	37.06	37.71	0.98
16	100	120	12	8	8	4 <i>d</i>	64	58.0	40.53	40.26	1.01
19	125	150	16	8	10	3 <i>d</i>	57	28.0	42.03	43.51	0.97
19	125	150	16	8	10	3 <i>d</i>	57	38.0	47.79	49.76	0.96
19	125	150	16	8	10	3 <i>d</i>	57	48.0	52.01	53.16	0.98
19	125	150	16	8	10	3 <i>d</i>	57	58.0	55.98	57.13	0.98
19	125	150	16	8	10	4 <i>d</i>	76	28.0	45.11	43.51	1.04
19	125	150	16	8	10	4 <i>d</i>	76	38.0	50.64	49.76	1.02
19	125	150	16	8	10	4 <i>d</i>	76	48.0	55.25	53.16	1.04
19	125	150	16	8	10	4 <i>d</i>	76	58.0	58.80	57.13	1.03
22	125	150	16	10	12	3 <i>d</i>	66	28.0	53.15	53.28	1.00
22	125	150	16	10	12	3 <i>d</i>	66	38.0	61.63	61.65	1.00
22	125	150	16	10	12	3 <i>d</i>	66	48.0	67.09	66.65	1.01
22	125	150	16	10	12	3 <i>d</i>	66	58.0	72.76	70.68	1.03
22	125	150	16	10	12	4 <i>d</i>	88	28.0	56.60	53.28	1.06
22	125	150	16	10	12	4 <i>d</i>	88	38.0	64.81	61.65	1.05
22	125	150	16	10	12	4 <i>d</i>	88	48.0	71.01	66.65	1.07
22	125	150	16	10	12	4 <i>d</i>	88	58.0	76.79	70.68	1.09

It is concluded that the presence of angles in demountable connections with discontinuous slabs over the beam provides a considerable contribution to the shear connection resistance and ductility. The vertical angle leg reinforces the slab edge and prevents the splitting of concrete and early failure. When angles are applied, the minimum stud-to-edge distance of  $6d$ , required in EN 1994-1-1 [27], might be reduced, retaining the high connection resistance to shear.

In order to provide further directions for the selection of the optimum stud-to-edge distance, parametric analysis was extended to connections with different headed stud diameters (16, 19 and 22 mm), stud heights (100 and 125 mm) and concrete classes (C20/25–C50/60). Models of demountable

connections with discontinuous slabs were formed by applying stud-to-edge distances of  $3d$  and  $4d$ . All models included U-bars with a diameter of at least  $0.5d$ , whereas the bolt diameter and angle thickness greater than  $0.4d$  were adopted as previously done for demountable connections with continuous slabs (Section 4.1). A comparison between ultimate loads obtained for demountable connections with discontinuous slabs and corresponding models with continuous slabs is presented in Table 10. A direct proportionality between stud-to-edge distance and the ratio comparing ultimate loads of two corresponding connections with continuous and discontinuous slabs was not observed. However, analysing the set of data, an adequate correlation between the ratio

$P_{ult,fea,DLU}/P_{ult,fea,D}$  and value of  $e_s f_{cm}^{0.1}$  was detected:

$$\frac{P_{ult,fea,DLU}}{P_{ult,fea,D}} = 2.2797 e_s f_{cm}^{0.1} 10^{-3} + 0.7799 \quad (10)$$

where  $e_s$  is the stud-to-edge distance in mm, and  $f_{cm}$  is the cylinder compressive strength of concrete in MPa. For the defined linear regression model, the coefficient of determination  $R^2$  is 0.93.

According to the proposed equation, the appropriate stud-to-edge distance for accomplishing equal resistance of the shear connections with continuous and discontinuous composite concrete slabs is possible to define. According to values presented in Fig. 18, the resistance of the connection with a discontinuous slab for the adopted stud-to-edge distance of at least 70 mm is not expected to be smaller than that of the corresponding demountable connection with a continuous slab.

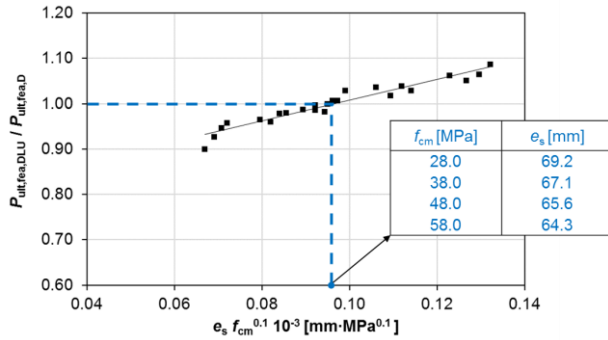


Fig. 18 Relation between shear resistance of demountable shear connections with discontinuous and continuous slabs

#### 4.3. Effect of the stirrup bars

Experimental results showed that the presence of stirrup reinforcement passing around headed studs increases resistance and ductility of demountable shear connections with discontinuous slabs over the support. Numerical models confirmed the activation of U-bars during the loading, showing that the increase of stress in stirrup bars follows the loading of the specimen. The highest stress in U-bars corresponds to the moment when the ultimate load is reached, as presented in Fig. 19.

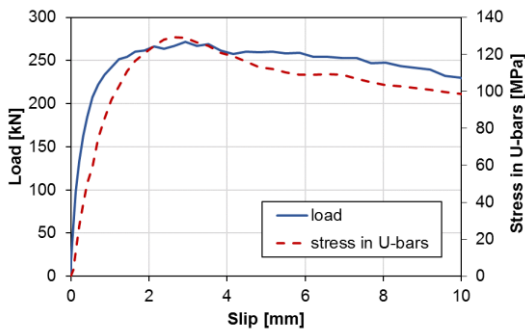


Fig. 19 Activation of U-bars during the loading of model DLU

In the experiment, U-bars were put at the level of the top surface of profiled sheeting ribs, as such a position enabled simple installation (marked as position 1 in Fig. 20). By avoiding the bar placement inside the rib, enough space inside the sheeting rib was provided for concrete casting. Bar position along the stud height was varied in numerical models, and results are compared in Fig. 20 and Table 11. Although EN 1994-1-1 [27] suggests placing U-bars as low as possible to account for the concrete cover layer, differences in the connection behaviour between models with U-bars closer to the weld collar (positions 2 and 3) were not considerable compared to the basic model (position 1). However, the resistance is decreased in the model with U-bars placed just below the stud head (position 4). Finally, it is recommended to place U-bars at the level of the top surface of profiled sheeting ribs or within the sheeting rib if adequate concrete compaction is possible to accomplish.

Table 11

Ultimate loads for the varied stirrup position

No.	Stirrup position	Concrete strength	Ultimate load		Ratio
		$f_{cm}$ [MPa]	$P_{ult,fea}$ [kN]	$P_{ult,fea(i)}/P_{ult,fea(1)}$	
(1)	1	37.3	271.6	-	
(2)	2	37.3	263.3	0.97	
(3)	3	37.3	263.4	0.97	
(4)	4	37.3	255.2	0.94	

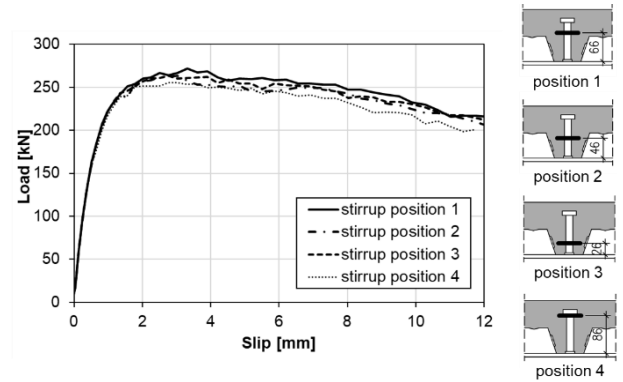


Fig. 20 Load-slip curves for the varied stirrup position

#### 5. Conclusions

This study presents a demountable shear connection with welded headed studs and bolts. Load-slip behaviour of the connection was investigated experimentally through static push-out tests, and numerically through corresponding finite element models. Numerical parametric studies were conducted analysing the effects of the plate and angle thickness, stud-to-edge distance and stirrup reinforcement position. A database of numerical models including different connection geometries and concrete strengths was formed. According to the findings, several conclusions can be inferred:

(1) Demountable shear connections with bolts and welded headed studs cast in profiled steel sheeting could be realised with continuous or discontinuous concrete slabs over the supporting beam. Both proposed solutions show a similar resistance and failure mode as the corresponding non-demountable shear connection with welded headed studs. The failure is characterised by the separation of the concrete cone from the rest of the slab.

(2) The main difference in the response of demountable and non-demountable connections is reflected in the slip. The total slip of the demountable connection is the sum of the bolt slip and the slip of welded headed studs. Bolt slip is dominant in the initial loading stage due to the presence of bolt-to-hole clearances. In the later stages of loading, after bolt-to-hole clearances have been voided, the slip of headed studs becomes a dominant component in the total slip of the connection.

(3) The thickness of the plate and angles affects the behaviour of the demountable shear connection. Insufficient plate or angle thickness may induce plate deformation and result in a lower connection resistance. In order to avoid the reduction in the connection resistance, the plate or angle thickness should be greater than  $0.4d$ , where  $d$  is the stud shank diameter.

(4) In addition to the primary function of accomplishing connection demountability, angles applied on the edges of discontinuous concrete slabs have a reinforcing role. Connections without the vertical angle leg on the slab edge have smaller resistance and ductility than those with angles. Reduction in the resistance when angles are avoided is in the range of 11–21% for the analysed connections.

(5) The transverse distance between welded headed studs and the slab edge affects the resistance of the demountable connection with a discontinuous slab. However, if angles are applied on the slab edge, a decrease in the connection resistance with the reduction of the stud-to-edge distance is less pronounced. Moreover, the minimum stud-to-edge distance of  $6d$ , required according to EN 1994-1-1, might be reduced in the case angles are used. It is recommended to place headed studs at a distance of at least 70 mm from the vertical angle leg.

(6) Implementation of stirrup U-bars passing around headed studs increases resistance and ductility of the demountable connections with discontinuous slabs over the beam. U-bars with a diameter of at least  $0.5d$  should be placed around headed studs at the level of the top surface of profiled sheeting ribs or within the sheeting rib.

All listed conclusions apply if the demountable connection with welded

headed studs and bolts is appropriately designed to avoid the plastic deformation of bolts. Resistance of the shear connection designed according to the proposed recommendations may be assumed to be equal to the resistance of the corresponding non-demountable shear connection with welded headed studs and continuous slab over the beam.

## Funding

This investigation is supported by the Ministry of Education, Science and

## References

- [1] Brambilla G, Lavagna M, Vasdravellis G, Castiglioni CA. Environmental benefits arising from demountable steel-concrete composite floor systems in buildings. *Resources, Conservation and Recycling* 2019;141:133–42. <https://doi.org/10.1016/j.resconrec.2018.10.014>.
- [2] Dallam LN. Pushout tests with high strength bolt shear connectors. Missouri State Highway Department; 1968.
- [3] Dallam LN, Harpster JL. Composite beam tests with high-strength bolt shear connectors. Missouri State Highway Department; 1968.
- [4] Marshall W, Nelson H, Banerjee H. An Experimental Study of the Use of High-Strength Friction Grip Bolts as Shear Connectors In Composite Beams. *Structural Engineer* 1971;49:171–8.
- [5] Jakovljević I, Spremić M, Marković Z. Demountable composite steel-concrete floors: A state-of-the-art review. *Journal of the Croatian Association of Civil Engineers* 2021;73:249–63. <https://doi.org/10.14256/JCE.2932.2020>.
- [6] Pardeshi RT, Patil YD. Review of various shear connectors in composite structures. *Advanced Steel Construction* 2021;17:394–402. <https://doi.org/10.18057/IJASC.2021.17.4.8>.
- [7] Kwon G, Engelhardt MD, Klingner RE. Behavior of post-installed shear connectors under static and fatigue loading. *Journal of Constructional Steel Research* 2010;66:532–41. <https://doi.org/10.1016/j.jcsr.2009.09.012>.
- [8] Chen Y-T, Zhao Y, West JS, Walbridge S. Behaviour of steel–precast composite girders with through-bolt shear connectors under static loading. *Journal of Constructional Steel Research* 2014;103:168–78. <https://doi.org/10.1016/j.jcsr.2014.09.001>.
- [9] Liu X, Bradford MA, Lee MSS. Behavior of High-Strength Friction-Grip Bolted Shear Connectors in Sustainable Composite Beams. *Journal of Structural Engineering* 2015;141:04014149. [https://doi.org/10.1061/\(ASCE\)ST.1943-541X.0001090](https://doi.org/10.1061/(ASCE)ST.1943-541X.0001090).
- [10] Ataie A, Zeynalian M. A study on structural performance of deconstructable bolted shear connectors in composite beams. *Structures* 2021;29:519–33. <https://doi.org/10.1016/j.jstruc.2020.11.065>.
- [11] Kwon G, Engelhardt MD, Klingner RE. Experimental Behavior of Bridge Beams Retrofitted with Postinstalled Shear Connectors. *Journal of Bridge Engineering* 2011;16:536–45. [https://doi.org/10.1061/\(ASCE\)BE.1943-5592.0000184](https://doi.org/10.1061/(ASCE)BE.1943-5592.0000184).
- [12] Pavlović M, Marković Z, Veljković M, Budevac D. Bolted shear connectors vs. headed studs behaviour in push-out tests. *Journal of Constructional Steel Research* 2013;88:134–49. <https://doi.org/10.1016/j.jcsr.2013.05.003>.
- [13] Henderson IEJ, Zhu XQ, Uy B, Mirza O. Dynamic behaviour of steel-concrete composite beams with different types of shear connectors. Part I: Experimental study. *Engineering Structures* 2015;103:298–307. <https://doi.org/10.1016/j.engstruct.2015.08.035>.
- [14] Ban H, Uy B, Pathirana SW, Henderson I, Mirza O, Zhu X. Time-dependent behaviour of composite beams with blind bolts under sustained loads. *Journal of Constructional Steel Research* 2015;112:196–207. <https://doi.org/10.1016/j.jcsr.2015.05.004>.
- [15] Pathirana SW, Uy B, Mirza O, Zhu X. Strengthening of existing composite steel-concrete beams utilising bolted shear connectors and welded studs. *Journal of Constructional Steel Research* 2015;114:417–30. <https://doi.org/10.1016/j.jcsr.2015.09.006>.
- [16] Pathirana SW, Uy B, Mirza O, Zhu X. Flexural behaviour of composite steel-concrete beams utilising blind bolt shear connectors. *Engineering Structures* 2016;114:181–94. <https://doi.org/10.1016/j.engstruct.2016.01.057>.
- [17] Dai XH, Lam D, Saveri E. Effect of Concrete Strength and Stud Collar Size to Shear Capacity of Demountable Shear Connectors. *Journal of Structural Engineering* 2015;141:04015025. [https://doi.org/10.1061/\(asce\)st.1943-541x.0001267](https://doi.org/10.1061/(asce)st.1943-541x.0001267).
- [18] Yang F, Liu Y, Jiang Z, Xin H. Shear performance of a novel demountable steel-concrete bolted connector under static push-out tests. *Engineering Structures* 2018;160:133–46. <https://doi.org/10.1016/j.engstruct.2018.01.005>.
- [19] Kozma A, Odenbreit C, Braun MV, Veljković M, Nijgh MP. Push-out tests on demountable shear connectors of steel-concrete composite structures. *Structures* 2019;21:0–1. <https://doi.org/10.1016/j.jstruc.2019.05.011>.
- [20] Suwaed ASH, Karavasilis TL. Novel Demountable Shear Connector for Accelerated Disassembly, Repair, or Replacement of Precast Steel-Concrete Composite Bridges. *Journal of Bridge Engineering* 2017;22:04017052. [https://doi.org/10.1061/\(asce\)be.1943-5592.0001080](https://doi.org/10.1061/(asce)be.1943-5592.0001080).
- [21] Suwaed ASH, Karavasilis TL. Removable shear connector for steel-concrete composite bridges. *Steel and Composite Structures* 2018;29:107–23. <https://doi.org/10.12989/scs.2018.29.1.107>.
- [22] Luo Y-B, Sun S-K, Yan J-B, Zhao Y-C, Lam D. Shear behavior of novel demountable bolted shear connector for prefabricated composite beam. *Advanced Steel Construction* 2022;18:745–52. <https://doi.org/10.18057/IJASC.2022.18.4.2>.
- [23] Wang L, Webster MD, Hajjar JF. Pushout tests on deconstructable steel-concrete shear connections in sustainable composite beams. *Journal of Constructional Steel Research* 2019;153:618–37. <https://doi.org/10.1016/j.jcsr.2018.10.020>.
- [24] Rehman N, Lam D, Dai X, Ashour AF. Experimental study on demountable shear connectors in composite slabs with profiled decking. *Journal of Constructional Steel Research* 2016;122:178–89. <https://doi.org/10.1016/j.jcsr.2016.03.021>.
- [25] Yang J, Lam D, Dai X, Sheehan T. Experimental study on demountable shear connectors in profiled composite slabs. *Proceedings 12th international conference on Advances in Steel-Concrete Composite Structures - ASCCS 2018, Valencia: Universitat Politècnica València*; 2018. p. 115–21. <https://doi.org/10.4995/ASCCS2018.2018.6959>.
- [26] Dai X, Lam D, Sheehan T, Yang J, Zhou K. Use of bolted shear connectors in composite construction. *Proceedings 12th international conference on Advances in Steel-Concrete Composite Structures - ASCCS 2018, Valencia: Universitat Politècnica València*; 2018. p. 475–82. <https://doi.org/10.4995/ASCCS2018.2018.7039>.
- [27] EN1994-1-1. Eurocode 4: Design of composite steel and concrete structures. Part 1-1: General rules and rules for buildings. Brussels: CEN; 2004.

Technological Development, Republic of Serbia (grant number 451-03-68/2020-14/200092).

## Acknowledgements

The authors are grateful to companies ArcelorMittal, Luxembourg, and EX BC, Serbia, for their support.

- [28] Girão Coelho AM, Lawson M, Lam D, Yang J, Lawson RM, Lam D, et al. Guidance on demountable composite construction systems for UK practice. Ascot: SCI; 2020.
- [29] Jakovljević I, Spremić M, Marković Z. Methods for life extension of multi-storey car park buildings. *Structural Engineering International* 2023;33:314–24. <https://doi.org/10.1080/10168664.2022.2073318>.
- [30] ArcelorMittal. Cofraplus® 60 n.d. <https://construction.arcelormittal.com/fr-en/product/floors/composite-floors/cofraplus-60> (accessed August 1, 2021).
- [31] EN1993-1-8. Eurocode 3: Design of steel structures. Part 1-8: Design of joints. Brussels: CEN; 2005.
- [32] Eggert F. Einfluss der Verdübelung auf das Trag- und Verformungsverhalten von Verbundträgern mit und ohne Profilblech. Universität Stuttgart; 2019.
- [33] Vigneri V. Load bearing mechanisms of headed stud shear connections in profiled steel sheeting transverse to the beam. University of Luxembourg; 2021.
- [34] Lawson RM, Aggelopoulos ES, Obiala R, Nellinger S, Kuhlmann U, Eggert F, et al. Development of Improved Shear Connection Rules in Composite Beams (DISCCO). Luxembourg: Publications Office of the European Union; 2017.
- [35] Spremić M, Marković Z, Veljković M, Budjevac D. Push-out experiments of headed shear studs in group arrangements. *Advanced Steel Construction* 2013;9:139–60.
- [36] EN1990:2010. Eurocode - Basis of structural design. Brussels: CEN; 2010.
- [37] ISO6892-1:2009. Metallic materials - Tensile testing - Part 1: Method of test at room temperature. Brussels: CEN; 2009.
- [38] Arrayago I, Real E, Gardner L. Description of stress-strain curves for stainless steel alloys. *Materials and Design* 2015;87:540–52. <https://doi.org/10.1016/j.matdes.2015.08.001>.
- [39] Abaqus/CAE. User's Guide. Providence: DS SIMULIA Corp.; 2009.
- [40] Patel VI, Uy B, Pathirana SW, Wood S, Singh M, Trang BT. Finite element analysis of demountable steel-concrete composite beams under static loading. *Advanced Steel Construction* 2018;14:392–411. <https://doi.org/10.18057/IJASC.2018.14.3.5>.
- [41] EN1992-1-1. Eurocode 2: Design of Concrete Structures. Part 1-1: General rules and rules for buildings. Brussels: CEN; 2004.
- [42] Spremić M, Pavlović M, Marković Z, Veljković M, Budjevac D. FE validation of the equivalent diameter calculation model for grouped headed studs. *Steel and Composite Structures* 2018;26:375–86. <https://doi.org/10.12989/scs.2018.26.3.375>.



# BEHAVIOURS OF STEEL-CONCRETE COMPOSITE BEAMS AT LOW TEMPERATURES: MATERIALS AND STRUCTURES

Jia-Bao Yan, Er-Cong Kang\* and Jian Xie\*

*School of Civil Engineering / Key Laboratory of Coast Civil Structure Safety of Ministry of Education, Tianjin University, Tianjin 300350, China*

*\*(Corresponding author: E-mail: kangercong2010@163.com; xiejian@tju.edu.cn)*

## ABSTRACT

This paper reported the low-temperature ultimate strength behaviours of steel-concrete composite beams (SCCBs) from material to structure levels. Firstly, low-temperature mechanical properties of constructional materials in SCCBs, e.g., concrete, headed studs, and mild steel plate for I-beams, were experimentally studied. The studies on constructional materials showed that decreasing the temperature ( $T$ ) from 20 to  $-80^{\circ}\text{C}$ , the strength and ductility of headed studs and I-beam were generally increased; the decreasing  $T$  increased the strength, but reduced the ductility of concrete. Followed, the shear and tensile behaviours of headed studs in concrete at different  $T$  levels of 20– $-80^{\circ}\text{C}$  were experimentally investigated. Test results showed that decreasing  $T$  from 20 to  $-80^{\circ}\text{C}$  increased the shear and tensile resistance of headed studs, but showed different effects on ductility. Four-point bending tests on three SCCBs were performed at  $T$  of 20,  $-30$  and  $-60^{\circ}\text{C}$  to investigate the low-temperature ultimate strength behaviours. These tests showed that at low temperatures all SCCBs failed in flexure with crushing of top concrete slab and yielding of bottom I-beam. Decreasing  $T$  from 20 to  $-30$  and  $-60^{\circ}\text{C}$  increased the ultimate strength of SCCBs by 10% and 24%, respectively. A series of prediction equations were proposed to incorporate the effects of the decreasing  $T$  on compressive and tensile strength of concrete, shear and tensile capacity of studs, and ultimate bending resistance of SCCBs. Their accuracies have been validated by these material and member tests.

## ARTICLE HISTORY

Received: 22 February 2023  
Revised: 22 May 2023  
Accepted: 25 May 2023

## KEYWORDS

Steel-concrete composite beam;  
Low temperature;  
Composite structure;  
Arctic engineering;  
Shear stud;  
Material test

Copyright © 2023 by The Hong Kong Institute of Steel Construction. All rights reserved.

## 1. Introduction

Steel-concrete composite (SCC) structure, in terms of an upper concrete slab connected to an underneath steel beam/plate (usually I-beam, or box section), is a relatively new type of structure that has been extensively applied in engineering structures. The extensive applications of SCC structures (SCCSs) in civil engineering constructions include composite floors, composite beams, bridge girders, and ice-resistant walls for the Arctic platforms. More recently, the applications of cold-region SCC engineering constructions keep increasing, e.g., the SCC bridge in Canada [1, 2], the Lhasa River Bridge in Northern China [3], and the Arctic oil platforms [4, 5].

In cold regions, the cooling environment with varying low temperatures in different seasons brings challenges to engineering constructions. According to the reports by Stepanova [6], the lowest temperature near the Arctic Circle at Verkhoysk Siberia was  $-72^{\circ}\text{C}$ . Meanwhile, the lowest temperature in the record of Northern China could drop to  $-50^{\circ}\text{C}$  [7]. These low temperatures definitely affect the mechanical properties of structural materials, steel-concrete interfacial bonding, and behaviours of SCCSs. Previous experimental investigations [8–10] showed that dropping temperature from the ambient to sub-zero increased the strengths but reduced the ductility of mild steel; however, due to the increased content of Niccolum in steel, the Arctic low temperatures have marginal influences on the ductility of high-strength steels, e.g., S690 [11], Q690 and Q960 [12]. Amounts of research works also showed that the concrete exposed to sub-zero temperatures received increased compressive strengths with large variations [13–15]. Moreover, the influences of sub-zero temperatures on the improved concrete compressive strength are independent of mix proportions and curing conditions of concrete [13]. MacLean and Lloyd [16] proposed the stress-strain constitutive law for concrete at low temperatures. Regarding the steel-concrete interfacial bonding strength at low temperatures, Yan et al. [17] observed that decreasing the temperature from 30 to  $-80^{\circ}\text{C}$  increased the bond strength by more than 200%. Dalen [1] contributed to the low-temperature shear resistance of connectors in SCC beams (SCCBs). However, the low temperatures studied by Dalen [1] were limited to  $-10$  and  $-20^{\circ}\text{C}$  which were still much higher than the severest low temperatures in cold regions. Low-temperature structural studies of reinforced concrete (RC) members have been reported on bridge columns [18–21], RC beams [22, 23], FRP reinforced RC beams [24–26], and FRP confined RC columns [27, 28]. These studies focused on the evaluation and retrofitting of aged cold-region infrastructures in Canada. However, they were mainly performed for RC structures. Long et al. [2] checked the fatigue behaviours of SCCBs at the low temperature of  $-29^{\circ}\text{C}$ , which provided limited information on the SCCBs at even lower temperatures. More recently, Yan et al. [29–34] contributed to compression performances of steel tubes and composite columns with mild strength, high strength and stainless steel tubes. More extended studies on compression behaviours of SCC walls have also been reported in Ref. [35–37].

All these researches showed that the sub-zero temperatures significantly improved the compression behaviours of composite members, e.g., improved compression capacity and ductility. However, as the key structural elements in the composite bridges or other infrastructures, the studies on behaviours of SCCBs are still very limited. Their low-temperature behaviours have not been understood. Therefore, it is necessary to carry out researches on ultimate strength behaviours of SCCBs at Arctic low temperatures.

This paper performed a series of studies on low-temperature ultimate strength behaviours of SCCBs from the material, component, and structural levels. Firstly, the low-temperature mechanical properties of steels and concretes involved in SCCBs were studied. Followed, push-out and pull-out tests were performed to study the shear and tensile behaviours of headed studs used in SCCBs, respectively. Finally, four-point bending tests on SCCBs at low temperatures were carried out. Including the experimental studies, corresponding analytical models were also developed to estimate the low-temperature ultimate strength of SCCBs.

## 2. Components in SCCBs and research objectives

Fig. 1 illustrates the different components in a typical SCCB, i.e., I-beam, concrete slab, steel reinforcements, and headed studs. Exposed to sub-zero temperatures, the mechanical properties of concretes and steels in SCCBs at low temperatures required detailed investigations. Moreover, the low-temperature bonding strength at steel-concrete interface also determines the cross-sectional bending behaviour of SCCB as well as uplifting of concrete slabs from the underneath I-beam. The low-temperature bonding strength at steel-concrete interface mainly comprises shear strength of bonding connectors along the tangent direction of interacting interface and pull-out resistance of connectors normal to this interacting interface. Finally, four-point bending tests on SCCBs were carried out for investigations on their sub-zero ultimate strength behaviours. All these experimental studies provided detailed information on the low-temperature ultimate strength behaviour of SCCBs.

## 3. Low-temperature materials properties of concrete in SCCBs

### 3.1. Concretes

Grade C45 normal weight concrete (NWC) was selected for SCCB in this study, and its mix proportions are given in Table 1. To obtain its low-temperature mechanical properties at  $-80$ ,  $-60$ ,  $-30$ , and  $20^{\circ}\text{C}$ , three concrete cubes (width=100 mm) and three prisms (width  $\times$  depth  $\times$  height =  $100 \times 100 \times 300 \text{ mm}^3$ ) at each  $T$  level were prepared for the compression tests whilst cubes with the same dimension were prepared for the splitting tension tests. All these cubes/prisms were standardly cured, and corresponding tests were carried out at 28 days after NWC casting.

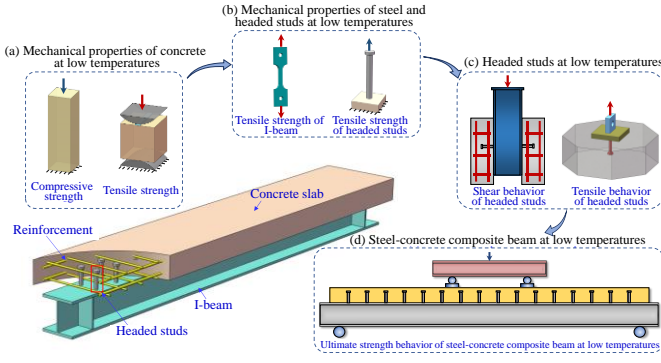


Fig. 1 Research objectives on steel-concrete composite beam at low temperatures

**Table 1**  
Mix proportions of the normal weight concrete

Concrete grade	w/c	$W_c$ (%)	Cement (kg/m <sup>3</sup> )	Water (kg/m <sup>3</sup> )	Fine aggregate (kg/m <sup>3</sup> )	Coarse aggregate (kg/m <sup>3</sup> )
C45	0.45	4.66	487	219	614	1080

w/c denotes water-to-cement ratio of NWC;  $W_c$  denotes moisture content of NWC.

### 3.2. Low-temperature uniaxial compressive behaviours of NWC

#### 3.2.1. Test setup

Sub-zero compressive behaviours of NWC were obtained from compression tests on NWC prisms in a 500-ton testing machine. The setup of low-temperature compression tests on NWC prisms is given in Fig. 2. The NWC prism was firstly cooled down to the target temperature at a rate of 1 °C/min in a cold storage and maintained at this temperature for at least 48 h. Then the prism was transferred to the 500-ton testing machine equipped with a cooling chamber. During the testing, a cooling chamber surrounding the prism with spraying liquid nitrogen gas (LNG) was adopted for the simulation of low-temperature environment. During the testing, one PT100 type of thermocouple, embedded in each prism during the casting, was used to measure the temperature of prism, and another four PT100 thermocouples were used for monitoring environmental temperatures of the chamber. All these readings of thermal couples assisted in controlling the testing temperatures for prisms within a tolerance of  $\pm 3$  °C. To obtain the recession branch of compressive sub-zero stress-strain ( $\sigma$ - $\varepsilon$ ) curves of NWC, displacement loading (0.2 mm/min) was used in this testing. Two LVDTs surrounding the prisms were adopted for the monitoring of their shortenings. The strain of each prism can be thus obtained through the shortening-to-height ratio of each test whilst the stress can be found from the measured reaction force over their sectional area.

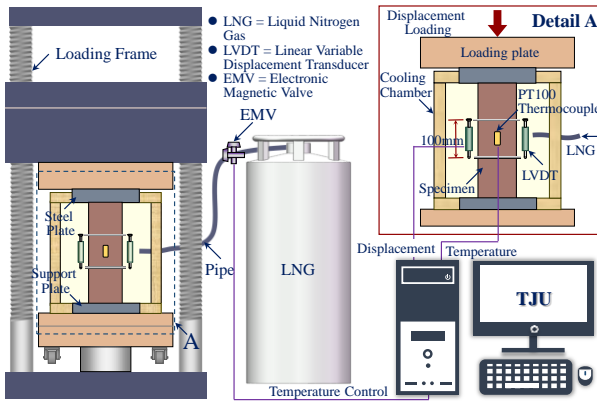


Fig. 2 Test setup of compressive tests on NWC prism at low temperatures

#### 3.2.2. Sub-zero stress-strain curves of NWC

Fig. 3(a) plots the low-temperature stress-strain ( $\sigma$ - $\varepsilon$ ) curves of NWC. Fig. 3(b) plots the influences of  $T$  on cubic compressive strength ( $f_{cu}$ ) and prism compressive strength of prisms ( $f_c$ ) of NWC. They show that the sub-zero temperatures significantly influence the compressive  $\sigma$ - $\varepsilon$  curves of NWC. As the sub-zero temperatures ( $T$ ) decreases from 20 to -80 °C, the compressive strength of NWC was increased; however, the ductility of NWC was slightly reduced. With  $T$  decreasing from 20 to -30, -60, and -80 °C, the  $f_{cu}$  of C45 NWC was increased by 16.9%, 34.5%, and 43.7% respectively; the  $f_c$  of C45 NWC

was increased by 28.1%, 64.0%, and 70.9%, respectively; meanwhile, the strain at  $f_c$  (i.e.,  $\varepsilon_0$ ) was increased by 35%, 15%, and 26%, respectively. These increments in compressive strength of NWC produced by the decreasing temperature are due to that the water in the pore of cement paste was frozen into ice, which increases the compactness of the NWC.

Based on the reported experimental  $\sigma$ - $\varepsilon$  curves of NWC, the following empirical equations were developed to describe the sub-zero compressive  $\sigma$ - $\varepsilon$  curves of NWC at low temperatures of -80 ~ 20 °C;

$$\frac{\sigma}{f_c} = \frac{\beta(\varepsilon / \varepsilon_0)}{(\beta - 1) + (\varepsilon / \varepsilon_0)^\beta} \quad (1)$$

$$\beta = \left( \frac{f_{cT}}{50.2} \right)^3 + 2.3 \quad (2)$$

where,  $\sigma$  and  $\varepsilon$  are stress and strain, respectively;  $f_{cT}$  is prism compressive strength of NWC at  $T$ , in MPa;  $\beta$  is shape parameter.

Fig. 3(a) compares these predicted low-temperature  $\sigma$ - $\varepsilon$  curves of NWC with those experimental ones that exhibit reasonable estimations.

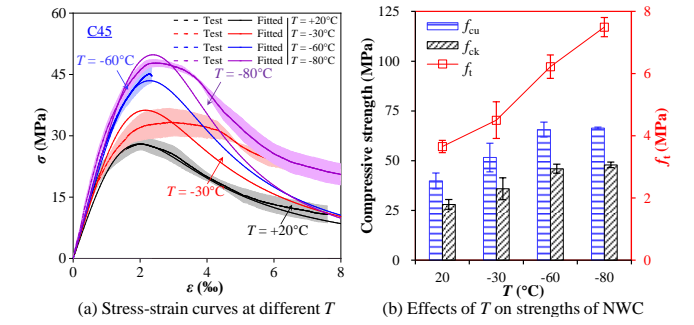


Fig. 3 Effects of  $T$  on stress-strain curves and strengths of NWC

### 3.3. Low-temperature splitting tensile strength of NWC

The splitting tensile strengths ( $f_t$ ) of NWC were obtained from the splitting tests on prisms following Chinese standard GB/T 50081 [38]. Twelve NWC cubes were prepared and tested at sub-zero temperatures of 20 to -30, -60, and -80 °C. The test setup is similar to that used for compression tests in Fig. 2, and a cooling chamber infilled with the spraying LNG was also adopted for the cold-region environment. Table 2 lists these obtained tensile strengths of NWC at different  $T$  values. Fig. 3(b) depicts influences of  $T$  on  $f_t$  of NWC. It shows that with the decrease of  $T$  from 20 to -30, -60, and -80 °C, the  $f_t$  of NWC receives average increments of 23%, 70%, and 105%, respectively.

**Table 2**  
Material properties of normal weight concrete

Item	$T$ (°C)	$f_{cu}$ (MPa)	$f_t$ (MPa)	$f_{ck}$ (MPa)	$\varepsilon_0$ ( $\mu\text{ε}$ )	$E_c$ (GPa)
CT+20-1	+20	39.4	3.44	29.1	2007	30.1
CT+20-2	+20	44.0	3.83	25.2	2014	25.0
CT+20-3	+20	36.2	3.69	29.8	1900	28.3
Mean		39.9	3.65	28.0	1974	27.8
COV		0.10	0.05	0.09		
CT-30-1	-30	59.6	4.76	36.8	2784	26.1
CT-30-2	-30	45.7	4.92	40.9	2351	32.9
CT-30-3	-30	49.6	3.83	30.0	2840	29.3
Mean		51.6/	4.50/	35.9	2658	29.4
COV		0.14	0.13	0.15		
CT-60-1	-60	63.9	6.62	43.4	2564	33.1
CT-60-2	-60	63.2	6.18	46.9	1965	28.7
CT-60-3	-60	69.9	5.87	47.6	2273	29.6
Mean		65.7	6.22	46.0	2267	30.5
COV		0.06	0.06	0.05		
CT-80-1	-80	66.9	7.17	49.5	2386	39.6
CT-80-2	-80	66.0	7.54	47.1	2491	35.4
CT-80-3	-80	66.4	7.78	47.1	2592	31.0
Mean		66.4	7.50	47.9	2490	35.3
COV		0.01	0.04	0.03		

$T$  is temperature level;  $f_{cu}$  and  $f_{ck}$  are cubic and prism compressive strength;  $f_t$  is splitting tensile strength;  $\varepsilon_0$  is peak strain;  $E_c$  is elastic modulus; COV is coefficient of variation.

#### 4. Low-temperature mechanical properties of steel in SCCBs

##### 4.1. Low-temperature mechanical properties of I-beam

Low-temperature mechanical properties of I-beam were obtained from tension tests according to GB/T 228.1-2010 [39] and GB/T 228.3-2019 [40]. Fig. 4(a) shows geometry of coupons cut from the I-beam. Nine coupons in total were prepared and they were tested at four temperatures of 20, -30, -60, and -80 °C. Table 3 provides the details of these testing parameters. Fig. 4(b) shows the tension test setup for these I-beam coupons. It shows that all the coupons were pin-connected to a set of holding rigid steel claps. Both the steel claps and coupon were surrounded by an insulation chamber that was used to maintain the low temperatures during the testing. LNG was also injected into the chamber to realize the low temperature of coupons. Once reached the target temperature, an additional 15 min were required to ensure the uniform distribution of the temperature of coupons. During the testing, two and four PT100 thermocouples were attached on the surfaces of coupons and chamber to measure the temperatures at different positions. The measured temperatures were used as the feedback for the inflowing rate of LNG to ensure that the coupons were maintained at the target temperature within a tolerance of  $\pm 3$  °C. To instrument the strains of steel coupons, two linear strain gauges (LSGs) were installed on coupons as shown in Fig. 4(b). A low-temperature extensometer (gauging length = 50 mm) was also adopted to instrument the strains in coupons after yielding.

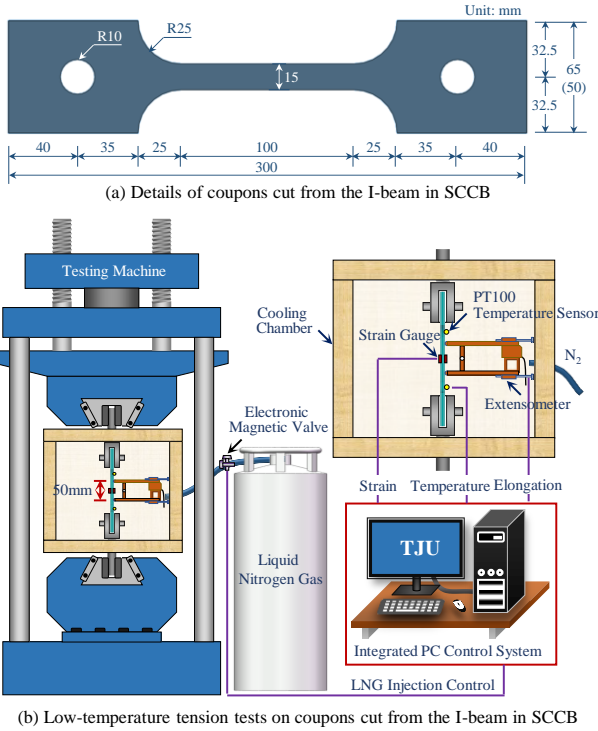


Fig. 4 Tensile test setup on steel coupons cut from I-beam at low temperatures

Table 3

Details and tensile test results of I-beam

Item	$T$ (°C)	$\varepsilon_y$ (%)	$\varepsilon_u$ (%)	$\varepsilon_F$ (%)	$\psi_s$ (%)	$E_s$ (GPa)	$f_y$ (MPa)	$f_u$ (MPa)	$I_y$	$I_u$
BS+20-1	+20	0.1579	14.19	24.30	25.00	216.4	328.9	459.3	0.988	0.988
BS+20-2	+20	0.1530	16.48	26.08	25.62	224.2	336.6	470.6	1.012	1.012
BS-30-1	-30	0.1679	16.12	25.45	25.90	242.7	375.7	519.1	1.117	1.129
BS-30-2	-30	0.1637	15.95	26.36	24.84	226.5	379.1	535.2	1.151	1.139
BS-30-3	-30	0.1585	16.53	27.33	27.96	226.5	372.9	517.5	1.113	1.121
BS-60-1	-60	0.1840	15.18	25.48	25.02	234.0	417.3	564.2	1.214	1.254
BS-60-2	-60	0.1751	16.19	27.34	26.66	241.3	416.3	544.4	1.171	1.251
BS-80-1	-80	0.1980	19.49	30.46	30.98	233.0	424.7	554.1	1.192	1.276
BS-80-2	-80	0.1947	14.81	27.59	26.74	234.0	440.6	553.2	1.190	1.324

$T$  is temperature level;  $E_s$  is elastic modulus;  $\varepsilon_y$ ,  $\varepsilon_u$ , and  $\varepsilon_F$  are yield, ultimate, and fracture strain, respectively;  $\psi_s$  is percentage elongation after fracture;  $f_u$  and  $f_y$  are yield strength and ultimate strength, respectively;  $I_y$  (or  $I_u$ ) equals yield (or ultimate) strength at  $T$  to its corresponding value at ambient temperature.

Fig. 5 plots the typical low-temperature  $\sigma$ - $\varepsilon$  curves of I-beam. Table 3 lists the strength and ductility indexes of I-beam at low temperatures. They reflect that the low temperatures significantly improved the yield ( $f_y$ ) and ultimate ( $f_u$ ) strength of Q235 I-beam, and its ductility was slightly increased. Fig. 6 plots the effects of  $T$  on strength and ductility index of I-beam. It shows that; (1) The  $f_y$ ,  $f_u$ , and elastic modulus ( $E_s$ ) of I-beam increase with the decreasing  $T$ . With the decrease of  $T$  from 20 to -30, -60, and -80 °C, the  $f_y$  (or  $f_u$ ) of I-beam is averagely improved by 13% (13%), 19% (25%), and 19% (30%), respectively; meanwhile, the  $E_s$  of I-beam is slightly increased by 5%, 8%, and 6%, respectively. These increments in strength and modulus of Q235 I-beam are due to that the decreasing  $T$  compacts the microstructure of I-beam and increases the molecular force. (2) The strain at ultimate strength ( $\varepsilon_u$ ) and fracture strain ( $\varepsilon_F$ ) increases with the decreasing  $T$ . With the decrease of  $T$  from 20 to -30, -60, and -80 °C, the  $\varepsilon_u$  (or  $\varepsilon_F$ ) of I-beam is averagely improved by 6% (5%), 2% (5%), and 11% (15%), respectively.

Fig. 7 depicts the failure modes of steel coupons of I-beam after tested at different low temperatures. It shows that obvious necking took place in all the coupons tested at low temperatures. This further confirmed that ductile failure modes occurred to those I-beam steel coupons, which is consistent with the previous findings in Fig. 5 and 6.

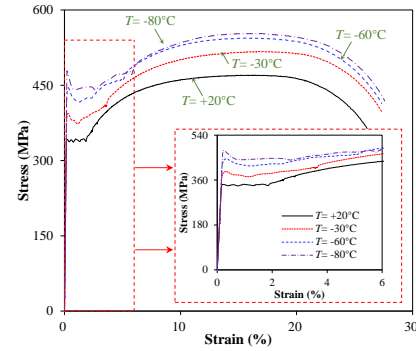


Fig. 5 Stress-strain curves of steel coupons cut from I-beam at low temperatures

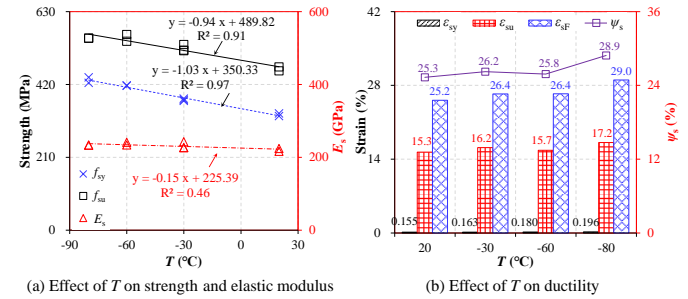


Fig. 6 Effect of low temperatures on strength and ductility index of I-beam

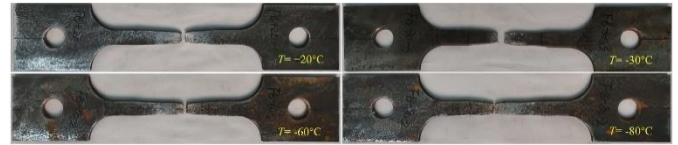


Fig. 7 Failure modes of steel coupons cut from I-beam at low temperatures

##### 4.2. Low-temperature mechanical properties of headed studs [41]

Low-temperature mechanical properties of heads shear studs were obtained from direct tension tests using the setup in Fig. 8 [41]. Headed studs with  $d = 13, 16$ , and  $19$  mm were tested at low temperatures of -80, -60, -30, 0, and 20 °C, respectively. As shown in Fig. 8, the similar testing setup to the tension tests on steel coupons of I-beam was adopted. The cooling method to maintain the low temperature for tensile tests also adopted the same method as tension tests on I-beam. All the headed studs were firstly welded to a square steel plate (width  $\times$  thickness = 100 mm  $\times$  30 mm). After that, the top heads of stud and the bottom steel plate were installed to the holding frame connected to the testing machine. The cooling chamber surrounding this testing setup as shown in Fig. 8 was also used to realize the simulation of cooling environment. In addition, LNG was used as the cooling method for the tested specimens. Strain gauges and an extensometer were also to instrument elongations of the headed studs during the testing.



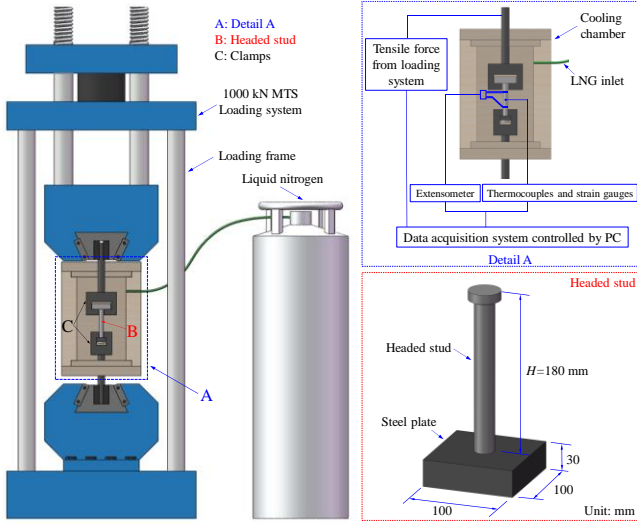


Fig. 8 Tensile test setup of headed studs at low temperatures [41]

Fig. 9 plots the low-temperature tensile  $\sigma$ - $\epsilon$  curves of headed studs. Table 4 provides the low-temperature mechanical properties of headed studs. They show that decreasing  $T$  significantly influences the tensile  $\sigma$ - $\epsilon$  curves of headed studs. Reducing  $T$  from 20 to  $-80$  °C improves yield/ultimate strength and ductility of headed studs used in SCCBs. Fig. 10 depicts the influences of  $T$  on  $f_y$ ,  $f_u$ , and  $E_s$ . It shows that with the reduction of  $T$  from 20 to 0,  $-30$ ,  $-60$ , and  $-80$  °C, the  $f_y$  value of  $d=13$  mm (or 16 mm, 19 mm) headed studs receives average increments of 2% (2%, 3%), 4% (4%, 7%), 8% (11%, 10%), and 19% (14%, 18%), respectively; the  $f_u$  value of  $d=13$  mm (or 16 mm, 19 mm) headed studs is averagely increased by 3% (3%, 5%), 6% (7%, 9%), 12% (14%, 15%), and 20% (22%, 22%), respectively; meanwhile, the  $E_s$  value of  $d=13$  mm (or 16 mm, 19 mm) headed studs receives slight average increase of 0% (0%, 3%), -2% (1%, 2%), 2% (2%, 3%), and 1% (2%, 2%), respectively. Moreover, Fig. 10 also reflects that the  $E_s$  value of headed studs exhibits low correlations with reducing  $T$  values, e.g., the correlation ratios ( $R^2$ ) for  $d=13$ , 16, and 19 mm headed studs are only 0.07, 0.07, and 0.17, respectively. However, both the  $f_y$  and  $f_u$  values exhibit very high correlations with the decreasing  $T$ .

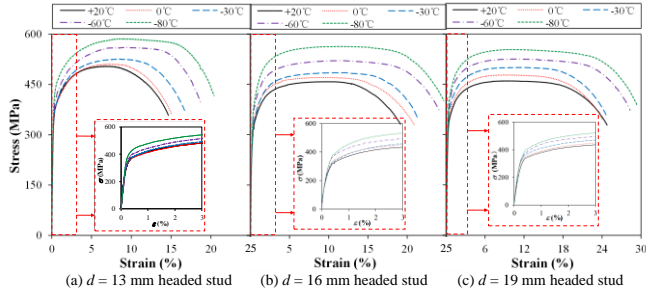


Fig. 9 Tensile stress-strain curves of headed studs at different low temperatures [41]

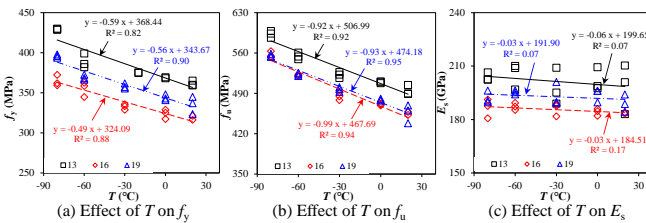


Fig. 10 Effect of low temperatures on tensile behavior of headed studs [41]

Based on the experimental results, Xie et al. [41] proposed empirical equations to estimate the influences of  $T$  on both  $f_y$  and  $f_u$  values of headed studs as follows;

$$f_{yT} = f_y e^{0.0012(T_0 - T)} \quad (3)$$

$$f_{uT} = f_u e^{0.0016(T_0 - T)} \quad (4)$$

where  $T$  is temperature, in °C, and  $-80$  °C  $\leq T \leq 20$  °C;  $f_{yT}$  and  $f_{uT}$  denote yield and ultimate strength at  $T$ , respectively.

Further validations proved that the proposed Eqns. (3) and (4) estimated reasonably the low-temperature yield and ultimate strength of headed studs [41].

Table 4

Details and tensile test results of headed studs

Item	$T$ (°C)	$d$ (mm)	$\epsilon_y$ (%)	$\epsilon_u$ (%)	$\epsilon_F$ (%)	$\psi_{st}$ (%)	$E_s$ (GPa)	$f_y$ (MPa)	$f_u$ (MPa)	$I_{fy}$	$I_{fu}$
HS1+20	+20	13	0.385	6.50	14.95	55.33	198.1	361.5	494.4	1.000	1.000
HS1+0	0	13	0.380	7.36	15.38	54.58	201.9	368.8	509.4	1.020	1.030
HS1-30	-30	13	0.391	7.80	16.22	54.07	197.7	375.1	522.1	1.038	1.056
HS1-60	-60	13	0.407	8.44	18.28	53.69	205.3	389.0	554.6	1.076	1.122
HS1-80	-80	13	0.408	8.60	19.81	53.54	203.8	429.3	592.8	1.188	1.199
HS2+20	20	16	0.378	10.06	20.20	57.64	183.7	318.8	455.3	1.000	1.000
HS2+0	0	16	0.379	9.36	21.28	56.97	184.2	323.7	470.7	1.015	1.034
HS2-30	-30	16	0.387	10.55	21.27	56.88	185.9	331.7	485.0	1.040	1.065
HS2-60	-60	16	0.392	11.72	24.42	56.53	187.3	355.2	521.3	1.114	1.145
HS2-80	-80	16	0.395	11.98	24.46	55.73	186.5	364.5	556.9	1.143	1.223
HS3+20	20	19	0.375	9.85	24.05	57.04	189.0	335.1	455.9	1.000	1.000
HS3+0	0	19	0.379	9.55	23.15	56.55	194.1	348.7	478.8	1.041	1.050
HS3-30	-30	19	0.381	10.57	24.42	56.32	193.4	358.1	496.9	1.069	1.090
HS3-60	-60	19	0.390	11.52	28.77	55.89	195.3	369.1	522.8	1.101	1.147
HS3-80	-80	19	0.404	11.81	29.06	55.90	192.2	395.8	555.3	1.181	1.218

$T$  is temperature level;  $E_s$  is elastic modulus;  $\epsilon_y$ ,  $\epsilon_u$ , and  $\epsilon_F$  are yield, ultimate, and fracture strain, respectively;  $\psi_{st}$  is reduction ratio in cross-sectional;  $f_y$  and  $f_u$  are yield and ultimate strength, respectively;  $I_{fy}$  (or  $I_{fu}$ ) equals yield (or ultimate) strength at  $T$  to its corresponding value at ambient temperature.

## 5. Low-temperature behaviours of headed studs in SCCBs

Behaviours of headed studs in SCCBs include concrete-steel interfacial shear behaviour and tensile behaviour in normal to the concrete-steel interface. The interfacial shear behaviour determines the cross-sectional bending resistance whilst the tensile behaviour of headed studs prevents the uplifting and separation of concrete slabs from the underneath I-beam.

### 5.1. Low-temperature shear behaviours of headed studs

#### 5.1.1. Low-temperature push-out tests on headed studs

To investigate the shear behaviour of the basic component in SCCBs at low temperatures, e.g., headed studs, four groups of push-out tests were performed at four  $T$  levels of 20,  $-30$ ,  $-60$ , and  $-80$  °C. Fig. 11 shows the representative specimen prepared for tests. Each specimen comprises two concrete slabs connected to an I-beam using two headed studs for each concrete slab. The depth, width, and height of the concrete slab are 120, 300, and 350 mm, respectively. The Q235 HW150×150×10×7 mm<sup>4</sup> mild steel I-beam was adopted for the testing specimens.  $\phi 8$  mm HRB 400 mild steel reinforcements with  $f_y=400$  MPa were selected for the vertical and horizontal reinforcement mesh in the concrete slabs. Their layout and geometric details are shown in Fig. 11. Table 5 provides details of these testing specimens.

Fig. 12 shows the setup for the low-temperature push-out tests of headed studs. Similar to those low-temperature compression tests on concrete prisms, all push-out test specimens were firstly frozen to the target  $T$  level and maintained for 48 hours following instructions in GB51081 [42]. Then, they were moved into the cooling chamber installed to a 300-ton testing machine as shown in Fig. 12. After that, LNG was inlet into the cooling chamber to maintain the studied  $T$  level within the range of  $\pm 3$  °C during the loading. The temperatures inside the concrete slab and on the surfaces of concrete slab and I-beam were measured by thermocouples embedded in the slab and installed on the surface of specimens, respectively. After achieving the target  $T$ , displacement loading (rate = 0.3 mm/min) directly acted on the top surface of I-beam (see Fig. 12). The beam-slab interfacial slips were measured by four LVDTs that were installed in the front of or below the headed studs along the

loading directions. The forces at each loading increment were automatically instrumented by the testing machine.

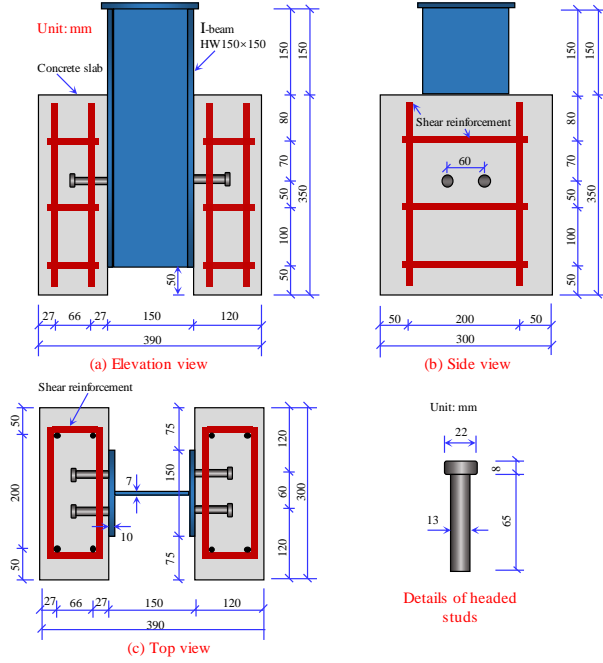


Fig. 11 Details of push-out specimens of headed studs

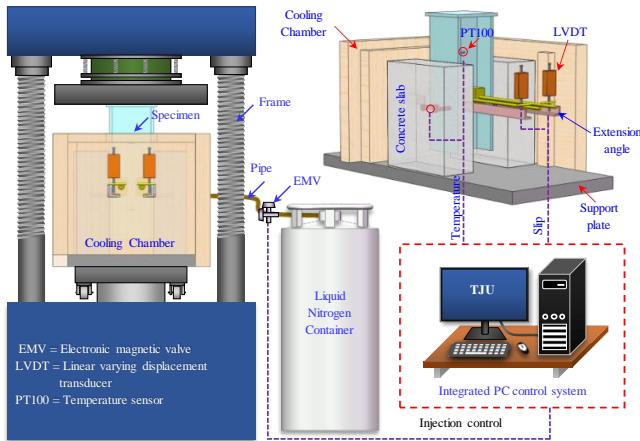


Fig. 12 Push-out test setup of headed studs at low temperatures

**Table 5**  
Results of push-out tests of headed stud

Item	$T$ (°C)	$N_u$ (kN)	$S_u$ (mm)	$S_{max}$ (mm)	$K_{0.7N_u}$ (kN/mm)	$N_{u,P}$ (kN)	$\frac{N_u}{N_{u,P}}$	Failure mode
ST+20-1	+20	82.4	6.69	6.97	86.9	50.5	1.63	S+C
ST+20-2	+20	80.3	5.69	6.26	115.9	50.5	1.59	S+C
ST-30	-30	77.3	3.35	5.05	77.7	61.6	1.25	S+C
ST-60	-60	82.0	6.11	6.53	123.9	67.8	1.21	S+C
ST-80	-80	92.5	5.77	6.27	179.4	71.9	1.29	S
Mean							1.39	
COV							0.14	

$T$  is temperature level;  $d$  and  $h$  are diameter and height of headed stud;  $N_u$  and  $N_{u,P}$  are experimental and predicted ultimate shear resistance of headed stud, respectively;  $S_u$  and  $S_{max}$  are slip corresponding to  $N_u$  and  $0.9N_u$  of the headed stud connectors;  $K_{0.7N_u}$  is secant stiffness at  $0.7N_u$ ; C and S are concrete splitting and stud fracture failure, respectively.

### 5.1.2. Failure modes

Fig. 13(a)-(d) plots the low-temperature failure modes of push-out specimen of headed studs. It shows that typical failure modes occurred to the push-out testing specimens are shear fracture of headed studs that occurred at their root positions, local crushing of NWC that took place near the root of studs,

and cracks in the concrete slabs in specimens ST+20, ST-30, and ST-60. It also shows that cracks in the concrete slab were not observed in specimen ST-80 which was tested at  $-80^\circ\text{C}$ . This is because the decreasing  $T$  improves the compressive and tensile strengths of NWC that deterred the cracking of concrete slab. No differences in the failure modes exist among push-out specimens at 20, -30, and  $-60^\circ\text{C}$ .



Fig. 13 Failure modes of push-out specimens of headed studs at low temperatures

### 5.1.3. Shear-slip behaviours

Fig. 14 plots the typical low-temperature shear-slip ( $N$ - $S$ ) curves of a single headed stud. Fig. 15 reports the general low-temperature  $N$ - $S$  curves for headed studs. They show that the low-temperature  $N$ - $S$  curves of headed stud exhibit no obvious differences to the ambient one except the curve of ST-30. Their behaviours can be summarized as elastic, nonlinear, hardening, and recession stages. The threshold point between elastic and nonlinear stages locates at about 50~70% ultimate shear resistance ( $N_u$ ). The nonlinearities of stage II are mainly produced by the yielding of headed studs and nonlinear behaviours of concrete slabs. After that, the strength hardening of the headed studs determines the behaviour of the third working stage. Finally, the  $N$ - $S$  curves reached their peak shear resistance and the headed studs at one side of the I-beam were sheared off from the I-beam. Thus, the recession  $N$ - $S$  curves exhibit sharp drops (shear fractures at one side of I-beam occurred to the two studs at the same time) or zigzag line (shear fractures of the two studs at one side of the I-beam did not occur at the same time).

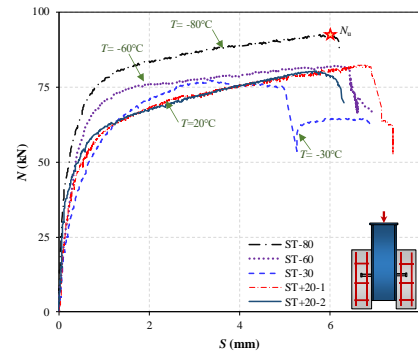


Fig. 14 Shear-slip curves of headed studs at different low temperatures

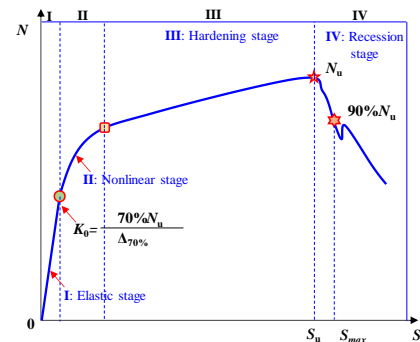


Fig. 15 General  $N$ - $S$  curves of headed studs at low temperatures

### 5.1.4. Stiffness, strength and ductility

Determining the shear stiffness ( $K_{0.7N_u}$ ) of  $N$ - $S$  curves follows the method as shown in Fig. 15 [43], which equals 70%  $N_u$  to its corresponding slip,  $\Delta_{70\%}$ .

The  $N_u$  of headed studs can be obtained from their  $N$ - $S$  curves. The ductility of these  $N$ - $S$  curves of headed studs can be evaluated by the index of  $S_{\max}$  at 90%  $N_u$  of recession  $N$ - $S$  curves as illustrated in Fig. 15 [44]. Finally, these values are determined as listed in Table 5.

### 5.1.5. Discussions

Fig. 16 plots the influences of  $T$  on low-temperature strength, stiffness, and ductility of headed studs. It reveals that decreasing  $T$  from 20 to  $-80$  °C generally increases the shear capacity, but slightly reduced the ductility of headed studs. With the decrease of  $T$  from 20 to  $-30$ ,  $-60$ , and  $-80$  °C, the  $N_u$  of studs was improved from 81.4 kN to 77.3, 82.0, and 92.5 kN with increments of  $-5\%$ ,  $1\%$ , and  $14\%$ , respectively ( “-” value means decrease); meanwhile, the  $K_{0.7N_u}$  of headed stud was increased from 101.4 kN/mm to 77.7, 123.9, and 179.4 kN/mm with increments of  $-23\%$ ,  $22\%$ , and  $77\%$ , respectively ( “-” value means decrease); however, the  $S_{\max}$  of headed stud was reduced from 6.62 mm to 5.05, 6.53, and 6.27 mm corresponding to reductions of  $24\%$ ,  $1\%$ , and  $5\%$ , respectively. The reason for these improvements in shear strength and stiffness is that the low temperatures improve the compressive strength of NWC and shear strength of headed studs. However, the decreasing  $T$  makes the frozen NWC more brittle which might cause the reduced slip capacity of headed studs.

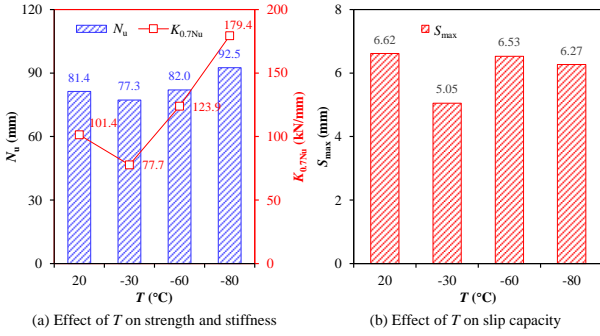


Fig. 16 Effect of  $T$  on shear strength, stiffness, and slip capacity of headed studs

### 5.1.6. Prediction equations on shear resistance of headed studs at low temperatures

The prediction equations on low-temperature shear resistance of headed studs are proposed by the main authors [44] as the following:

$$N_{uT} = 0.43A_s \sqrt{f_{cT} E_{cT}} \leq 5.8\kappa f_{uT} A_s \left( \frac{E_{cT}}{E_{sT}} \right)^{0.41} \left( \frac{f_{cT}}{f_{uT}} \right)^{0.39} \quad (5)$$

$$\kappa = \begin{cases} 0.2(h/d + 1) & \text{for } h/d \leq 4.0 \\ 1 & \text{for } h/d > 4.0 \end{cases} \quad (6)$$

where,  $A_s$  denotes the stud's cross-sectional area, in  $\text{mm}^2$ ;  $E_{cT}$  (or  $E_{sT}$ ) denotes elastic modulus of concrete (or stud) at  $T$ , in MPa;  $f_{cT}$  denotes compressive strength of NWC at  $T$ , in MPa;  $f_{uT}$  denotes ultimate strength of stud at  $T$ , in MPa;  $h$  (or  $d$ ) is the stud's height (or diameter), in mm.

Table 5 provides the theoretical predictions on low-temperature shear resistance of studs. It shows that the prediction equations provide conservative estimations on low-temperature shear resistances of studs. The average and COV for five predictions equal 1.39 and 0.14, respectively. Eqns. (5) and (6) could be used for the estimations on low-temperature shear resistance of headed studs.

### 5.2. Low-temperature pull-out behaviours of headed studs [45]

Low-temperature pull-out behaviours of studs embedded in the concrete slab resist the uplifting of concrete slab from the underneath I-beam in SCCBs. The tensile resistance of studs embedded in the concrete slab is obtained from the pull-out tests. The authors have performed the pull-out tests in Ref. [45] and herein summarize the relevant findings.

#### 5.2.1. Low-temperature pull-out tests on headed studs

Fig. 17 illustrates the low-temperature pull-out tests on headed studs. There are totally eight specimens reported in Ref. [45] that were tested at four  $T$  levels of  $-80$ ,  $-60$ ,  $-30$ , and  $20$  °C with two specimens for every  $T$  level. Each specimen comprised one stud, a steel plate that the stud was welded to, an octagonal concrete slab, and a holding plate as shown in Fig. 18. Each headed stud was welded to a square 25 mm-thick steel plate, and it was cast in an octagonal

concrete slab measuring  $450 \times 150$  mm<sup>2</sup> in width  $\times$  depth. A loading steel plate was welded to the square steel plate, and was pin-connected to the testing hydraulic jack as shown in Fig. 17. Before the pull-out testing, the specimens were reserved in a cold storage and maintained at the testing  $T$  level for 48 h following instructions in GB51081 [42]. After that, each specimen was moved into a chamber with insulation materials (see Fig. 17). A hydraulic jack was installed between the reaction frame and the concrete slab, and its loading end was connected to the pull-out specimen by the holding hole as shown in Fig. 17. After those installation procedures, this testing rig was sealed in the cooling chamber, and LNG was sprayed to keep the low temperatures. During this loading process, a PT100 thermocouple attached to the headed stud and four PT100 thermocouples installed in the cooling chamber were used to instrument temperatures inside and outside the pull-out testing specimens. After achieving the testing  $T$ , vertical tensile displacement (rate=0.5 mm/min) was applied to the headed studs. During this process, the vertical displacement/elongation ( $\Delta$ ) of the headed stud was measured by four LVDTs (see Fig. 17). The reaction force at each increment of  $\Delta$  was instrumented by a load cell. In addition, during the whole process, the temperatures of the pull-out specimen should be controlled within  $\pm 3$  °C. Table 6 provides more details of these pull-out test specimens.

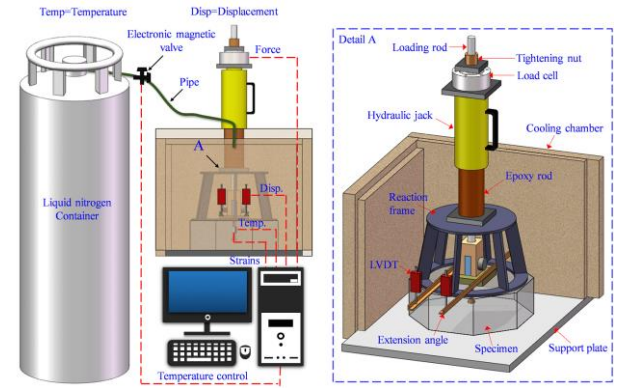


Fig. 17 Pull-out test setup of headed studs at low temperatures [45]

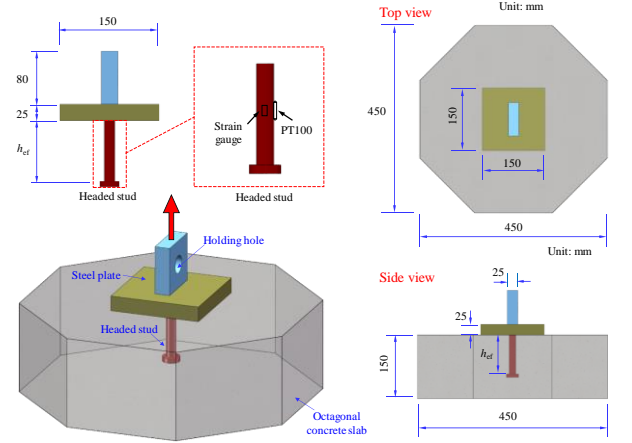


Fig. 18 Details of pull-out specimens of headed studs [45]

Table 6

Details and results of pull-out tests of headed studs

Item	$T$ (°C)	$h_{ef}/d$	$F_u$ (kN)	$\Delta F_u$ (mm)	$K_{0.3F_u}$ (kN/mm)	$F_{u,P}$ (kN)	$\frac{F_u}{F_{u,P}}$	Failure mode
SF+20-1	+20	5.75	106.3	1.98	318.9	100.3	1.06	C + SP
SF+20-2	+20	5.75	103.8	1.61	283.1	100.3	1.04	SP
SF-30-1	-30	5.75	111.9	5.40	335.7	113.3	0.99	S
SF-30-2	-30	5.75	110.2	5.55	330.6	113.3	0.97	S
SF-60-1	-60	5.75	119.3	5.75	340.9	119.9	1.00	S
SF-60-2	-60	5.75	117.7	5.68	353.1	119.9	0.98	S
SF-80-1	-80	5.75	125.0	5.61	304.9	123.8	1.01	S
SF-80-2	-80	5.75	98.8	0.87	370.5	123.8	0.80	W
Mean							0.98	
COV							0.08	



$T$  is temperature level;  $h_{ef}$  and  $d$  are effective embedment depth and diameter of a headed stud, respectively;  $h_{ef}/d$  is ratio of effective embedment depth of a headed stud to its diameter;  $F_u$  and  $\Delta F_u$  are ultimate pull-out resistance and corresponding displacement, respectively, of a headed stud in the test;  $F_{u,p}$  is predicted ultimate pull-out resistance of a headed stud;  $K_{0.3F_u}$  is secant stiffness at 30% of the ultimate load; C, SP, S, and W are concrete breakout, concrete splitting, steel fracture, and welding failure, respectively.

### 5.2.2. Failure modes

Fig. 19 shows the failure modes of pull-out specimens at low temperatures. For specimens tested at 20 °C, one specimen failed in concrete breakout failure with a characteristic of a pulled-out cone from the concrete specimen, and the other one failed in splitting of the concrete slabs due to insufficient splitting strength of NWC. For the rest pull-out testing specimens tested at -30, -60, and -80 °C, steel tensile fracture occurred to the headed studs except ST-80-1 which failed in the weld at the plate-stud connecting position. This clearly reveals that the low temperature deters the splitting or breakout failure of the concrete slab. This is because the low temperature increased the tensile strength of NWC which avoids the splitting or breakout failure of concrete slab.

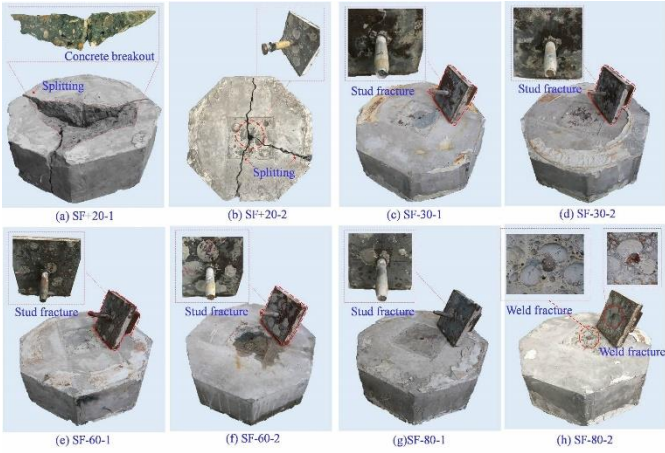


Fig. 19 Failure modes of pull-out test on headed studs at low temperatures [45]

### 5.2.3. Tension load-elongation ( $F$ - $\Delta$ ) curves

Fig. 20 plots the average low-temperature  $F$ - $\Delta$  curves of headed studs, and Fig. 21 summarizes the general low-temperature  $F$ - $\Delta$  behaviours of studs under tension. They show that these  $F$ - $\Delta$  curves can be summarized into three patterns depending on their failure modes. For pull-out test specimens exhibiting steel fracture of headed stud, the  $F$ - $\Delta$  curves exhibit a ductile pattern with a linear, nonlinear, strength hardening, and recession branch, which is similar to the tensile mechanical behaviours of headed studs. The strength hardening branch is mainly determined by the strength hardening of material mechanical behaviours as shown in Fig. 9. For pull-out specimens exhibiting splitting failure mode in concrete slab or weld fracture of headed studs, the  $F$ - $\Delta$  curves exhibit a brittle behaviour with a linear, short nonlinear, and a sharp recession branch. The reason for the brittle manner without strength hardening development and a short nonlinear branch of  $F$ - $\Delta$  curves is due to that the resistance of the specimen at splitting failure of concrete slab is much smaller than its tensile fracture resistance of studs, which stops the strength hardening of studs. For the specimen failed in breakout of concrete slab mode, the  $F$ - $\Delta$  curves exhibit the most brittle behaviour with only linear and recession branch in its curves, which means the concrete breakout resistance of concrete slab is even smaller than the tensile yielding resistance of studs.

One interesting finding is that the low temperatures do not reduce the ductility of headed studs in concrete slabs under tension, and they generally improve the ductility of tensile  $F$ - $\Delta$  curves of headed studs. As the low temperatures go down beyond -30 °C, the  $F$ - $\Delta$  curves do not exhibit brittle mode any more. This is because the low temperatures increased the tensile and compressive strength of NWC much faster than those increments in tensile strength of raw stud materials, which means the much larger improved concrete breakout/splitting resistance of concrete slabs than the tensile strength of headed stud, e.g., as  $T$  reduces from 20 to -80 °C, the increments of concrete cubic compressive strength, concrete tensile strength, and yield/ultimate strength of studs equal to 44%, 105%, and 17%/20%, respectively.

### 5.2.4. Discussions

Fig. 22 shows the effects of  $T$  on ultimate pull-out resistance ( $F_u$ ), initial stiffness ( $K_{0.3F_u}$ ), and elongation at  $F_u$  ( $\Delta F_u$ ). It shows that with the reduction of  $T$  from 20 to -30, -60, and -80 °C, the average  $F_u$  of headed stud is improved

from 105.1 kN to 111.1, 118.5, and 125.0 kN with increments of 6%, 13%, and 19%, respectively; meanwhile, the  $K_{0.3F_u}$  of headed stud is averagely increased from 301.0 kN/mm to 333.2, 347.0, and 370.5 kN/mm with increments of 11%, 15%, and 23%, respectively; however, the  $\Delta F_u$  of headed stud is averagely improved from 1.80 to 5.48, 5.72, and 5.61 mm with increments of 204%, 218%, and 212%, respectively. These increments in pull-out capacity are mainly due to the increased strength and modulus of both NWC and headed studs. Moreover, with the same reduction of  $T$ , both tensile and compressive strengths of NWC exhibit much larger increments than those of headed studs, which guarantees the tensile fracture of headed studs occurred prior to the occurrence of breakout or splitting of the concrete slab. This also explains the improved ductility of headed studs. Moreover, as reported in section 4.2, the ductility of raw material of headed studs was not reduced and even slightly increased as the  $T$  reduces from 20 to -80 °C.

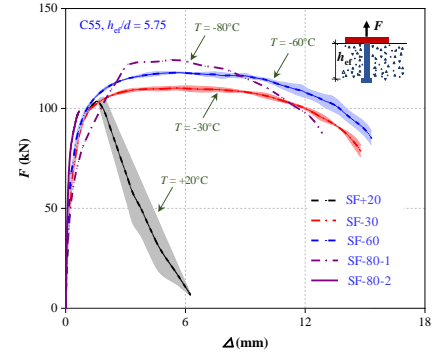


Fig. 20 Experimental  $F$ - $\Delta$  curves of headed studs at low temperatures [45]

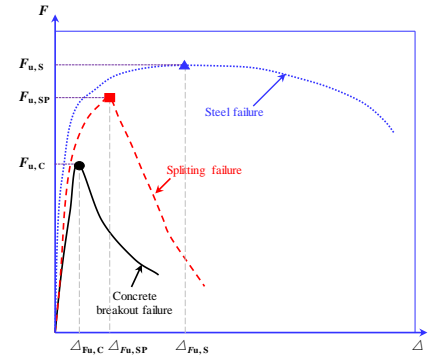


Fig. 21 General tension-elongation ( $F$ - $\Delta$ ) curves of headed studs at low temperatures

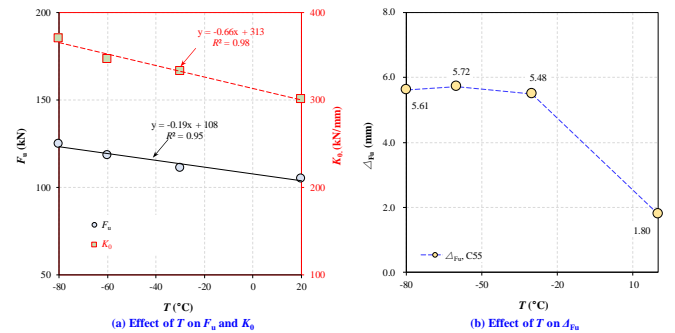


Fig. 22 Effect of  $T$  on tension strength, stiffness, and ductility of headed studs

### 5.2.5. Prediction equations on low-temperature pull-out resistance of headed studs

The low-temperature pull-out resistance of studs equals the smaller value of concrete breakout resistance ( $F_c$ ) and tension resistance of headed studs ( $F_T$ ) as the following:

$$F_{C,p} = \min\{F_c, F_T\} \quad (7)$$

$$F_c = k_{nc} \sqrt{f_{c,T}} h_{ef}^{1.5} \quad (8)$$



$$F_T = A_s f_{uT} \quad (9)$$

where,  $f_{c,T}$  denotes cylinder compressive strength of NWC at  $T$ , in MPa;  $h_{ef}$  is the effective height of stud, in mm;  $A_s$  denotes the stud's cross-sectional area, in  $\text{mm}^2$ ;  $f_{uT}$  denotes ultimate tensile strength of headed stud, in MPa.

Table 6 compares the predicted with those experimental low-temperature pull-out resistances of headed studs. It reflects that Eqns. (7)–(9) overestimates the pull-out resistance of stud by 2% with a COV of 0.08 for eight tests. This also proves the reasonable estimations of developed theoretical models on low-temperature pull-out resistance.

## 6. Ultimate strength behaviours of steel-concrete composite beams (SCCBs) at low temperatures

### 6.1. Four-point bending tests on SCCBs at low temperatures

#### 6.1.1. Specimens

To investigate the low-temperature ultimate strength behaviours of SCCBs, three SCCBs, namely SCB+20, SCB-30, SCB-60, were prepared as shown in Fig. 23. Each SCCB comprises a top NWC slab, a bottom I-beam, headed studs at the slab-beam interface, and reinforcement mesh in the concrete slab. The Q235 mild steel HW125×125×6×9 mm<sup>4</sup> was used for the I-beam, and its mechanical properties at different low temperatures were tested and reported in section 4.1. The length of I-beam equals 1800 mm with stiffeners welded at the positions 100 mm off its both ends, where are the positions of the supports. The top NWC slab equals 1700, 300, and 85 mm in length, width, and depth, respectively. Headed studs ( $d=16$  mm, height= 65 mm) are used for the fabrication of SCCBs. C45 NWC was used for the fabrication of NWC slab, and Table 7 lists its mechanical properties.  $\phi 8$  and  $\phi 6$  mm HRB 400 steel reinforcements ( $f_y=400$  MPa) were used for reinforcement mesh in the NWC slabs as plotted in Fig. 23 (b). The main studied parameter is the low-temperature levels. Specimens SCB+20, SCB-30, SCB-60 were tested at 20, -30, and -60°C, respectively.

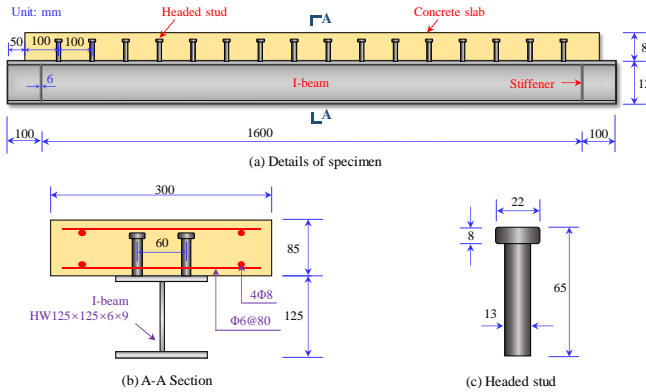


Fig. 23 Details of SCCBs for four-point bending tests at low temperatures

**Table 7**  
Test results of steel-concrete composite beams

Item	$T$ (°C)	$f_c$ (MPa)	$f_{sy}$ (MPa)	$\delta_y$ (mm)	$\delta_u$ (mm)	$\delta_{max}$ (mm)	$K_0$ (kN/mm)	$P_y$ (kN)	$P_u$ (kN)	$P_{u,E}$ (kN)	$\frac{P_u}{P_{u,E}}$	$P_{max}$ (kN)
SCB+20	+20	28.0	332.8	5.61	21.10	23.88	38.66	218.4	321.9	316.9	1.07	273.6
SCB-30	-30	38.8	375.9	4.69	20.84	31.85	40.83	186.0	355.0	368.0	1.02	301.8
SCB-60	-60	46.0	416.8	5.13	22.68	29.63	44.80	224.1	398.3	410.4	1.02	338.6
Mean											1.04	
COV											0.03	

$T$  is temperature level;  $P_y$  denotes yield load in tests;  $P_u$  denotes ultimate load in tests;  $P_{max}$  denotes 85% of  $P_u$ ;  $P_{u,E}$  denotes predicted ultimate load;  $\delta_y$ ,  $\delta_u$ , and  $\delta_{max}$  denote the deflection of SCCB corresponding to  $P_y$ ,  $P_u$ , and  $P_{max}$ ;  $K_0$  denotes secant stiffness of SCCB.

#### 6.1.2. Setup and instrumentation

Fig. 24 plots the setup for the four-point bending tests on SCCBs. Before the testing, each SCCB was stored in the cold storage to maintain the target low temperature for 48 hours accordingly to GB51081 [42]. Then, the SCCB was moved to the loading machine equipped by a cooling chamber as shown in Fig. 24. The cooling chamber surrounded the SCCB with insulation materials and prevented the heat loss of specimens. Moreover, LNG was sprayed to SCCBs

through openings in the top surface of chamber as shown in Fig. 24. During this process, two PT100 thermocouples were installed in the concrete slabs, and another four PT100 thermocouples attached to the surfaces of NWC slab and I-beam were used to measure the temperatures of specimens (see Fig. 24). These measurements of temperatures assisted the inflow control of the injecting LNG into the cooling chamber to ensure that the SCCBs remained within the target temperature range of  $\pm 3$  °C.

Each specimen was installed to the rigid base on two round supports at both ends, which simulates the pin-pin boundary condition. The span of these two supports equals 1600 mm. Vertical loading in the displacement mode was transferred from the testing machine to the SCCB by a spreading I-beam. These two loading points locate 200 mm away from the mid-span (see Fig. 25). Three LVDTs were installed under the I-beam at mid-span and  $\pm 200$  mm off mid-span to instrument deflections of SCCBs (see Fig. 25). To measure the steel-concrete interfacial slips, another four LVDTs were also installed along I-beam-slab interface at distances of 0, 200, 400, and 600 mm away from the mid-span as illustrated in Fig. 25. In addition, two more LVDTs were adopted at both ends of SCCB to record the slips between the concrete slab and I-beam. To measure strains along heights of the mid-span cross section, LSGs were installed as shown in Fig. 26.

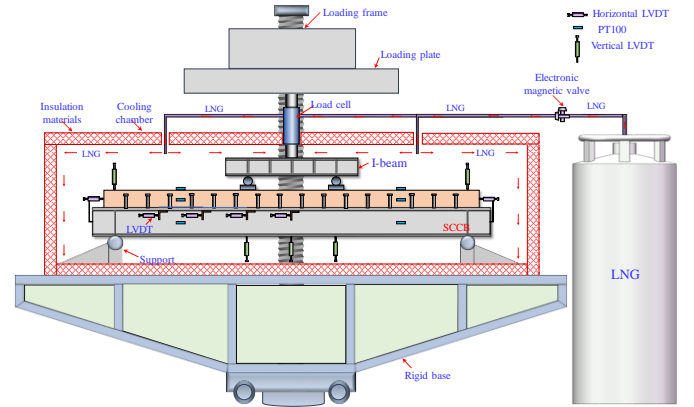


Fig. 24 Four-point bending test setup of SCCBs at low temperatures

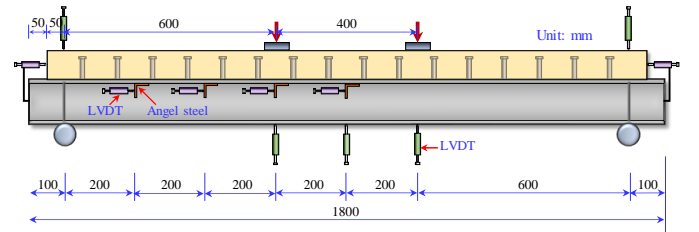


Fig. 25 Layout of LVDTs used in the bending tests on SCCBs

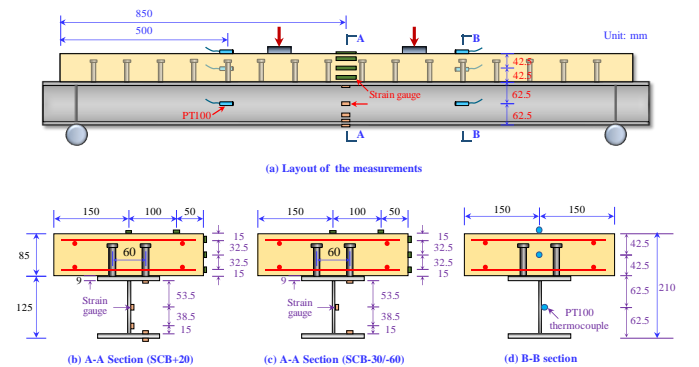


Fig. 26 Layout of strain gauges and thermocouples used in the bending tests on SCCBs

#### 6.2. Failure modes

Figs. 27–29 plot the typical failure modes of SCCBs subjected to low-temperature four-point bending. They reflect that under sagging bending moment, concrete crushing occurred to the mid-span top flange of NWC slab. The depth of the crushed top flange of NWC slab equals about its 0.5 times depth. All the I-beams exhibited excessive deformation without occurrence of local buckling in their web or flange.

### 6.3. Load-deflection behaviours

The load-deflection ( $P$ - $\delta$ ) curves of SCB+20, SCB-30, and SCB-60 are given in Fig. 30(a)-(c). These curves show that the  $P$ - $\delta$  curves of SCCBs exhibit a ductile manner with four stages of elastic, nonlinear developing, strength hardening, and recession stages. As the loading process, the curve of initial elastic stage (OA) ends as the bottom flange of I-beam starts to yield. Then, in stage II, the  $P$ - $\delta$  curves of SCCBs show a parabolic behaviour due to nonlinearities of I-beam and concrete. In the followed stage III, the SCCB exhibits hardening manner due to the strength hardening of I-beam, and the increasing rate of resistance slows down. Finally, the SCCBs achieve their peak resistances at the end of stage III. At the peak resistance, concrete crushing took place at the mid-span where suffered the maximum bending moment. The final recession stage exhibits decreased load carrying capacity.

Fig. 30 (d) compares the  $P$ - $\delta$  curves of SCCB tested at different  $T$  levels. Fig. 31 plots the influences of  $T$  levels on elastic stiffness ( $K_0$ ), ultimate resistance ( $P_u$ ), central deflection at  $P_u$  ( $\delta_u$ ), and ultimate deflection capacity ( $\delta_{max}$ , the deflection at 85%  $P_u$  in recession  $P$ - $\delta$  curves). These curves show that the decreasing  $T$  slightly increased the elastic stiffness, but significantly increased the ultimate resistance of SCCBs. Moreover, the slope of strength hardening  $P$ - $\delta$  curves at low temperatures is larger than that at ambient temperatures. In addition, the ductility of SCCB was not reduced as the  $T$  level goes down from 20 to -60 °C. As  $T$  decreases from 20 to -30, and -60°C, the  $P_u$  of SCCB is increased from 321.9 kN to 355.0 and 398.3 kN with increments of 10% and 24%, respectively; meanwhile, the  $K_0$  of SCCB is increased from 38.7 kN/mm to 40.8 and 44.8 kN/mm with increments of 5% and 16%, respectively; however, the  $\delta_u$  (or  $\delta_{max}$ ) of SCCB is increased from 21.1 (23.9) mm to 20.8 (31.9) and 22.7 (29.6) mm with increments of -1% (33%) and 8% (24%), respectively. This is because the decreasing  $T$  improves the compressive strength of NWC and yield strength of I-beam which explains the improved  $P_u$  of SCCB. Moreover, the low temperature also increases the elastic modulus of NWC and I-beam. As pointed in section 3 and 4, as the  $T$  reduces from 20 to -30 and -60 °C, the  $E_{ct}$  of NWC is improved by 16% and 12%, respectively. However, sections 3 and 4 also show that the decreasing  $T$  did not reduce the ductility of headed studs and I-beam, which makes sure the marginal influences on the ductility of SCCBs.

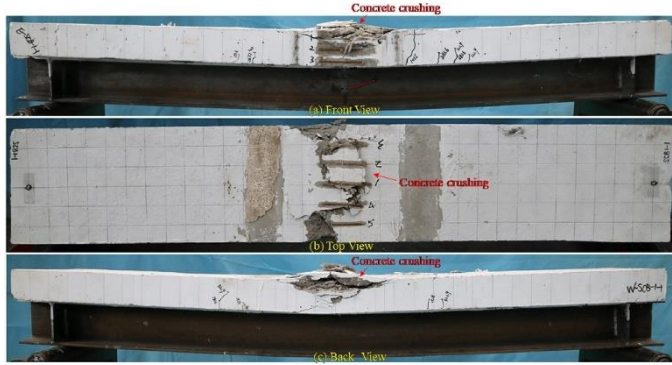


Fig. 27 Failure mode of SCB+20

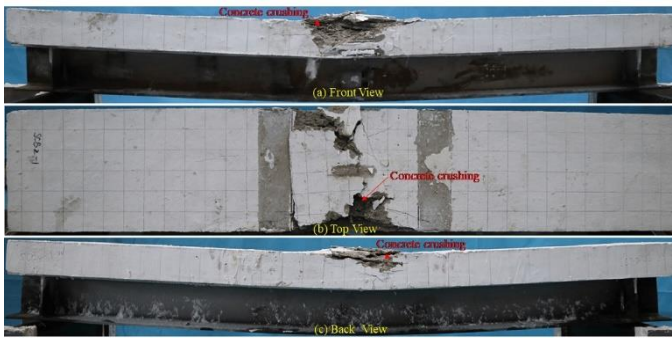


Fig. 28 Failure mode of SCB-30

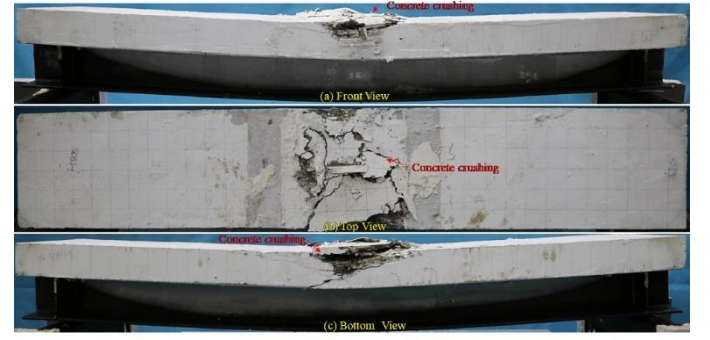


Fig. 29 Failure mode of SCB-60

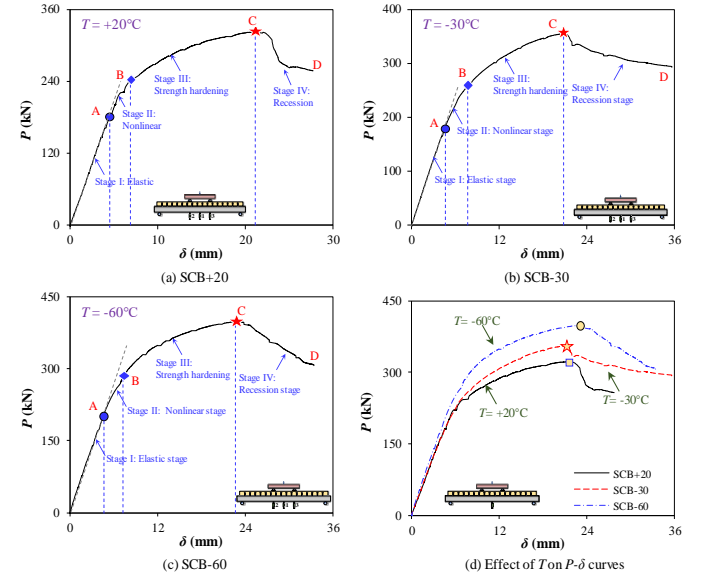


Fig. 30 Load-deflection curves of SCCBs under low-temperature four-point bending

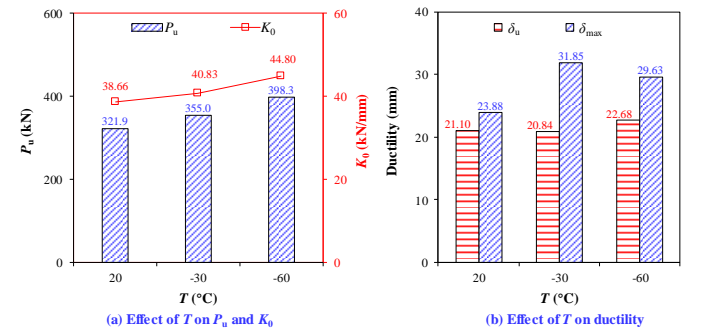


Fig. 31 Effect of  $T$  on strength and ductility index of SCCBs

### 6.4. Load-strain behaviours

Fig. 32 depicts the load-strain curves of mid-span cross-section as marked in Fig. 26. It shows that load-strain curves exhibit the same four-stage behaviour as those  $P$ - $\delta$  curves of SCCBs. It further confirms that the nonlinearities of load-strain (or  $P$ - $\delta$  curves) at the second working stage initiate as the bottom tip of I-beam yields. Thus, after stage II, strength hardening starts and the SCCBs achieved their  $P_u$  values whilst the top tip of NWC slab achieved their ultimate compressive strains of about 3000~5000 $\mu\epsilon$ .

Fig. 33 depicts the mid-span strain versus height profiles at different loading levels. It reveals that as the reaction force of the SCCB is smaller than  $0.9P_u$  the strain profiles are almost in a linear relationship with the height; as the reaction force of the SCCB is beyond  $0.9P_u$  until  $P_u$  the linear strain distribution principle almost works even though there are some slight interfacial slips occurred. These observations confirm that the assumption of plane section still works for the SCCBs subjected to low-temperature bending since they were designed as the full-composite action.

### 6.5. Load-slip behaviours

Fig. 34 depicts the load-slip curves at different positions along SCCBs. It shows that these load-slip curves exhibit a similar four-stage manner to those  $P$ - $\delta$  (or strain) curves. At working stages I and II, the slips are almost in a linear relationship with the applied load, and the slips are smaller than 0.2 mm. The slips start to increase fast in the strength hardening stage and the maximum slip is about 1.0 mm which occurs at the locations of 400 ~ 600 mm away from the mid-span. Fig. 35 plots the slip profiles of different measured locations at different loading levels. It shows that (1) the slip starts to increase fast as the applied load is beyond  $0.7P_u$ ; (2) at the same loading level, the slips firstly increase and then decrease as the distance away from the mid-span increases, and the maximum slips occurred to the cross section locating 400 mm and 600 mm away from the mid-span for SCCB tested at ambient and low temperatures, respectively. This may be explained by the bending moment distribution and inner layout of the headed studs in the SCCBs.

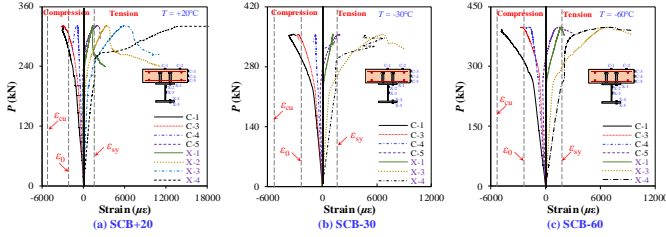


Fig. 32 Load-strain curves of concrete slab and I-beam at mid-span cross section

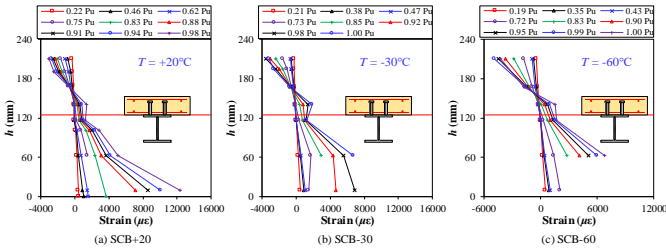


Fig. 33 Strain distribution profile along the height of the mid-span cross section at different loadings

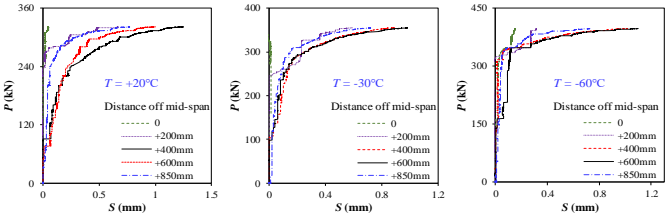


Fig. 34 Load-slip curves of SCCBs at different temperatures

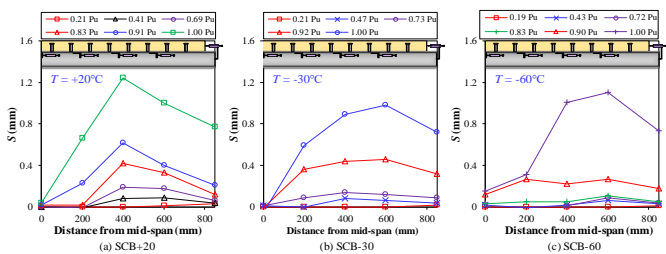


Fig. 35 Slip distribution file along the length of SCCBs at different loadings

### 6.6. Analysis on ultimate resistance of SCCB at low temperatures

Since the SCCBs failed in flexure, the bending resistance of SCCB at low temperatures ( $M_{uT}$ ) can be obtained based on the following assumptions;

(1) Plane section remains plane (this has been checked in section 6.4); (2) Ignoring the NWC low-temperature tensile strength; (3) The I-beam achieves its yielding strength in both tension and compression zones.

Suffering sagging moment, the neutral axis may locate at different heights of the cross section, e.g., in the NWC slab, in the flange or web of I-beam. Therefore, the bending resistance of SCCBs at low temperatures can be found by assuming different positions of the neutral axis.

#### Case 1: Neutral axis in the NWC slab ( $x < h_c$ )

Fig. 36(a) plots the stress and internal force distribution diagram of the cross section at  $P_u$  as  $x < h_c$ . The low-temperature bending resistance of the SCCB can be found by finding the neutral axis position, i.e., the resultant internal compression force of the cross section equals to the internal tension force as the following;

$$C_c = T_{s1} + T_{s2} + T_{s3} \quad (10)$$

$$C_c = 0.85 f_{cT}' x b_e; T_{s1} = f_{yT} h_t b_f; T_{s2} = f_{yT} h_w t_w; T_{s3} = f_{yT} h_b b_f \quad (11)$$

where  $b_e$  and  $b_f$  denote width of concrete slab and steel flange, respectively;  $h_t$ ,  $h_b$  and  $h_w$  denote height of steel top and bottom flange, and steel web, respectively;  $h_c$  denotes depth of concrete slab;  $t_w$  denotes web thickness;  $x$  denotes distance between the neutral axis and top tip of compression concrete slab;  $f_{cT}'$  denotes cylinder compressive strength of NWC at  $T$ ;  $f_{yT}$  denotes yield strength of I-beam at  $T$ ;  $C_c$  denotes internal resultant force of compression concrete;  $T_{s1}$ ,  $T_{s2}$  and  $T_{s3}$  denote internal resultant load of top flange, web and bottom flange of I-beam, respectively.

Thus, the  $x$  is determined as the following;

$$x = \frac{f_{yT} (h_t b_f + h_w t_w + h_b b_f)}{0.85 f_{cT}' b_e} \quad (12)$$

The ultimate bending moment of SSCB at  $T$ , i.e.,  $M_{uT}$ , is determined by;

$$M_{uT} = 0.85 f_{cT}' x b_e \left( h_c + \frac{h_t + h_w + h_b - x}{2} \right) \quad (13)$$

#### Case 2: Neutral axis in the flange of I-beam [ $h_c \leq x \leq (h_c + h_t)$ ]

Fig. 36(b) plots the stress distribution diagram of cross section at  $P_u$  as  $h_c \leq x \leq (h_c + h_t)$ . As the neutral axis lies in the I-beam flange, the  $x$  value is determined by the resultant internal force equalling zero, i.e.,

$$C_c + C_{s1} = T_{s1} + T_{s2} + T_{s3} \quad (14)$$

$$C_c = 0.85 f_{cT}' h_c b_e; C_{s1} = f_{yT} (x - h_c) b_f \quad (15)$$

$$T_{s1} = f_{yT} (h_c + h_t - x) b_f; T_{s2} = f_{yT} h_w t_w; T_{s3} = f_{yT} h_b b_f \quad (16)$$

where,  $C_c$  and  $C_{s1}$  denote internal resultant compressive forces of concrete slab and top flange of I-beam, respectively;  $T_{s1}$ ,  $T_{s2}$ , and  $T_{s3}$ , denote internal resultant tensile load of top flange, web, and bottom flange of I-beam, respectively.

Thus, the  $x$  value is solved by the following equation;

$$x = \frac{f_{yT} (2h_c b_f + h_t b_f + h_w t_w + h_b b_f) - 0.85 f_{cT}' h_c b_e}{2 f_{yT} b_f} \quad (17)$$

The  $M_{uT}$  of SCCB at low temperatures can be determined as the following;

$$M_{uT} = 0.5 T_{s1} (h_c + h_t - x) + T_{s2} (0.5 h_w + h_c + h_t - x) + T_{s3} (0.5 h_b + h_w + h_c + h_t - x) + C_c (x - 0.5 h_c) + 0.5 C_{s1} (x - h_c) \quad (18)$$

#### Case 3: Neutral axis in the web of I-beam [ $x > (h_c + h_t)$ ]

Fig. 36(c) plots the stress distribution diagram of cross section at  $P_u$  as  $x > (h_c + h_t)$ . As the neutral axis lies in the I-beam web, the  $x$  value can be found as the following;

$$C_c + C_{s1} + C_{s2} = T_{s2} + T_{s3} \quad (19)$$



$$C_c = 0.85 f_{ct} h_c b_e; C_{s1} = f_{yT} h_t b_f; C_{s2} = f_{yT} (x - h_t - h_c) t_w \quad (20)$$

$$T_{s2} = f_{yT} (h_w + h_c + h_t - x) t_w; T_{s3} = f_{yT} h_b b_f \quad (21)$$

where,  $C_c$ ,  $C_{s1}$ , and  $C_{s2}$  denote internal resultant compressive forces of concrete slab, I-beam top flange, and I-beam web, respectively;  $T_{s2}$  and  $T_{s3}$  denote internal resultant tensile loads of I-beam web and I-beam bottom flange, respectively.

Thus, the  $x$  is solved as the following;

$$x = \frac{f_{yT} (h_w t_w + 2h_c t_w + 2h_t t_w + h_b b_f - h_t b_f) - 0.85 f_{ct} h_c b_e}{2 f_{yT} t_w} \quad (22)$$

The  $M_{u,T}$  of SCCB now becomes;

$$M_{u,T} = 0.5 T_{s2} (h_c + h_t + h_w - x) + T_{s3} (0.5 h_b + h_c + h_t + h_w - x) + C_c (x - 0.5 h_c) + C_{s1} (x - h_c - 0.5 h_t) + 0.5 C_{s2} (x - h_c - h_t) \quad (23)$$

Thus, the low-temperature bending resistance of SCCB can be found by procedures in Fig. 37. In addition, one point needs to be clarified is that the SCCB should be designed as a full-composite beam using Eqn. (5) for low-temperature shear resistance of studs in SCCBs. Regarding the partial composite SCCB, further studies are still required.

The ultimate load ( $P_{u,T}$ ) of the SCCB is determined as follows;

$$P_{u,T} = 2 M_{u,T} / a \quad (24)$$

### 6.7. Validations

Table 7 lists the predicted  $P_{u,T}$  by the developed theoretical models with test values. It shows that theoretical models underestimate the load capacity of SCCBs SCB+20, SCB-30, and SCB-60 by 7%, 2%, and 2%, respectively. The average discrepancy of theoretical predictions is less than 4% that confirms their accurate estimations on ultimate load capacities of SCCB at low temperatures. However, these theoretical models still require more extensive validations.

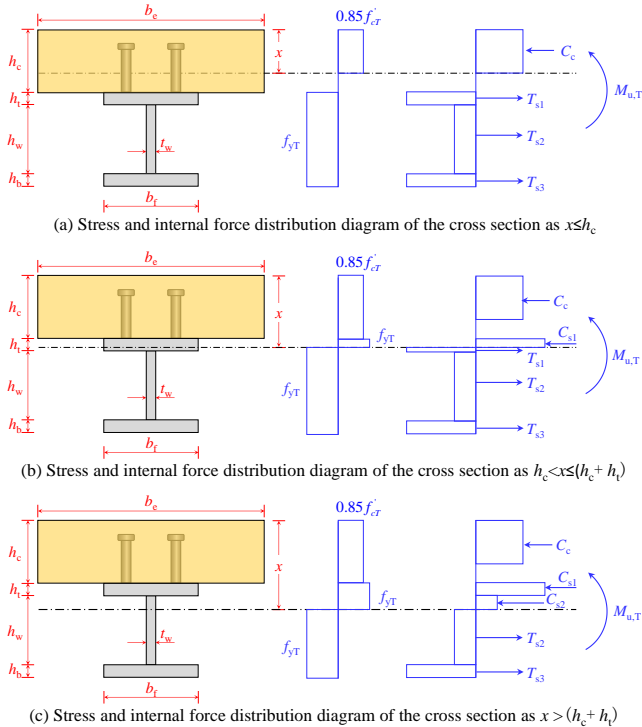


Fig. 36 Stress, stress and internal force distribution diagrams for SCCBs

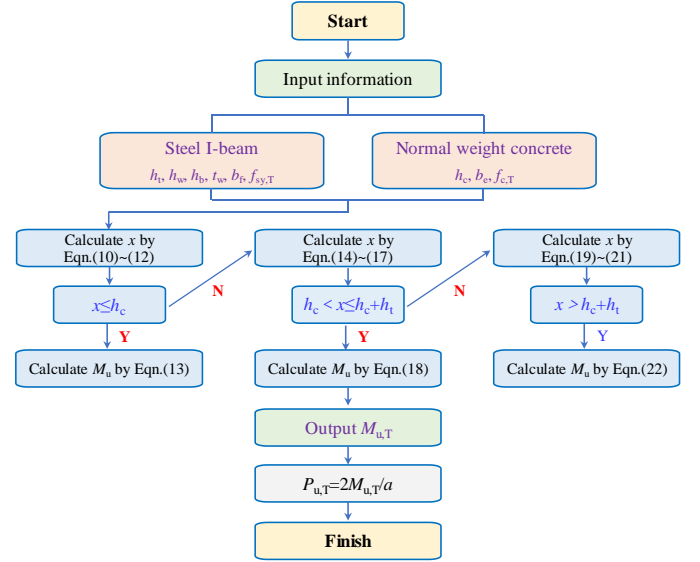


Fig. 37 Flow chart on determining low-temperature ultimate bending resistance of SCCBs

### 7. Conclusions

This paper reported a series of tests and analytical studies on behaviours of constructional materials in SCCBs and low-temperature ultimate strength behaviour of SCCBs. These studies on material and structural members support the following findings;

- (1) With the decrease of  $T$  from 20 to -30, -60, and -80 °C, the  $f_c$  of C45 NWC was increased by 28%, 64%, and 71%, respectively; meanwhile, the strain at  $f_c$  (i.e.,  $\epsilon_0$ ) was increased by 35%, 15%, and 26%, respectively; the  $f_t$  of NWC receives average increments of 23%, 70%, and 105%, respectively. Eqn. (1)-(2) are developed to estimate the low-temperature stress-strain curves of NWC.
- (2) The strength and modulus of mild steel Q235 for I-beam increases with the decreasing  $T$ , and its ductility was also improved with the decreasing  $T$  from 20 to -60 °C. With the decrease of  $T$  from 20 to -30, -60, and -80 °C, the  $f_y$  (or  $f_u$ ) of I-beam is averagely increased by 13% (13%), 19% (25%), and 19% (30%), respectively; meanwhile, the  $E_s$  of I-beam is slightly increased by 5%, 8%, and 6%, respectively; meanwhile, the average fracture strain of I-beam is improved by 5%, 5%, and 15%, respectively.
- (3) The decreasing  $T$  slightly changed the modulus of headed studs within 3%. With the reduction of  $T$  from 20 to 0, -30, -60, and -80 °C,  $f_y$  of  $d=16$  mm headed studs receives average increments of about 2%, 4%, 11%, and 14%, respectively; the  $f_u$  value of  $d=16$  mm headed studs is averagely increased by 3%, 7%, 14%, and 22%, respectively. Eqns. (3) and (4) were developed to estimate the influences of  $T$  on  $f_y$  and  $f_u$  of headed studs.
- (4) The typical failure modes of low-temperature push-out tests were shear fracture of headed studs at their roots, local crushing of NWC, and cracks in the concrete slabs. Reducing  $T$  from 20 to -80 °C generally improved the shear capacity, but slightly reduced the ductility of the headed studs. With the decrease of  $T$  from 20 to -80 °C, the  $N_u$  of headed stud was improved by 14%; however, the  $S_{max}$  of the headed stud was slightly reduced from 6.6 to 6.3 mm. Eqns. (5)-(6) were recommended to estimate the low-temperature  $N_u$  of headed studs.
- (5) Low temperatures generally improved the pull-out ductility and resistance of headed studs. With the reduction of  $T$  from 20 to -80 °C, the  $F_u$  of headed stud is averagely increased by 19%; the ultimate elongation ( $\Delta F_u$ ) of headed stud is averagely increased from 1.8 mm to 5.6 mm. Eqns. (7)-(9) were proposed for determining the low-temperature pull-out resistance of studs.
- (6) The SCCBs subjected to low-temperature four-point bending exhibited flexural mode with concrete-slab crushing and yielding of bottom I-beam. The low temperature increased the ductility, elastic stiffness and ultimate resistance of SCCBs. As  $T$  decreased from 20 to -30, and -60 °C, the  $P_u$  of SCCB was improved by 10% and 24%, respectively; the  $K_0$  of SCCB was improved by 5% and 16%, respectively; the  $\delta_u$  (or  $\delta_{max}$ ) of SCCB is increased by -1% (33%) and 8% (24%), respectively.
- (7) The developed theoretical models, i.e., Eqns. (10)-(24) predicted reasonably the low-temperature ultimate bending resistance of SCCBs. The average discrepancy of three theoretical predictions on ultimate load capacities of SCCBs at low temperatures is less than 4%. However, these theoretical models still require more extensive validations.



## Nomenclature

$C_c$	Internal resultant compression force of concrete slab
$C_{s1}$	Internal resultant compressive force of I-beam top flange
$C_{s2}$	Internal resultant compressive force of I-beam web
$E_c$	Modulus of elasticity of NWC
$E_{cT}$	Modulus of elasticity of NWC at $T$
$E_s$	Elastic modulus of steel
$F_C$	Concrete breakout resistance of headed stud
$F_T$	Tension resistance of headed stud
$F_u$	Ultimate pull-out resistance of headed stud
$F_{u,P}$	Predicted ultimate pull-out resistance of headed stud
$I_{fu}$	Ultimate strength at $T$ to its corresponding value at ambient temperature of steel
$I_{fy}$	Yield strength at $T$ to its corresponding value at ambient temperature of steel
$K_0$	Initial stiffness of SCCB
$K_{0.3Fu}$	Secant stiffness at 30% $F_u$
$K_{0.7Nu}$	Secant stiffness at 70% $N_u$
$M_{u,T}$	Predicted ultimate bending moment of SCCB
$N_u$	Ultimate shear resistance of headed stud
$N_{u,P}$	Predicted shear resistance of headed stud
$P_{max}$	0.85 $P_u$ of recession of $P$ - $\delta$ curve of SCCB
$P_u$	Ultimate resistance of SCCB
$P_{u,E}$	Predicted ultimate resistance of SCCB
$P_y$	Yield load of SCCB
$S_{max}$	Slip at 0.9 $N_u$ of recession of $N$ - $S$ curves
$S_u$	Slip corresponding to $N_u$ of headed stud
$T$	Temperature level
$T_{s1}$	Internal resultant tensile load of I-beam top flange
$T_{s2}$	Internal resultant tensile load of I-beam web
$T_{s3}$	Internal resultant tensile load of I-beam bottom flange
$a$	Shear span of SCCB
$b_c$	Width of concrete slab
$b_f$	Width of I-beam flange
$d$	Diameter of headed stud
$f_c$	Prism compressive strength of NWC
$f_{cu}$	Cubic compressive strength of NWC
$f_{cT}$	Cylinder compressive strength of NWC at $T$
$f_c'$	Cylinder compressive strength of NWC
$f_t$	Tensile strength of NWC
$f_u$	Ultimate strength of steel
$f_{uT}$	Ultimate strength of I-beam at $T$
$f_y$	Yield strength of steel
$h$	Height of headed stud
$h_b$	Height of I-beam bottom flange
$h_c$	Depth of concrete slab
$h_{ef}$	Effective embedment depth of stud
$h_t$	Height of I-beam top flange
$h_w$	Height of I-beam web
$x$	Distance between concrete compression top tip fiber and neutral axis
$\Delta F_u$	Elongation corresponding to $F_u$ of headed stud
$\psi_f$	Percentage elongation of I-beam after fracture
$\psi_{st}$	Reduction in cross section of headed stud after fracture
$\delta_{max}$	Deflection of SCCB corresponding to $P_{max}$
$\delta_u$	Deflection of SCCB corresponding to $P_u$
$\delta_y$	Deflection of SCCB corresponding to $P_y$
$\epsilon_0$	Peak strain at $f_c$ of NWC
$\epsilon_F$	Fracture strain of steel
$\epsilon_u$	Ultimate strain of steel
$\epsilon_y$	Yielding strain of steel
$\kappa$	Factor for $N_{u,P}$
$\sigma$ - $\epsilon$	Stress versus strain

## Acknowledgement

The authors would like to acknowledge the National Natural Science Foundation of China (Grant No. 51978459, 52178494, and 52278201) and Tianjin University (Grant no. 2019XRX-0026). The authors gratefully express their gratitude for the financial supports.

## References

- [1] Dalen K.V., "The strength of stud shear connectors at low temperatures", Canadian Journal of Civil Engineering, 10, 429-435, 1983.
- [2] Long A.E., Dalen K.V., and Csagoly P., "The fatigue behavior of negative moment regions

- of continuous composite beams at low temperatures", Canadian Journal of Civil Engineering, 2, 98-115, 1975.
- [3] Li X., Xia Z., Pu Q., and Yang Y., "Dynamical test and vehicle-bridge coupling analysis of Lasa River Bridge", Journal of Vibration and Shock, 26 (11), 129-132, 2007. (in Chinese)
- [4] Yan J.B., Liu X.M., Liew J.Y.R., Qian X., and Zhang M.H., "Steel-concrete-steel sandwich system in Arctic offshore structures: materials, experiments, and design", Materials and Design, 91, 111-121, 2016.
- [5] Yan J.B., Wang Z., and Wang X., "Behaviour of steel-concrete-steel sandwich plates under different ice-contact pressure", Advanced Steel Construction, 15 (1), 116-122, 2019.
- [6] Stepanova N.A., "On the lowest temperatures on earth", Monthly Weather Review, 6-10, 1958.
- [7] Yan J.B., Xie J., and Ding K.R., "Stress relaxation behavior of prestressing strands under low temperatures", PCI Journal, 65 (1), 41-56, 2020.
- [8] Elices M., Corres H., and Planas J., "Behaviour at cryogenic temperatures of steel for concrete reinforcement", ACI Journal Proceedings, 84 (3), 405-411, 1986.
- [9] Dahmani L., Khenane A., Kaci S., "Behavior of the reinforced concrete at cryogenic temperatures", Cryogenics, 47, 517-525, 2007.
- [10] Yan J.B., and Xie J., "Experimental studies on mechanical properties of steel reinforcements under cryogenic temperatures", Construction and Building Materials, 151, 661-672, 2017.
- [11] Yan J.B., Liew J.Y.R., and Zhang M.H., "Mechanical properties of normal strength mild steel and high strength steel S690 in low temperature relevant to Arctic environment", Materials and Design, 61, 150-159, 2014.
- [12] Yan J.B., Luo Y.L., Lin X.C., Luo Y.B., and Zhang L.X., "Effects of the Arctic low temperature on mechanical properties of Q690 and Q960 high-strength steels", Construction and Building Materials, 300 124022, 2021.
- [13] Krstulovic-Opara N., "Liquefied natural gas storage: Material behavior of concrete at cryogenic temperatures", ACI Materials Journal, 104 (3), 297-306, 2007.
- [14] Lee G.C., Shih T.S., and Chang K.C., "Mechanical properties of concrete at low temperature", Journal of Cold Regions Engineering, 2 (1) 13-24, 1988.
- [15] Xie J., Li X.M., and Wu H.H., "Experimental study on the axial-compression performance of concrete at cryogenic temperatures", Construction and Building Materials 72, 380-388, 2014.
- [16] MacLean T.J., and Lloyd A., "Compressive stress-strain response of concrete exposed to low temperatures", Journal of Cold Regions Engineering, 33 (4), 04019014, 2019.
- [17] Yan J.B., Xie W.J., Zhang L.X., and Lin X.C., "Bond behaviour of concrete-filled steel tubes at the Arctic low temperatures", Construction and Building Materials, 210, 118-131, 2019.
- [18] Montejo L.A., Sloan J.E., Kowalsky M.J., and Hassan T., "Cyclic response of reinforced concrete members at low temperatures", Journal of Cold Regions Engineering, 22, 79-102, 2008.
- [19] Montejo L.A., Kowalsky M.J., and Hassan T., "Seismic behavior of flexural dominated reinforced concrete bridge columns at low temperatures", Journal of Cold Regions Engineering, 23 (1), 18-42, 2009.
- [20] Montejo L.A., Kowalsky M.J., and Hassan T., "Seismic behavior of shear-dominated reinforced concrete columns at low temperatures", ACI Structural Journal, 106 (4), 445-454, 2009.
- [21] Montejo L.A., Marx E., and Kowalsky M.J., "Seismic design of reinforced concrete bridge columns at subfreezing temperatures", ACI Structural Journal, 107 (4), 427-433, 2010.
- [22] Mirzazadeh M.M., Noël M., and Green M.F., "Effects of low temperature on the static behaviour of reinforced concrete beams with temperature differentials", Construction and Building Materials, 112, 191-201, 2016.
- [23] Mirzazadeh M.M., Noël M., and Green M.F., "Fatigue behavior of reinforced concrete beams with temperature differentials at room and low temperature", Journal of Structural Engineering, 143 (7), 04017056, 2017.
- [24] El-Hacha R., Wight R.G., and Green M.F., "Prestressed carbon fiber reinforced polymer sheets for strengthening concrete beams at room and low temperatures", Journal of Composites for Construction, 8 (1) 3-13, 2004.
- [25] Saiedi R., Fam A., and Green M.F., "Behavior of CFRP-prestressed concrete beams under high-cycle fatigue at low temperature", Journal of Composites Construction, 15 (4), 482-489, 2011.
- [26] Bryan P.E., and Green M.F., "Low temperature behaviour of CFRP prestressed concrete beams", Canadian Journal of Civil Engineering, 23 464-470, 1996.
- [27] Karbhari V.M., and Eckel D.A., "Effect of cold regions climate on composite jacketed concrete columns", Journal of Cold Regions Engineering, 8 (3), 73-86, 1994.
- [28] Green M.F., Bisby L.A., Fam A.Z., and Kodur V.K.R., "FRP confined concrete columns: Behaviour under extreme conditions", Cement and Concrete Composites, 28, 928-937, 2006.
- [29] Yan J.B., Dong X., and Zhu J.S., "Behaviours of stub steel tubular columns subjected to axial compression at low temperatures", Construction and Building Materials, 228, 116788, 2019.
- [30] Yan J.B., Wang T., and Dong X., "Compressive behaviours of circular concrete-filled steel tubes exposed to low-temperature environment", Construction and Building Materials, 245, 118460, 2020.
- [31] Yan J.B., Dong X., and Zhu J.S., "Compressive behaviours of CFST stub columns at low temperatures relevant to the Arctic environment", Construction and Building Materials, 223, 503-519, 2019.
- [32] Yan J.B., Dong X., and Wang T., "Axial compressive behaviours of square CFST stub columns at low temperatures", Journal of Constructional Steel Research, 164, 105812, 2020.
- [33] Yan J.B., Luo Y.L., Su L.F., Lin X.C., Luo Y.B., and Zhang L.X., "Low-temperature compression behaviour of square CFST columns using Q960 ultra-high strength steel", Journal of Constructional Steel Research, 183, 106727, 2021.
- [34] Yan J.B., Zhang B., Feng J.Y., Du Y.S., Luo Y.B., and Shi Y.D., "Low-temperature compression behaviour of circular stub stainless-steel tubular columns", Advanced Steel Construction, 18 (3), 670-678, 2022.
- [35] Yan J.B., Wang Z., and Xie J., "Compressive behaviours of double skin composite walls at low temperatures relevant to the arctic environment", Thin-Walled Structures, 140, 294-303, 2019.
- [36] Yan J.B., Wang Z., and Wang T., "Compressive behaviours of steel-concrete-steel sandwich walls with J-hooks at low temperatures", Construction and Building Materials, 207, 108-121, 2019.
- [37] Wang Z., Yan J.B., and Liu X.M., "Numerical and theoretical studies on double steel plate composite walls under compression at low temperatures", Advanced Steel Construction, 17 (4), 376-384, 2021.
- [38] GB/T 50081-2019, Standard for test methods of concrete physical and mechanical properties, China Architecture and Building Press, Beijing, 2019 (in Chinese).
- [39] GB/T 228.1-2010, Metallic materials-Tensile testing-Part 1: Methods of test at room temperature, China Standards Press, Beijing, China, 2010 (in Chinese).

- [40] GB/T 228.3-2019, Metallic materials-Tensile testing-Part 3: Methods of test at low temperature, China Standards Press, Beijing, China, 2019 (in Chinese).
- [41] Xie J., Zhu G.R., and Yan J.B., "Mechanical properties of headed studs at low temperatures in the Arctic infrastructures", *Journal of Constructional Steel Research*, 149, 130-140, 2018.
- [42] GB 51081-2015, Technical code for application of concrete under cryogenic circumstance, China Planning Press, Beijing, China, 2015 (in Chinese).
- [43] EN 1994-1-1: 2004, Eurocode 4, Design of composite steel and concrete structures-Part 1-1: General rules and rules for buildings, European Committee for Standardization, Brussels, Belgium, 2004.
- [44] Yan, J.B., and Xie, J., "Shear behavior of headed stud connectors at low temperatures relevant to the Arctic environment", *Journal of Structural Engineering*, 144 (9), 04018139, 2018.
- [45] Xie J., Kang E.C., Yan J.B., and Zhu G.R., "Pull-out behaviour of headed studs embedded in normal weight concrete at low temperatures", *Construction and Building Materials*, 264, 120692, 2020.

# INVERSION METHOD OF UNCERTAIN PARAMETERS FOR TRUSS STRUCTURES BASED ON GRAPH NEURAL NETWORKS

Zhang-Qi Wang<sup>1, 2, 3</sup>, Zhe Zheng<sup>1</sup>, Jun-Wei MengXiang<sup>1</sup> and Wen-Qiang Jiang<sup>1, 2, 3, \*</sup>

<sup>1</sup> Department of Mechanical Engineering, North China Electric Power University, Baoding, China

<sup>2</sup> Hebei Engineering Research Center for Advanced Manufacturing & Intelligent Operation and Maintenance of Electric Power Machinery,  
North China Electric Power University, Baoding, China

<sup>3</sup> Hebei Key Laboratory of Electric Machinery Health Maintenance & Failure Prevention, North China Electric Power University, Baoding 071003, China

\* (Corresponding author: E-mail: wenqiang.jiang@ncepu.edu.cn)

## ABSTRACT

Uncertainty exists widely in practical engineering. It is an important challenge in engineering structural analysis. In truss structures, the uncertainties of axial stiffness of bolted joints will significantly affect the mechanical behavior of the structure as the axial load is dominated by the member internal forces. Structural response analysis based on determined structural parameters is a common forward problem that can be solved by modeling analysis methods. However, the uncertainties parameter of axial stiffness of bolted joint cannot be determined during the design and analysis of truss structure in the direct nonlinear analysis method. Structural parameter identification based on structural response is a typical inverse problem in engineering, which is difficult to solve using traditional analysis tools. In this paper, an inverse model based on Graph Neural Network (GNN) is proposed. The feature encoding method for transforming truss structures into graph representations of GNN is defined. A parameterized acquisition method for large-scale datasets is presented, and an innovative inversion model based on GNN for the inversion of uncertain parameters of truss structures is proposed. The proposed method is shown to perform well with an inversion accuracy, and accurate results can be obtained with limited data sets. The inversion method has strong data mining capability and model interpretability, making it a promising direction for exploring engineering structural analysis.

## ARTICLE HISTORY

Received: 7 April 2023  
Revised: 6 June 2023  
Accepted: 20 June 2023

## KEYWORDS

Truss structures;  
Uncertain parameters;  
Inversion method;  
GNN

Copyright © 2023 by The Hong Kong Institute of Steel Construction. All rights reserved.

## 1. Introduction

Parameter uncertainty is a common problem in practical engineering, which is a significant challenge to the current field of engineering analysis<sup>[1,2]</sup>. Engineering structures, such as steel buildings<sup>[3]</sup>, bridges<sup>[4,5]</sup> and towers<sup>[6-8]</sup>, are commonly simplified as ideal truss structures. Bolted connections are usually regarded as pin or rigid joints. Recent research indicates that the mechanical behavior of bolted connection has a significant impact on the overall structure as the axial load is dominated the member's internal forces. The direct nonlinear analysis method considering joint effects can greatly improve the results which is in accordance with the experimental results very well<sup>[9,10]</sup>. However, the mechanical behavior of bolted connection is greatly influenced by bolt preload force, processing and manufacturing errors and structural gaps between bolts

and bolt holes. There are many uncertainties in the pore structure, interface and load transfer path of bolted connection nodes, which can cause uncertain mechanical behavior of the bolted connection, further complicating the analysis of truss structure. A large number of tower tests and finite element simulations have revealed that the test results of internal forces and nodal displacements deviate greatly from calculated values, mainly because the slip of bolted connections is not taken into account<sup>[11,12]</sup>. As illustrated in Fig. 1, conventional finite element modeling makes it relatively easy to obtain the response from determined structural parameters (i.e., the forward problem). However, it is quite difficult to obtain the uncertain parameters of the structure affected by the bolted joint slip from the structural response (i.e., the reverse problem). Since structural parameters cannot be determined in advance as the uncertainty of structure parameters, finite element calculations cannot be performed.

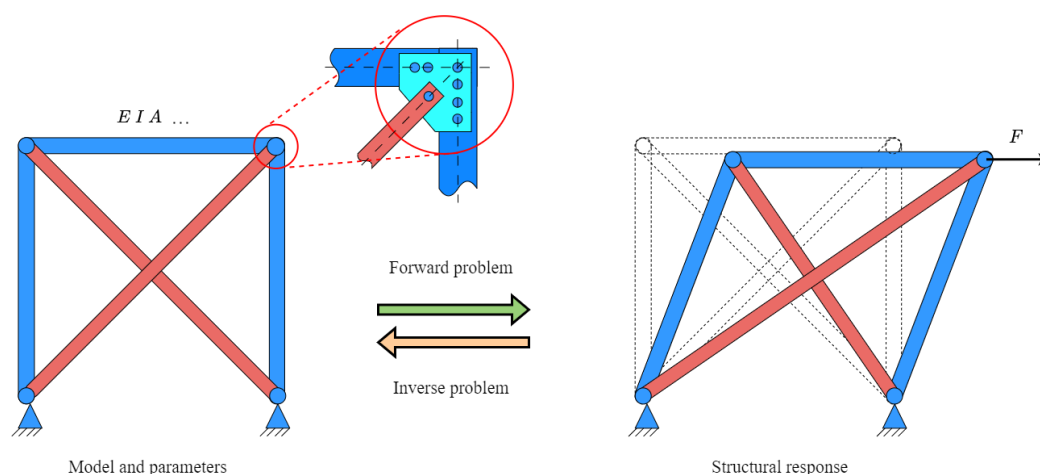


Fig. 1 The forward and inverse problems of truss structure

Structural parameter identification based on structural response is a typical inverse problem in engineering. The traditional method to solve the inverse problem is the Monte Carlo Simulation, which is widely used in probabilistic analysis and simulates the real behavioral characteristics of the actual problem. However, the uncertainty of bolted connection in truss structures cannot be expressed by a single random variable or random field, and a large number of uncertain parameters leads to difficulties in solving the description methods

based on parametric probabilities, which becomes particularly challenging in inversion analysis. Therefore, It is important to put forward more effective methods to resolve the problem of uncertainty analysis and inversion of truss structures.

The inverse problem is a real challenge to solve due to the complexity of practical problems, which makes it difficult to prove the existence, uniqueness, and stability of the solution. The study of inverse problems originated in the

field of mathematics, and has progressed from classical statistical/Bayesian methods<sup>[13]</sup> to cutting-edge deep neural networks<sup>[14,15]</sup>. The classical statistical/Bayesian method uses probabilistic approaches to establish a probability model based on known measurement data. However, this method is time-consuming and inefficient<sup>[16]</sup>. With the development of computer technology, neural networks have emerged as a powerful tool for solving inverse problems. The neural network methods have excellent nonlinear fitting ability and good performance in solving inverse problems in various fields<sup>[17-19]</sup>. However, for engineering problems, it is challenging to convert the actual structure into input features for the neural network model<sup>[20]</sup>.

Graph Neural Network (GNN) is a method of applying deep neural networks to graph structure data, which has powerful graph data processing ability, and brings new vitality to various fields<sup>[21-23]</sup>. In recent years, GNN is integrating with the field of physical structure analysis<sup>[24]</sup>, such as predicting the motion state of objects<sup>[25]</sup>, and shows great potential in engineering applications. However, there are few studies related to the inversion method of engineering structures based on GNN at present. The truss structure, for example, can be represented by nodes and edges, which correspond naturally to the graph structure data. Therefore, it is easy to establish the correspondence between truss structure parameters and graph structure data, and consider whether it is possible to solve the difficult inverse problems in truss structure based on GNN.

In order to solve the inverse problems of uncertain parameters in truss structures, an innovative computational model based on GNN is studied. This approach will provide significant advances in the field of structural engineering, provide greater design optimization and enhanced safety for engineering structures.

## 2. Parametric uncertainty model of bolted connections

In practice, most bolted joints in truss structures such as bridges, lattice towers, etc. are suffering from transverse load. Therefore, the load direction of the bolted joint is perpendicular to the axial of the bolt rod (see Fig.2). The joint slippage is the relative displacement of bolted joints, which occurs under the action of a shear load larger than the friction force between the fastened parts<sup>[11]</sup>. Initially, the shear load in the joint is counteracted by the friction force between the fastened parts, the relative slip does not occur and the clearance between bolt and bolt hole exists. Then, the shear load eventually reaches and exceeds the maximum frictional force between the fastening parts as the external load increases, which will cause relative slip until the available clearance disappears completely. Finally, as the external load is further increased, the bolt will be extruded with the bolt-hole wall, and the bolt-hole wall will experience a complex nonlinear deformation process, which ranges from elastic deformation to plastic deformation and eventual destruction.

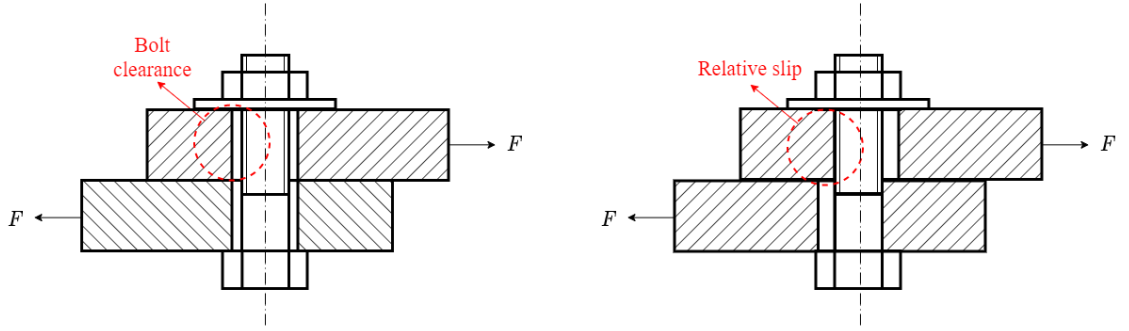


Fig. 2 Bolted joint slippage

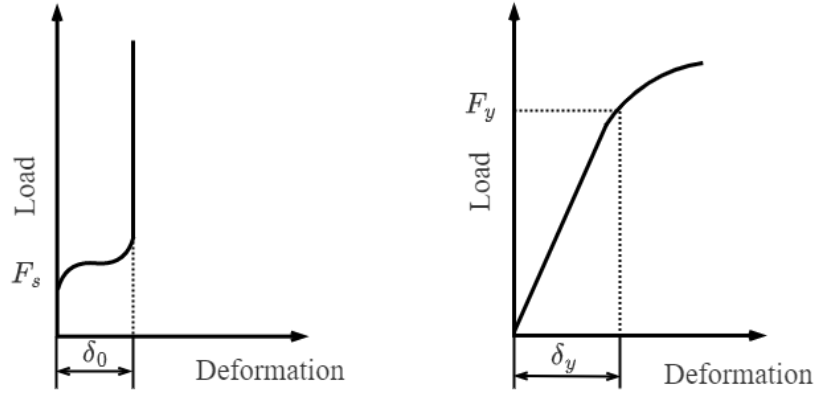


Fig. 3 Joint slippage model

In order to investigate the influence of joint slippage, various numerical models are proposed such as the numerical model<sup>[26]</sup>, parametric model<sup>[27]</sup>, and micro-slip model<sup>[28]</sup>. In this paper, the four parameters joint slippage model is selected, which divide joint slippage processes into clearance filled slip and extrusion deformation slip<sup>[29]</sup> (see Fig.3), the load-deformation relationship can be expressed as:

$$\delta_s = \delta_0 \left[ \frac{F / F_s}{1 + (F / F_s)^n} \right]^m + \alpha_s \delta_y \left( \frac{F}{F_y} \right)^{N_s} + \delta_y \frac{F}{F_y} \quad (1)$$

Where  $\delta_s$  is the total deformation of the joint slip,  $\delta_0$  is the bolt clearance,  $\delta_y$  is the deformation at yield;  $F$  is the external load,  $F_s$  is the critical slip load,  $F_y$  is the yield load;  $m$ ,  $n$ ,  $a_s$  and  $N_s$  are the shape parameters of the curve which can be determined from the tensile tests of bolted joints.

However, due to the complexity of the bolt connection slip process, the bolted joint mechanical behavior can be affected by many uncertainties, such as bolt preload force, processing and manufacturing errors and the bolt hole structure, etc. In truss structures, the bolted joint slippage is inevitable as the

bolt clamping forces are relatively low, which led to the discrepancy between the test results and simulation results<sup>[7,11,29]</sup>. However, these joint slippage effects cannot be determined in advance during the analysis of truss structures because the bolted joint states are not easy to obtain. Most of the currently used truss analysis models ignore the influence of the slip of bolted joints, therefore the member internal forces cannot be accurately obtained.

In order to take joint slippage uncertainties into account, the equivalent reduction method of axial stiffness is adopted. The members in the truss structure are assumed to be in an elastic state during loading. Therefore, the total deformation of the member ( $\delta$ ) is the sum of the joint slip ( $\delta_s$ ) and the elastic deformation ( $\delta_e$ ), expressed as:

$$\delta = \delta_s + \delta_e \quad (2)$$

The elastic deformation of the member is determined by

$$\delta_e = \frac{Fl}{EA} \quad (3)$$



Where  $F$  is the axial force,  $l$  is the length of the member,  $E$  is the elastic modulus, and  $A$  is the cross-sectional area. The axial stiffness of the member is obtained from the formula:

$$K = \frac{F}{\delta} = \frac{EA\delta_e / l}{\delta} = \frac{\delta_e}{\delta} \frac{EA}{l} = \left(1 - \frac{\delta_s}{\delta}\right) \frac{EA}{l} \quad (4)$$

Let  $\eta = 1 - \delta_s / \delta$ , then the axial stiffness is expressed as:

$$K = \eta \frac{EA}{l} \quad (5)$$

Where  $\eta$  is the axial stiffness reduction factor. The uncertainties of the joint slip can be represented by the uncertainties of the axial stiffness reduction factor of the member.

### 3. The inversion method of uncertain parameters

In this paper, the uncertain parameter problem of the truss structure caused by the slip of bolted connections is considered, and an innovative method based

on GNN is proposed to solve the uncertain parameters identification problem based on structural response.

#### 3.1. Graph representation of truss structure

In practice, truss structures are commonly represented visually as a graph consisting of nodes and edges. This representation method is exactly similar to GNN, which is also composed of nodes and edges. Therefore, the graph representation can be easily defined as: graph nodes represent the nodal connections (bolted connections) of the truss, and graph edges represent the members of the truss.

In order to illustrate clearly, a basic truss structure is isolated from the whole structure of the lattice transmission tower as shown in Fig.4. The graph structure of GNN is composed of 4 nodes and 6 edges (there are 12 edges if considering the direction of the edge). The boundary conditions assume as nodes 1 and 2 are free, and nodes 3 and 4 are fixed and fully constrained. A horizontal force is loaded on Node 2. In the presented truss structure model, the uncertainty of diagonal members due to bolted joint slippage is considered, while the other members are defined as deterministic parameters. As shown in Fig.4, the red line and blue line are used to represent the difference in member parameters. The node features and edge features inputted in GNN are defined respectively according to the node parameters and edge parameters, which are listed in Table 1.

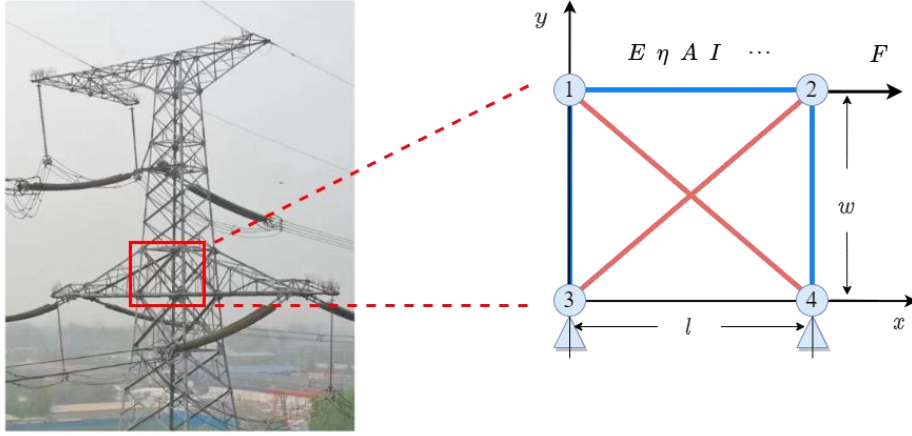


Fig. 4 Graph representation of truss structure

Table 1  
Graph feature coding

Parameter	Data type	Feature description
Node features: $[C_x, C_y, x, y, F_x, F_y, D_x, D_y]$		
$C_x$	int	The constraint of the node in the x direction. 0 represents no constraints, and 1 represents constraints.
$C_y$	int	The constraint of the node in the y direction. 0 represents no constraints, and 1 represents constraints.
$x$	float	Node coordinate in the x direction (m).
$y$	float	Node coordinate in the y direction (m).
$F_x$	float	Node force in the x direction (N).
$F_y$	float	Node force in the y direction (N).
$D_x$	float	Node displacement in the x direction (m).
$D_y$	float	Node displacement in the y direction (m).
Edge features: $[T, E, \eta, A, I]$		
$T$	int	Member type. 0 represents the beam, and 1 represents the rod.
$E$	float	Elastic modulus of member (Pa).
$\eta$	float	Stiffness reduction factor. Randomly obtained within [0, 1].
$A$	float	The cross-sectional area of member ( $m^2$ ).
$I$	float	Cross-sectional moment of inertia ( $m^4$ ).

#### 3.2. Parametrized acquisition of datasets

Considering the high cost of experiments, it is generally difficult to obtain enough experimental datasets of engineering structures. Therefore, numerical simulation methods were used to obtain datasets required for the training of GNN in this paper. The uncertainties of truss structure caused by joint slip can

be represented by the uncertainties of the axial stiffness reduction factor of the member, which is assumed to be randomly varied in the range of [0, 1]. The large datasets of deterministic structural parameters can be acquired by random sampling of axial stiffness reduction factor  $\eta$ . The node displacements can be obtained through finite element simulation to generate the required datasets for the training of GNN. The datasets acquisition process is shown in Fig. 5.

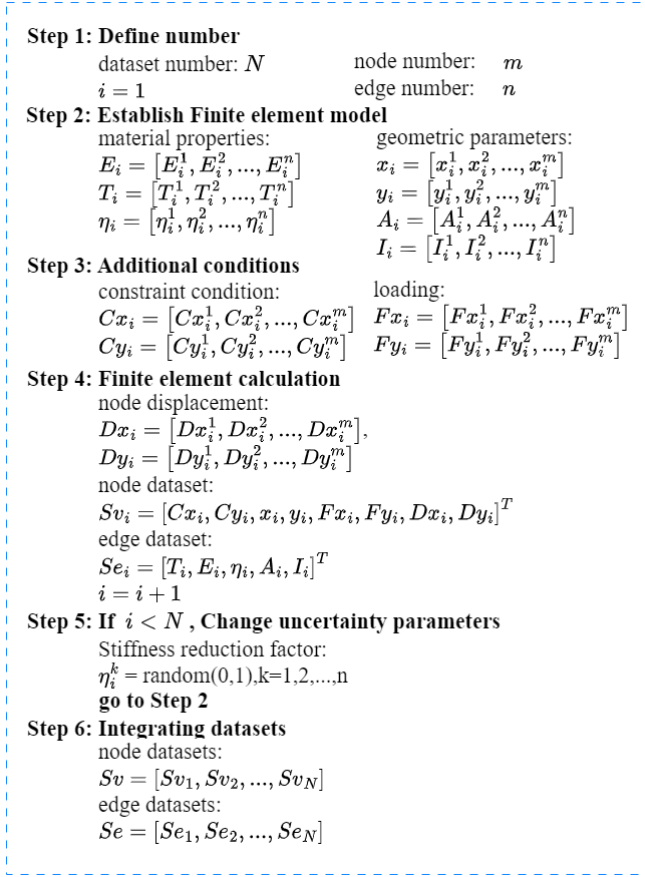


Fig. 5 The datasets acquisition process

Commonly used parameter units, such as modulus of elasticity (GPa), area (mm<sup>2</sup>), and length (mm), need to be converted to international standard units, which leads to great differences in quantitative value. In order to avoid the effect of inconsistent parameter units on feature weights, the feature parameters are normalized as follows:

$$\bar{X} = \frac{X - X_{\min}}{X_{\max} - X_{\min}} \quad (6)$$

### 3.3. The inversion model based GNN

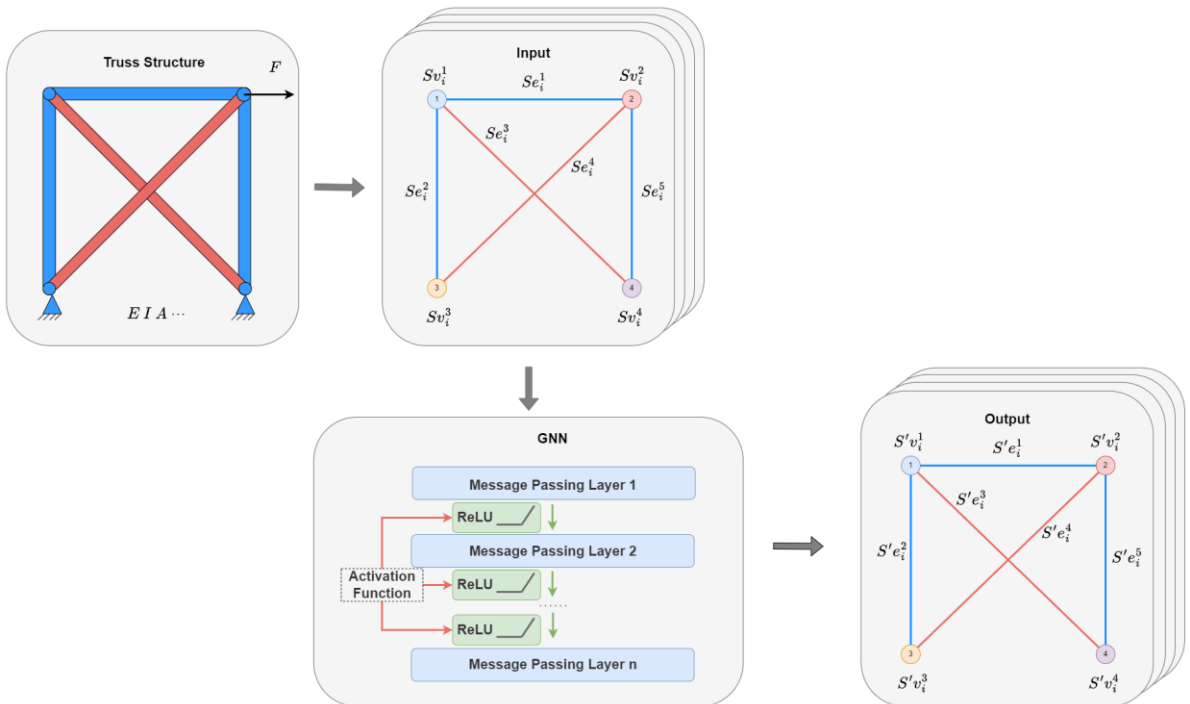


Fig. 6 The GNN-based inversion model

The member internal forces commonly need to be determined by the response of the truss structure in engineering. This problem can be easily conquered by the Finite Element Analysis method (FEA method) for the deterministic analysis model whether it is linear or non-linear. However, the traditional FEA method cannot be effectively solved if the structural parameters are uncertain. This parametric inversion can be challenged based on GNN.

GNN is the method designed to apply deep neural networks to graph-structured data. Compared with general neural networks, GNN can not only deal with non-Euclidean graph structure data but also capture the correlation between adjacent nodes, with strong graph feature mapping capabilities. GNN is a feature learning process on graphs, taking node features and graph structure as input and a new set of node features as output. This process can be expressed as

$$X_{out} = \phi(A, X_{in}) \quad (7)$$

where  $A$  is the adjacency matrix expressing the graph structure,  $X_{in}$  and  $X_{out}$  are the input features and output features respectively, and  $\phi$  is the operator. Importantly, this process only changes the features, not the graph structure.

The framework of the GNN-based inversion model is illustrated in Fig. 6. The general engineering structural parameters cannot be used as the input of the GNN, so the truss structure parameters need to be preprocessed and transformed into graph structure data according to the graph representation method proposed in the previous paper. Then the adjacency matrix  $A$  and node features  $X$  representing the graph structure data are taken as inputs, and the adjacent node features are aggregated and updated through multiple message passing networks. In order to better mine relevant features and alleviate the overfitting problem, the ReLU activation function is used. The function expression is as follows:

$$\text{ReLU}(x) = \max(0, x) \quad (8)$$

Finally, a new set of node features is output for parameter inversion. It should be noted that the graph structure can be any spatial structure, and both the edge features and graph features can be included in the input node features. Therefore the presented inversion model is appropriate for any other truss structure analysis.

The critical process of GNN is the design of the message passing layer. A message passing layer consists of three update operators: edge update, node update, and global update. In the following description,  $u$  represents the graph features,  $v$  represents the node features and  $e$  represents the edge features.

During the edge update step, the edge update function  $\phi^e$  generates new edge features by computing graph features, adjacent node features and edge features. The edge update can be expressed as:

$$e' = \phi^e(e, v, u) \quad (9)$$

In the node update step, it is necessary to aggregate the adjacent edge features of each node through an aggregation function  $\rho^{e \rightarrow v}$  as each node may have multiple edges. Then node update function  $\phi^v$  generates new node features by computing graph features, own node features and aggregated edge features. The node update can be expressed as:

$$v' = \phi^v(\rho^{e \rightarrow v}(e'), v, u) \quad (10)$$

In the global update step, edge features are aggregated globally through aggregation functions  $\rho^{e \rightarrow u}$ , and node features are aggregated globally through aggregation functions  $\rho^{v \rightarrow u}$  according to specific global problems. Then global update function  $\phi^u$  generates new graph features by computing graph features, aggregated node features and aggregated edge features. The global update can be expressed as:

$$u' = \phi^u(\rho^{e \rightarrow u}(e'), \rho^{v \rightarrow u}(v'), u) \quad (11)$$

For the inverse problems of uncertain parameters for truss structure, it can be seen that member axial stiffness parameters belong to edge features, and node displacement parameters belong to node features. Therefore, the message passing in the truss structure only occurs between node and edge features, and the global update is unnecessary. In the edge update step, the features of each edge are updated by a multilayer perceptron (MLP) network. The adjacent node features and the original edge features are spliced as the input, and the new edge features are obtained as the output. It should be noted that the new node feature dimension is consistent with the original node feature dimension to ensure that the new node feature can be used as input again. In the node update step, the MLP network is also used to update each node. The difference is that edge feature aggregation steps need to be added in the update. Here the SUM aggregation function is used to aggregate all edge features connected to the same node. The message passing layer constructed is illustrated in Fig. 7. It should be noted that in the message passing layer, the update function  $\phi$  needs to be trained and learned, and the aggregation function  $\rho$  is selected independently.

For simple truss inversion analysis, parameter inversion can be achieved by using a single message passing layer. It should be noted that for GNN models, the over-smoothing problem can lead to degradation of the model performance as the number of message passing layers increases.

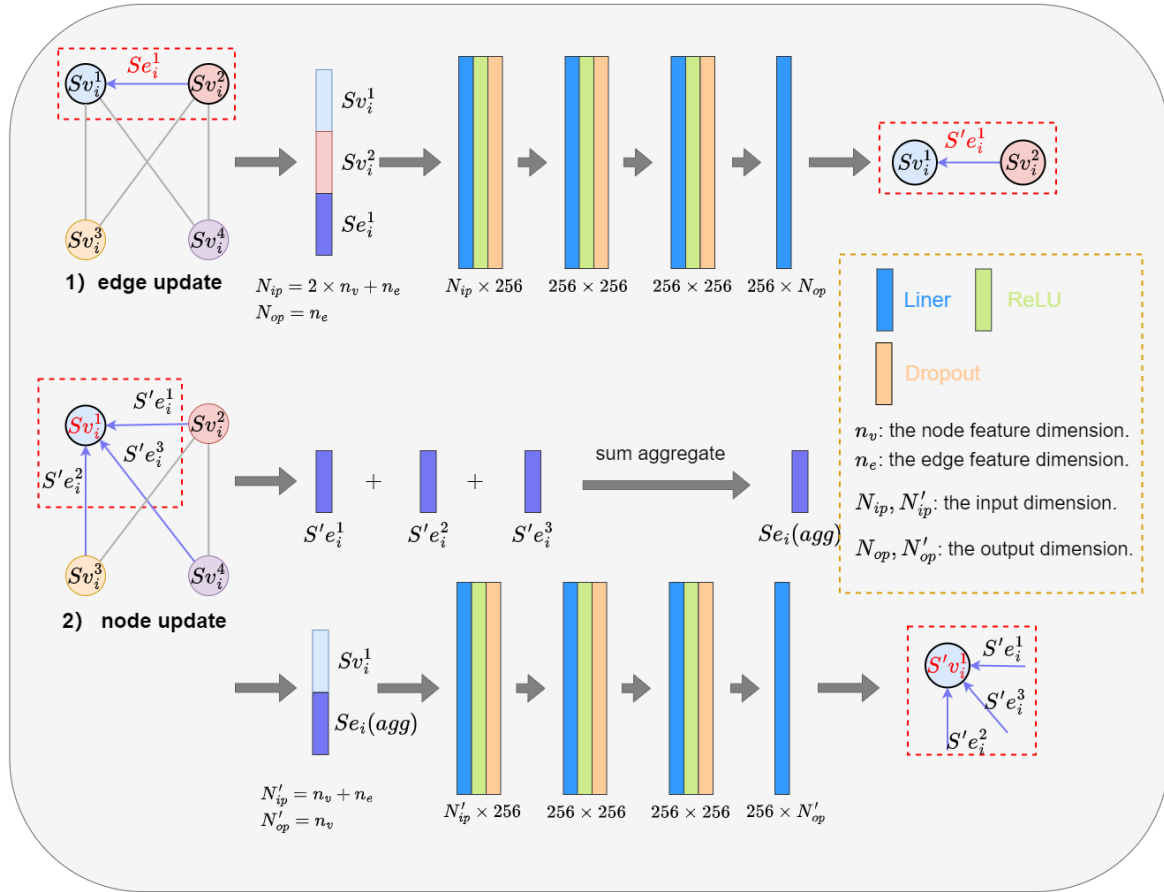


Fig. 7 The message passing mechanism

### 3.4. Model training and optimization

In GNNs training, the input datasets are shuffled to avoid the influence of the order of input datasets on feature learning. The Adam optimizer is selected for training. The inversion problem studied in this paper is to obtain the member stiffness and inner forces parameters from the node displacement response parameters. Therefore, the elastic modulus parameters in the edge features need to be initialized to 0 in the input features, while the actual elastic modulus parameters are used as the target labels. The inversion error is defined as follows:

$$E_{error} = \sqrt{\frac{\sum (E_{out} - E_{target})^2}{n}} \times 100\% \quad (12)$$

Where  $E_{out}$  is the output stiffness parameters of the inversion model,  $E_{target}$  is the actual stiffness parameters, and  $n$  is the number of the output stiffness parameters.

### 3.5. Case study

In order to validate the computational effectiveness of the inverse model presented in this paper, the numerical tests of a basic planar truss structure are analyzed as shown in Fig. 4. The implementation steps are as follows:

#### (1) Graph representation of the truss structure

The graphical representation of the truss structure studied in this paper is shown in Fig. 8, the geometry and physics parameters of the truss structure are listed in Table 2, and the defined features of the corresponding graph structure are listed in Table 3.

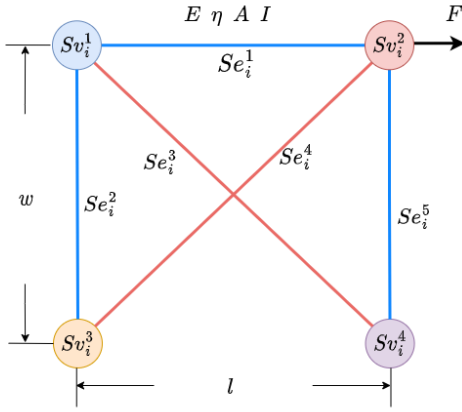


Fig. 8 Graphical representation of the studied trusses

**Table 2**  
The truss structure parameters

$L$ (m)	$W$ (m)	$A$ (m <sup>2</sup> )	$I$ (m <sup>4</sup> )	$E$ (GPa)	$F$ (kN)	$\eta$
1	1	$7.854 \times 10^{-3}$	$4.9087 \times 10^{-6}$	206	10	Random(0,1)

**Table 3**  
The defined features of graph structure

	Feature number	Feature description
Node feature	$Sv^1$	$[0, 0, 0, 1, 0, 0, Dx^1, Dy^1]$
	$Sv^2$	$[0, 0, 1, w, F, 0, Dx^2, Dy^2]$
	$Sv^3$	$[1, 1, 0, 0, 0, 0, Dx^3, Dy^3]$
	$Sv^4$	$[1, 1, 1, 0, 0, 0, Dx^4, Dy^4]$
Edge feature	$Se^1$	$[0, \eta^1 \times E, A, I]$
	$Se^2$	$[0, \eta^2 \times E, A, I]$
	$Se^3$	$[1, \eta^3 \times E, A, I]$
	$Se^4$	$[1, \eta^4 \times E, A, I]$
	$Se^5$	$[0, \eta^5 \times E, A, I]$

## (2) Parametric acquisition of datasets

In order to meet the characteristics of difficult data acquisition in engineering practice, 1000 sets of numerical simulation datasets are obtained according to the computational flow shown in Fig. 5. To avoid the effect of inconsistent parameter units on feature weights, the features are normalized by Equation (6) and then involved in the GNN model training. To ensure the

efficiency of the training process and the correctness and accuracy of the training results, the datasets are divided into training sets, test sets and validation sets in the ratio of 8:1:1.

## (3) Construction of GNN-based inversion model

The inverse model is constructed according to Fig. 6, and the message passing network is constructed according to Fig. 7. The input features of the network are first preprocessed by initializing the stiffness feature in the edge features to 0, while the stiffness true values are used as the target label. The input features are the preprocessed node features and edge features:

$$\begin{aligned} Sv &= [Cx, Cy, x, y, Fx, Fy, Dx, Dy] \\ Se &= [T, 0, A, I] \end{aligned} \quad (13)$$

The inverse model contains two message passing layers, and then the edge features are output through a linear transformation layer. In the message passing layer, the message passing is realized through edge update and node update in turn. The update process is as follows:

$$\begin{aligned} Se^{(1)} &= \phi^e \left( Se^{(0)}, Sv^{(0)} \right) \\ Sv^{(1)} &= \phi^v \left( \rho^{e \rightarrow v} \left( Se^{(1)} \right), Sv^{(0)} \right) \\ Se^{(2)} &= \phi^e \left( Se^{(1)}, Sv^{(1)} \right) \\ Sv^{(2)} &= \phi^v \left( \rho^{e \rightarrow v} \left( Se^{(2)} \right), Sv^{(1)} \right) \end{aligned} \quad (14)$$

The updated edge features are then passed through a linear transformation layer to obtain the final output

$$Se_{out} = Linear \left( Sv^{(2)} \right) = [T^{(2)}, E_{out}, A^{(2)}, I^{(2)}] \quad (15)$$

## (4) Model training and optimization

The model optimization uses Adam Optimizer with an initial learning rate of  $1 \times 10^{-5}$ , and the learning rate decreases with the training epoch. The output error is calculated by Equation (12). To reduce the hardware requirements for inversion training, this training was performed using only an i5-10400 CPU. Finally, the model parameters are optimized by the back propagation algorithm until the model results meet the requirements.

The convergence of different data sets during the training process is shown in Fig. 9. It can be seen in the figure that the model converges rapidly during the training process, and the inversion accuracy is stable at about 99%. In particular, the model training accuracy is higher than 0.978 as can be seen in the local enlargement of the first 50 epochs, and the model has a good inversion performance with less training volume. Therefore, the inversion results fully satisfy the engineering calculation requirements.

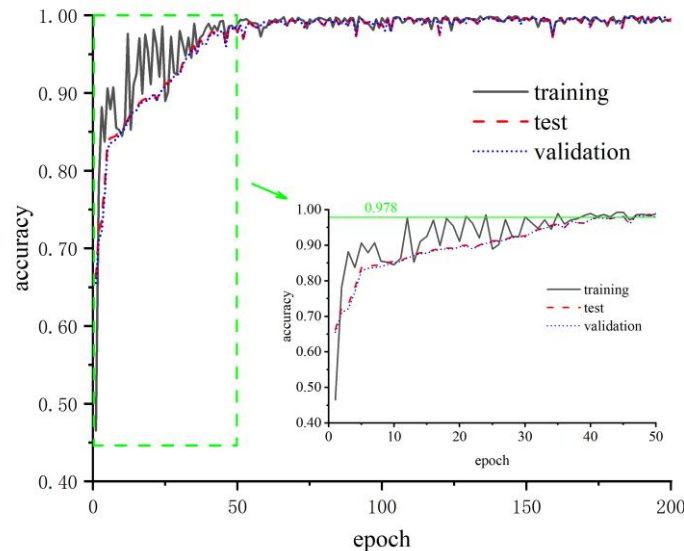


Fig. 9 The convergence curves of different datasets



## 4. Discussion

### 4.1. Performance of inversion model

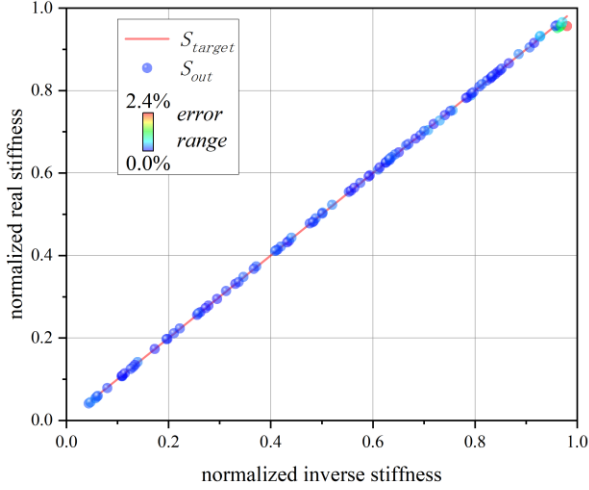
In order to study the performance of the inversion model, the GNN model trained over 200 epochs is used to solve the inverse problem of uncertain stiffness of the truss structure. Since the graph structure in the GNN considers the direction of edges, the final result of the edge stiffness values is obtained by averaging the stiffness values of two directions on the same edge. The inversion results of member  $Se_i^3$  (see Fig. 8) are shown in Fig.10, the inversion results of member  $Se_i^4$  are illustrated in Fig. 11, and the inversion results of the

other members are illustrated in Fig. 12. The stiffness of the member is calculated according to the following formula:

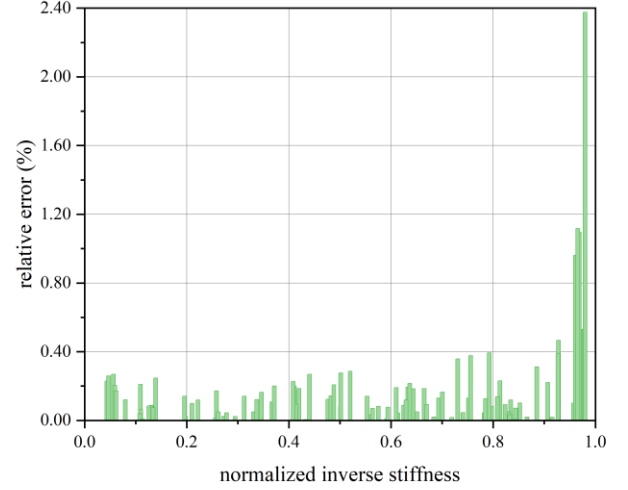
$$S = EA / l \quad (16)$$

The relative error is calculated according to the formula:

$$RE = |S_{target} - S_{inverse}| \times 100\% \quad (17)$$

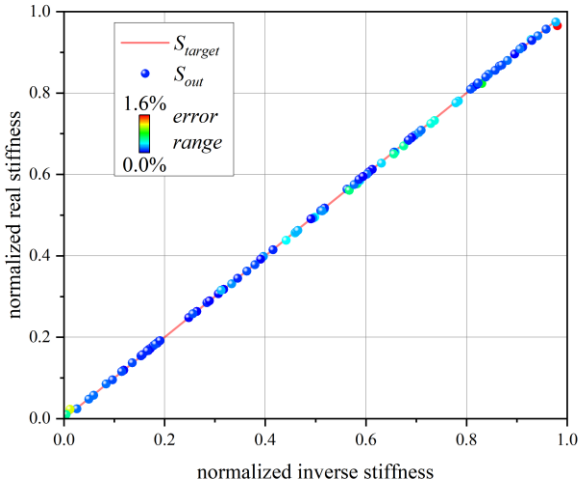


(a) Inverse results

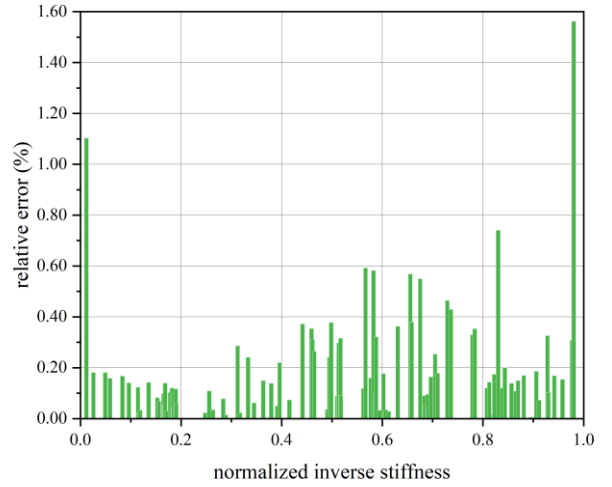


(b) Inverse error

Fig. 10 Inversion results of member  $Se_i^3$

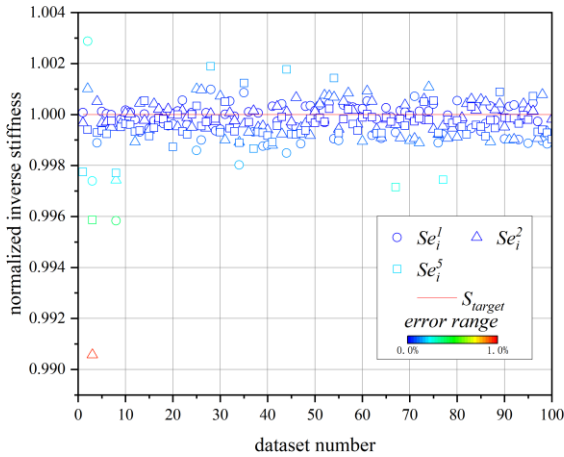


(a) Inverse results

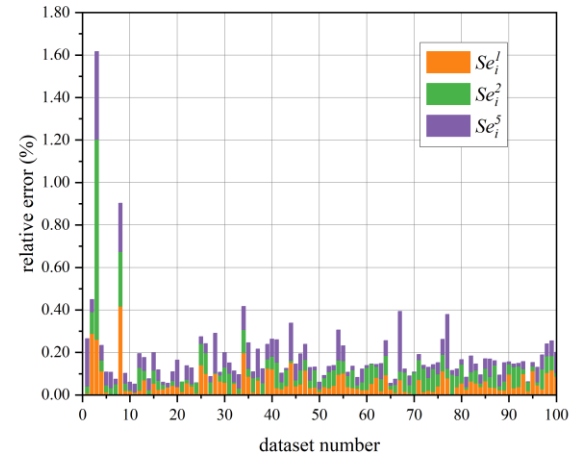


(b) Inverse error

Fig. 11 Inversion results of member  $Se_i^4$



(a) Inverse results



(b) Inverse error

Fig. 12 Inversion results of other members

As can be seen in Fig. 10(a) and Fig. 11(a), the red line represents the normalized target value, the ball represents the normalized inversion output, and the colors of the ball represent the error range between the output and the target. The relative error in Fig. 10(b) and Fig. 11(b) is obtained from Equation (16). In Fig. 12(a), the inversion results of 100 datasets are indicated by different symbols and colors. The colors represent the error range of the inversion results. In Fig. 12(b), the relative error and error accumulation results of the inversion are illustrated.

It can be seen in Fig.10(a) and Fig.11(a) that the inverse stiffness results are almost in a straight line with the real stiffness, and the relative error is basically within 1%, which proves that the model achieves the stiffness inversion of the truss structure with good results. As can be seen in Fig. 10(b) and Fig. 11(b), the overall inversion error of the inversion model is very small, with only a few outliers with relative errors greater than 1%, which occurs when the member stiffness values close to 0 or 1. In addition, the inversion accuracy of the model is significantly higher in the moderate stiffness (between 0 and 1), which commonly represent semi-rigid in structure analysis. Since most of the member stiffness reduced due to bolt slip in the actual engineering structure is in the range of 0.3-0.5<sup>[11]</sup>, this inversion model will perform better in practical engineering applications.

As can be seen in Fig.12, the inversion errors of most of the other members are within 0.2%, which is much smaller than the inversion errors of

members  $Se_i^3$  and  $Se_i^4$ . It proves that the inversion of the fixed stiffness parameter is better than that of the variable stiffness parameter. However, there are also outliers in the stiffness inversion results, which are caused by the extreme stiffness of members  $Se_i^3$  and  $Se_i^4$ .

In conclusion, the inversion model based on GNN can complete the inversion of the uncertain stiffness parameters of the truss structure with high precision, which meets the requirement of engineering accuracy. Meanwhile, the presented model performs better when member stiffness is moderate in actual structural parameters.

#### 4.2. Data requirements of the inversion model

In many engineering problems, there is a lack of experimental data due to technical or economic reasons. Therefore, it is necessary to reduce the number of datasets needed for training and to improve the generality of the model. For this purpose, training datasets of size  $N=100, 200, 400, 800$  are studied for model training. The 100 sets of displacement-stiffness datasets are randomly obtained as the validation datasets. During the training process, the inversion accuracy of the validation set with different datasets sizes is shown in Fig. 13. The inversion error of the model trained over 200 epochs for different datasets is shown in Table 4.

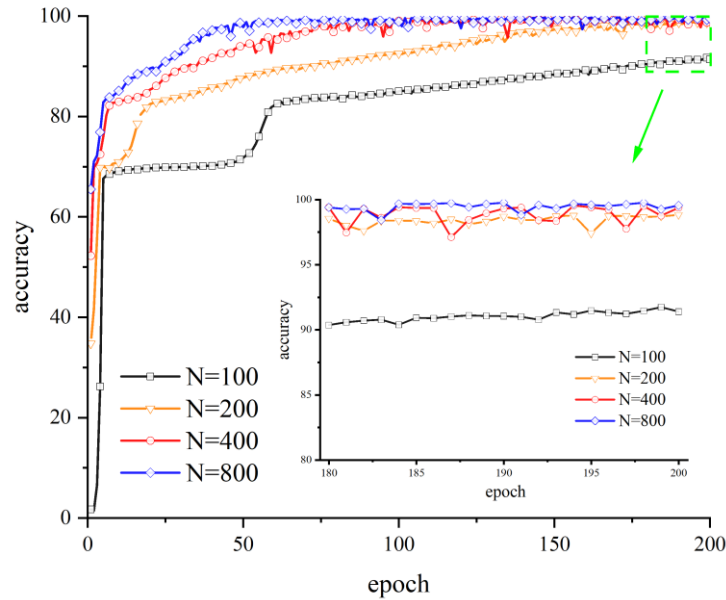


Fig. 13 The inversion accuracy of different training dataset sizes

**Table 4**  
The inversion error for different datasets

training data sizes	training	test	validation
N=100	5.11%	8.86%	8.60%
N=200	2.06%	1.10%	1.17%
N=400	0.66%	0.63%	0.62%
N=800	0.74%	0.44%	0.43%

It can be seen in Fig. 13 that the inversion accuracy curves for different training dataset sizes increase rapidly within the first 50 epochs, which indicates that the inversion method is effective for different training dataset sizes. As the size of datasets increases, the accuracy can be improved in stages. Therefore, the more data, the faster the training speed, and the better the performance. It also can be found that the size of the training datasets has less impact on the degree of accuracy improvement when the accuracy is higher than 99%. For example, when the dataset size increases from 100 to 200, the inversion error decreases from 8.60% to 1.17%. When the size of the dataset increases from 200 to 400, the inversion error only decreases from 1.17% to 0.62%. The relationship between inversion error (IE) and datasets sizes  $N$  is approximately  $IE \propto N^{-1.4}$ . Therefore, a suitable dataset size can be obtained by pre-training to avoid wasting resources due to too little training data or too much data in the project.

As can be seen in Table 4, when  $N=100$ , the training data set is insufficient in this simple truss structure. The inversion error of the test set and validation set is larger than the training set, and the inversion error is around 10%. However, when  $N=200$ , the inversion error of the test and validation sets is smaller than the training set, which indicates that the model has learned the mapping relationship of truss structure inversion. Compared with  $N=400$  and  $N=800$ , the inversion error of the validation set decreases from 0.62% to 0.43%, and the inversion performance of the model does not improve significantly, but the training time increases and resources are wasted. In summary, the inversion method of uncertain parameters for truss structure based on GNN requires a smaller dataset size and is more suitable for difficult data acquisition in engineering.

#### 4.3. Integration of inversion method with engineering applications

There are various uncertain factors in practical engineering. In order to accurately analyze and solve engineering problems, various uncertainties need to be considered. It will become very difficult to solve the inverse problem by traditional analysis methods with the increase of uncertain factors. While these problems can be easily solved by the inversion method proposed in this paper. This is because all uncertainty factors can correspond to the features of the graph structure. For example, the uncertainty of the structure itself corresponds to the node features and edge features, while the external uncertainty factors correspond to the graph features. In the inversion method of uncertain

parameter based GNN, the study of multiple uncertainties corresponds to the study of the mapping relationship of multiple features. To verify the feasibility of simultaneous inversion of multiple uncertain parameters, uncertain axial force features were added to the original graphical neural network model. It is shown that the model can realize the simultaneous inversion of nodal displacements on axial force and stiffness parameters, but the inversion accuracy will decline. It will be a further research direction to solve the inversion problem of multiple uncertain factors in specific engineering problems.

On the other hand, the actual engineering structure is more complex than the simple truss structure studied in this paper. The more complex the structure is, the more difficult it is to analyze by traditional finite element methods. However, this problem can be perfectly solved by the inversion method, due to the powerful ability of GNN to process graph data. In GNN models, complex structures only increase the number of nodes and edges, corresponding to increasing the dimension of node features and edge features. Therefore, the inversion method can be applied to all kinds of complex space structures.

## 5. Conclusions

The inverse problem in engineering has been extensively studied, but remains challenging to fully solve. However, with the integration of machine learning and engineering, the GNN method offers a promising solution to the inverse problem. The inversion method proposed in this paper not only allows

for easy integration of the network model with the structural model but also significantly improves the accuracy and efficiency of the inversion of uncertain parameters. The main conclusions are as follows:

(1) The feature encoding method for converting truss structure to graph representation of GNN is defined. The connection relations, dimensional parameters, material properties and constraints of the truss structure are encoded as graph feature expressions, and the mapping conversion between truss structural analysis and GNN graph representation is realized.

(2) The inversion model proposed in this study effectively identified the uncertain parameters of the truss structure, which considers the effect of bolt slip on the uncertain stiffness parameters and uses the structural displacement response for inversion. The accuracy can meet the requirement of engineering.

(3) The inversion method based on GNN requires fewer data, which is suitable for the characteristics of difficult data acquisition in engineering, and it also has good inversion performance with the limited data set.

(4) The inversion method has great potential for application in engineering analysis and further research value in the combination of engineering analysis, which will become a new direction for exploring engineering structural analysis methods.

## Acknowledgement

This study has been supported by the "Three Three Three Talent Project" in Hebei Province(C20231056).

## Reference

- [1] Gallet A., Rigby S., Tallman T. N., et al., "Structural engineering from an inverse problems perspective", *Proceedings. Mathematical, Physical and Engineering Sciences*, 2022, Vol. 478, No. 2257, pp. 1-37.
- [2] Zhao Z. W., Liu H. Q., Liang B., et al., "Influence of random geometrical imperfection on the stability of single-layer reticulated domes with semi-rigid connection", *Advanced Steel Construction*, 2019, Vol. 15, No. 1, pp. 93-99.
- [3] Srinivasan K., Selvakumar K., "Comparative study of pre-engineered building and space truss building with different span", *Indian Journal of Engineering and Materials Sciences*, 2022, Vol. 29, No. 4, pp. 428-431.
- [4] Fairclough H. E., Gilbert M., Pichugin A. V., et al., "Theoretically optimal forms for very long-span bridges under gravity loading", *Proceedings. Mathematical, Physical and Engineering Sciences*, 2018, Vol. 474, No. 2217, pp. 1-21.
- [5] He G., Shao X. D., Chen Y. B., et al., "Preliminary design of a steel-UHPFRC composite truss arch bridge and model tests of K-joints", *Journal of Bridge Engineering*, 2022, Vol. 27, No. 10, 04022090.
- [6] Grzywnski M., "Optimization of spatial truss towers based on Rao algorithms", *Structural Engineering and Mechanics*, 2022, Vol. 81, No. 3, pp. 367-378.
- [7] Jiang W. Q., Liu Y. P., Chan S. L., Wang Z. Q., "Direct analysis of an ultrahigh-voltage lattice transmission tower considering joint effects", *Journal of Structural Engineering*, 2017, Vol. 143, No. 5, pp.04017009.1-04017009.14.
- [8] Wang F. Y., Xu Y. L., Zhan S., "Concurrent multi-scale modeling of a transmission tower structure and its experimental verification", *Advanced Steel Construction*, 2017, Vol. 13, No.3, pp. 258-272.
- [9] Hussain A., Liu Y. P., Chan S. L., "Finite element modeling and design of single angle member under bi-axial bending", *Structures*, 2018, Vol. 16, pp. 373-389.
- [10] Chan S. L., Fong M., "Experimental and analytical investigations of steel and composite trusses", *Advanced Steel Construction*, 2011, Vol. 7, No. 1, pp. 17-26.
- [11] An L. Q., Wu J., Jiang W. Q., "Experimental and numerical study of the axial stiffness of bolted joints in steel lattice transmission tower legs", *Engineering Structures*, 2019, Vol. 187, pp. 490-503.
- [12] Li J. X., Cheng J. P., Zhang C., et al., "Seismic response study of a steel lattice transmission tower considering the hysteresis characteristics of bolt joint slippage", *Engineering Structures*, 2023, Vol. 281, 115754.1-115754.15.
- [13] Habek M., "Bayesian approach to inverse statistical mechanics", *Physical Review E*, 2014, Vol. 89, No. 5, pp. 052113.1-052113.7.
- [14] Adler J., Öktem O., "Solving ill-posed inverse problems using iterative deep neural networks", *Inverse Problems*, 2017, Vol. 33, 124007.
- [15] Kamyab S., Azimifar Z., Sabzi R., Fieguth P., "Deep learning methods for inverse problems", *PeerJ. Computer Science*, 2022, Vol. 8, e951.
- [16] Han X., Liu J., Chen J. L., "A manifold learning method for inverse problems with structural multi-source uncertainties", *Chinese Journal of Computational Mechanics*, 2021, Vol. 38, No. 4, pp. 523-530.
- [17] Keshavarzadeh V., Kirby R.M., Narayan A., "Variational inference for nonlinear inverse problems via neural net kernels: Comparison to Bayesian neural networks, application to topology optimization", *Computer Methods in Applied Mechanics and Engineering*, 2022, Vol. 400, pp.1-35.
- [18] Jagtap A.D., Mao Z.P., Adams N., Karniadakis G.E., "Physics-informed neural networks for inverse problems in supersonic flows", *Journal of Computational Physics*, 2022, Vol. 466, pp. 1-19.
- [19] Raissi M., Perdikaris P., Karniadakis G.E., "Physics-informed neural networks: A deep learning framework for solving forward and inverse problems involving nonlinear partial differential equations", *Journal of Computational Physics*, 2019, Vol. 378, pp. 686-707.
- [20] Wang C., Fan J. S., "A general intelligent computation framework for structural responses in civil engineering based on deep learning", *Journal of Building Structures*, 2023, Vol. 44, No. 1, pp. 259-268.
- [21] Battaglia P. W., Hamrick J. B., Bapst V., et al., "Relational inductive biases, deep learning, and graph networks", 2018, ArXiv Preprint ArXiv: 1806.01261.
- [22] Fout A., Byrd J., Shariat B., et al., "Protein interface prediction using graph convolutional networks", *In Proc. of NIPS*, 2017, Vol. 30, pp. 6530-6539.
- [23] Hamaguchi T., Oiwa H., Shimbo M., et al., "Knowledge transfer for out-of-knowledge-base entities: A graph neural network approach", *In Proc. of IJCAI*, 2017, pp. 1802-1808.
- [24] Battaglia P., Pascanu R., Lai M., et al., "Interaction networks for learning about objects, relations and physics", *In Proc. of NIPS*, 2016, Vol. 29, pp. 4502-4510.
- [25] Sanchez A., Heess N., Springenberg J. T., et al., "Graph networks as learnable physics engines for inference and control", *In Proc. of ICLR*, 2018, Vol. 80, pp. 4467-4476.
- [26] Zhao Z. W., Liang B., Liu H. Q., Li Y. J., "Simplified numerical model for high-strength bolted connections", *Engineering Structures*, 2018, Vol. 164, pp. 119-127.
- [27] Wang D., Zhang Z. S., "A four-parameter model for nonlinear stiffness of a bolted joint with non-Gaussian surfaces", *Acta Mechanica*, 2020, Vol. 231, No. 5, pp. 1963-1976.
- [28] Li C. F., Jiang Y. L., Qiao R. H., Miao X. Y., "Modeling and parameters identification of the connection interface of bolted joints based on an improved micro-slip model", *Mechanical Systems and Signal Processing*, 2021, Vol. 153, pp. 1-16.
- [29] Jiang W. Q., Wang Z. Q., McClure G., et al., "Accurate modeling of joint effects in lattice transmission towers", *Engineer Structure*, 2011, Vol. 33, No. 5, pp. 1817-27.

# AN EXPERIMENTAL STUDY ON SEISMIC PERFORMANCE OF STEEL COMPOSITE BEAM-COLUMN RIGID JOINT AND BUCKLING RESTRAINED KNEE-BRACED JOINT

Feng Xu <sup>1,\*</sup>, Zhe Yuan <sup>1</sup>, Na Liu <sup>1</sup>, Zhen-Xing Li <sup>1,2</sup>, Lian-Guang Jia <sup>1</sup> and Wei Xu <sup>1</sup>

<sup>1</sup> School of Civil Engineering, Shenyang Jianzhu University, Shenyang 110168, China

<sup>2</sup> China Southern Airlines Co., Ltd., Shenyang Maintenance Base, Shenyang 110169, China

\* (Corresponding author: E-mail: cefxu@sjzu.edu.cn)

## ABSTRACT

This paper evaluates the seismic performance of conventional steel composite beam-column rigid joints, and a novel buckling restrained knee-braced joint (BRKBJ), considering the impact of the floor slab. A series of quasi-static comparative tests were conducted to analyze the failure mode, load-bearing capacity, hysteresis performance, and ductility of both types of joints. Our findings revealed that the hysteretic curve of the BRKBJ exhibits a robust and shuttle-like shape, suggesting an adequate energy dissipation performance. However, its yield displacement is relatively small. Conversely, there is a marginal increase in the yield displacement of the beam and column, along with a significant rise in the yield load when compared to the rigid joint. The ultimate load-bearing capacity increases by 32.6%, and the displacement under this ultimate load decreases by 19.2%. Furthermore, the equivalent viscous damping coefficient and the ductility coefficient see an increase of 14.5% and 21.6%, respectively. When damage occurs to the joint, the buckling restrained knee brace helps shift the plastic hinge outwards, safeguarding the beam-column joint. It was also observed that the impact of the buckling restrained knee brace on the hysteretic behavior of the composite beam-column rigid connection at the beam end during the tension phase is notably more than during the compression phase. The presence of a floor has minimal effect on the BRKBJ.

Copyright © 2023 by The Hong Kong Institute of Steel Construction. All rights reserved.

## ARTICLE HISTORY

Received: 27 November 2022  
Revised: 29 June 2023  
Accepted: 27 August 2023

## KEYWORDS

Steel structure;  
Combined beam-column joint;  
Buckling restrained knee brace;  
Quasi-static test;  
Seismic performance

## 1. Introduction

Buckling restrained knee-braced joint (BRKBJ) is a new type of joint installed near the joint of steel beam and frame column. Moreover, the buckling restrained sleeve is placed outside to prevent its buckling instability. The core plate of the knee brace is composed of a low-yield-point steel plate. Under a small earthquake load, the knee brace can improve the lateral stiffness of the structure and meet the lateral displacement requirements of steel structural systems. Under a large earthquake load, the knee brace core plate yields before the beam-column main component and dissipates the seismic energy through its plastic deformation with no damage to the main component. Thus, it overcomes the weakness of the traditional design. Additionally, the BRKBJ of a steel frame structure has the advantages of large stiffness and good ductility. A buckling restrained knee brace (BRKB) is small, easy to replace and repair after damage, and can be assembled on site. Note that a BRKB can be used as lateral force resistance and energy dissipation component in the reinforcement and reconstruction of existing steel structures.

BRKBs of steel frames and joints have been studied theoretically and experimentally. Hsu and Li [1] studied the steel frame with an I-shaped steel knee brace. The results indicate that incorporating a knee brace enhances the load-bearing capacity of steel frame structures, although out-of-plane instability remains a significant concern. Junda et al. [2] investigated the seismic behavior of hinged steel structures with viscous damping knee brace joints. The results show that the viscous damping knee brace can remarkably improve the energy dissipation capacity of the frame. Yin et al. [3] proposed a double-tube BRKB system that can be employed in steel frame structures. This knee-braced system is founded on a cast steel connection. The author demonstrated the advantages of using a ductile cast steel material to enhance the energy dissipation of the buckling restrained brace. Chen et al. [4] analyzed the energy dissipation performance of a BRKB in bridge engineering, concluding that it effectively mitigates earthquake damage. Zhou [5,6] studied the angle, length, stiffness, and other parameters of the knee brace and obtained a more rational layout form of the knee brace. Conti et al. [7] introduced a design method focused on the overall collapse mechanism of seismic knee-braced frames. Li et al. [8] first proposed the knee braced frame system. This system is a new type of energy-consuming braced frame system, which has the advantages of large stiffness, low cost, simple repair and strong deformability. Under the action of medium or large earthquakes, the knee brace first yields and consumes energy. At this time, the main body of the beam and column is still in the elastic stage, so that the main body of the structure is not destroyed and easy to replace after the earthquake. Ji K H [9] carried out experiments and finite element simulation. The results show that the knee brace has serious plastic deformation and the beam-column body is not damaged at this time, which verifies that the energy-consuming knee brace has good ultimate bearing capacity, elastic stiffness,

ductility and hysteresis performance. H.-L.Hsu [10] carried out low cyclic quasi-static test on buckling restrained knee brace steel frame. The test results show that the arrangement of knee brace in steel frame structure can obviously improve the strength and stiffness of the structure, and make the structure have good deformation ability and energy dissipation ability, which changes the performance of traditional steel frame. Jia et al. [11] executed a design experiment to study a buckling-restrained brace composite frame system. The outcomes demonstrate that installing braces markedly improves the lateral stiffness, ultimate load-bearing capacity, and energy dissipation performance of the composite frame. Xie et al. [12] performed reverse loading tests on sandwich buckling restrained brace specimens with varying gaps. The test results confirmed that the structure possesses stable hysteretic performance and energy dissipation capacity, aligning with the specific values outlined in AISC2010. The compressive strength adjustment coefficient increases as the gap widens. However, the maximum number of cycles under large axial strain sees a significant reduction, leading to a decrease in energy dissipation capacity. Xu et al. [13–15] analyzed the buckling restrained knee-braced steel frame under unidirectional static and low cyclic loads. Xu et al. performed the modal and dynamic time-history analyses under three different seismic waves. The results show that the buckling restrained knee-braced steel frame has good seismic performance, and the arrangement of knee brace can effectively reduce structures' seismic response.

Following Refs. [16–25], the present paper studies the influence of BRKBs on the performance and failure mechanism of steel frame composite beam-column joints considering the floor effect. Thus, a BRKBJ and an ordinary beam-to-column rigid joint (BTCRJ) were selected for quasi-static tests under low cyclic loading and seismic performance analysis.

## 2. Experiment description

### 2.1. Specimen dimension design

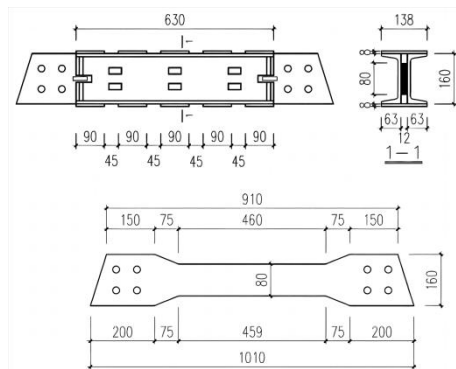
In this experiment, the steel frame under horizontal seismic load was taken as the prototype and the composite beam-column rigid joint in the frame was selected as the experimental model. The distance between column inflection points, i.e., column height plus the distance between column's upper and lower hinge supports, is 2300 mm. The middle inflection point of the beam span is 1660 mm away from the outer edge of the endplate. The size of beam and column of the joints are H 350 × 172 × 7 × 12 mm, and H 300 × 300 × 12 × 16 mm, respectively. The lengths of the column and beam are 1780 mm and 2320 mm, respectively. The concrete floor is C30 with thickness and width of 70 mm and 1020 mm, respectively. The internal reinforcement is double-layer and double-direction, and HRB400 steel bars with 6mm@100 are used for longitudinal and transverse reinforcements. The stud is 16 cylindrical head stud,



Technical drawing of a mechanical assembly (Fig. 1.1) showing a cross-section of a shaft with a pulley and a gear. The drawing includes dimensions for the shaft diameter (220), pulley diameter (260), gear diameter (260), and various other components and dimensions.

Technical drawing of a mechanical assembly, likely a bracket or support structure, showing dimensions in millimeters. The drawing includes a side view and a top view. Key dimensions include: overall width 2620 mm, overall height 2320 mm, and various section widths and offsets such as 770, 850, 410, 250, 1485, 115, 590, 350, 230, 40, 270, 165, and 240 mm.

**Fig. 1** Joint structure (unit: mm)



**Fig. 2** BRKB structure (unit: mm)

Materials	$t(\text{mm})$	$f_y(\text{N/mm}^2)$	$f_u(\text{N/mm}^2)$	$E(\text{N/mm}^2)$	$\delta(\%)$
Q355	8	367.2	455.8	196100	22.2
	10	304.4	469.6	200000	27.0
	12	380.1	539.6	204600	22.7
	14	330.4	472.7	206000	24.6
Q235	12	272.7	448.1	201400	32.3

Material	Bar diameter	$f_y(\text{N/mm}^2)$	$f_u(\text{N/mm}^2)$
Steel bar	φ6	410.3	566.7

Material	Strength grade	$f_{cu,k}$ (N/mm <sup>2</sup> )	$f_{ck}$ (N/mm <sup>2</sup> )
Concrete	C30	31.38	20.98

1-Reaction wall; 2-Reaction frame; 3-Column end vertical actuator; 4-Beam vertical actuator; 5-Ball hinge; 6-The specimen of knee brace joint; 7-Lateral constraint; 8- Horizontal constraint

(a) Test schematic diagram



(b) BRKBJ experimental device diagram

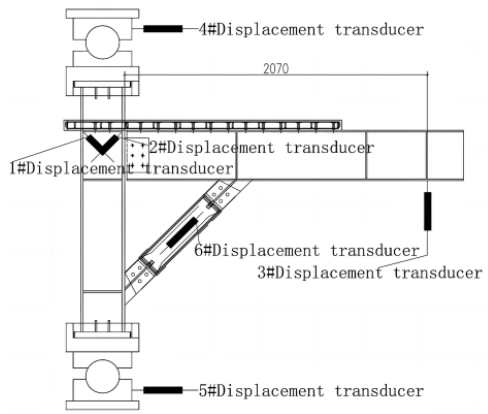


(c) BTRCJ experimental device diagram

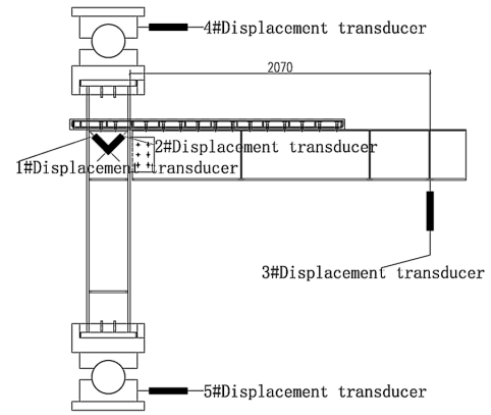
**Fig. 3** Test loading device diagram

#### 2.4. Displacement meter and strain gauge layout

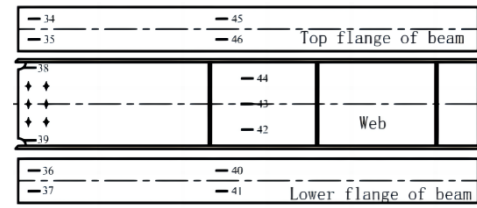
BRKBJ arrangement of 6 displacement meters, BTRCJ specimen arrangement of 5 displacement meters. The displacement meters No. 1 and No. 2 were used for monitoring the diagonal displacement of the beam and column joint domain. The displacement meter No. 3 was used to monitor the displacement of the beam end loading point. The displacement meters No. 4 and No. 5 were used for monitoring the displacement of column ends. The displacement meter No. 6 was used to monitor the axial tension and compression deformation displacement of the buckling restrained corner brace. The strain of the beam, column joint domain, corner brace, column intersection point, and the beam-column near the joint were observed. Note that the strain gauge numbers of both joints near the joint domain were the same. The displacement meter and the arrangement of key measuring points are illustrated in Fig. 4 and Fig. 5.



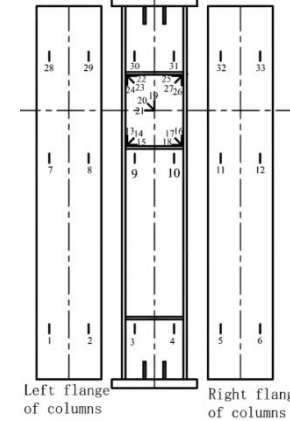
(a) BRKBJ displacement sensor layout



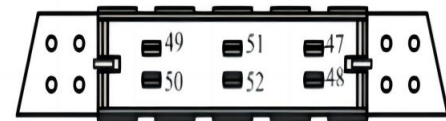
(b) BTRCJ displacement sensor layout

**Fig. 4** Layout of displacement sensors of joints

(a) Layout of strain gauges at beam's key position



(b) Layout of strain gauges at columns' key positions



(c) Layout of strain gauges at BRKBs

**Fig. 5** Layout of measuring points

### 3. Experimental process

#### 3.1. BRKBJ pseudo-static test process

In the elastic loading stage, when the vertical load of 154.2 kN along the pressure direction was applied to the beam's end, the strain at the gauge No. 52 at the core of the buckling restrained corner brace reached  $1358\mu\epsilon$ , which is the maximum of all strains of the core. As shown in Fig. 6, It can be determined that the core material part yields at this time, and the yield strength is measured by the material performance test of the sample. After one loading cycle in the elastic loading stage, the maximum displacement along the beam's pressure direction was 7.6 mm. Thus, the yield displacement was 7.6 mm, and the yield load was 154.2 kN. The cyclic load was carried out with the integral multiple yield displacement, and each stage was loaded twice. As shown in Fig. 7, when the vertical displacement imposed by MTS at the beam end along the compressive direction reached 10.51 mm, the load at the beam end was 195.4 kN, and cracks appeared in the middle of the concrete slab. Also, when the displacement applied by MTS at the beam end along the compressive direction

reached 21.1 mm, the corresponding load was 290.71 kN, and the maximum strain of the reinforcement in the upper floor reached 1390. Thus, the reinforcement was expected to yield at this time. When the vertical displacement applied by MTS at the end of the beam along the compressive direction reached 24.13 mm, the load at the end of the beam reached 346.61 kN. The data monitoring reveals that the maximum strain measured by strain gauge No. 41 at the lower edge of the beam and corner brace is 1798. Thus, the yield of the beam can be determined at this time. When the vertical displacement applied by MTS at the beam end along the compressive direction reached 32.34 mm, the load at the beam end was 333.38 kN. As shown in Fig. 8, the concrete slab detached from the steel column, and the penetrating cracks appeared in the middle of the slab. Fig. 9 shows that the fracture occurred in the middle of buckling restrained knee-braced core material when the load is up to 9 times the yield displacement. At this point, the connection between the beam and the corner brace yielded, while the beam end near the joint domain did not yield. When the load to the buckling restrained corner brace reached 11 times the upward yield displacement, a crack with a width of 8 mm appeared on the floor, the floor edge began to fall off, and the bearing capacity of the specimen decreased to less than 80%. At this point, the test is complete. The buckling restrained corner brace was broken, a large crack on the concrete slab and many penetrating cracks appeared, and the slab fell off. However, the beam and column were not damaged and unstable, and the beam-column joint domain maintained good mechanical properties, which was consistent with the two-stage yield design concept of the BRKBJ specimen.



Fig. 6 BRKBJ knee brace yield



Fig. 7 Crack on the concrete floor



Fig. 8 Crack on the concrete floor

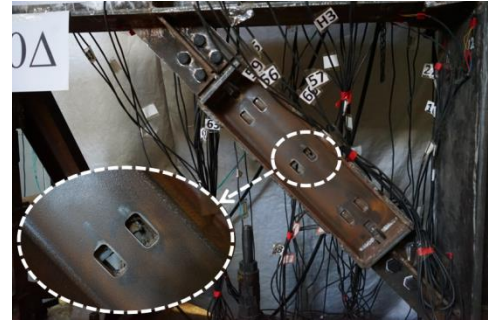


Fig. 9 BRKBJ core material failure

### 3.2. BTCRJ pseudo-static test process

Fig. 10 suggests that, in the elastic loading stage, when the force was loaded to 50 kN, cracks appeared near the joint domain of the floor and fell off. When the force was loaded to 140 kN along the pressure direction, penetrating cracks appeared near the joint domain of the floor. When a vertical load of 226 kN was applied in the direction of pressure, the strain at the root of the lower flange of the beam, at gauge No. 37, reached 1908  $\mu\epsilon$ , the maximum value recorded among all strains. Moreover, a clear inflection point appeared on the load-displacement curve of the beam endpoint. Thus, the yield of the beam can be realized at this time, which was after one loading cycle in the elastic loading stage. The load-displacement curve also shows that the maximum displacement of the beam endpoint along the pressure direction reached 20 mm. The yield displacement was 20 mm, and the corresponding yield load was 226 kN. It should be noted that 20 mm integral multiple yield displacements were used to increase the cyclic load amplitude. At each displacement stage, the loading cycle was imposed twice. When the vertical displacement along the pressure direction applied by MTS at the beam endpoint reached 28.74 mm, the load at the beam endpoint was 290.71 kN, and the maximum steel bar strain at the upper floor reached 1472  $\mu\epsilon$ . It can be realized that the steel bar yielded at this time. When the vertical displacement in the compression direction applied by MTS at the beam endpoint reached 60 mm, the load at the beam endpoint was 305.98 kN, and cracks appeared near the joint domain of the floor. When the load reached 4 times yield displacement, the lower flange of the beam near the joint domain buckled, and the load at the beam endpoint was 313.5 kN (Fig. 11). When the loading was up to 6 times the yield displacement, the lower flange and web of the beam near the joint domain were torn (Fig. 12). At this point, the test was terminated.



Fig. 10 Crack on the concrete floor



Fig. 11 Beam flange deformation





Fig. 12 Beam flange failure

#### 4. Test result analysis

##### 4.1. Load-displacement curve

The load-displacement hysteresis curves of both specimens are compared as depicted in Fig13-Fig14.

Before BRKBs fracture, the hysteresis curve of BRKBJ is shuttle-shaped and full, and it has good energy dissipation performance. In the early loading stage, due to the coupling effect of buckling restrained brace and beam-column, BRKBJ has greater stiffness than BTCRJ. The BRKBJ specimen's stiffness decreases with increasing the number of cycles in the displacement control stage. The hysteresis curve of the BRKBJ specimen has three distinct stages, which imply that the buckling restrained brace and beam-column yield successively. When the cycle reaches 9 times the yield displacement, the fracture occurred in the middle part of the core material, the bearing capacity of BRKBs decreased to 59.6 % of the ultimate bearing capacity. At this time, the main body of the beam and column maintained good integrity except the core material, indicating that BRKBs had good energy dissipation capacity. After that, the BRKBs were continuously loaded to 11 times the yield displacement, and the beam-column joints were loaded, indicating that the beam-column joint domain still had good energy dissipation capacity after BRKBs fracture. Overall, the hysteresis curve is "symmetrical" in the tension and compression directions, indicating that the influence of floor slab on the hysteretic behavior of buckling restrained corner braced joints is not significant.

The hysteresis curve of the BTCRJ specimen is relatively stable and full, and the specimen has large stiffness at the initial loading stage. With the increase of loading multiple, the stiffness decreases. When the cycle reaches five times the yield displacement, the total load of the load-displacement curve no longer increases, and the hysteresis loop shows a downward trend. The lower flange of the beam at the beam-column connection is torn, and the bearing capacity decreases to 58.3% of its ultimate bearing capacity. The hysteresis curve of the BTCRJ specimen is overall "asymmetric". The hysteresis curve in the tensile direction is fuller because the floor is in a tensile state when the beam ends are compressed. Once the concrete cracks and the steel bars yield, the floor fails. When the beam end is pulled, the floor and the concrete are in a pressurized state. Therefore, when the beam end displacement is large, the joint stiffness is obviously degraded in the compression direction, while the beam endpoints are in the tensile state and the concrete is still in the compression state.

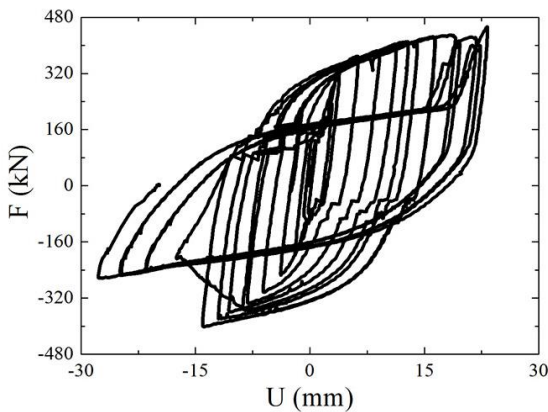


Fig. 13 Core material load - displacement curve

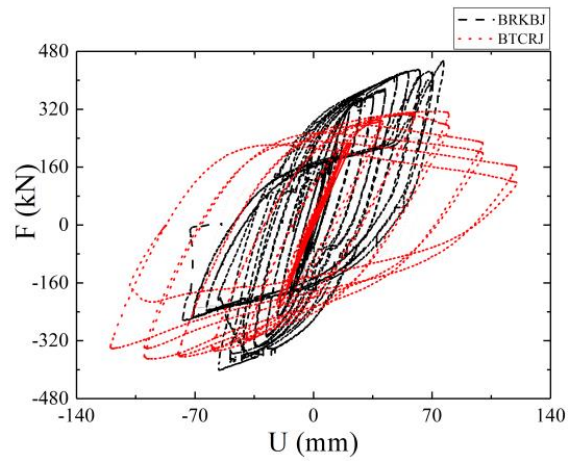


Fig. 14 Comparison of load-displacement curves of BRKBJ and BTCRJ specimens

##### 4.2. Skeleton curve

The skeleton curves of both specimens are compared as illustrated in Fig. 15. The ultimate bearing capacity of the BRKBJ specimen is 453.73 kN. The skeleton curve of the specimen changes linearly before the buckling restrained corner core material yields. The whole specimen is in the elastic stage. After the core material yields, the skeleton curve has obvious bending. Meanwhile, with gradually increasing the displacement, the specimen stiffness gradually decreases. After the beam and column yield, the stiffness will decrease again. The skeleton curve has an obvious inflection point. When the BRKBJ specimen is loaded in the tensile direction to 9 times the yield displacement of the energy dissipation knee brace, the middle part of BRKBs fractured. Before the fracture of the core material, the displacement and stiffness in the tensile and compressive directions are symmetrical, indicating that the floor slightly influences the BRKBJ specimen's stiffness. The ultimate bearing capacity of the BTCRJ specimen is 342.14 kN, and the skeleton curve changes linearly before the beam and column yield. After the beam and column yield, the stiffness decreases significantly when the displacement in the compressive direction reaches 80 mm. However, the stiffness begins to decrease when the displacement in the tensile direction reaches 105 mm, indicating that the floor has a significant enhancement effect on the stiffness in the BTCRJ specimen's tensile direction. The loads and corresponding displacements of both specimens at each stage are shown in Table 3. It can be realized that setting BRKBs can effectively increase the yield displacement of beam and column, improve the yield strength, and effectively delay the cracking of concrete and the yield of steel bars. The ultimate bearing capacity increases by 32.6%, and the displacement decreases by 19.2% under ultimate load.

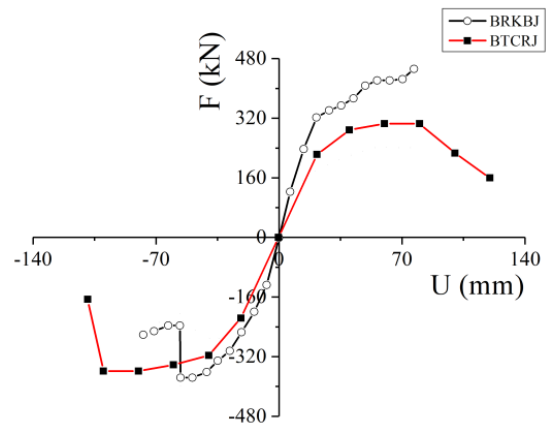


Fig. 15 Comparison of skeleton curves of BRKBJ and BTCRJ specimens

Table 3

Core material, beam-column yield displacement and load.

Specimen	Core yield		concrete crack		Beam-column yield		limiting condition	
	$\Delta_c$	$F_c$	$\Delta_f$	$F_f$	$\Delta_y$	$F_y$	$\Delta_u$	$F_u$
BRKBJ	7.55	154.21	11.42	195.4	24.13	346.6	78.83	453.7
BTCRJ	-	-	4.26	50	19.95	222.1	93.97	342.1



#### 4.3. Stiffness degradation curve

Note that the secant stiffness ( $K_i$ ) represents the specimen stiffness under low cyclic loading. The stiffness degradation curves of both specimens are compared as provided in Fig. 16, the curves of both specimens are relatively smooth before the BRKBJ yields. The BRKBJ specimen has the characteristics of large stiffness and small displacement. After the displacement increases to the failure point of the knee brace, the stiffness in the tensile direction decreases rapidly, and the stiffness degradation in the compression direction is still gentle. This is because the knee brace fails when the beam end is tensioned, while the knee brace in the compression direction is still in function due to the existence of the buckling restrained sleeve. When the BRKBJ specimen reaches the ultimate bearing capacity state, it still maintains 42% of the initial stiffness, indicating that the BRKB is arranged based on the rigid connection of the beam and column. Note that it can meet the requirements of seismic fortification. For BTCRJ, with the increase of load displacement, the degradation trend in the tensile direction is smaller than that in the compressive direction. This is because even if the concrete cracks and the steel bars yield, the floor slab can partially provide stiffness when the beam ends are pulled. When the specimen reaches the ultimate bearing capacity state, the specimen has an initial stiffness of about 41%.

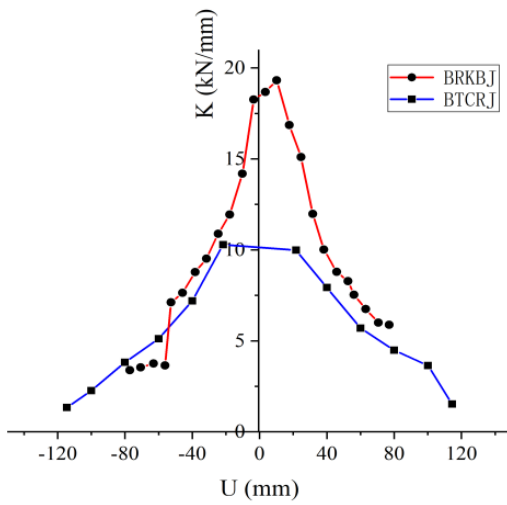


Fig. 16 Contrast diagram of stiffness degradation curve of two specimens

#### 4.4. Ductility analysis

The equivalent viscous damping coefficient ( $h_e$ ) is used to determine the joint's energy dissipation capacity, and the displacement ductility coefficient ( $\mu$ ) is used to determine the structure ductility. These coefficients of both specimens are tabulated in Table 4.

Table 4

Equivalent viscous damping and displacement ductility coefficients

Specimen	BRKBJ	BTCRJ
$h_e$	0.387	0.338
$\mu$	7.3	6.0

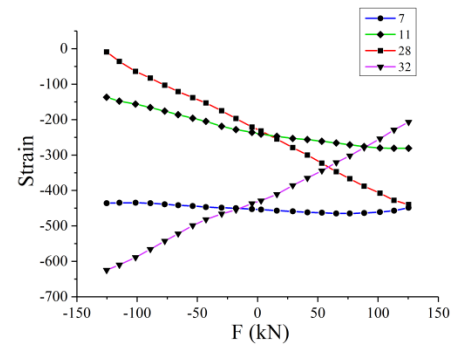
The structure ductility is one of the important indexes to evaluate the structure's seismic performance. In this test, both joint specimens were destroyed before the bearing capacity decreased to 85% of the ultimate bearing capacity. Thus, the specimen displacement was taken when the maximum bearing capacity was reached. The seismic ductility coefficient of the frame structure specified in the code is 4.0, and the displacement ductility coefficient of both specimens meets the code requirements. The equivalent viscous damping coefficient and displacement ductility coefficient of the buckling restrained corner braced joint are increased by 14.5% and 21.6%, respectively, indicating that the buckling restrained corner braced joint has good ductility performance.

The greater the equivalent viscous damping coefficient, the better the energy dissipation capacity of the specimen. Among them, BRKBJ specimens take the hysteretic loop calculation when the beam and column just enter the yield after the yield of the energy dissipation core material, and BTCRJ takes the hysteretic loop calculation when the beam and column just enter the yield.

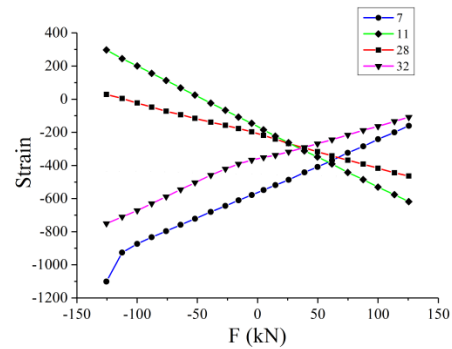
#### 4.5. Strain analysis of key positions

The strain changes of the measuring points 7 and 28 at the left flange and 11 and 32 at the right flange are illustrated in Fig. 17.

The comparative analysis reveals that the strain of the flange on both sides of the column in the elastic stage is small enough to meet the requirements of the strong column design. For the BTCRJ specimen, the beam end is not fully relaxed when the axial force of the column end is applied. Thus, it partially impacts the strain of the column flange. With increasing the load, the strain increasing trend of the BRKBJ specimen is less than that of the BTCRJ specimen. It shows that the buckling restrained corner brace can share the load at the end of the column in the traditional beam-column frame joint. Furthermore, the buckling restrained corner brace can reduce the effect of load on the column, and change the mechanical performance of the traditional beam-column frame joint. Under reciprocating load, the lower flange at the connection between the beam and the corner brace experiences a bending instability, while the column still maintains good performance and no instability occurs. These observations illustrate that the strategic placement of buckling restrained braces can shift the joint's plastic hinge outward to the joint between the brace and the beam, thereby fulfilling seismic design requirements.



(a) BRKBJ column flange strain



(b) BTCRJ column flange strain

Fig. 17 Strain contrast diagram on the wing edge of a column

The strain changes of measuring point 5 at the connection between the column and the knee support of the BRKBJ specimen, measuring point 41 at the connection between the beam and the knee support, and measuring point 37 at the beam endpoint near the joint domain are plotted in Fig. 18.

The yield load at the connection between beam and knee brace support of the BRKBJ specimen is significantly greater than that at the beam end of the BTCRJ specimen. At this time, no yield occurs at the connection between the column of the BRKBJ specimen and the knee brace support and near the joint domain. This phenomenon can indicate that the layout of BRKBs can effectively absorb energy. In the later loading stage, the knee braces and the beam near the connection of knee braces take energy. Thus, not only the yield-load curve of the whole beam and column is improved, but also the formation of plastic hinges at the beam end near the joint domain is prevented. Therefore, the overall energy dissipation capacity of the whole joint domain is improved.

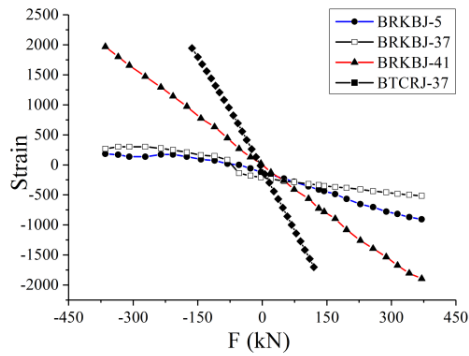
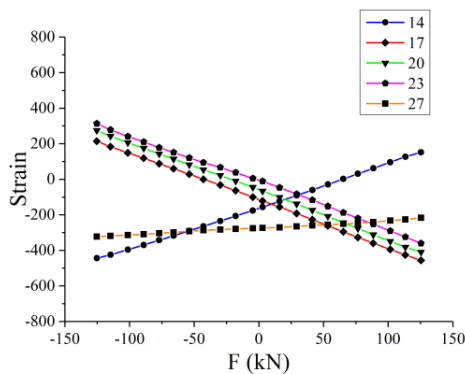


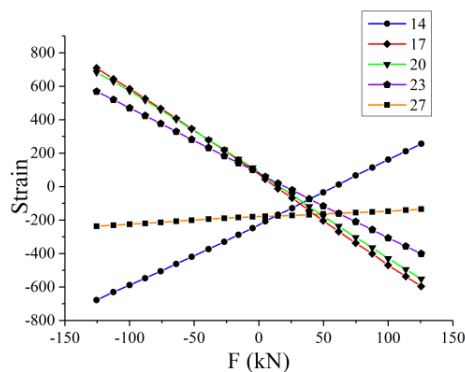
Fig. 18 The yield-strain curves of BRKBJ and BTCRJ specimens

The strain changes of the five measuring points 14, 17, 20, 23, and 27 in the joint domain of both specimens are presented in Fig. 19.

In the elastic stage, the strain in joint domains of both specimens change linearly, while the strain change trend of the BRKBJ specimen is significantly less than that of the BTCRJ specimen. This fact indicates that adding the buckling restrained corner brace can significantly reduce the stress level in the joint domain, ensure the stiffness of the joint domain, avoid large shear deformation in the joint domain of the specimen, and meet the design requirements of strong joints.



(a) BRKBJ strain in the joint domain



(b) BTCRJ strain in the joint domain

Fig. 19 Strain contrast diagram in the column joint domain

## 5. Conclusion

The seismic performance of the traditional steel composite beam-column rigid joint and the BRKBJ considering the influence of the floor slab was explored. A BRKBJ and a BTCRJ were selected for quasi-static tests under low cyclic loading and for seismic performance analysis. Moreover, the failure mode, bearing capacity, hysteresis performance, and ductility of both joints

were analyzed. Our study has led us to the following conclusions:

(1) It was determined that the incorporation of a BRKB into the BTCRJ specimen led to a 32.6% increase in the BRKBJ specimen's ultimate load-bearing capacity. The displacement is reduced by 19.2% when the ultimate bearing capacity is reached. When the ultimate bearing capacity is reached, the initial stiffness remains about 42%, the yield displacement of beam and column increases slightly, the yield load is greatly improved, and the mechanical performance of the joint is improved.

(2) The hysteresis curve of the BRKBJ specimen is robust. Compared to BTCRJ, BRKBJ exhibits a 14.5% increase in the viscous damping coefficient, and a 21.6% increase in the ductility coefficient. Under cyclic loading, the BRKBJ specimen displays superior symmetry and heightened load-bearing capacity. This suggests that the use of buckling restrained braces can enhance the energy dissipation capacity of composite joints and also improve seismic performance.

(3) The layout of the floor slab has minimal impact on the BRKBJ specimen under seismic activity. The joints present almost equal energy dissipation and stiffness in both tension and compression directions. Additionally, the floor slab can significantly enhance the stiffness and energy dissipation capacity of the beam end under tension after the beam and column yield. However, the effect of the floor slab in the compression direction is not obvious.

(4) The BRKBJ specimen has a two-stage yield. First, the core material of the buckling restrained corner brace and the main part of the beam and column yield. When the plastic failure occurs, the increase of buckling restrained corner brace can move the plastic hinge of the beam end of the traditional beam-column joint to the connection between the corner brace and the beam. Moreover, the buckling restrained corner brace reduces the stress level of the joint domain and improves the energy dissipation capacity of the joint domain under seismic action.

## Acknowledgement

The research was funded by the Ministry of Housing and Urban-Rural Development(No. 2018-K5-001), the Natural Science Foundation of Liaoning Province (2019-ZD-0664) and the Department of Education of Liaoning Province (No. LNJ202005), which is gratefully acknowledged.

## References

- [1] Hsu H L, Li Z C. Seismic performance of steel frames with controlled buckling mechanisms in knee braces[J]. *Journal of Constructional Steel Research*, 2015, 107: 50-60.
- [2] Junda E, Leelataviwat S, Doung P. Cyclic testing and performance evaluation of buckling-restrained knee-braced frames[J]. *Journal of Constructional Steel Research*, 2018, 148: 154-164.
- [3] Yin Z Z, Feng D Z, Yang B, et al. The seismic performance of double tube buckling restrained brace with cast steel connectors[J]. *Advanced Steel Construction*, 2022, 18(1): 436-445.
- [4] Chen Z Y, Ge H B, Usami T. Analysis and design of steel bridge structures with energy absorption members[J]. *Advanced Steel Construction*, 2008, 4(3): 173-183.
- [5] Zhou D M. Influential analysis of changing parameters of the knee brace on seismic performance of steel story-adding structure[J]. *Engineering Construction*, 2017, 49 (4) :1-7. (in Chinese))
- [6] Zhou D F. Analysis on seismic performance of the knee brace in steel story- adding structure[D]. Shandong. Qingdao Technological University, 2016. (in Chinese))
- [7] Conti M A, Mastrandrea L, Piluso V. Plastic design and seismic response of knee braced frames[J]. *Advanced Steel Construction*, 2009, 5(3): 343-366.
- [8] Li Q S, Huang Z, Chen L Z. Elastic-plastic analysis of braced frame system with inclined corner bracing [J]. *Industrial Buildings*, 2005, 35 ( 5 ) : 85-87.
- [9] Ji K H. Study on seismic behavior of steel frame with corner braces [D]. Nanjing University of Technology, 2006.
- [10] H.-L.Hsu,Z.-C.Li. Seismic performance of steel frames with controlled buckling mechanisms in knee braces[J]. *Journal of Constructional Steel Research*, 2015,(107):50-60.
- [11] Jia M M, Li L, Hong C, et al. Experiment of hysteretic behavior and stability performance of buckling-restrained braced composite frame[J]. *Advanced Steel Construction*, 2021, 17(2): 149-157.
- [12] Xie L, Wu J, Shi J, et al. Influence of the core-restrainer clearance on the mechanical performance of sandwich buckling-restrained braces[J]. *Advanced Steel Construction*, 2020, 16(1): 37-46.
- [13] Xu F, Wang X Z. Seismic Performance for Steel Frames with Different Layouts of Knee Brace[C]. *Proceedings of The 2016 International Conference on Architectural Engineering and Civil Engineering*, 2016(72): 624-627.
- [14] Xu F, Gong T B, Jia L G. Seismic performance of steel frame beam-column connection with single-braced energy dissipative joint[C]. *National Forum of Civil Engineering Graduates in Green Construction and Industrialization*, 2015. 12. (in Chinese))
- [15] Gong T B. Study on seismic performance of buckling-constrained concrete braced steel frame[D]. Laoning, Shenyang Jianzhu Univesity, 2017. 3. (in Chinese))
- [16] WANG Yan, FENG Shuang, WANG Yutian. Experimental study on hysteretic behavior for rigid-reinforced connections[J]. *China Civil Engineering Journal*, 2011, 4(5): 57-68. (in Chinese))
- [17] ZHAO Junxian, YU Haichao, PAN Yi. Seismic performance of sliding gusset connections in buckling-restrained braced steel frame[J]. *Journal of Building Structures*, 2019, 40(2): 117-127. (in Chinese)
- [18] Jia B, Zhang Q L, Luo X Q. Study on hysteretic behavior of aluminum alloy energy dissipation braces[J]. *Journal of Building Structures*, 2015, 36(08): 49-57. (in Chinese))
- [19] Jinkoo Kim, Youngill Seo. Seismic design of steel structures with buckling-restrained knee braces [J]. *Journal of Constructional Steel Research*, 2003, 59(12): 1477-1497.

- [20] Amador Tera'n-Gilmore, Jorge Ruiz-Garci'. Comparative seismic performance of steel frames retrofitted with buckling-restrained braces through the application of Force-Based and Displacement-Based approaches [J]. Soil Dynamics and Earthquake Engineering, 2010.
- [21] Qu Z ,Xie J Z, Wang T, Shoichi Kishiki. Seismic retrofit design method for RC buildings using buckling-restrained braces and steel frames [J]. Engineering Structures, 2017. 139: 1-14.
- [22] Hamdy Abou-Elfath, Mostafa Ramadan, Fozeya Omar Alkanai. Upgrading the seismic capacity of existing RC buildings using buckling restrained braces [J]. Alexandria Engineering Journal, 2017. 56(2): 251-262.
- [23] Fatih Sutcu, Toru Takeuchi, Ryota Matsui. Seismic retrofit design method for RC buildings using buckling restrained braces and steel frames [J]. Journal of Constructional Steel Research, 2014. 101: 304-313.

# A REVIEW OF DIRECT FASTENING STEEL JACKET FOR STRENGTHENING OF REINFORCED CONCRETE COLUMNS

Zhi-Wei Shan <sup>1</sup>, R.K.L. Su <sup>2,\*</sup>, D.T.W. Looi <sup>3</sup> and Li-Jie Chen <sup>2</sup>

<sup>1</sup> Key Laboratory of Concrete and Prestressed Concrete Structures of the Ministry of Education, Southeast University, Nanjing 210096, China

<sup>2</sup> Department of Civil Engineering, The University of Hong Kong, Hong Kong, China

<sup>3</sup> Civil Engineering, Faculty of Engineering, Computing and Science, Swinburne University of Technology, Sarawak, Malaysia

\* (Corresponding author: E-mail: klsu@hku.hk)

## ABSTRACT

A novel retrofit method for reinforced concrete (RC) columns using a direct fastening steel jacket has been newly developed. This novel retrofit method features a simple and quick retrofit procedure, whereby high-strength fasteners are actuated and driven through to connect steel angles, steel plates and the concrete surface surrounding the column. Steel plates in direct fastening steel jackets can carry axial load and lateral load directly because they are appropriately interacted with RC columns. Direct fastening connections in direct fastening steel jackets behave in the manner of transverse reinforcement, which can share shear load and generate passive confinement to concrete columns. Given that limited research has been undertaken on direct fastening steel jackets, this paper summarizes state-of-the-art work on the experimental study, theoretical study and design methods of direct fastening connections used to strengthen RC columns. Interesting findings include the significant improvement of the strength and flexural stiffness of RC columns strengthened by the developed method and subjected to axial and cyclic lateral loads, as observed in experiments. Furthermore, the theoretical study based on fundamental mechanical derivations lays down the groundwork for the development of the design methods of RC columns strengthened by this innovative method.

## ARTICLE HISTORY

Received: 18 May 2023  
Revised: 18 May 2023  
Accepted: 12 July 2023

## KEYWORDS

Direct fastening steel jacket;  
RC column;  
Strengthening;  
Flexural stiffness;  
Strengthening design

Copyright © 2023 by The Hong Kong Institute of Steel Construction. All rights reserved.

## 1. Introduction

RC columns are used to resist vertical loads and lateral loads in frame structures. However, when they experience a fire or earthquake event, load carrying capacity and flexural stiffness can be impaired. Such damaged RC columns may fail to resist subsequent extreme loading events, such as impact or earthquake. This situation becomes more critical during seismic events, where seismic demand exceeds the designed capacity [1-8]. It can be seen from Fig. 1 that damaged structures with reduced flexural stiffness may suffer more notable lateral deformation during a strong earthquake, as shown in Fig. 1. When seismic displacement demand exceeds inelastic displacement capacity, the collapse failure of columns may occur. Restoring flexural stiffness is an effective method by which to decrease displacement demand. Indeed, although previous retrofitting methods have mainly concentrated on improving the strength of RC columns, the necessity to enhance the flexural stiffness of RC columns is also necessary.

The use of a fiber-reinforced polymer (FRP) jacket is an effective strengthening method that can improve the strength of an RC column by way of the passive confinement effect. However, it does not effectively enhance the flexural stiffness of RC columns [9-12]. Moreover, FRP jacketing is made up of composite materials with poor fire resistance, which impedes their prevalent application. To overcome these disadvantages, a strengthening method increasing the cross-sectional area was studied [13-17]. Although structural behavior can thereby be improved, this method cannot meet the demand for rapid strengthening because the adding of the further layer of concrete is time consuming. Although steel jackets can overcome these disadvantages, few studies have been conducted.

A steel jacket formed by four steel angle brackets at the corners of the RC columns was first proposed by Nagaprasad et al. [18]. Two adjacent steel angle brackets were connected by steel battens using a welding connection. Experimental results indicated that this method can improve the flexural strength and flexural stiffness of RC columns. However, flexural stiffness increase was limited (44%) as it was only provided by four steel angle brackets.

Roca et al. [19] subsequently conducted experimental tests on RC columns retrofitted with steel jackets. In their tests, a load mechanism of monotonic lateral loading with constant axial loading was used. Similar conclusions were drawn. Sahoo and Rai [20] applied this strengthening method to an RC frame, and dynamic tests were carried out on a strengthened and unstrengthened RC frame. Based on the natural frequencies of strengthened and unstrengthened RC frames, it can be concluded that the flexural stiffness of the strengthened RC frame was improved by 20%. More recently, Xu et al. [21] proposed a steel cage that was not affixed to the footing but rather was composited with the RC

column using steel glue. Flexural stiffness was found to increase by 60%, which is also insignificant. The mechanisms of these two strengthening methods were very similar, wherein the function of four steel angle brackets was identical to the longitudinal rebar. The contribution to resisting bending behavior was provided by the limited cross-sectional area of the four steel angle brackets. Therefore, enhancement of the flexural stiffness of the strengthened RC columns was not significant.

It can be seen that few studies have focused on enhancing the flexural stiffness of RC columns. Furthermore, the improvement of existing steel jackets on flexural stiffness is not remarkable. Therefore, a strengthening method that can significantly enhance flexural stiffness is necessarily developed. Here, a novel retrofit method for RC columns using a direct fastening steel jacket has been newly developed. In this method, an innovative direct fastening connection – distinguishable from the traditional welding connection – was utilized [22-26]. In this paper, a comprehensive review on the experimental study and theoretical study of this innovative strengthening method is conducted to facilitate its application to practical design.

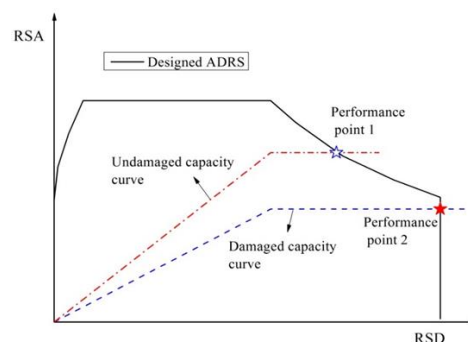


Fig. 1 Capacity spectrum subject to fire attack or earthquake event

## 2. Direct fastening steel jacket

A novel steel jacket is developed herein, as illustrated in Fig. 2. This novel retrofit method features a simple and quick retrofit procedure, as a result of the direct fastening connection method used. In this method, high strength fasteners can be easily driven into two steel plates using an actuated gun. Compared to welding connections, this method is more easily manipulated. With this proposed steel jacket, steel plates contribute to axial and lateral load capacity



because they are composited with the RC column. Direct fastening steel connections can provide passive confinement and contribute to shear strength because their behavior is analogous to the transverse reinforcement. Therefore, the strength, stiffness and deformability of RC columns can be improved.

This direct fastening jacket and fastening connection can directly undertake shear force, and can resist the in-plane shear force generated from passive confinement. Therefore, the behavior of direct fastening connections subjected to in-plane shear force should be comprehensively studied. The mechanism of RC columns composited with the developed direct fastening steel jacket and subjected to axial and lateral loading can then be studied. Based on these studies, a design procedure can be developed. Therefore, the behavior of direct fastening connections subjected to in-plane shear force is first reviewed. The behavior of RC columns composited with the developed direct fastening steel jacket and subjected to axial and seismic loading is then analyzed before the design procedure is reviewed.

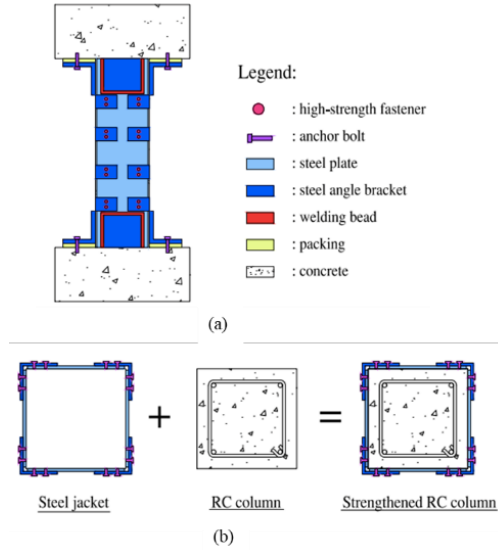


Fig. 2 Proposed strengthening scheme: (a) front view; and (b) plane view

### 3. Behavior of direct fastening connections subjected to in-plane shear force

One hundred samples connected by two types of fastener were tested, under in-plane shear force [22]. Parameters, including number of fasteners, spacing of fasteners, arrangement of fasteners, surface condition of fasteners and effect of protuberance were examined; see Fig. 3.

Typical displacement versus in-plane shear force is shown in Fig. 4. It can be seen that this type of connection possesses preferable plastic deformation before failure. This lays a foundation for the prevalent application of this connection. To better describe this process, a simplified three-linear curve (i.e., OABC) is proposed, by which the passive confinement force provided by this direct fastening connection in the strengthened RC columns can be determined. To determine this simplified three-linear curve (see Fig. 4), the effective stiffness, bearing shear strength and displacement at pull-out point should be separately studied.

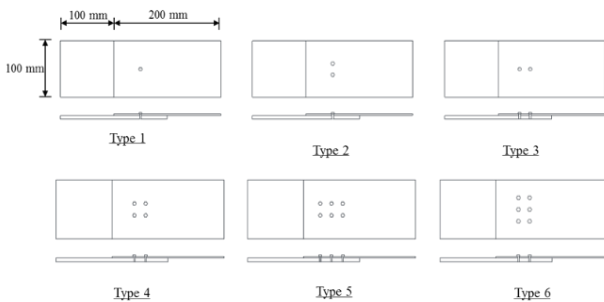


Fig. 3 Types of connection

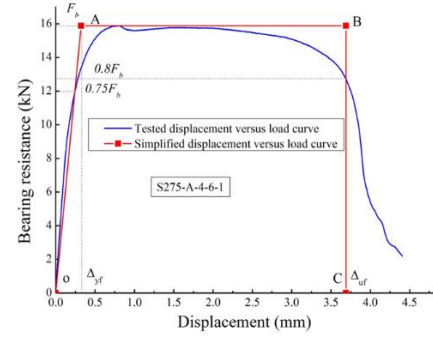


Fig. 4 Displacement versus load curve

#### 3.1. Effective stiffness

Effective stiffness can be used to obtain the deformation of a direct fastening connection when the deformation lies within the OA stage. A direct fastening connection is formed using high strength fasteners driven into two steel plates. Therefore, fastener diameter, thickness of steel plate and the elastic of the steel plate are the critical parameters affecting the effective stiffness [22]. This is given as:

$$K_{ef} = \varphi_{kn} \varphi_{kef} E_p t_p d_n \quad (1)$$

where  $\varphi_{kn}$  is the factor considering the effect of fastener number (FN), which is calibrated by test results and given in Table 1.  $\varphi_{kef}$  represents the factor considering the effect of other parameters excluding the above-mentioned three critical parameters. It is also calibrated by test results and a value of 0.017 is recommended.  $E_p$ ,  $d_n$  and  $t_p$  are the elastic modulus of the steel plate, nominal fastener diameter and thickness of the steel plate, respectively. In general, the fastener diameters are 3 mm and 4 mm, such that effective stiffness is mainly affected by fastener number and thickness of the steel plate, considering that the elastic modulus of steel is almost constant.

Table 1

Recommended values of FN factor

Number of fasteners	$n=1$	$n=2$	$n=3$	$n=4$
FN factor	1	1.4	1.9	2.1

#### 3.2. Bearing shear strength

In accordance with the expressions used to determine the bearing capacity of bolt connections recommended in previous specifications (e.g., ANSI/AISC 360-16), the expression determining the bearing capacity of direct fastening connections is given as [22]:

$$F_b = \varphi_p \varphi_k \alpha_{br} d_n t_p f_{up} \quad (2)$$

where  $f_{up}$  is the tensile strength of the steel plate. In this innovative direct fastening connection, when fasteners are driven into steel plates, protuberance is generated which positively contributes to bearing capacity. Therefore, a factor ( $\varphi_p$ ) was introduced to consider this effect. Furthermore, the surface condition of the fasteners (i.e., knurling) also plays a key role in bearing capacity. A factor ( $\varphi_k$ ) for the effect of knurling is thus brought in. Other stochastic effects are included in bearing capacity factor ( $\alpha_{br}$ ). The recommended values of these three factors are presented in Table 2.

#### 3.3. Ultimate displacement

Owing to the fact that plastic deformation is significantly larger than elastic deformation (which can be seen from the displacement versus in-plane shear force curve), the rotation of the fastener determines the ultimate displacement of direct fastening connections, as shown in the following expression:

$$\Delta_{uf} = \frac{t_1 + t_2}{2} \theta_f \quad (3)$$

where  $\theta_f$  is the ultimate rotation of the fastener, which corresponds to pull-out

time. When the friction force between the fasteners and holes of the steel plate can no longer resist the pull-out force, pull-out failure occurs, indicating that the ultimate rotation is affected by the surface condition of the fasteners. Therefore, the ultimate rotation of different types of fastener should be separately determined. According to the test results, ultimate rotations of 0.43 rad and 0.75 rad are recommended for the two types of fasteners, respectively.

**Table 2**

Recommended values of three factors in bearing capacity

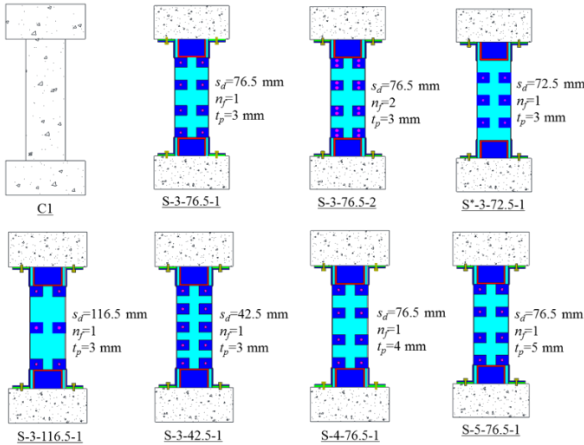
$\alpha_{br}$		$\Psi_{fp}$		$\Psi_{fk}$	
Tight contact with top steel plate	Non-tight contact with top steel plate	With pre-drilled holes on connected plates	Without pre-drilled holes on connected plates	Unknurled fasteners	Knurled fasteners
1.6	1.36	1.0	1.35	1.0	1.17

#### 4. Behavior of RC columns strengthened by direct fastening steel jackets subjected to axial loading

##### 4.1. Experimental study

To investigate the behavior of RC columns encompassing direct fastening steel jackets, eight specimens were designed and tested [23]; see Fig. 5. To better distinguish between the specimens, they are each named using a notation. For example, S-3-76.5-1 represents a thickness of the steel plate used of 3 mm, connected by a direct fastening connection consisting of one fastener, with a connection spacing of 76.5 mm. Four parameters, including connection spacing, number of fasteners, thickness of steel plate and end connection, were examined.

Both axial load capacity and ductility are greatly enhanced by the proposed direct fastening jacket. For the two specimens in which the steel jacket is joined with one fastener and two fasteners, peak axial loading is 1548 kN and 1765 kN, respectively. This demonstrates that the confinement effect for connections with a higher number of fasteners is more notable. Regarding the effect of connection spacing, the peak axial loads of S-3-42.5-1, S-3-76.5-1 and S-3-116.5-1 are 1498 kN, 1548 kN and 1676 kN, respectively. Smaller connection spacing results in a smaller slenderness ratio for steel plates, which delays buckling time. Therefore, when the axial strength is determined, the effect of confinement and buckling should be considered.

**Fig. 5** Types of connection sample

##### 4.2. Theoretical study

###### 4.2.1. Confined concrete strength

As shown in Fig. 6, the concrete was divided into three parts to distinguish between the confinements of the concrete core. Concrete core 1 is confined by both stirrups and direct fastening connections. Concrete core 2 is only confined by direct fastening connections while concrete core 3 comprises plain concrete without confinement.

When a column is subjected to axial loading, transverse deformation generates due to Poisson's effect. If there is no transverse confinement, transverse deformation can expand freely; see the dashed line in Fig. 7(a). In the case of transverse confinement, interaction between the concrete and transverse reinforcement occurs. As a result, passive confinement stress (see Fig. 7(b)) acts

on the concrete core and transverse deformation is constrained; see the solid line in Fig. 7(a). Transverse reinforcements can be regarded as beams on an elastic foundation, and then the governing equations are derived [24].

$$\frac{d^4 \omega_x}{dy^4} + \frac{\kappa_x s_a}{E_{TR} I_{TR}} (\omega_x - \delta_x) = 0 \quad (4a)$$

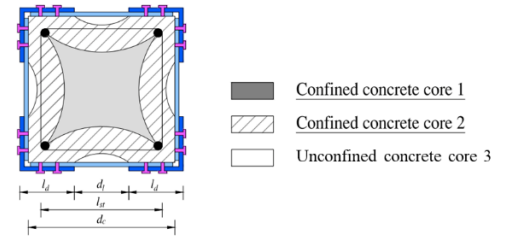
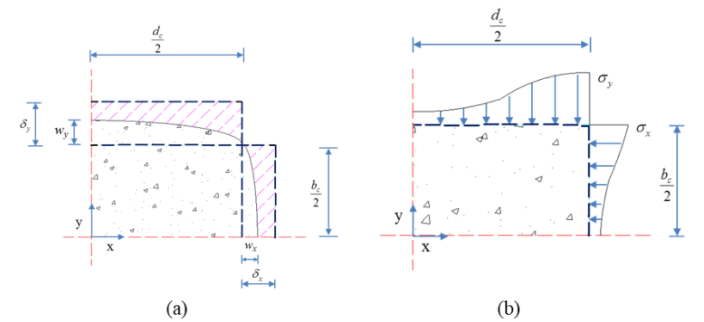
$$\frac{d^4 \omega_y}{dx^4} + \frac{\kappa_y s_a}{E_{TR} I_{TR}} (\omega_y - \delta_y) = 0 \quad (4b)$$

$$\kappa_x = \frac{1}{\frac{d_c}{2}} \frac{E_c (1 - \mu_c)}{(1 + \mu_c)(1 - 2\mu_c)} \left( 1 + \frac{\mu_c}{1 - \mu_c} \frac{b_c}{d_c} \right) \quad (4c)$$

$$\kappa_y = \frac{1}{\frac{b_c}{2}} \frac{E_c (1 - \mu_c)}{(1 + \mu_c)(1 - 2\mu_c)} \left( 1 + \frac{\mu_c}{1 - \mu_c} \frac{d_c}{b_c} \right) \quad (4d)$$

where  $\kappa_x$  and  $\kappa_y$  in Eqs. (4c) and (4d) are the bending stiffness of transverse reinforcement provided by the RC column along the  $x$  and  $y$  axes. With the exception of the elastic modulus ( $E_c$ ) and Poisson's ratio ( $\mu_c$ ) of the concrete, the geometric parameters of the depth ( $d_c$ ) and width ( $b_c$ ) of the RC column also affect the bending stiffness.  $E_{TR} I_{TR}$  represents the mechanical characteristic of the deflection of the transverse reinforcement.  $I_{TR}$  and  $E_{TR}$  are the second moment and elastic modulus of transverse reinforcement, respectively. Deflections of the transverse reinforcement along the  $x$  and  $y$  axes are respectively depicted by  $\omega_x$  and  $\omega_y$ , while transverse expansion of the RC column along the  $x$  and  $y$  axes is respectively denoted by  $\delta_x$  and  $\delta_y$ .  $s_a$  is the width of the transverse reinforcement.

The passive confinement stress generated from direct fastening connections and stirrups, combining corresponding boundary conditions, can then be determined according to the derived governing equation. Once passive confinement stress is derived, confined concrete strength can be obtained.

**Fig. 6** Division of concrete cross-section**Fig. 7** Confinement effect: (a) profile of plane deformation; and (b) profile of passive confinement stress

###### 4.2.2. Buckling strength of longitudinal steel rebar

Longitudinal rebars are restrained by concrete cover. Longitudinal rebar buckling may occur following concrete cover spalling. During the post-buckling process, part of the cross-section of the longitudinal rebar is unloaded. Because

loading stiffness and unloading stiffness are different, the average stress of the cross-section of the longitudinal rebar should be used instead of the local stress on the stress-strain curve of the steel material. Dhakal and Maekawa [27] verified that the former average stress is less than the latter local stress; see Fig. 8. They proposed a method to estimate this average stress and the expressions are given by:

$$\sigma_{\text{back}} = \begin{cases} 1 - (1 - \frac{\sigma^*}{\sigma_l^*})(\frac{\epsilon_{\text{ave}} - \epsilon_{\text{yl}}}{\epsilon^* - \epsilon_{\text{yl}}}), & \epsilon_{\text{yl}} < \epsilon_{\text{ave}} \leq \epsilon^* \\ \sigma^* - 0.02E_s(\epsilon_{\text{ave}} - \epsilon^*), & \epsilon_{\text{ave}} > \epsilon^* \end{cases} \quad (5)$$

where  $\epsilon_{\text{ave}}$  is the average strain. It is equal to the value when the maximum axial load of the strengthened RC column is reached.  $\sigma^*$  and  $\epsilon^*$  are used to depict the strain and stress of the turning point in Fig. 8.  $\sigma_l^*$  is the corresponding stress on the simplified stress-strain curve of the steel material at a strain of  $\epsilon^*$ .  $\epsilon_{\text{yl}}$  is the nominal yield strain of longitudinal rebar.

#### 4.2.3. Buckling strength of steel plates

In this proposed steel jacket study, the steel plates are only restrained at the direct fastening connections. Steel plates between connections are simply supported by the RC column. When steel plates are subjected to compressive stress, outgoing buckling occurs. This was investigated in a previous test. To predict the buckling strength of steel plates, a theoretical study was conducted by Shan et al. [24] and an expression was proposed combining the experimental results.

$$P_{p,\text{critical}} = \frac{4\pi^2 D d_p}{s_d^2} (1 - \alpha_i) \quad (6a)$$

$$D = \frac{E_p t_p^3}{12(1 - \mu_p^2)} \quad (6b)$$

where  $D$  is the bending stiffness of steel plates that are restrained by direct fastening connections at two ends.  $E_p$ ,  $\mu_p$  and  $t_p$  are the elastic modulus, Poisson's ratio and thickness of the steel plate, respectively.  $\alpha_i$  ( $0 < \alpha_i \leq 1.0$ ) is the initial imperfection factor, which is used to consider imperfections induced during the manufacture and welding processes. It is an empirical factor and was calibrated in accordance with experimental results.

$$\alpha_i = 1.046 - \frac{0.73\lambda_{sr}}{100} \quad (7)$$

It can be seen that this factor is related to the slenderness ratio ( $\lambda_{sr}$ ) of the steel plates, which is defined by  $s_d/t_p$ .

Based on the above-mentioned methods, the strength of confined concrete core 1, confined concrete core 2, unconfined concrete core 3, longitudinal steel rebar and steel plates can be predicted. As a result, the axial loading capacity of the strengthened RC columns can then be determined.

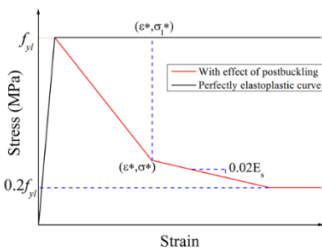


Fig. 8 Stress-strain curve of longitudinal rebar

## 5. Behavior of strengthened columns subjected to seismic loading

### 5.1. Experimental study

To further investigate the mechanical behavior of RC columns encompassing the direct fastening steel jackets under investigation, subject to seismic lateral loading, eight specimens were designed and tested. Four parameters, including connection spacing, number of fasteners, thickness of the

steel plate and axial load ratio (ALR), were examined [25]. The configuration of each specimen is shown in Fig. 9. The notation criterion follows that used for the specimens under axial load action, except that the ALR is added in. For example, the label of S-0.16-4-60-4 represents the ALR of the specimen being 0.16.

Lateral load capacity, ultimate drift ratio and flexural stiffness were examined. A larger ALR negatively affected the seismic behavior of the strengthened RC column, as expected. Reduced connection spacing means a smaller slenderness ratio, which improves the buckling behavior of steel plate. In response, the seismic behavior of a strengthened RC column using the steel jacket with closer connection spacing is preferable, which accords with observations from experimental study. The behavior of direct fastening connections was also investigated. It was found that two fasteners were sufficient to maintain the stability of the direct fastening connection. Regarding steel plate thickness, the seismic behavior of strengthened RC columns using a steel jacket with thick steel plates was greatly improved.

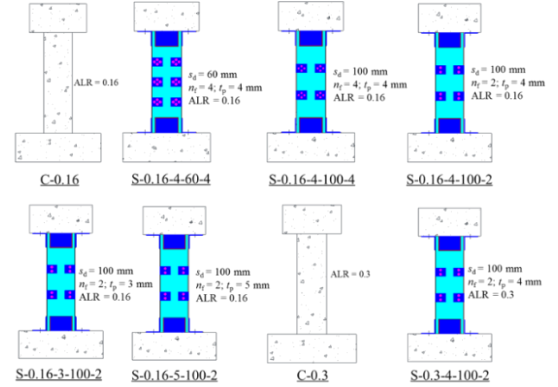


Fig. 9 Specimen configurations

### 5.2. Theoretical study

#### 5.2.1. Lateral load capacity

Following the plane-section assumption, the stress distribution profile can be obtained (see Fig. 10), based on which the expressions that can be used to predict lateral load are derived [30]. Because the ends of the steel jackets were fixed, detaching between the RC column and the tensile steel plate perpendicular to the lateral load was observed in tests. The contribution of this steel plate to the lateral load should be reduced, considering this incompatible deformation. Therefore, a reduction factor of  $\eta_i = 0.6$  is introduced [25].

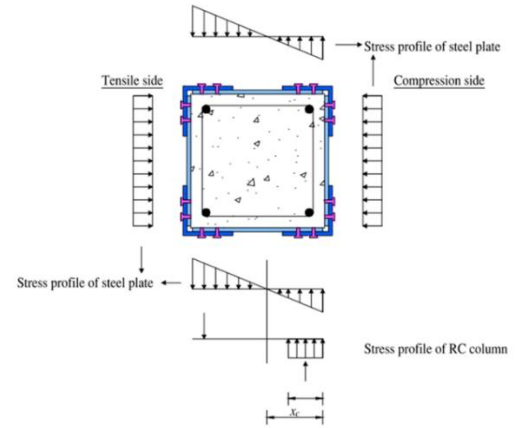


Fig. 10 Stress profile of strengthened RC column

#### 5.2.2. Effective flexural stiffness

RC columns strengthened by this proposed method behave in the manner of composite columns. Therefore, the flexural stiffness of strengthened RC columns can refer to the expressions of flexural stiffness for composite columns in previous specifications [28,29].

$$K_i = (EI)_s + \alpha_c (EI)_c \quad (8)$$

It can be seen that flexural stiffness is generated from two areas: the RC

column ( $(EI)_c$ ) and the steel jacketing ( $(EI)_s$ ).  $\alpha_c$  is the reduction factor, which is taken as 0.6, in accordance with [28], while it is related to the ratio of the cross-sectional area of the steel jacketing ( $A_{\text{jacketing}}$ ) to the cross-sectional area of the RC column ( $A_c$ ), as recommended in [29].

$$\alpha_c = 0.45 + \frac{3A_{\text{jacketing}}}{A_c} \leq 0.9 \quad (9)$$

By comparing with the flexural stiffness obtained from the test results, it is recommended that reduction factor  $\alpha_c$  takes a value of 0.6.

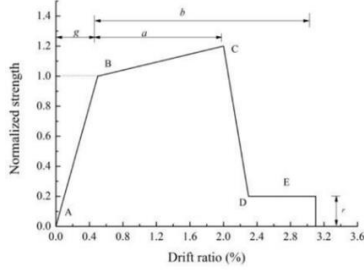


Fig. 11 Generalized force-deformation curve (ASCE 41-13)

### 5.2.3. Generalized force-deformation relationship

In order to undertake nonlinear analysis, the generalized force-deformation relationship is proposed in ASCE 41-13 [30], as shown in Fig. 11. Point B can be determined by effective stiffness and load capacity. Points C, D and E are controlled by three critical parameters: ALR, transverse reinforcement ratio and shear capacity ratio, which is defined by the capacity of flexural loading over the capacity of shear loading. This is an index used to identify failure mode. Because direct fastening connections act as stirrups in strengthened RC columns, this effect should be appropriately considered in the shear capacity and transverse reinforcement ratio.

For strengthened RC columns, the shear capacity contribution arises from three areas, as shown in the following equation:

$$V_0 = V_c + V_s + V_d \quad (10)$$

where  $V_c$ ,  $V_s$  and  $V_d$  are the shear loading undertaken by the concrete, stirrup and steel jacketing, respectively.

Two components of  $V_c$  and  $V_s$  can be determined by:

$$V_c = 0.17(1 + \frac{N_0}{14A_c})\lambda\sqrt{f_c}d_w \quad (11)$$

$$V_s = \frac{A_{st}f_{yst}d_w}{s_{st}} \quad (12)$$

where  $N_0$  depicts axial loading acting on the RC column.  $f_c'$  denotes concrete strength.  $d_w$  is the effective depth of the RC column.  $\lambda$  is a factor which can refer to ACI 318-14 [32].  $A_{st}$ ,  $f_{yst}$  and  $s_{st}$  are the cross-sectional area, yield strength and spacing of stirrups, respectively.

Analogous to stirrups, the shear contribution arising from the direct fastening connection is given as [25]:

$$V_d = 0.5 \frac{d_c}{s_d + d_d} 2nF_b \quad (13)$$

where  $F_b$  is the bearing strength of the direct fastening connection, which can be determined by Eq. (2).  $d_d$  signifies steel angle bracket length.

In strengthened RC columns, because direct fastening connections contribute to shear capacity, this effect should be considered in determining the transverse reinforcement ratio, which influences the generalized force-deformation relationship. As a result, an equivalent transverse reinforcement ratio, including stirrup ratio ( $\rho_v$ ) and the contribution from the direct fastening connection, was proposed by Shan et al. [25].

$$\rho_{veq} = \rho_v + \frac{2nF_b}{f_{yst}d_c(s_d + d_d)} \quad (14)$$

The generalized force-deformation curve can then be determined, combining the recommended parameter values in Table 3. Fig. 12 presents a comparison of generalized force-deformation curves determined by the equivalent transverse reinforcement ratio and the stirrup ratio. This indicates that use of the equivalent transverse reinforcement ratio is appropriate.

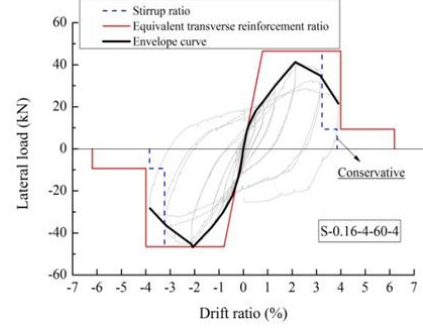


Fig. 12 Generalized force-deformation curve of strengthened RC column

Table 3

Parameters for generalizing force-deformation curve of RC column

	ALR	$\rho_{veq}$	Modeling parameter		
			$a$	$b$	$r$
Condition	$\leq 0.1$	$\geq 0.006$	0.035	0.060	0.2
(i)	$\geq 0.6$	$\geq 0.006$	0.010	0.010	0.0
	$\leq 0.1$	0.002	0.027	0.034	0.2
	$\geq 0.6$	0.002	0.005	0.005	0.0

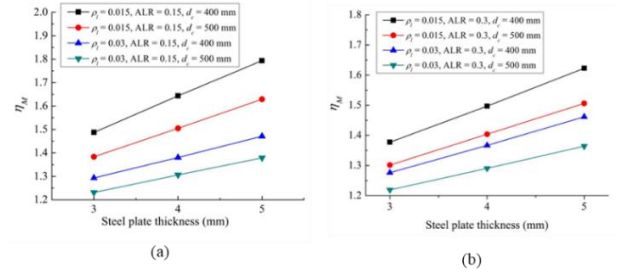


Fig. 13 Relationship between thickness of steel plates and enhancement ratio of flexural strength: (a) ALR = 0.15; and (b) ALR = 0.3

## 6. Design procedure of strengthened columns

To facilitate the application of the novel strengthening method in strengthening damaged RC columns with flexural strength and flexural stiffness deficiency, a design procedure was developed by Shan et al. [26]. In this section, the critical steps in the design procedure are presented.

Three parameters must be determined in direct fastening steel jackets: spacing of direct fastening connection, steel plate thickness and number of fasteners.

### (1) Spacing of direct fastening connection

Preferable flexural failure is the expected failure mode in design. Existing lateral loading, flexural capacity and shear capacity should satisfy the following relationship to guarantee the occurrence of this failure mode:

$$V \leq V_{cap, stren} \leq 0.6V_{stren} \quad (15)$$

where  $V$  signifies the existing lateral load.  $V_{stren}$  and  $V_{cap, stren}$  are the shear capacity and flexural capacity of the strengthened RC columns.

Since the existing lateral load is known, connection spacing can be determined by combining Eqs. (10) and (15). In this way, direct fastening connection spacing can be determined.

### (2) Steel plate thickness



The flexural capacity of strengthened RC columns is related to the thickness of the steel plates. A parameter study was carried out to investigate the relationship between the thickness of steel plates and the enhancement ratio of flexural strength ( $\eta_M = V_{cap,strengthen}/V_{cap}$ , where  $V_{cap}$  is the flexural capacity of the RC column requiring strengthening). Fig. 13 shows the parameter study results, which can be used to select the thickness of steel plates during practical design.

### (3) Number of fasteners

The axial load capacity and shear capacity of strengthened RC columns were influenced by the number of fasteners. It was evident from the experimental study on the seismic behavior of strengthened RC columns that two fasteners are sufficient to maintain connection stability. Therefore, the number of fasteners is initially taken as two.

The design procedure of strengthened RC columns is summarized in Fig. 14. Firstly, the flexural capacity of the damaged RC column ( $V_{cap}$ ) should be estimated. Secondly, in accordance with the enhancement ratio of flexural strength ( $\eta_M = V/V_{cap}$ ), the thickness of the steel plates can be determined from Fig. 13. Thirdly, connection spacing can be initially determined by satisfying the relationship set out in Eq. (15). Lastly, three conditions should be satisfied: Condition (i) should guarantee that flexural capacity is not less than lateral demand; Condition (ii) requires that the axial load ratio is not higher than 0.65, as recommended in EN 1998-1:2004 [31]; and Condition (iii) aims to keep the deformation demand of the strengthened RC column comparable to that of the undamaged RC column, which requires the effective flexural stiffness of the strengthened RC column to be comparable to that of the undamaged RC column. If these three conditions cannot be satisfied, the number of fasteners, direct fastening connection and steel plate thickness should be updated until these three conditions are satisfied.

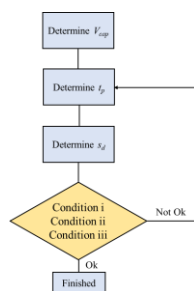


Fig. 14 Design procedure of strengthened RC column

## References

- [1] Wang, L. and Su, R.K.L., "Repair of fire-exposed preloaded rectangular concrete columns by postcompressed steel plates", *Journal of Structural Engineering*, 140(3), 04013083, 2014.
- [2] Lin, C.H. and Tsay, C.S., "Deterioration of strength and stiffness of reinforced concrete columns after fire", *Journal of the Chinese Institute of Engineers*, 13(3), 273-283, 1990.
- [3] Li, H.W., Xu, Z.D., Wang, F., Gai, P.P., Gomez, D. and Dyke, S.J., "Development and Validation of a Nonlinear Model to Describe the Tension-Compression Behavior of Rubber-Like Base Isolators", *Journal of Engineering Mechanics*, 149(2), 04022104, 2023.
- [4] Li, Q.Q., Xu, Z.D., Dong, Y.R., He, Z.H., He, J.X. and Yan, X., "Hyperelastic Hybrid Molecular Chain Model of Thermal-Oxidative Aging Viscoelastic Damping Materials Based on Physical-Chemical Process", *Journal of Engineering Mechanics*, 149(1), 04022099, 2023.
- [5] Hwang, E., Kim, G., Choe, G., Yoon, M., Gucunski, N. and Nam, J., "Evaluation of concrete degradation depending on heating conditions by ultrasonic pulse velocity", *Construction and Building Materials*, 171, 511-520, 2018.
- [6] Xu, Z.D., Liao, Y.X., Ge, T. and Xu, C., "Experimental and theoretical study on viscoelastic dampers with different matrix rubbers", *Journal of Engineering Mechanics*, 142(8), 04016051, 2016.
- [7] Xu, Z.D., "Earthquake mitigation study on viscoelastic dampers for reinforced concrete structures", *Journal of Vibration and Control*, 13(1), 29-45, 2007.
- [8] Vieira, J.P.B., Correia, J.R. and De Brito, J., "Post-fire residual mechanical properties of concrete made with recycled concrete coarse aggregates", *Cement and Concrete Research*, 41(5), 533-541, 2011.
- [9] Demers, M. and Neale, K.W., "Confinement of reinforced concrete columns with fibre-reinforced composite sheets – an experimental study", *Canadian Journal of Civil Engineering*, 26(2), 226-241, 1999.
- [10] Wu, H.L., Wang, Y.F., Yu, L. and Li, X.R., "Experimental and computational studies on high-strength concrete circular columns confined by aramid fiber-reinforced polymer sheets", *Journal of Composites for Construction*, 13(2), 125-134, 2009.
- [11] Yan, Z. and Pantelides, C.P., "Concrete column shape modification with FRP shells and expansive cement concrete", *Construction and Building Materials*, 25(1), 396-405, 2011.
- [12] Silva, M.A., "Behavior of square and circular columns strengthened with aramid or carbon fibers", *Construction and Building Materials*, 25(8), 3222-3228, 2011.
- [13] Chang, S.Y., Chen, T.W., Tran, N.C. and Liao, W.I., "Seismic retrofitting of RC columns with RC jackets and wing walls with different structural details", *Earthquake Engineering and Engineering Vibration*, 13(2), 279-292, 2014.
- [14] Júlio, E.N.B.S., Branco, F.A. and Silva, V.D., "Reinforced concrete jacketing-interface influence on monotonic loading response", *ACI Structural Journal*, 102(2), 252-257, 2005.
- [15] Meda, A., Mostosi, S., Rinaldi, Z. and Riva, P., "Corroded RC columns repair and strengthening with high performance fiber reinforced concrete jacket", *Materials and*

## 7. Conclusions

This paper focuses on reviewing an innovative strengthening method (i.e., direct fastening steel jackets), by which the strength and flexural stiffness of RC columns can be simultaneously enhanced. Some key conclusions of this innovative strengthening method are summarized below.

(1) The protuberance and knurling of the surface impact positively on bearing capacity, the effects of which have been considered alongside two empirical factors. Effectiveness stiffness relates to the number of fasteners, fastener diameter, the elastic modulus of the steel material and steel plate thickness, while the expression of ultimate displacement is based on the rotation and friction mechanisms of the fastener.

(2) Both axial load capacity and deformation capacity are greatly improved. The confinement effect and buckling effect should be considered when axial load capacity is determined.

(3) The seismic behavior of strengthened RC columns is significantly improved. The detaching of tensile steel plate and buckling of compressive steel plate were observed during the test. To consider this effect, a reduction factor of 0.6 was introduced into the flexural capacity model. Effective flexural stiffness was significantly enhanced, which can be predicted by the expression recommended in EN 1994-1-1:2004. A method of evaluating the generalized force-deformation relationship was developed, in which an equivalent transverse reinforcement ratio was used.

(4) For the design procedure of strengthened RC columns, the number of fasteners, thickness of the steel plates and direct fastening connection spacing should initially be determined. For the initially determined direct fastening connection spacing and thickness of the steel plates, three specified conditions should be checked.

## Acknowledgements

The work described in this paper was supported by the National Natural Science Foundation of China (Grant No. 52208465), the Major Project of Fundamental Research on Frontier Leading Technology of Jiangsu Province (No. BK20222006) and a grant from the high level personnel project of Jiangsu Province.

- [16] Deng, M. and Zhang, Y., "Cyclic loading tests of RC columns strengthened with high ductile fiber reinforced concrete jacket", *Construction and Building Materials*, 153, 986-995, 2017.
- [17] Mourad, S.M. and Shannag, M.J., "Repair and strengthening of reinforced concrete square columns using ferrocement jackets", *Cement and concrete composites*, 34(2), 288-294, 2012.
- [18] Nagaprasad, P., Sahoo, D.R. and Rai, D.C., "Seismic strengthening of RC columns using external steel cage", *Earthquake Engineering and Structural Dynamics*, 38(14), 1563-1586, 2009.
- [19] Garzon-Roca, J., Ruiz-Pinilla, J., Adam, J.M. and Calderón, P.A., "An experimental study on steel-caged RC columns subjected to axial force and bending moment", *Engineering Structures*, 33(2), 580-590, 2011.
- [20] Sahoo, D.R. and Rai, D.C., "A novel technique of seismic strengthening of nonductile RC frame using steel caging and aluminum shear yielding damper", *Earthquake Spectra*, 25(2), 415-437, 2009.
- [21] Xu, C.X., Peng, S., Deng, J. and Wan, C., "Study on seismic behavior of encased steel jacket-strengthened earthquake-damaged composite steel-concrete columns", *Journal of Building Engineering*, 17, 154-166, 2018.
- [22] Shan, Z.W. and Su, R.K.L., "Behavior of shear connectors joined by direct fastening", *Engineering Structures*, 196, 109321, 2019.
- [23] Shan, Z.W. and Su, R.K.L., "Axial strengthening of RC columns by direct fastening of steel plates", *Structural Engineering and Mechanics*, 77(6), 705-720, 2021.
- [24] Shan, Z.W., Looi, D.T.W. and Su, R.K.L., "Confinement model for RC columns strengthened with direct-fastened steel plate", *Steel and Composite Structures*, 39(4), 367-381, 2021.
- [25] Shan, Z.W., Looi, D.T.W. and Su, R.K.L., "A novel seismic strengthening of RC columns by direct fastening steel plates", *Engineering Structures*, 218, 110838, 2020.
- [26] Shan, Z.W., Chen, L.J., Liang, K., Su, R.K.L. and Xu, Z.D., "Strengthening design of RC columns with direct fastening steel jackets", *Applied Science*, 11(8), 3649, 2021.
- [27] Dhakal, R.P. and Maekawa, K., "Modeling for postyield buckling of reinforcement", *Journal of Structural Engineering*, 128(9), 1139-1147, 2002.
- [28] EN 1994-1-1:2004, Design of Composite Steel and Concrete Structures. Part 1-1: General Rules and Rules for Buildings, European Committee for Standardization, 2004.
- [29] ANSI/AISC 360-16, Specification for Structural Steel Buildings. American Institute of Steel Construction, Chicago, US, 2016.
- [30] ASCE/SEI 41-13, Seismic Evaluation and Retrofit of Existing Buildings, ASCE Standard. Reston, Virginia, US, 2014.
- [31] EN 1998-1:2004, Design of Structures for Earthquake Resistance. Part 1: General Rules, Seismic Actions and Rules for Buildings, European Committee for Standardization, 2004.
- [32] ACI Committee 318, Building Code Requirements for Structural Concrete (ACI 318RM-14) and Commentary (ACI 318RM-14), Farmington Hills, American Concrete Institute, 2015.

# DEEP LEARNING DAMAGE IDENTIFICATION METHOD FOR STEEL-FRAME BRACING STRUCTURES USING TIME–FREQUENCY ANALYSIS AND CONVOLUTIONAL NEURAL NETWORKS

Xiao-Jian Han<sup>1</sup>, Qi-Bin Cheng<sup>1</sup> and Ling-Kun Chen<sup>2, 3, 4, \*</sup>

<sup>1</sup> College of Civil Engineering, Nanjing Tech University, Nanjing, 211800 Jiangsu, China

<sup>2</sup> College of Civil Science and Engineering, Yangzhou University, Yangzhou, 225127 Jiangsu, China

<sup>3</sup> Department of Civil and Environmental Engineering, University of California, Los Angeles, CA 90095 USA

<sup>4</sup> School of Civil Engineering, Southwest Jiaotong University, Chengdu, 610031 Sichuan, China

\* (Corresponding author: E-mail: lingkunchen08@hotmail.com)

## ABSTRACT

Lattice bracing, commonly used in steel construction systems, is vulnerable to damage and failure when subjected to horizontal seismic pressure. To identify damage, manual examination is the conventional method applied. However, this approach is time-consuming and typically unable to detect damage in its early stage. Determining the exact location of damage has been problematic for researchers. Nevertheless, detecting the failure of lateral supports in various parts of a structure using time–frequency analysis and deep learning methods, such as convolutional neural networks, is possible. Then, the damaged structure can be rapidly rebuilt to ensure safety. Experiments are conducted to determine the vibration acceleration modes of a four-storey steel structure considering various support structure damage scenarios. The acceleration signals at each measurement point are then analysed with respect to time and frequency to generate appropriate three-dimensional spectral matrices. In this study, the MobileNetV2 deep learning model was trained on a labelled picture collection of damaged matrix images. Hyperparameter tweaking and training resulted in a prediction accuracy of 97.37% for the complete dataset and 99.30% and 96.23% for the training and testing sets, respectively. The findings indicate that a combination of time–frequency analysis and deep learning methods may pinpoint the position of the damaged steel frame support components more accurately.

## ARTICLE HISTORY

Received: 18 July 2022  
Revised: 15 June 2023  
Accepted: 27 August 2023

## KEYWORDS

Damage identification;  
Bracing system;  
Deep learning;  
Convolutional neural networks (CNNs);  
Time–frequency analysis;  
MobileNetV2

Copyright © 2023 by The Hong Kong Institute of Steel Construction. All rights reserved.

## 1. Introduction

A support system is an important part of a steel structure. It ensures that the entire steel structure and individual components have sufficient stability and stiffness. Moreover, the system enables the transfer of horizontal forces and absorption of seismic energy as well as improves the overall performance of the steel structure. Among all types of supports, supports between two adjacent columns are vital for ensuring overall stability, horizontal load transfer, and earthquake resistance. Cross-diagonal bracing, splay diagonal bracing, and door-type support are typically adopted as column supports. Because the stiffness of the column support system must be consistent, steel angles or channels are typically used.

However, owing to the inherent defects of steel materials, environmental corrosion, natural disasters, and other factors, the inter-column support system in a steel may be damaged during use. With the accumulation of damage, the failure of the support, particularly under the action of a seismic load, may lead to the inability of the structure to transfer horizontal load effectively, resulting in significant deformation, structural instability, or collapse.

For a given steel structure, the damage identification method typically involves several steps, such as locating the damage, identifying the type and degree of damage, and estimating the remaining life of the structure. The current damage detection methods are primarily manual visual observation or the use of special detection equipment. Generally, the bolts in steel structures have been found to be loose, rusted, broken, or sustaining other types of damage.

With the application of various structural health monitoring (SHM) systems, the number of sensors used to obtain the state data of a structure for evaluating the health status continues to increase. These sensors provide supporting data for the subsequent design of structural reinforcement and maintenance scheme [1–5]. Therefore, analysing the location and degree of damage of structural support systems using the dynamic response data of structures obtained by an SHM system or detection instrument is advantageous.

Structural damage identification methods are typically designed considering three aspects: (a) optimisation of modal structural parameters to identify indicators susceptible to structural damage; (b) use of an artificial intelligence algorithm to determine the location and degree of damage; and (c) structural damage identification using the combination of structural dynamics, finite element (FE) modelling, vibration tests, and artificial intelligence algorithms. Yazdanpanah et al. [6–7] employed incremental non-linear dynamic analysis to diagnose damage to steel moment-resisting frames in different seismic scenarios. Tam et al. [8] used noise, incomplete modal data, and a depth

feedforward neural network to locate and quantify damage in truss structures. Xin et al. [9] proposed an effective method for detecting non-linear structural degradation based on variational modal decomposition. Liu et al. [10] analysed the sensitivity of structural modal parameters to damage and quantified the degree of reduction in structural stiffness. Han et al. [11] proposed a method based on the Hilbert–Huang transform to identify structural modal parameters and diagnose structural damage. Paral et al. [12] analysed the overall vibration signal using a wavelet transform and convolutional neural network (CNN) to identify the damage to the local connection of a two-storey structural steel frame. Pathirage et al. [13–14] developed a deep learning framework for a sparse automatic encoder for structural damage identification. Hakim et al. [15–16] used an integrated neural network to locate and evaluate damage to an I-steel structure. Seventekidis et al. [17] used the data samples of an optimised FE model as input into a CNN for structural damage identification. Liu et al. [18] created a large-scale dataset based on a structural transfer function and established a new framework for structural damage identification using a one-dimensional CNN. Figueiredo et al. [19] combined the SHM field data and FE modelling data of a bridge structure to form a machine learning model input for bridge damage assessment.

Nadith et al. [20] developed an autoencoder-based deep neural network capable of analysing the link between structural vibrations and structural damage, laying the groundwork for diagnosing non-linear structural damage. Gordan et al. [21] used the vibration testing of a plate and beam bridge model to extract the top four orders of their inherent frequencies as input vectors for support vector machines, neural networks, and classification regression trees. Their findings indicated that the procedure was entirely accurate. Ali and Cha [22] suggested a technique based on deep learning for identifying subsurface damage to steel members in steel truss bridges; the field test results on a steel bridge demonstrated the high accuracy and practicality of the approach. Kourehli and Ghadimi [23] used the emergency learning algorithm of an inline sequential limit learning machine to anticipate the fracture depth and position of a Timoshenko beam. Teng et al. [24] used FE numerical analysis and experimental data to provide a considerable amount of damage data for a CNN. This improved the CNN-based damage detection algorithms in engineering practice.

Typically, lateral bracing is used to ensure the overall rigidity of a steel structural system; however, it is prone to damage and failure when the structure is subjected to horizontal seismic loads. A typical approach to determine damage is manual examination; however, this requires a considerable amount of time, and some damage points may not be detected. This problem has long been a

source of contention among academics attempting to identify the exact location of damage. The time–frequency domain and CNNs have been used to identify lateral bracing failure in various parts of a structure. Then, the damaged part of the structure is located and repaired to ensure structural safety.

In this study, modal information is obtained from structural detection. The spectrum of structural time–frequency domain analysis is obtained to establish a labelled spectrum sample library. The spectrum is classified through an image recognition method based on a CNN; MobileNetV2 derives the classification model. In subsequent stages, the spectrum analysis diagram can be inputted into the model to determine the damage location. Limited research has been conducted on damage identification methods combining signal analysis and image processing. This method is explored in this study, and satisfactory results are obtained.

The remainder of this paper is organised as follows. The details of the steel frame vibration testing procedure covering the test object, design, instruments, outcome analysis are presented in Section 2. The construction and results of the FE modelling process for the steel frame structure are discussed in Section 3. The characteristics, construction, and performance evaluation of the MobileNetV2 model for structural damage identification are presented in Section 4. Finally, the conclusions drawn based on the MobileNetV2 classification performance and vibration testing results are summarised in Section 5.

## 2. Vibration testing of steel frame model

### 2.1. Steel frame model description

A four-storey steel frame model is used in this study. Because this model was evaluated on a seismic simulation shaker with associated equipment and structure, it was designed with a geometric similarity ratio of 1:10. The model height, span spacing, floor height, beam length are 1.8, 0.6, 0.45, and 0.56 m, respectively. For the beam and inter-column support sections,  $60 \times 30 \times 2.5$ -mm

cold-formed thin-walled channels are used. According to the dynamic similarity ratio theory, the model weighs 45.1 kg, and the counterweight is 155 kg. The fundamental frequency of the structure is 5.165 Hz.

The parameters of the steel frame members are listed in Table 1. A steel frame without a bracing system is illustrated in Fig. 1.



Fig. 1 Steel frame model without bracing system (left) and with bracing member (right)

**Table 1**  
Parameters of members of steel frame model

Parameters		
Height (mm)		1800
Quality (kg)		45.1
Counterweight (kg)		766.20
Column	Column height (mm)	450
	Section size (mm)	40×40×2
	Area (mm <sup>2</sup> )	287
	Moment of inertia (mm <sup>4</sup> )	66600
	Moment of area (mm <sup>3</sup> )	3330
Beam	Beam length (mm)	560
	Section size (mm)	60×30×2.5
	Area (mm <sup>2</sup> )	240
	Moment of inertia (mm <sup>4</sup> )	143800
	Moment of area (mm <sup>3</sup> )	4890

### 2.2. Test scheme design

Eight bracing members were placed on both sides of each of the four layers of the steel frame model. The spatial layout and serial numbers of members are shown in Fig. 2. The serial numbers facilitate the construction of the deep learning model and image dataset as well as associated labels.

Five dismantling conditions were set for the bracing members in the vibration test. Under the first condition, no dismantling of the bracing members was set. The second condition requires the dismantling of the bracing element. Two, three, and four bracing members are removed for the third, fourth, and fifth types of structures, respectively. A total of 69 dismantling conditions are listed in Table 2, and vibration tests are conducted under these conditions. When three or four members are dismantled, note that not all potential combinations are listed in the table.

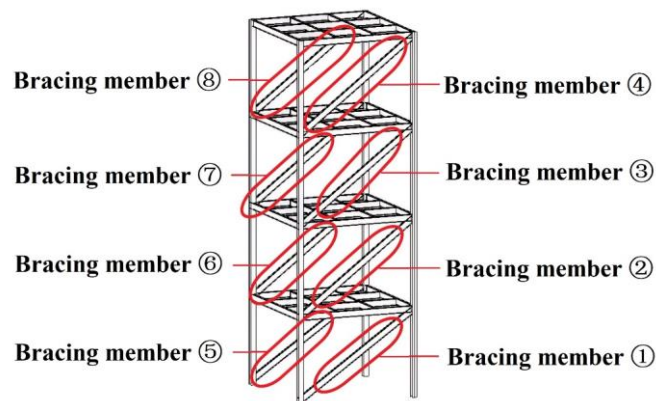


Fig. 2 Spatial layout and serial numbers of eight bracing members

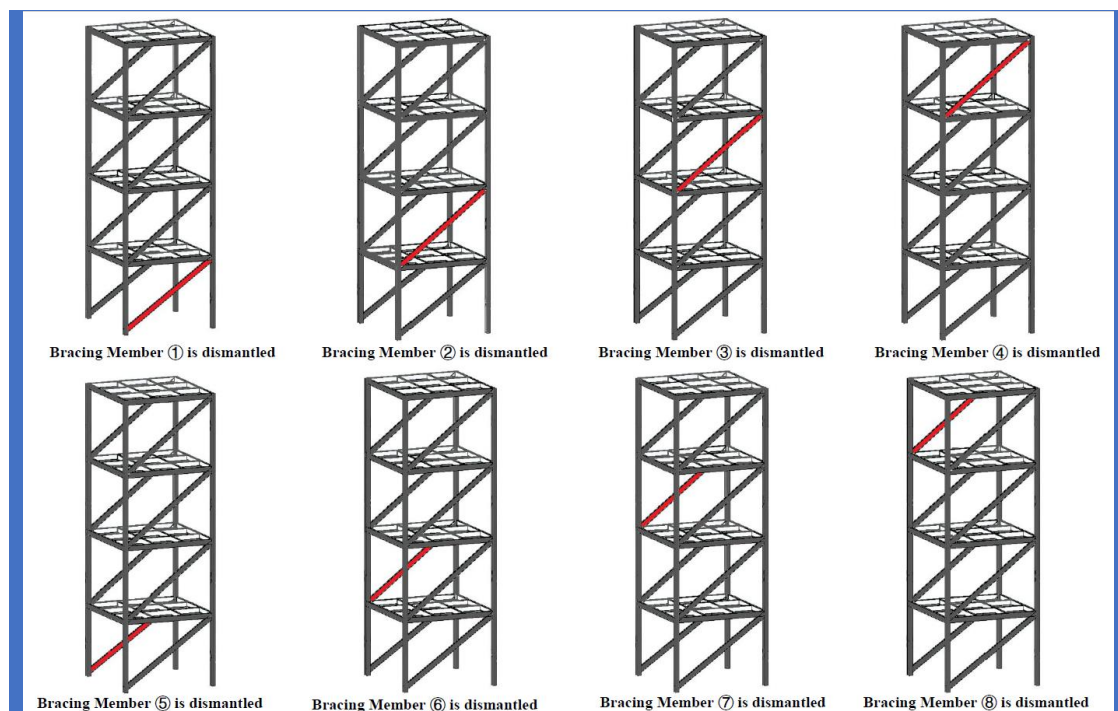


Fig. 3 Schematic of dismantling working condition of bracing member

Under each dismantling condition, a displacement load of 1 cm is applied to the top layer of the steel frame. Then, the resulting acceleration signals of each layer are acquired during the natural vibration stage. The vibration direction of the steel frame is shown in Fig. 4, and the spatial layout of the acceleration measurement points is shown in Fig. 5.

The selection of the appropriate sampling frequency of structural vibration signals is crucial. The use of a low sampling frequency results in signals with limited information content, whereas the use of a high sampling frequency leads to low-frequency resolution. Hence, the sampling frequency must satisfy or slightly exceed the Nyquist sampling frequency [25–28]. Specifically, to retain the information content of continuous signals in the sampled signal to the extent possible, the sampling frequency used is generally 2.56–4 times the highest frequency of the constant signal.

The preliminary results of the FE simulations indicate that the first-order and fourth-order frequency ranges of the steel frame are 5.7–6.5 and 30–31 Hz, respectively. A sampling frequency of 128 Hz was selected, and the signal acquisition time was set to 10 s. To reduce the test error, the acquisition of acceleration signals was repeated three times under each working condition.



Fig. 4 Vibration direction of steel frame

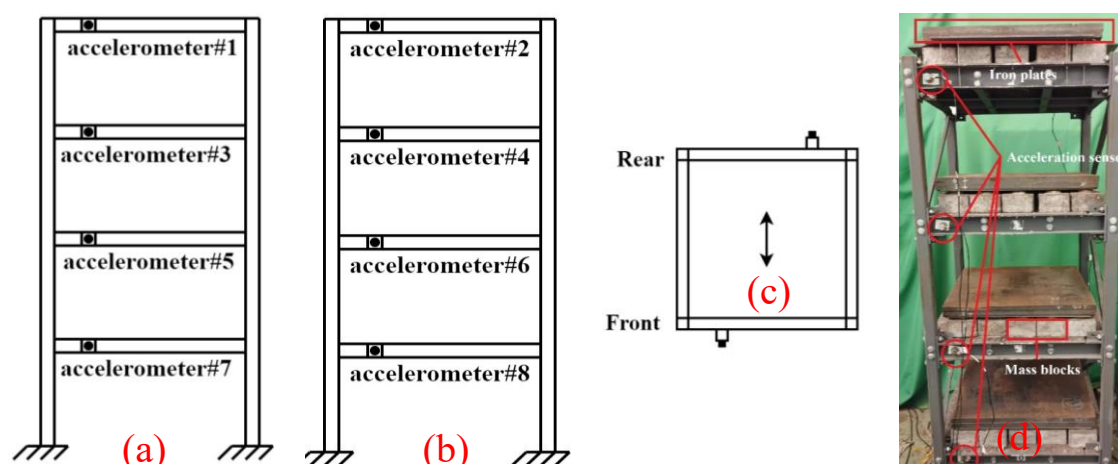


Fig. 5 Arrangement of acceleration measurement points: (a) front view, (b) rear view, (c) top view, and (d) sensor arrangement



### 2.3. Test instruments

A vibration test was conducted using an NI9234 signal acquisition device with an LC0108 IEPE acceleration sensor as well as the DASP acquisition and processing software. The sensor and acquisition equipment are shown in Fig. 6. This type of acceleration sensor fits the criteria of this test owing to its light weight, high sensitivity, and wide frequency range. The sensors were calibrated

to obtain accurate and reliable data. The performance parameters of the acceleration sensors are listed in Table 2. A magnetic base was attached to the acceleration sensor at the steel measuring site. The acquisition software includes tools for signal and modal analyses. The acquisition frequency employed in the test was 120 Hz, and the sampling frequency was determined using the maximum value of  $\text{FFT} \times 2$ .

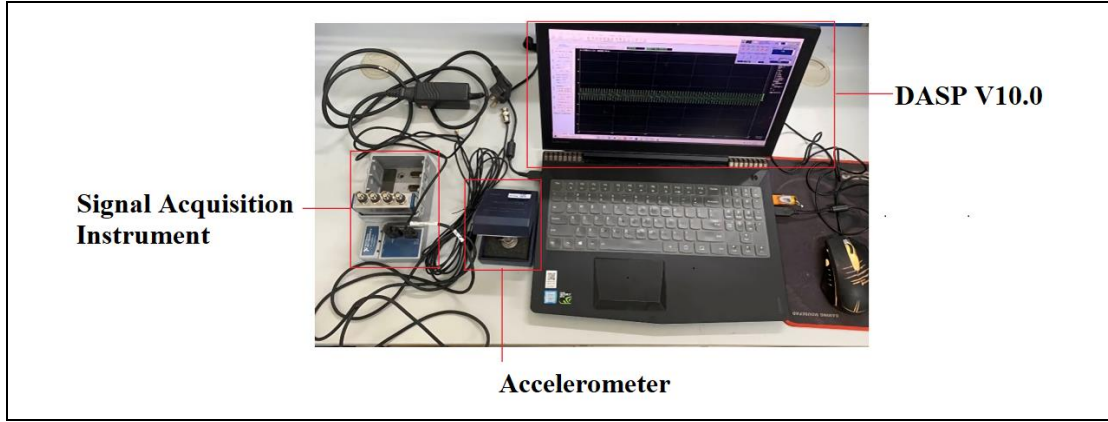


Fig. 6 Test instrument

Table 2

Performance parameters of LC0108 acceleration sensors

Frequency range (Hz)	Sensitivity (Mv/EU)	Weight (mg)	Thread Specification	Boundary Dimension
0.35-5000	497-504	17	M5	Hexagon Side length: 14mm Height: 20mm

### 2.4. Analysis of vibration test results

Fourier transform can be used to analyse the frequency content of non-stationary signals; its computational algorithms demonstrate high precision and efficiency. This transform converts the time-domain acceleration signals into frequency-domain signals. The forward and inverse discrete-time Fourier transforms for the discrete-time signal,  $X[n]$ , are determined using Equations (1) and (2), where  $N$  is the number of signal samples:

$$X(e^{j\omega}) = \sum_{n=-(N)}^N X[n]e^{-j\omega n} \quad (1)$$

$$X[n] = \frac{1}{2\pi} \int_{-\pi}^{\pi} X(e^{j\omega})e^{j\omega n} d\omega \quad (2)$$

The discrete-time Fourier transform analyses the acquired acceleration signals using 1024 signal samples. The time-domain acceleration signals are converted into frequency-domain signals, and the natural vibration frequencies of the steel frame are extracted. Under each operating condition, the average frequency is computed over three test repetitions and used as the final frequency result.

To account for the influence of torsion, each layer has two diagonally arranged accelerometers. The overlaid time-domain signals acquired by the accelerometers can be used to calculate both advection and torsion components; however, only the advection component is utilised in this study. The time-domain and frequency-domain analysis results for the top layer are presented in Figs. 7 and 11, respectively. In Figs. 9 and 10, the time-domain plots depict the two acceleration averages of the top layer. The frequency-domain plots show the torsional components at 5.25 (Fig. 9) and 5.125 Hz (Fig. 10).

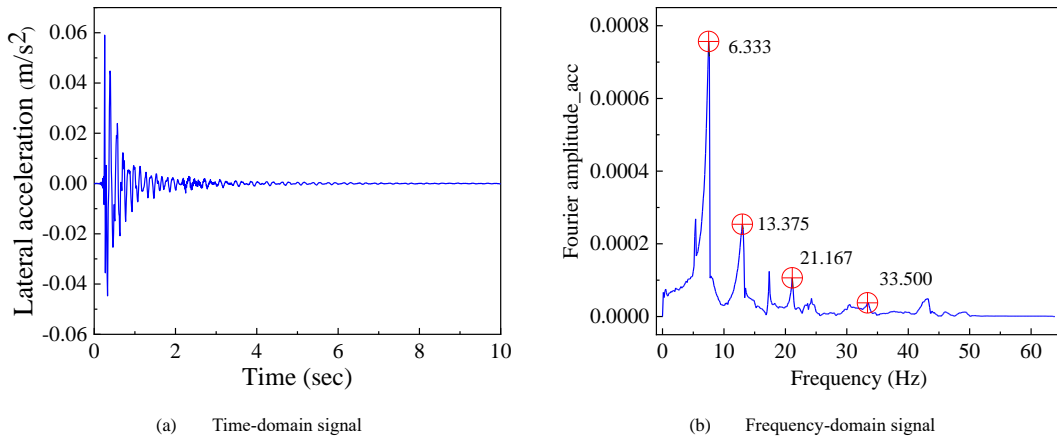
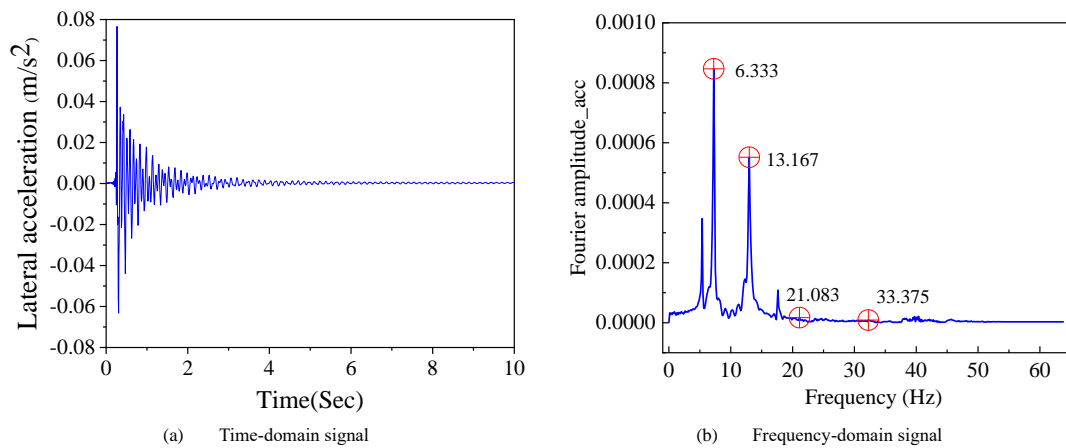
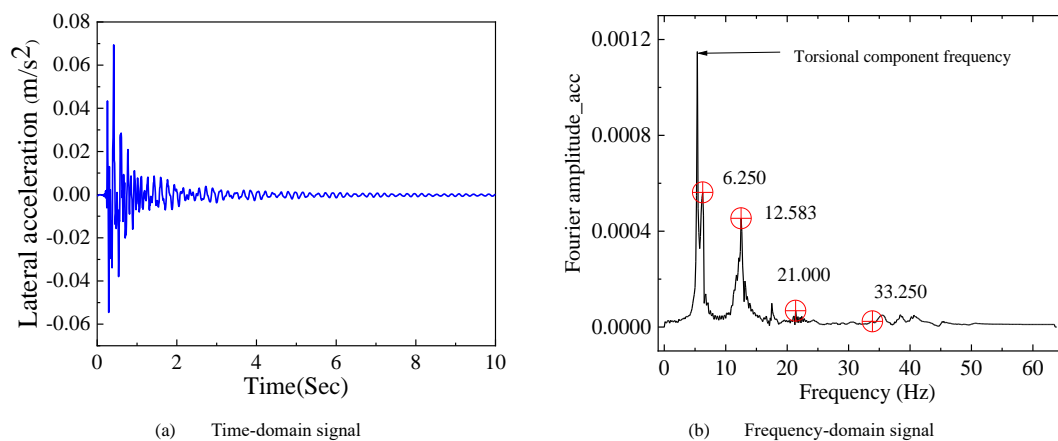


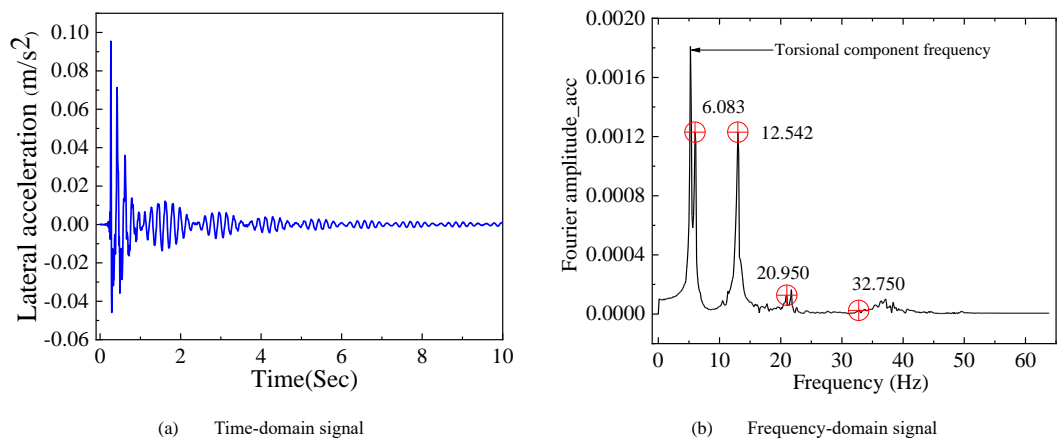
Fig. 7 Time-domain and frequency domain curves when no support member is removed



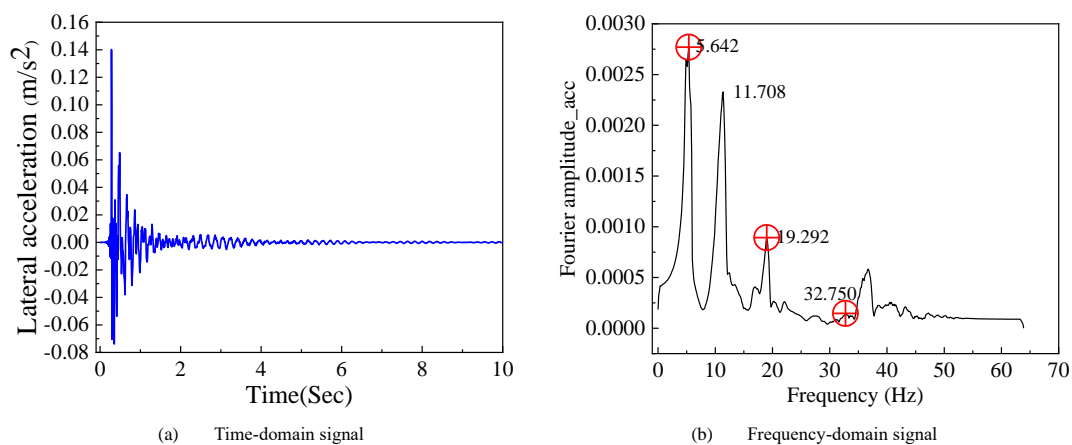
**Fig. 8** Time-domain and frequency-domain curves of one support member removed (#1)



**Fig. 9** Time-domain and frequency-domain plots for two support members removed (#12)



**Fig. 10** Time-domain and frequency-domain diagrams of three support members removed (#123)



**Fig. 11** Time-domain and frequency-domain diagrams of four support members removed (#1234)

**Table 3**

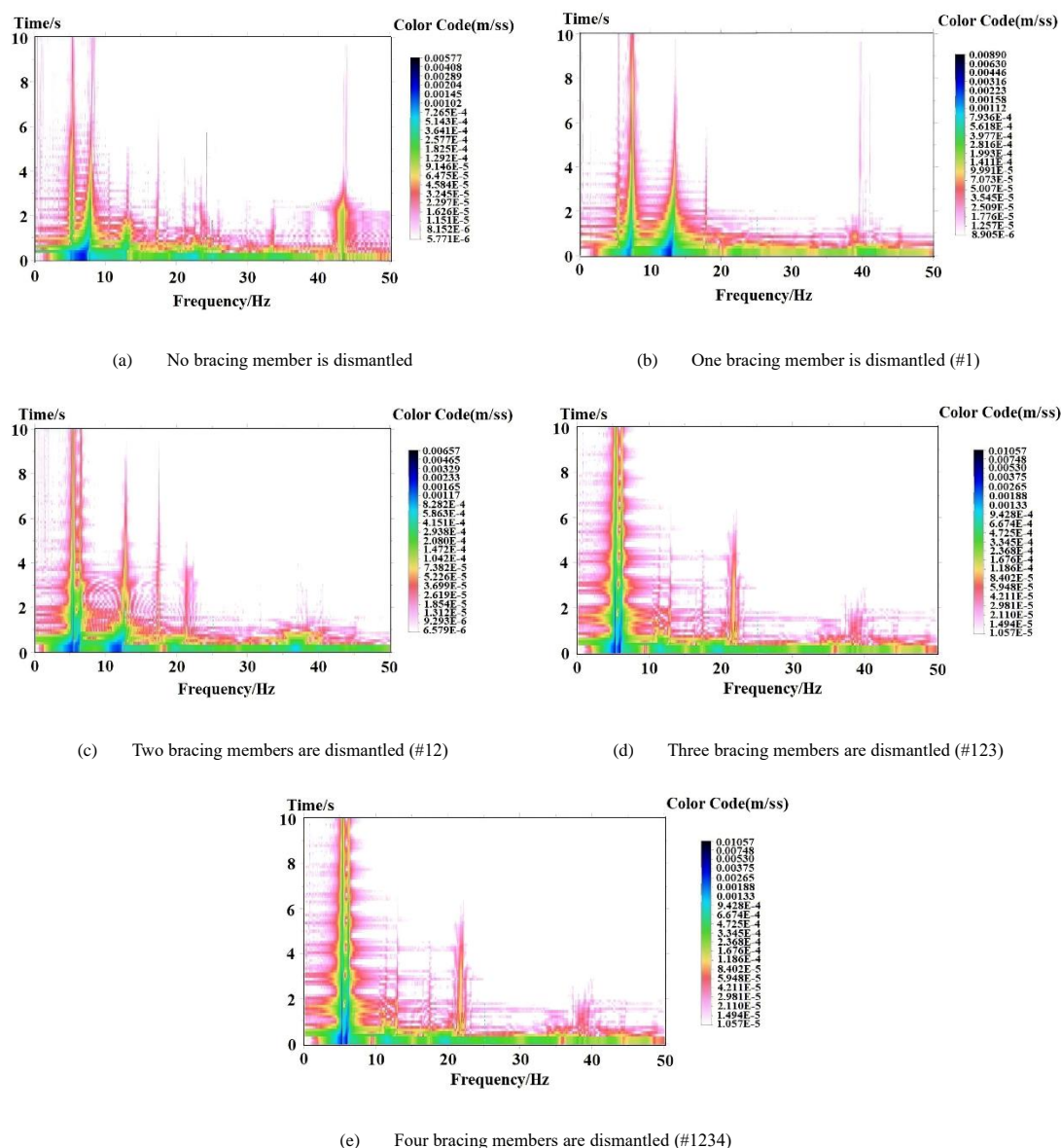
First-order to fourth-order steel frame frequencies under some working conditions

Working Condition	The frequencies/Hz			
	1 <sup>st</sup> order	2 <sup>nd</sup> order	3 <sup>rd</sup> order	4 <sup>th</sup> order
Undamaged	6.333	13.375	21.167	33.500
#1	6.333	13.167	21.083	33.375
#12	6.250	12.583	21.000	33.250
#123	6.083	12.542	20.950	32.750
#1234	5.642	11.708	19.292	32.750

The maximum energy signal increases with the frequency-domain peak amplitude. By combining the spectral signals with preliminary FE analysis results, the first-order up to the fourth-order steel frame frequencies can be obtained. The frequencies under some working conditions are listed in Table 3.

The wavelet transform was used to analyse the acceleration signals in the

time-frequency domain; the corresponding three-dimensional spectral matrices were obtained. Examples of these matrices under certain operating conditions are shown in Fig. 12. The horizontal and vertical axes correspond to frequency and time values, respectively. Colours are used to code the scale of acceleration values at specific time-frequency points.

**Fig. 12** Three-dimensional time-frequency matrices of acceleration signals under some working conditions

Each three-dimensional spectral matrix contains joint time–frequency information, which can characterise structural damage more accurately than time-domain or frequency-domain representation. Additionally, the proposed time–frequency representations are more sensitive to the dismantling of the bracing members of the steel frame model.

### 3. Numerical simulation of steel frame model

#### 3.1. FE modelling

FE modelling and analysis of the steel frame were performed using the ABAQUS software. The FE model was modified according to the frequencies obtained from the vibration tests to maintain the error within an acceptable range. The steel frame was geometrically modelled as a rod-like system structure. Some of the geometric modelling details are as follows. First, the node coordinates are specified according to the geometric dimensions of the steel

frame. Additionally, line units are created using a node-to-node correspondence method where all nodes are rigidly set, and the bottom of columns is fully fixed. Datum planes and reference points are established to divide the steel frame and generate floor slabs and frame beams. The frame beams must be longitudinal to form common coupling nodes with the floor slabs.

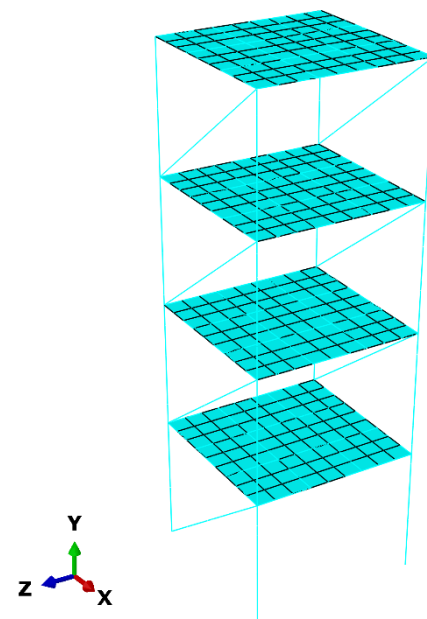
The unit system, material properties, and section properties are set during modelling. The unit system is set as follows: length, force, and stress are measured in meter, newton, and pascal, respectively. The characteristics of steel and iron materials, including density, elastic modulus, and Poisson's ratio, are listed in Table 4. The sections to be modelled are those of the steel column, frame beam, bracing member, and floor.

**Table 4**  
Material characteristics for steel frame model

Material	Density(kg/m <sup>3</sup> )	Elastic modulus (Pa)	Poisson's ratio
Steel	7850	2.06E11	0.3
Iron	7870	2.05E11	0.28

The structural analysis of the FE model is further subdivided into analysis steps using different methods in ABAQUS. To identify the steel frame frequencies, the frequency option of the linear perturbation method is selected, and three frequency feature methods are explored: Lanczos method [29–30], subspace method, and automatic multi-level substructure method. Because extracting the frequency of steel frames is limited to low orders, the Lanczos method is used to obtain the frequencies because it demonstrates high speed and accuracy in obtaining such low-order frequencies.

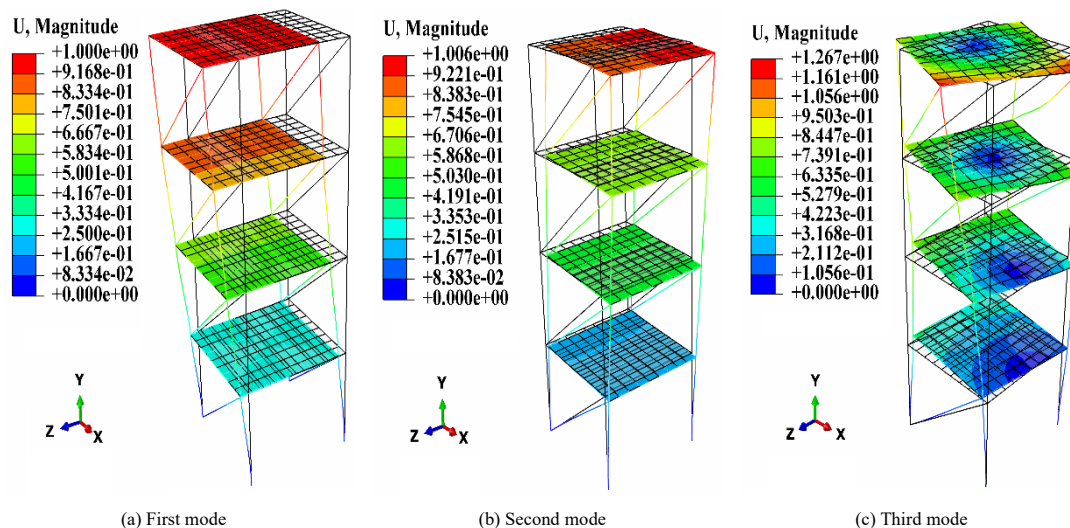
The grid type, size, and partitioning significantly affect the computational complexity and accuracy of the FE modelling process. Considering the computational burden, a four-node curved thin shell is selected as the grid element, and simplified integration and hourglass control are adopted. The global grid size is determined to be 0.075. The resulting model after grid partitioning is shown in Fig. 13.



**Fig. 13** Steel frame model after grid partitioning

### 3.2. Analysis of FE modelling results

The first, second, and third vibration modes of the steel frame are shown in Fig. 14; the black and coloured lines indicate the states of the steel frame before and after deformation, respectively. These three vibration modes conform to the structural vibration theory. The first and second vibration modes are translational in the directions of the weak (direction without bracing members) and strong (direction with bracing members) axes, respectively. The third vibration mode is torsional.



**Fig. 14** First three vibration modes of steel frame

**Table 5**  
FE analysis steel frame frequencies from first order to fourth order under some working conditions

Working Condition	The frequencies/Hz and error							
	1 <sup>st</sup> order	Error 1 (%)	2 <sup>nd</sup> order	Error 2 (%)	3 <sup>rd</sup> order	Error 3 (%)	4 <sup>th</sup> order	Error 4 (%)
Undamaged	6.530	3.11	14.385	7.55	20.862	1.44	33.926	1.27
#1	6.528	3.08	13.349	1.38	18.863	10.53	33.920	1.63
#12	6.525	4.40	13.345	6.06	18.208	13.30	33.913	1.99
#123	6.524	7.25	13.340	6.36	18.169	13.27	33.867	3.41
#1234	6.523	15.62	13.337	13.91	18.168	5.83	33.808	3.23



A comparison of the frequencies between the FE analysis and the vibration test is summarised in Table 5. Under the no-damage condition, the errors in the results are within 8%. The error between the third-order frequency of the FE model and test results is greater than 10% under the following working conditions: (a) only bracing member ① is dismantled; (b) bracing members ① and ② are simultaneously dismantled; and (c) bracing members ①, ②, and ③ are simultaneously dismantled. Under the working condition in which four bracing members (①, ②, ③, and ④) are dismantled simultaneously, the errors between the first-order and second-order frequencies of the FE model and test results are relatively large. The overall error between the FE analysis and test results shows close agreement. Therefore, using the FE model of the steel frame is reasonable.

#### 4. Construction of damage identification model for bracing members

##### 4.1. Overview of MobileNetV2 deep learning model

MobileNetV2 is a deeply separable CNN with linear bottlenecks and inverted residual blocks based on the MobileNetV1 model [32–36]. Deep separable convolution distinguishes convolutional channel correlation from spatial channel correlation. In contrast, conventional convolution achieves the collaborativel mapping of channel and spatial correlations [31]. Therefore, deep separable convolution compared with conventional convolution can improve network speed to a certain extent.

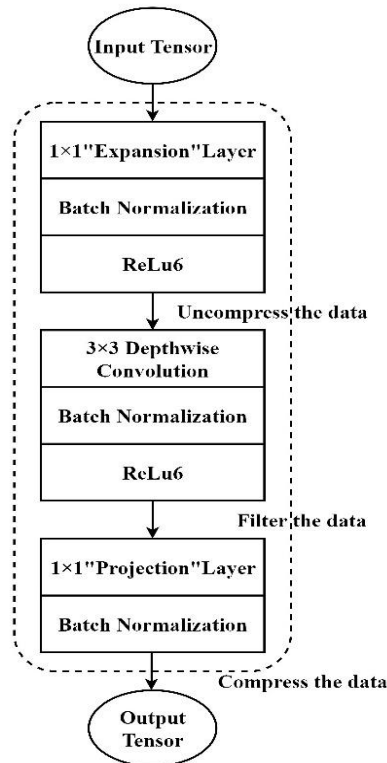


Fig. 15 Schematic of bottleneck residual block [26]

Table 6  
Composition of MobileNetV2 network [26]

The size of the input	Operator
224×224×3	Convolution layer
112×112×32	Bottleneck
112×112×16	Bottleneck
56×56×24	Bottleneck
28×28×32	Bottleneck
14×14×64	Bottleneck
14×14×96	Bottleneck
7×7×160	Bottleneck
7×7×320	Convolution layer (size: 1×1)
7×7×1280	Average pooling layer (size: 7×7)
1×1×160	Convolution layer (size: 1×1)

The use of linear bottlenecks is necessary because non-linear activation functions, such as rectified linear units (ReLU), result in the loss of image information. Furthermore, the linear bottleneck layer contains essential information, whereas the expansion layer provides a non-linear activation layer with rich information. The inversion of residual blocks involves upscaling low-dimensional image features using convolution, filtering, feature downscaling using the convolution kernel, and ReLU function to obtain the feature output. This maintains all necessary information and increases the expressiveness of the deep network.

A schematic of the bottleneck residual block is presented in Fig. 15. The composition of MobileNetV2 is listed in Table 6.

##### 4.2. Image preprocessing

The time–frequency analysis of acceleration signals results in 69 classes of working conditions; with 24 images per class, this results in a total of 1656 images. To facilitate data labelling, the images of each class are saved in a corresponding class folder. The naming convention of image folders is consistent with that of the dismantling conditions of bracing members (Table 2).

Owing to the small number of images per class, the model cannot learn the image features well. Therefore, an image augmentation method is used to expand the dataset. Image augmentation operations commonly include image flipping, translation, clipping, and rotation [37]. Each image is uniformly resized to 224 × 224 × 3 pixels. Examples of image augmentation results are shown in Fig. 16.

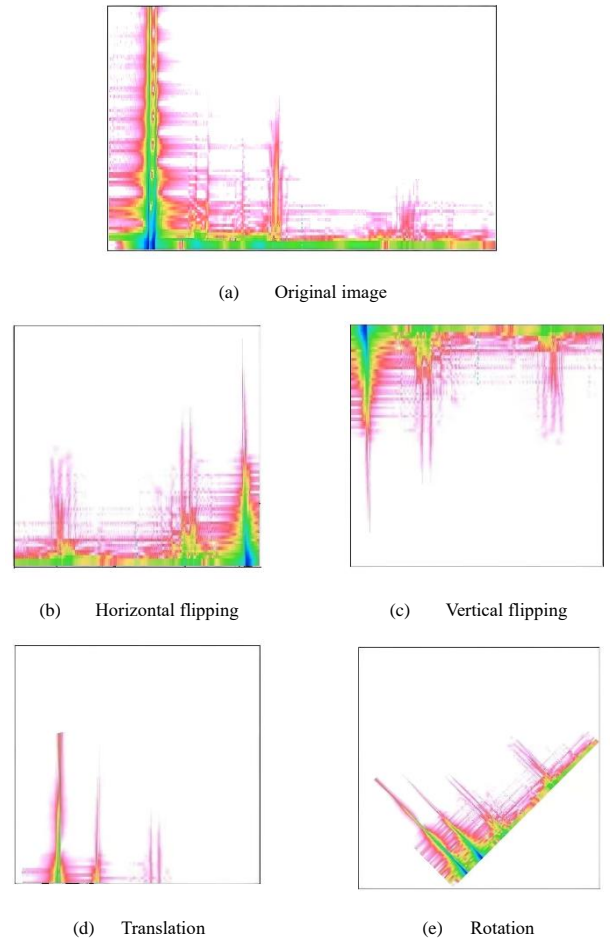


Fig. 16 Effects of image operations for data augmentation

##### 4.3. Setup and training of MobileNetV2 model

The MobileNetV2 model is established based on Python 3.6.7 and TensorFlow 1.13. The training process was implemented on a DellG3 computer with Windows 10, Intel® Core™ i7-9750H CPU@2.60GHz, a solid-state hard drive, 16-GB RAM, and a 6-GB GPU with NVIDIA GTX1660 Ti.

The model is trained using a transfer learning approach [38]. The percentage of randomly discarded neurones in the dropout layer is set to 40%. In contrast, the number of output classes in the dense layer is set to 15, and a softmax activation function is employed. For network training and testing, 80% of the images were randomly selected to form a training set, and the remaining photos

were used for testing and evaluation. The training hyperparameters are as follows.

1. The number of training epochs is 300 with 12 iterations per epoch for 3600 iterations.
2. A small learning rate of 0.0001 is employed to enhance the learning of image features.
3. Stochastic gradient descent is used as the optimisation method because of its online learning capability and fast convergence characteristics.

4. The minimum batch size for each training iteration is 10.

An accuracy of 99.30% is achieved relative to both the training and testing sets for the prediction accuracy of MobileNetV2. The predicted outcomes of photograph selection for this project are shown in Fig. 17. The trained model for each image outputs the picture classification probabilities. As shown in Fig. 17, the probability values associated with the class predictions for the 7th and 20th images are relatively low.

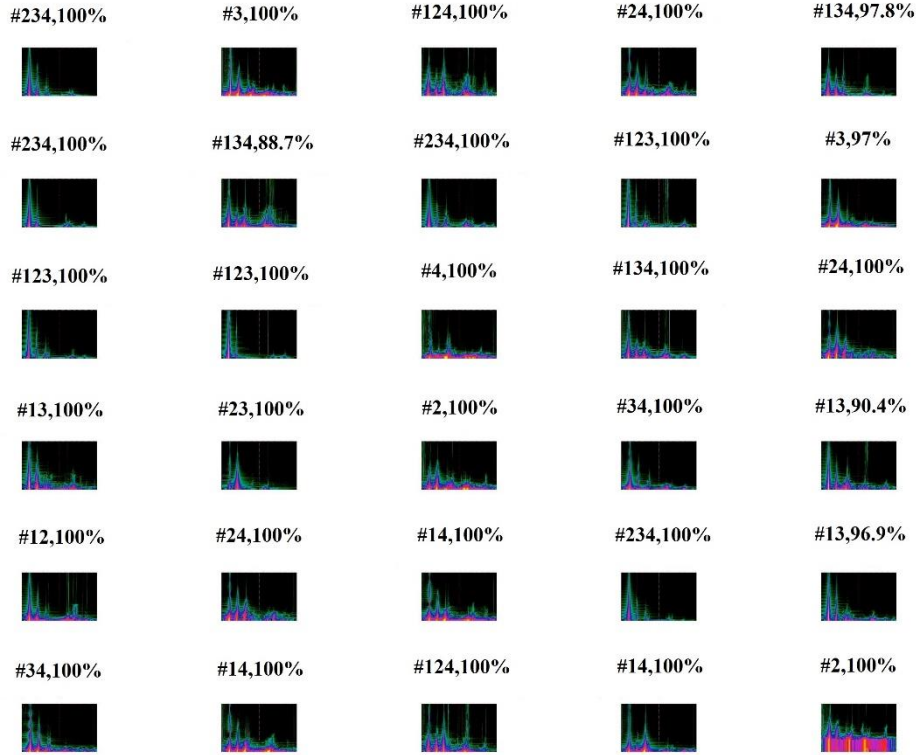


Fig. 17 Prediction results of MobileNetV2 model for some images

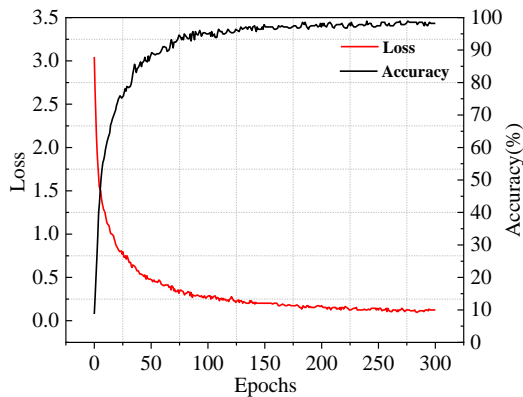


Fig. 18 Accuracy and loss curves of MobileNetV2 model for training set

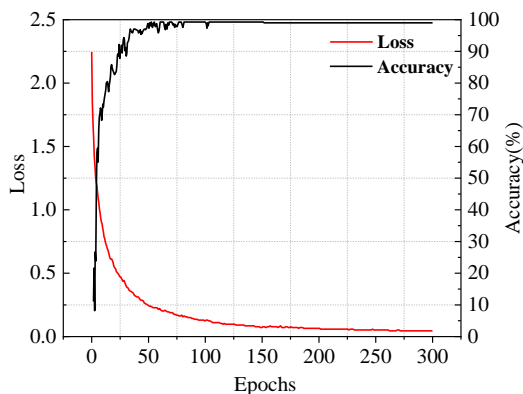


Fig. 19 Accuracy and loss curves of MobileNetV2 model for test set

The growth curves of accuracy and prediction loss over the training iterations are plotted for the training and test sets, as shown in Figs. 18 and 19, respectively. The training accuracy and loss remain stable even after 100 epochs. However, the test accuracy and loss were not smooth and did not reach relatively stable values. The final training and test loss values are 0.04557 and 0.12492, respectively.

#### 4.4. Performance evaluation of MobileNetV2 model

Classification accuracy alone may not be a reliable indicator of model performance. For example, suppose that 90% of the data samples for a binary classification task belong to the positive class and the remaining samples belong to the negative class. Suppose a model is established to classify all data samples as positive. Although a 90% classification accuracy is considerably high, the model predicts all negative data samples as positive. Accordingly, the performance of the MobileNetV2 model is comprehensively evaluated using a confusion matrix (or contingency table) and three indicators (precision (or positive predictive value), recall (or sensitivity), and F1-score) derived from it.

The confusion matrix visually illustrates the classification results by describing the relationship between the true and predicted classes of data samples. The rows and columns of the matrix correspond to the predicted and true classes of the actual data samples, respectively.

Precision and recall are primarily used in binary classification tasks. The two evaluation indices can be derived from the four metrics of a binary classifier: number of true positives (TP), true negatives (TN), false positives (FP), and false negatives (FN). Precision and recall are computed as follows:

$$\text{Precision} = \frac{TP}{TP + FP} \quad (3)$$

$$Recall = \frac{TP}{TP + FN} \quad (4)$$

Precision and recall are not totally consistent for some classification tasks and unwarranted situations where one of the two indices is low and the other is high. Therefore, a reasonable performance analysis may not be possible using these two indices. Alternatively, the F-score index can be used to weigh and reconcile precision and recall. According to the different weights of accuracy and recall under various classification tasks, the F-score can be extended to many alternatives. Three indices are most important: F0.5-score, F1-score, and F2-score. The F1-score is used to evaluate the performance of MobileNetV2; it is calculated as follows:

$$F1 = 2 \times \frac{Precision \times Recall}{Precision + Recall} \quad (5)$$

The F1-score assigns equal importance to precision and recall and hence assigns them equal weights. For multivariate classification tasks, an F1-score can be calculated separately for each class; hence, the final F1-score can be calculated as the average of class-specific scores. This calculation can be expressed as

$$F1-score_{final} = \left( \frac{1}{n} \sum_{k=1}^n f1-score_k \right) \quad (6)$$

where  $k = 1, 2, 3, \dots, n$ , and  $n$  is the number of classes.

Satisfactory improvement is introduced by the F1-score over individual precision and recall indicators; however, enhancement is limited. In general, not all F-scores incorporate inverse precision or recall. Hence, they are inferior to indicators involving all four fundamental binary classification metrics (i.e., precision, recall, inverse precision, and inverse recall). Although the F1-score suffices for the current objective in this study, it is not comparable with the Matthew correlation coefficient, which depends on the four fundamental metrics [40–41].

Owing to the several dismantling conditions of bracing members, the performance of the deep learning model is evaluated under four types of conditions or states under which one, two, three, or four bracing members are dismantled. The confusion matrices of the test set are used to evaluate model performance under each dismantling condition.

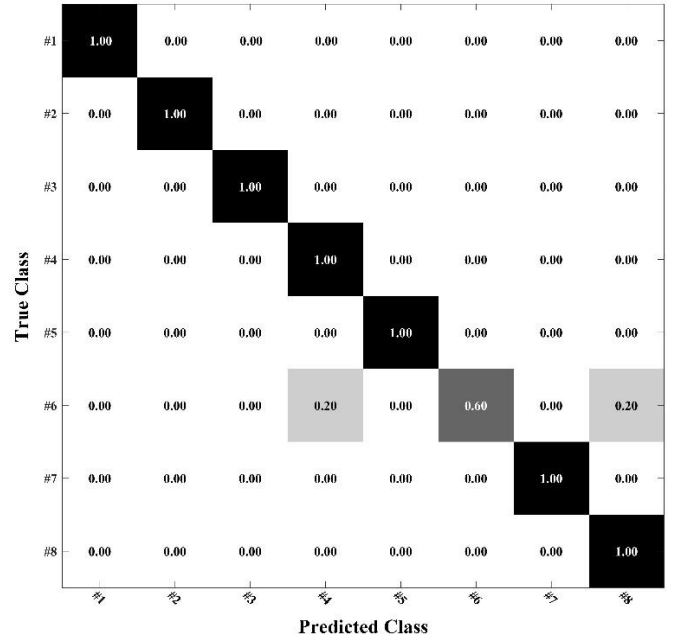


Fig. 20 Confusion matrix of MobileNetV2 model for test set when one bracing member is dismantled

#### 4.4.1. One bracing member dismantled

The confusion matrix for the test set under the working conditions in which one bracing member is dismantled is shown in Fig. 20. The model incorrectly classifies 40% of the images in class #6 as either class #4 or class #8. The precision, recall, and F1-score of the model for the test samples of various classes are shown in Fig. 21. Because the model misclassifies the test samples of class #6 as class #4 or class #8, not all of the resulting precision and recall values reach 100% for these three classes. Incorrect classification also led to low F1-score values for the samples associated with the three classes, particularly class #6. The F1-score for the entire dataset was 0.9460, indicating good classification and prediction performance for samples collected under working conditions in which a single bracing member was dismantled.

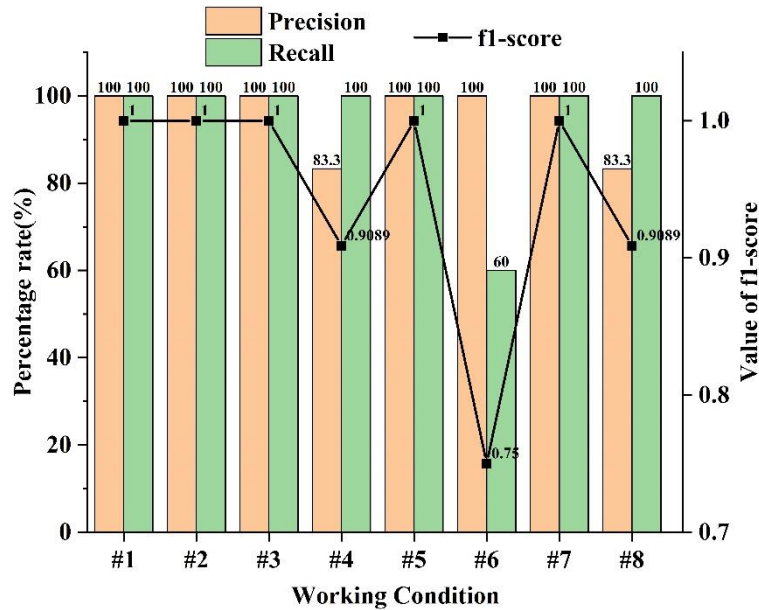


Fig. 21 Precision, recall, and F1-score of damage identification model for samples with various classes when one bracing member is dismantled

#### 4.4.2. Two bracing members dismantled

The confusion matrix for the test set under the working conditions in which two bracing members are dismantled is shown in Fig. 22. The deep learning model correctly predicts the actual classes of all 22 sample types; however, the predictions of the model for the remaining six types are incorrect. In particular, for the samples of class #37, the model incorrectly predicted 20% of the samples,

indicating that it did not adequately learn the features of class #37. The precision, recall, and F1-score of the test set are shown in Fig. 23. The models associated with classes #23, #37, and #48 showed relatively low precision or recall values, resulting in low F1-scores. The F1-score for the entire dataset is 0.9505, indicating good classification and prediction performance under the working condition in which two bracing members are dismantled.

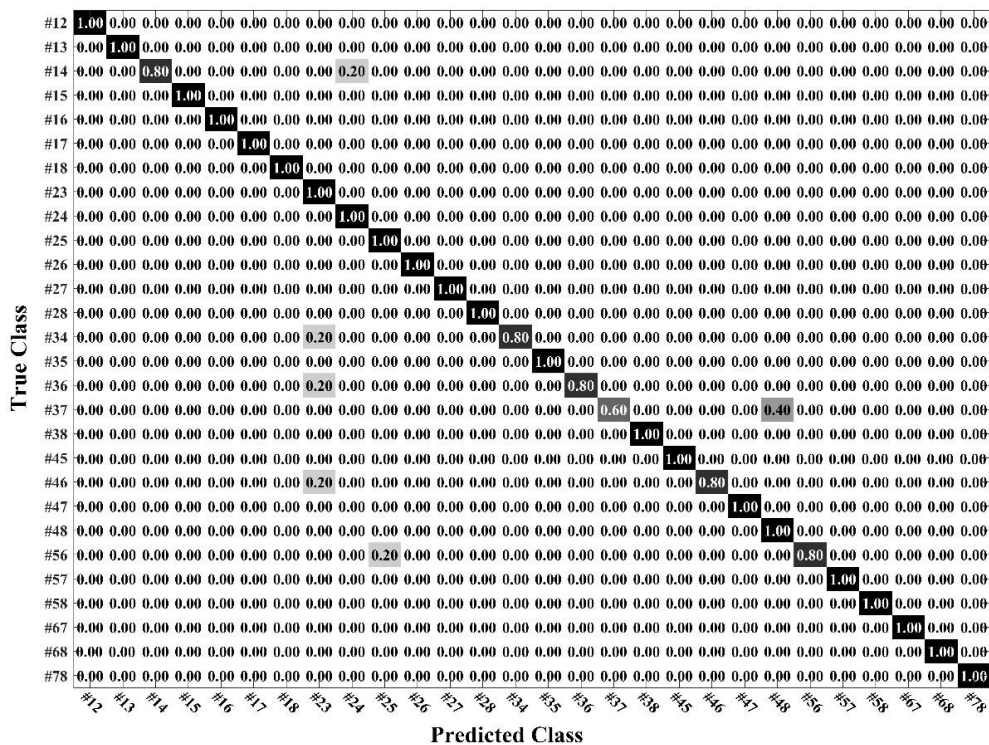
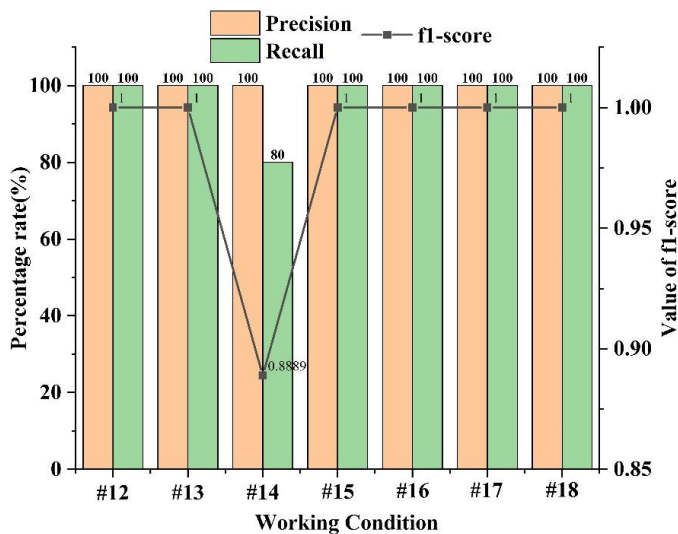
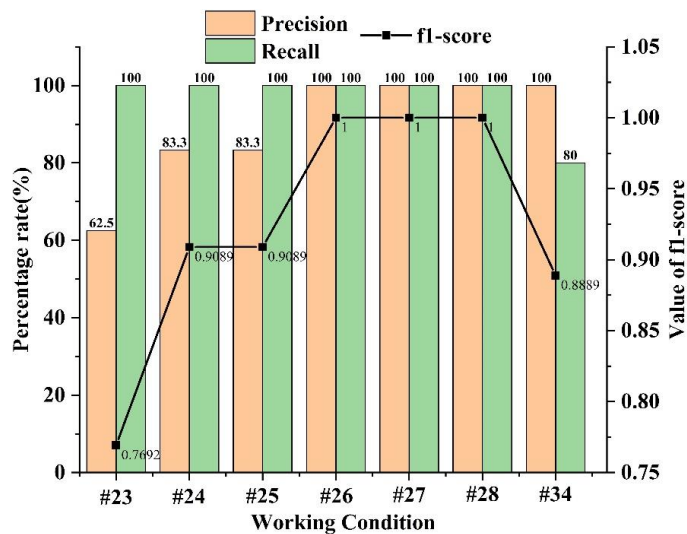


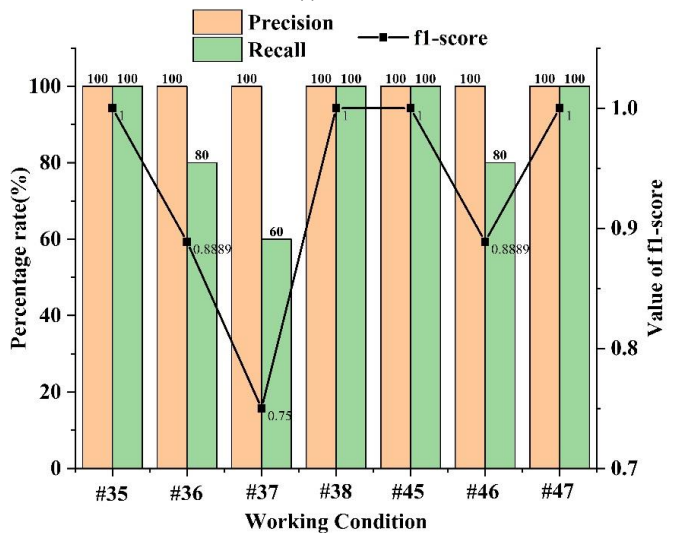
Fig. 22 Confusion matrix of MobileNetV2 model for test set where two bracing members are dismantled



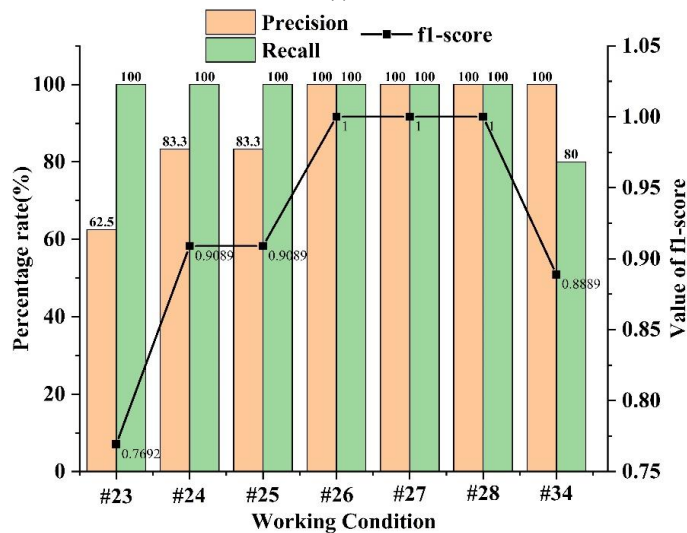
(a) Part I



(b) Part II



(c) Part III



(d) Part IV

Fig. 23 Precision, recall, and F1-score of damage identification model for samples with various classes where two bracing members are dismantled



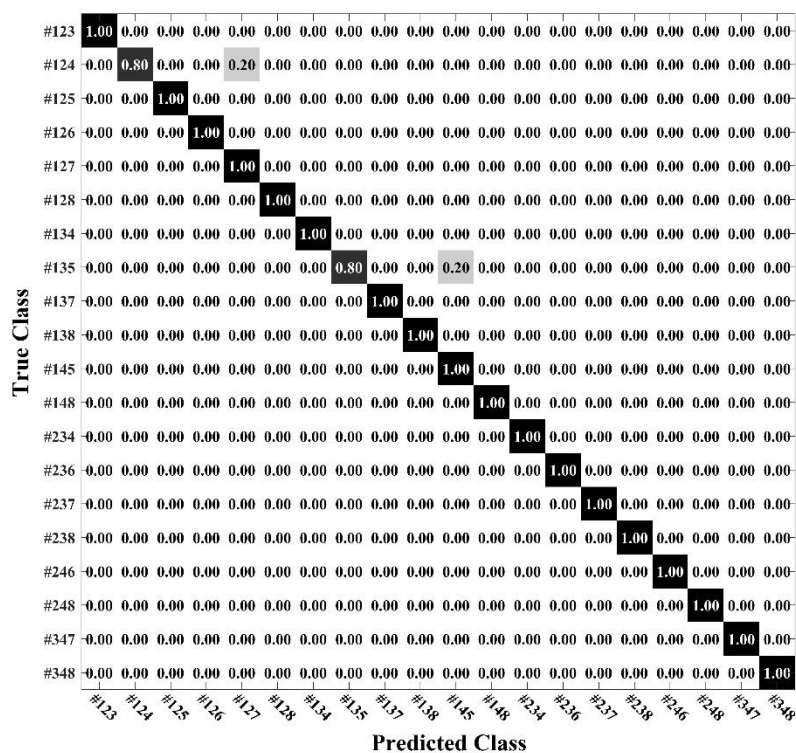


Fig. 24 Confusion matrix of MobileNetV2 model for test set where three bracing members are dismantled

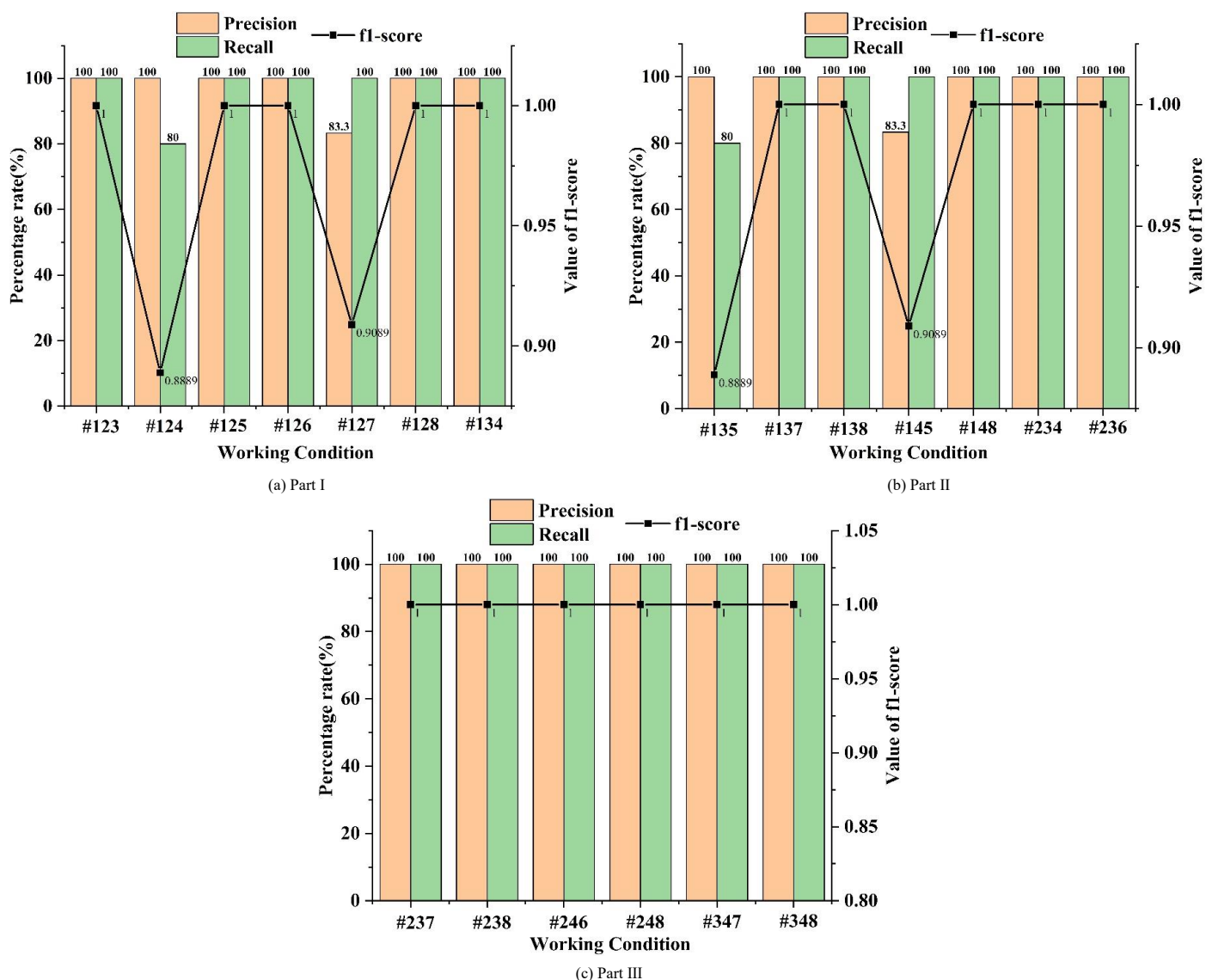


Fig. 25 Precision, recall, and F1-score of damage identification model for samples with various classes where three bracing members are dismantled

#### 4.4.3. Three bracing members dismantled

The confusion matrix of the test set under the working conditions in which the three bracing members are dismantled is shown in Fig. 24. The model made incorrect predictions for the samples of two classes: 20% of the samples of class #124 are predicted as class #127, and 20% of the samples of class #135 are expected to be those of class #145. Compared with the other classes, the model prediction performance for these two classes is relatively inadequate. The precision, recall, and F1-score of the test set are shown in Fig. 25. Because the model misclassified some samples of classes #124 and #135, not all associated precision and recall values reached 100%. The F1-score for the entire dataset was 0.9798, indicating excellent classification and prediction performance under the working condition in which three bracing members were dismantled.

#### 4.4.4. Four bracing members dismantled

The confusion matrix of the test set under the working condition in which four bracing members are dismantled is shown in Fig. 26. The model incorrectly predicted the samples of two classes: 20% of class #1235 was predicted as class #2345 and 20% of class #2345 was predicted as class #2348. Compared with the other classes, the generalisation performance of the model for these two classes was relatively inadequate. The precision, recall, and F1-score of the test set are shown in Fig. 27. Because the model incorrectly classified some samples of classes #1235 and #2345, not all associated precision and recall values reached 100%. Misclassification also caused the model precision for class #2348 to decrease from 100% to 83.3%.

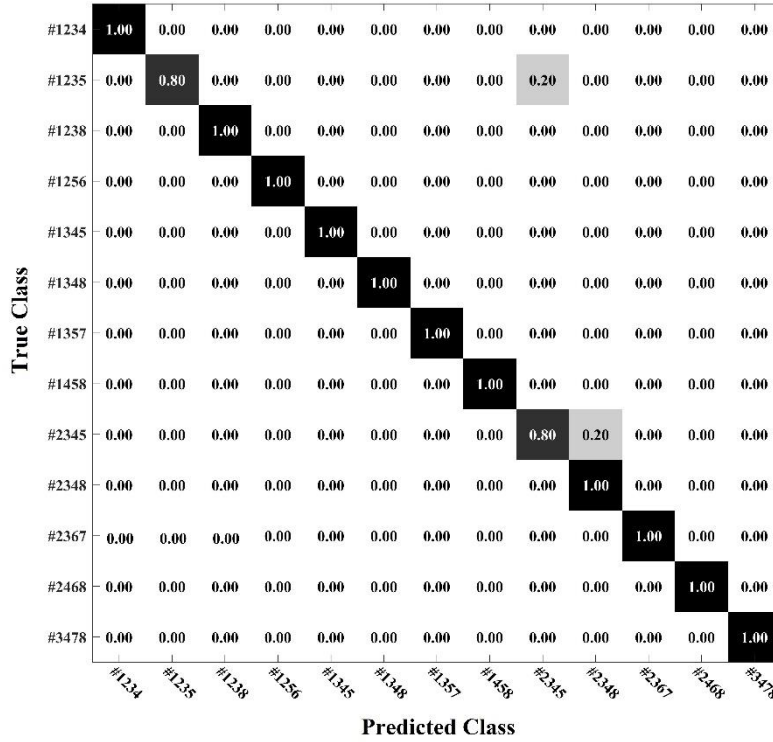


Fig. 26 Confusion matrix of MobileNetV2 model for test set where four bracing members are dismantled

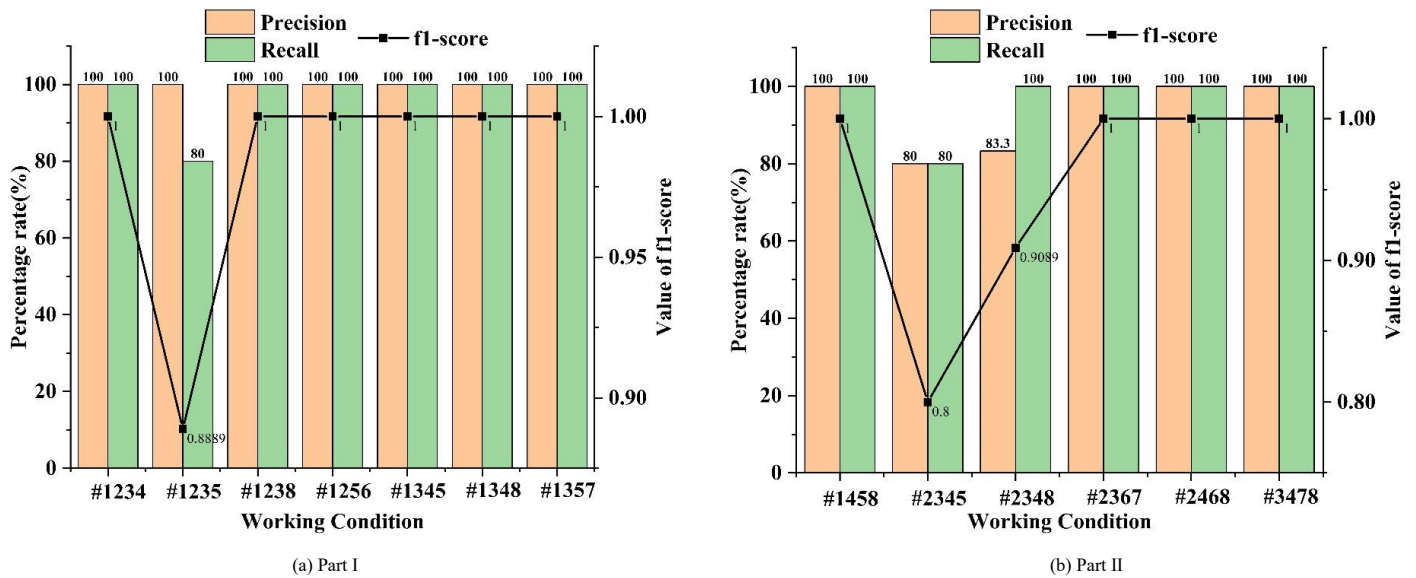


Fig. 27 Precision, recall, and F1-score of damage identification model for samples with various classes where four bracing members are dismantled

Overall, the prediction accuracy of the trained model on the full dataset is 97.37%. Hence, the damage location of steel frame support members can be determined relatively well. However, the accuracy of the model for certain support removal conditions is low: (a) 60% when support member #6 is removed; (b) 60% when support members #3 and #7 are simultaneously removed; (c) 80%

when support members #1, #2, and #4 as well as support members #1, #3, and #5 are simultaneously removed; and (d) 80% accuracy when support members #1, #2, #3, and #5 and support members #2, #3, #4, and #5 are simultaneously removed.

## 5. Conclusions

Time–frequency domain analysis and CNNs are used to identify lateral support failures in different parts of a steel structure. The damaged member is identified and rapidly replaced as soon as possible to ensure safety. A four-layer steel frame model with a bracing system is used to investigate a new approach for damage identification in steel structures. Specifically, a deep learning model for identifying the dismantling position of bracing members is established using transfer learning. The following conclusions are obtained based on the vibration testing and FE modelling results of the steel frame structure combined with the performance evaluation of the MobileNetV2 model.

1. The actual dynamic measurements of the model are used to obtain the modalities of the structure in each order and the modalities after the failure of various supports. These test findings are utilised to improve the FE model, enabling the acquisition of a considerable amount of more accurate training data for subsequent FE simulations.

2. Vibration tests on intact and broken support structures reveal a specific variance in the time–frequency domain. This indicates the viability of utilising CNN as a deep-learning image recognition approach.

3. The chosen MobileNetV2 network from CNN exhibits improved performance in recognising time–frequency domain images. Moreover, the

## References

- [1] H. Shokravi, N. Bakhary, S.R. Koloor, M. Petru, Health Monitoring of Civil Infrastructures by Subspace System Identification Method: An Overview, *Applied Sciences*. 10 (8) (2020) 1–29.
- [2] C. Scuro, P.F. Sciammarella, F. Lamonaca, R.S. Olivito, D.L. Carni, Iot for Structural Health Monitoring, *IEEE Instrumentation and Measurement Magazine*. 21 (6) (2018) 4–9 and 14.
- [3] K. Geissler, N. Steffens, R. Stein, Basics of the safety-equivalent assessment of bridges with structural health monitoring, *STAHLBAU*. 88 (4) (2019) 338–353.
- [4] S.O. Sajedi, X. Liang, Uncertainty - assisted deep vision structural health monitoring, *Computer-Aided Civil and Infrastructure Engineering*. 36 (2) (2021) 126–142.
- [5] Y. Kankaname, Y. Hu, X. Shao, Application of wavelet transform in structural health monitoring, *Earthquake Engineering and Engineering Vibration*. 19 (02) (2020) 515–532.
- [6] O. Yazdanpanah, B. Mohebi, M. Yakhchalian, Seismic damage assessment using improved wavelet-based damage-sensitive features, *Journal of Building Engineering*. 33 (2020) 101311.
- [7] B. Mohebi, O. Yazdanpanah, F. Kazemi, A. Formisano, Seismic damage diagnosis in adjacent steel and RC MRFs considering pounding effects through improved wavelet-based damage-sensitive feature, *Journal of Building Engineering*. 33(2020) 101847.
- [8] T. Tam, D. Dinh, J. Lee, T. Nguyen, An effective deep feedforward neural networks (DFNN) method for damage identification of truss structures using noisy incomplete modal data, *Journal of Building Engineering*. 30 (2020) 101244.
- [9] Y. Xin, J. Li, H. Hao, Damage Detection in Initially Non-linear Structures based on Variational Mode Decomposition, *International Journal of Structural Stability & Dynamics*. 20 (10) (2020) 2042009.
- [10] J. Liu, Z. Lu, M. Yu, Damage identification of non-classically damped shear building by sensitivity analysis of complex modal parameter, *Journal of Sound and Vibration*. 438 (2019) 457–475.
- [11] J. Han, P. Zheng, H. Wang, Structural modal parameter identification and damage diagnosis based on Hilbert-Huang transform, *Earthquake Engineering and Engineering Vibration*. 13 (1) (2014) 101–111.
- [12] A. Parai, D. Roy, A.K. Samanta, A deep learning-based approach for condition assessment of semi-rigid joint of steel frame, *Journal of Building Engineering*. 34, 2021, 101946.
- [13] C. Pathirage, J. Li, L. Li, H. Hao, W. Liu, R. Wang, Development and application of a deep learning-based sparse autoencoder framework for structural damage identification, *Structural Health Monitoring*. 18 (1) (2019) 103–122.
- [14] C. Pathirage, J. Li, L. Li, H. Hao, W. Liu, R. Wang, P.H. Ni, Structural damage identification based on autoencoder neural networks and deep learning, *Engineering Structures*. 172 (2018) 13–28.
- [15] S. Hakim, H.A. Razak, Frequency Response Function-based Structural Damage Identification using Artificial Neural Networks-A review, *Research Journal of Applied Sciences Engineering & Technology*. 7 (9) (2014) 1750–1764.
- [16] S. Hakim, H.A. Razak, S.A. Ravanfar, Ensemble neural networks for structural damage identification using modal data, *International Journal of Damage Mechanics*. 25 (3) (2016) 400–430.
- [17] P. Seventekidis, D. Giagopoulos, A. Arailopoulos, O. Markogiannaki, Structural Health Monitoring using deep learning with optimal FE model generated data, *Mechanical Systems and Signal Processing*. 145 (2020) 106972.
- [18] T. Liu, H. Xu, M. Ragulskis, M. Cao, W. Ostachowicz, A Data-Driven Damage Identification Framework Based on Transmissibility Function Datasets and One- Dimensional Convolutional Neural Networks: Verification on a Structural Health Monitoring Benchmark Structure, *Sensors*. 20 (4) (2020) 1059.
- [19] E. Figueiredo, I. Moldovan, A. Santos, P. Campos, C.W. Costa, Finite Element-Based Machine-Learning Approach to Detect Damage in Bridges under Operational and Environmental Variations, *Journal of Bridge Engineering*. 24 (7) (2019) 1432.
- [20] Nadith P, Li J, Ling L, et al. Structural damage identification based on autoencoder neural networks and deep learning, *Engineering Structures*, 2018, 172: 13–28.
- [21] Gordan M, Ismail Z, Razak H A, et al. Data mining-based damage identification of a slab-on-girder bridge using inverse analysis. *Measurement*, 2019, 151.
- [22] Ali R, Cha Y J. Subsurface damage detection of a steel bridge using deep learning and uncooled micro-bolometer. *Construction and Building Materials*, 2019, 226(30): 376–387.
- [23] Kourehli S S, Ghadimi R. Vibration analysis and identification of breathing cracks in beams subjected to single or multiple moving mass using online sequential extreme learning machine. *Inverse Problems in Science and Engineering*. 2019, 27(08): 1057–1080.
- [24] Teng Z Q, Teng S, Zhang J Q, et al. Structural Damage Detection Based on Real-Time Vibration Signal and Convolutional Neural Network. *Applied Sciences*, 2020, 10(14): 4720.
- [25] Luke, H. D. The origins of the sampling theorem. *IEEE Communications Magazine*, 1999, 37(4), 106–108.
- [26] Jerri, A. J.. The Shannon sampling theorem—Its various extensions and applications: A tutorial review. *Proceedings of the IEEE*, 1977, 65(11), 1565–1596.
- [27] Song, Z., Liu, B., Pang, Y., Hou, C., & Li, X.. An improved Nyquist–Shannon irregular sampling theorem from local averages. *IEEE transactions on information theory*, 2012, 58(9), 6093–6100.
- [28] Vaidyanathan, P. P.. Generalizations of the sampling theorem: Seven decades after Nyquist. *IEEE Transactions on Circuits and Systems I: Fundamental Theory and Applications*, 2001, 48(9), 1094–1109.
- [29] Paige, C. C.. Computational variants of the Lanczos method for the eigenproblem. *IMA Journal of Applied Mathematics*, 1971, 10(3), 373–381.
- [30] Golub, G. H., & Underwood, R.. The block Lanczos method for computing eigenvalues. In *Mathematical software*. 1977, 361–377. Academic Press.
- [31] Chollet F. Xception: Deep learning with depthwise separable convolutions. *Proceedings of the IEEE conference on computer vision and pattern recognition*. 2017: 1251–1258..
- [32] Sandler M, Howard A, Zhu M, et al. Mobilenetv2: Inverted residuals and linear bottlenecks. *Proceedings of the IEEE conference on computer vision and pattern recognition*. 2018: 4510–4520.
- [33] Nguyen H. A lightweight and efficient deep convolutional neural network based on depthwise dilated separable convolution, *Journal of Theoretical and Applied Information Technology*. 98 (15) (2020) 2937–2947.
- [34] Ananthanarayana T, Ptucha R, Kelly S C. Deep learning based fruit freshness classification and detection with CMOS image sensors and edge processors. *Electronic Imaging*, 2020, 2020(12): 172–1–172–7.
- [35] Nguyen H. Fast object detection framework based on mobilenetv2 architecture and enhanced feature pyramid. *J. Theor. Appl. Inf. Technol*, 2020, 98(05). 812–824.
- [36] Buiu C, Dănilă V R, Răduță C N. MobileNetV2 ensemble for cervical precancerous lesions classification. *Processes*, 2020, 8(5): 595–624.
- [37] Li, W., Chen, C., Zhang, M., Li, H., & Du, Q.. Data augmentation for hyperspectral image classification with deep CNNs. *IEEE Geoscience and Remote Sensing Letters*, 2018, 16(4), 593–597.
- [38] Torrey, L., & Shavlik, J.. Transfer learning. In *Handbook of research on machine learning applications and trends: algorithms, methods, and techniques*. 2010, 242–264. IGI global.

trained model can discriminate distinct damage components with 99.3% accuracy.

4. As described in this research, a better approach to locate steel structure support damage is to identify damage from the structure’s dynamic response. Then, the findings of the time–frequency domain analysis of the response can be inputted into the trained model.

5. The number of comparable training samples can be increased to improve damage detection. Based on the overall classification accuracy and F1-score, the MobileNetV2 model combined with time–frequency analysis provides a high degree of sensitivity and accuracy for detecting damage to support members.

## Acknowledgments

The work in this paper was supported by the 2023 Yangzhou Key R&D Program (Social Development) Project Grant No SSF2023000101, Natural Science Foundation of Jiangsu Province of China under Grant No BK20200705, and the Key Technologies Research and Development Program (CN) under Grant No. 2021YFB2600600. The corresponding author expresses gratitude to the 2018 Jiangsu Provincial Government Scholarship Program (No. 228) for supporting the visit to the University of California, Los Angeles, USA.

# CONFORMATION AND STATIC PERFORMANCE ANALYSIS OF PENTAGONAL THREE-FOUR STRUT HYBRID OPEN-TYPE CABLE DOME

Hui Lv <sup>1, 2, \*</sup>, De-Wang Liu <sup>1, 4</sup>, Shi-Lin Dong <sup>2, 3</sup> and Yan-Fen Zhong <sup>1, 4</sup>

<sup>1</sup> College of Civil Engineering and Architecture, Nanchang Hangkong University, Nanchang 330063, China

<sup>2</sup> Space Structures Research Center, Zhejiang University, Hangzhou 310058, China

<sup>3</sup> Zhejiang Provincial Key Laboratory of Space Structures, Zhejiang University, Hangzhou 310058, China

<sup>4</sup> Nanchang Hangkong University Smart Construction Research Center, Nanchang 330063, China

\* (Corresponding author: E-mail: lvhui@nchu.edu.cn)

## ABSTRACT

Traditional cable domes exhibit many defects, such as irregular grids and weak circumferential stiffness. This paper proposes a new cable dome and elaborates on the topological form of the new cable dome. Furthermore, the pre-stress state of the structure is deduced by establishing the nodal equilibrium equations. In addition, load states analysis and parametric analysis were conducted using finite element simulations in ANSYS software. The results show that the pre-stress distribution of this structure is reasonable because of the regular grids. Compared to traditional cable domes, the new design shows superior static performance and enhanced circumferential stiffness. As a result, the cables hardly slack under different load conditions. Moreover, it can improve structural stiffness by appropriately adjusting the initial pre-stress, rise-span and thickness-span ratios. Finally, recommended ranges of the above parameters are provided, offering valuable engineering design guidance.

## ARTICLE HISTORY

Received: 6 July 2023  
Revised: 9 September 2023  
Accepted: 12 September 2023

## KEYWORDS

Cable dome;  
Static performance;  
Parametric analysis;  
Initial pre-stress;  
Rise-span ratio;  
Thickness-span ratio

Copyright © 2023 by The Hong Kong Institute of Steel Construction. All rights reserved.

## 1. Introduction

Large spatial structures have recently been used in public buildings, such as sports venues [1, 2], convention centers [3] and airports. In addition to meeting the functions and appearance requirements, modern large spatial structures pursue higher utilization of material properties and lower economic efficiency. Therefore, the study of cable-stayed structures [4] must be conducted. Cable dome has notable advantages including its lightweight nature and structural aesthetics. It is widely regarded as the main super-span structure form for the future [5]. Cable domes have their origins in the concept of tensegrity structures developed by the renowned architect R. B. Fuller. In the 1980s, D. H. Geiger invented the cable dome structure and implemented it for the first time in practical engineering.

The cable dome consists of tension cables, compressed struts and supports. In contrast to other spatial structures, such as reticulated shells [6] or cable-truss systems [7], initial pre-stress in the cable dome plays an important role in establishing the out-of-plane stiffness of the structure to bear external loads and limit the deformation [8]. However, traditional cable domes often exhibit weak out-of-plane stiffness, making them prone to destabilization under asymmetric loading conditions [9, 10]. To address the problem, M.P. Levy proposed the Levy-type cable dome, which incorporates ridge cables, diagonal cables and struts to form a three-dimensional truss. The stability of the structure was significantly improved. However, the grid of the Levy-type cable dome is irregular, increasing the membrane installation difficulty. To overcome this limitation, Fan et al. improved the Levy-type cable dome and proposed the inclined-strut cable dome [11]. In addition, scholars have proposed alternative methods such as replacing the cable trusses with rigid components [12, 13] or combining reticulated shells with cable domes [14] to enhance stiffness. However, these methods cannot fully utilize the mechanical properties of materials.

The topological form determines the stiffness of the cable dome. Many scholars seek to improve the structural performance of cable domes through topological innovation. Some scholars abandoned the traditional Tensile-Integrity concept and proposed multi-strut cable domes and hybrid cable domes, such as honeycomb-type multi-strut series cable domes [15], drum-shaped honeycomb-type cable domes [16], alternated cable domes with single and double brace struts [17], and other cable domes. Compared to traditional cable domes, these multi-strut and hybrid ones have significant advantages in membrane installation and structural stiffness. Moreover, some scholars have proposed bird-nest-type cable domes [18], sunflower-type cable domes [19], star-type tetrahedral cable domes [20], etc. These innovative cable dome designs enrich the array of available options and give new insights for cable dome selection.

An adaptive cable dome [21] has recently been proposed, equipped with an actuator that enables self-adjustment and the ability to accommodate various loading conditions. While the adaptive cable dome maintains its ability to meet the load requirements by changing its topological form, this method introduces a new approach to enhance structural stiffness.

Research has demonstrated that structural parameters (rise-span ratio, strut cross-sectional area and strut height) are closely associated with the mechanical properties of the structure. Meanwhile, parametric analysis has shown that the structural performance can be improved by limiting these structural parameters within specific ranges [22–24]. Therefore, it is necessary to carry out a parametric analysis.

This paper introduces a novel pentagonal three-four strut hybrid open-type cable dome, which is based on the concept of a multi-strut cable dome. Firstly, the topological form of the new cable dome is elucidated, and the pre-stress state of the structure is determined using nodal equilibrium equations. Secondly, a load state analysis is conducted to study the mechanical response of the structure. Finally, a parametric analysis is performed on the structure. The appropriate ranges for the rise-span ratio, thickness-span ratio and pre-stress level of the cable dome are recommended.

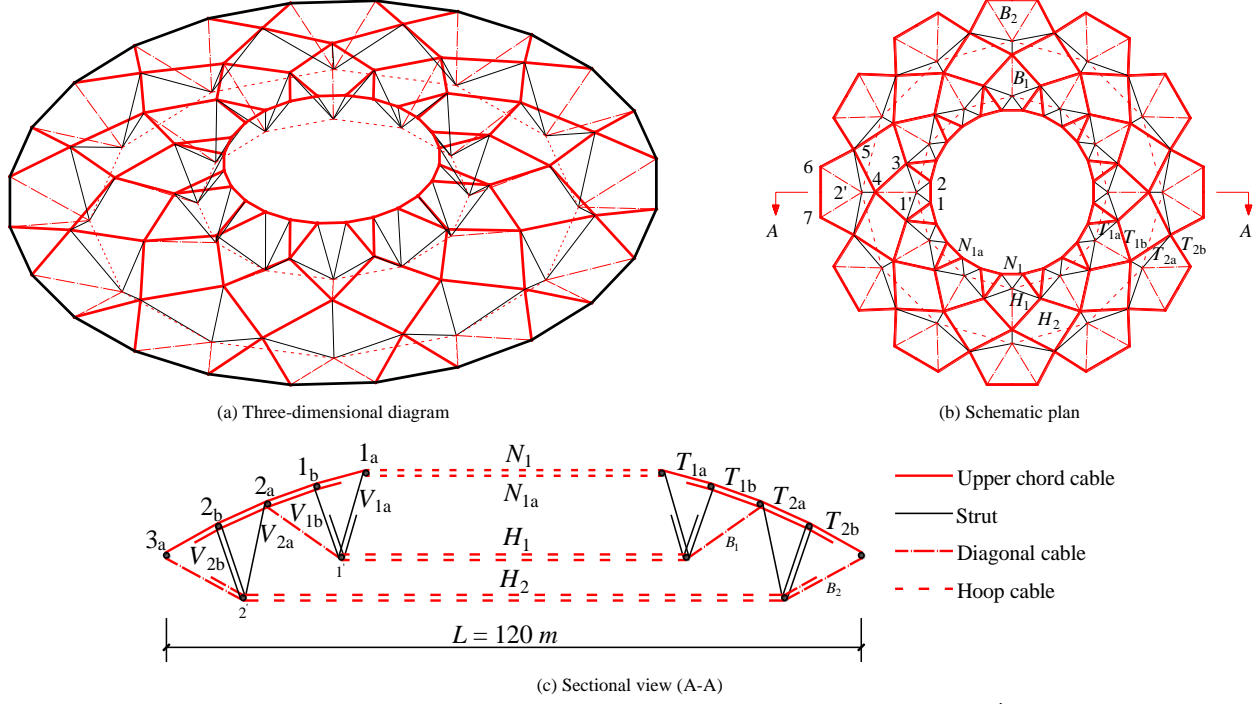
## 2. Structural configuration and pre-stress state analysis

### 2.1. Structural configuration

The pentagonal three-four strut hybrid open-type cable dome consists of cables, struts and rigid hoop beams. The topological form is shown in Fig. 1. In contrast to the traditional Tensile-Integrity concept, the new cable dome adopts the multi-strut cable dome concept. The upper chord grid of the structure is pentagonal. Starting from the center of the cable dome and extending towards the outer hoop, the struts are arranged in an alternating pattern of four and three. The struts are connected to form a hoop, and the connections between each substructure are designed to be sufficient. This arrangement helps enhance the circumferential stiffness of the structure and improves its ability to resist asymmetric loads.

A comparison is made between the new and the traditional cable domes in four aspects, as outlined in Table 1. Compared with the Geiger-type cable dome, the struts in the new structural arrangement form a hoop, increasing the circumferential stiffness of the structure. The number of hoop cables in the new structure is twelve fewer than that in the levy-type cable dome. Specifically, the new cable dome comprises 84 struts and 184 cables; resulting in a strut-cable ratio of 1:2.2. Comparatively, the strut-cable ratio is approximately 1:3 in the Geiger-type cable dome and 1:5 in the Levy-type cable dome.





Note:  $H_i$ -hoop cable;  $N_1, N_{1a}$ -upper chord hoop cable;  $T_{ia}, T_{ib}$ -ridge cable;  $B_i$ -diagonal cable;  $V_{ia}, V_{ib}$ -strut;  $i_a, i_b$ -upper chord node;  $i'$ -lower chord node.

Fig. 1 Schematic diagram of the pentagonal three-four strut hybrid open-type cable dome

Table 1

Comparison of component connected relation

Title	Traditional cable domes		New cable dome
	Geiger-type cable dome	Levy-type cable dome	
Number of components connected to the upper chord node	4	5 or 7	4 or 6
Number of components connected to the lower chord node	4	5	7
Number of diagonal cables per hoop	12	24	12 or 24
Characteristics of the struts	A vertical strut		Struts are arranged by four and three alternately
Characteristics of the horizontal projection of the cables and struts	The projection of the struts is in a discontinuous point system; The projection of diagonal cables coincides with the ridge cable projection		The projection of the ridge cables, diagonal cables and struts are symmetrically distributed along the radial axis

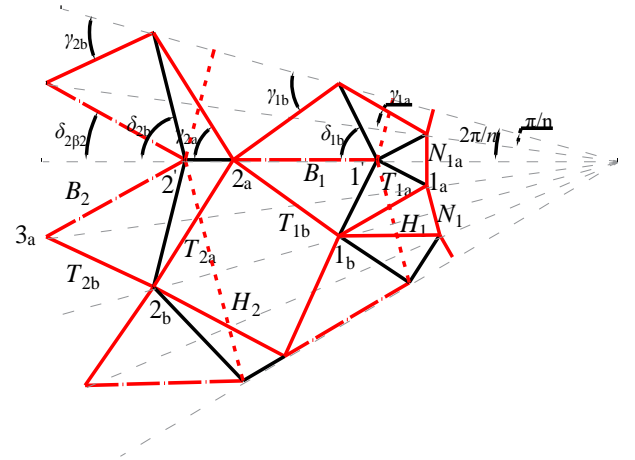
## 2.2. Pre-stress state analysis

The schematic diagram of the pentagonal three-four strut hybrid open-type cable dome is shown in Fig. 1. In the inner hoop grid, four struts and one diagonal cable intersect at the lower chord node, with one hoop cable passing through the lower chord node. In comparison, three struts and two diagonal cables intersect at the lower chord node in the outer hoop grid. The lower chord node is only positioned along the radial axis of the main grid. The inner hoop upper chord hoop cable is an important feature distinguishing it from other cable domes.

The pentagonal three-four strut hybrid open-type cable dome is symmetrical. Both the plan and section views of the dome are shown in Fig. 2. To facilitate calculations, the tilt angles with the horizontal plane of ridge cable, strut and diagonal cable are denoted as  $\alpha_{ia}, \alpha_{ib}, \phi_{ia}, \phi_{ib}, \beta_i$ , respectively. The angle between the horizontal projection and radial axis of ridge cable, strut and diagonal cable are denoted as  $\gamma_{ia}, \gamma_{ib}, \delta_{ia}, \delta_{ib}, \delta_{i\beta i}$ , respectively. Additionally, the upper chord nodes are denoted as  $i_a, i_b$ , while the lower chord node is denoted as  $i'$  ( $i = 1, 2$ ).

In a substructure with six nodes, 13 equilibrium equations [25] can be formulated. However, since the internal forces of the 14 types of components are unknown, it indicates that the structure is a first-order hyperstatic structure.

Suppose the internal force of any one type of member is known. The internal forces of the remaining 13 types of members can be obtained through the nodal equilibrium equations.



(a) Analysis model (plan view)

(b) Analysis model (section view)

Fig. 2 Analysis model of the pentagonal three-four strut hybrid open-type cable dome

When formulating the nodal equilibrium equations, two equations can be established for nodes located on the radial symmetric axis, while three equations can be established for nodes located off the radial symmetric axis. The nodal equilibrium equation group is as follows:

Node 1<sub>a</sub>:

$$\left. \begin{aligned} T_{1a} \cos \alpha_{1a} \cos \gamma_{1a} + V_{1a} \cos \phi_{1a} \cos \left( \delta_{1a} + \frac{\pi}{n} \right) - N_1 \sin \frac{\pi}{n} - N_{1a} \sin \frac{\pi}{n} &= 0 \\ T_{1a} \cos \alpha_{1a} \sin \gamma_{1a} - V_{1a} \cos \phi_{1a} \sin \left( \delta_{1a} + \frac{\pi}{n} \right) + N_1 \cos \frac{\pi}{n} - N_{1a} \cos \frac{\pi}{n} &= 0 \\ T_{1a} \sin \alpha_{1a} + V_{1a} \sin \phi_{1a} &= 0 \end{aligned} \right\} \quad (1)$$

Node 1':

$$\left. \begin{aligned} -2V_{1a} \cos \phi_{1a} \cos \delta_{1a} + 2V_{1b} \cos \phi_{1b} \cos \delta_{1b} + B_1 \cos \beta_1 - 2H_1 \sin \frac{2\pi}{n} &= 0 \\ 2V_{1a} \sin \phi_{1a} + 2V_{1b} \sin \phi_{1b} + B_1 \sin \beta_1 &= 0 \end{aligned} \right\} \quad (2)$$

Node 1<sub>b</sub>:

$$\left. \begin{aligned} -2T_{1a} \cos \alpha_{1a} \cos \left( \gamma_{1a} - \frac{\pi}{n} \right) + 2T_{1b} \cos \alpha_{1b} \cos \gamma_{1b} \\ -2V_{1b} \cos \phi_{1b} \cos \left( \delta_{1b} - \frac{2\pi}{n} \right) &= 0 \\ -2T_{1a} \sin \alpha_{1a} + 2T_{1b} \sin \alpha_{1b} + 2V_{1b} \sin \phi_{1b} &= 0 \end{aligned} \right\} \quad (3)$$

Node 2<sub>a</sub>:

$$\left. \begin{aligned} -2T_{1b} \cos \alpha_{1b} \cos \left( \gamma_{1b} - \frac{2\pi}{n} \right) + 2T_{2a} \cos \alpha_{2a} \cos \gamma_{2a} \\ + V_{2a} \cos \phi_{2a} - B_1 \cos \beta_1 &= 0 \\ -2T_{1b} \sin \alpha_{1b} + 2T_{2a} \sin \alpha_{2a} + V_{2a} \sin \phi_{2a} + B_1 \sin \beta_1 &= 0 \end{aligned} \right\} \quad (4)$$

Node 2':

$$\left. \begin{aligned} -V_{2a} \cos \phi_{2a} + 2V_{2b} \cos \phi_{2b} \cos \delta_{2b} + 2B_2 \cos \beta_2 \cos \delta_{2\beta_2} - 2H_2 \sin \frac{2\pi}{n} &= 0 \\ V_{2a} \sin \phi_{2a} + 2V_{2b} \sin \phi_{2b} + 2B_2 \sin \beta_2 &= 0 \end{aligned} \right\} \quad (5)$$

Node 2<sub>b</sub>:

$$\left. \begin{aligned} -2T_{2a} \cos \alpha_{2a} \cos \left( \gamma_{2a} - \frac{2\pi}{n} \right) + 2T_{2b} \cos \alpha_{2b} \cos \gamma_{2b} \\ -2V_{2b} \cos \phi_{2b} \cos \left( \delta_{2b} - \frac{2\pi}{n} \right) &= 0 \\ -2T_{2a} \sin \alpha_{2a} + 2T_{2b} \sin \alpha_{2b} + 2V_{2b} \sin \phi_{2b} &= 0 \end{aligned} \right\} \quad (6)$$

Before solving the equations, it is necessary to determine the angle parameters. For example, if the span of the dome is 120 meters, and both the rise-span and thickness-span ratios are 0.07. Then, the vertical projection and horizontal projection of the components can be calculated. The angle parameters can be calculated based on the projection geometric relations. Finally, by incorporating the angle parameters into the nodal equilibrium equations, the relative internal force of the components can be obtained.

Assuming the internal force of the outer hoop cable  $H_2$  is 10000 kN, the internal force of each component is obtained through nodal equilibrium equations. The results are shown in Table 2.

**Table 2**  
Sectional size and initial pre-stress of the components

Component	Pre-stress (kN)	Cross-section (mm <sup>2</sup> )
$N_1$	3711	$\Phi 155$
$N_{1a}$	4206	$\Phi 155$
$T_{1a}$	1196	$\Phi 131$
$T_{1b}$	1722	$\Phi 131$
$T_{2a}$	4108	$\Phi 155$
$T_{2b}$	3733	$\Phi 155$
$V_{1a}$	-156	$\Phi 114 \times 7.5$
$V_{1b}$	-113	$\Phi 114 \times 7.5$
$V_{2a}$	-1263	$\Phi 630 \times 11$
$V_{2b}$	-449	$\Phi 630 \times 11$
$B_1$	1086	$\Phi 131$
$B_2$	2823	$\Phi 155$
$H_1$	2085	$\Phi 131$
$H_2$	10000	$\Phi 190$

### 3. Load state analysis

#### 3.1. Finite element model

The full-scale model used in this study is a stadium with a span of 120 meters and both rise-span and thickness-span ratios of 0.07. The cable dome model consists of 264 elements, 84 struts, 180 cables and 24 edge supports. The structure is divided into 12 substructures. The cables are made of steel strands, and the struts are made of Q345B seamless steel pipe. Material parameters can be found in Table 3. Boundary conditions are applied to Nodes 3a (Fig. 1c), restraining displacements in all directions (X, Y and Z) while allowing rotations (pin connection).

Furthermore, the structure underwent static analysis using ANSYS software, with the non-linear system of equations solved using the New-Raphson method. The struts and cables were simulated using Link180 and Link10 elements, respectively. Although research shows that tensioned membranes can improve the stiffness of a structure [26], the improvement observed in the study was insignificant. Therefore, the effect of tensioned membranes on the stiffness of the structure was not considered [27]. Moreover, the external load was applied to the nodes as the equivalent concentrated load.

**Table 3**  
Material properties

Property	Cable	Strut
Steel grade	1860-grade steel	Q345B steel
Tensile strength (MPa)	1860	345
Poisson's ratio	0.3	0.3
Modulus of elasticity (MPa)	$1.95 \times 10^5$	$2.06 \times 10^5$
Coefficient of linear expansion	$1.36 \times 10^{-5}$	$1.2 \times 10^{-5}$
Density (kg/mm <sup>3</sup> )	$7.85 \times 10^{-6}$	$7.85 \times 10^{-6}$

Load state analysis is carried out to investigate the static performance of the pentagonal three-four strut hybrid open-type cable dome. The initial live load is 0.6 kN/m<sup>2</sup>, and the initial dead load is 0.1 kN/m<sup>2</sup>. All load state analyses consider the effect of gravity.

The analysis includes four cases, which are defined as follows (where  $\lambda$  is the scale factor):

- Case 1: DL 1 +  $\lambda \times$  LL 1
  - Case 2: DL 1 +  $\lambda \times$  LL 2
  - Case 3:  $1.3 \times$  DL 1 +  $1.5 \times$  LL 1
  - Case 4:  $1.3 \times$  DL 1 +  $1.5 \times$  LL 1 +  $0.7 \times 1.5 \times$  WL 1
- where DL 1: Full-span dead load  
LL 1: Full-span live load  
LL 2: Half-span live load  
WL 1: Wind load (0.45 kN/m<sup>2</sup>)

#### 3.2. Full-span uniform load

In Case 1, as the vertical live load increases, the internal forces of the components and the displacement of nodes undergo changes (see Fig. 1b for node numbering, which applies for all cases) that are illustrated in Fig. 3.

- Fig. 3a shows that as the vertical load increases, the internal forces of both the upper chord hoop cable and the ridge cable decrease. At a scale factor of  $\lambda=3.5$ , slackness occurs in the ridge cable, resulting in a decrease in the internal force of  $T_{1a}$  to 0. Additionally, the inner hoop experiences a higher rate of decrease compared to the outer hoop.
- Fig. 3b and 3c demonstrate that as the vertical load increases, the internal forces of both the diagonal and hoop cables exhibit a lower rate of increase. Additionally, the inner hoop experiences a higher rate of increase compared to the outer hoop.
- It can be seen from Fig. 3d that the internal forces of the struts increase, with the outer hoop exhibiting a higher rate of increase in comparison to the inner hoop.
- Fig. 3e and 3f show that the maximum displacement occurs at nodes 1 and 2, and the maximum displacement increases with the increase of load. The maximum vertical displacement measures -285.708 mm, which is less than  $L/250$  and complies with the limitation set by the standard "JGJ 257-2012 Technical Specification of Cable Structure". Notably, the changes in internal forces and displacements of the inner hoop components are significantly larger than those of the outer hoop.

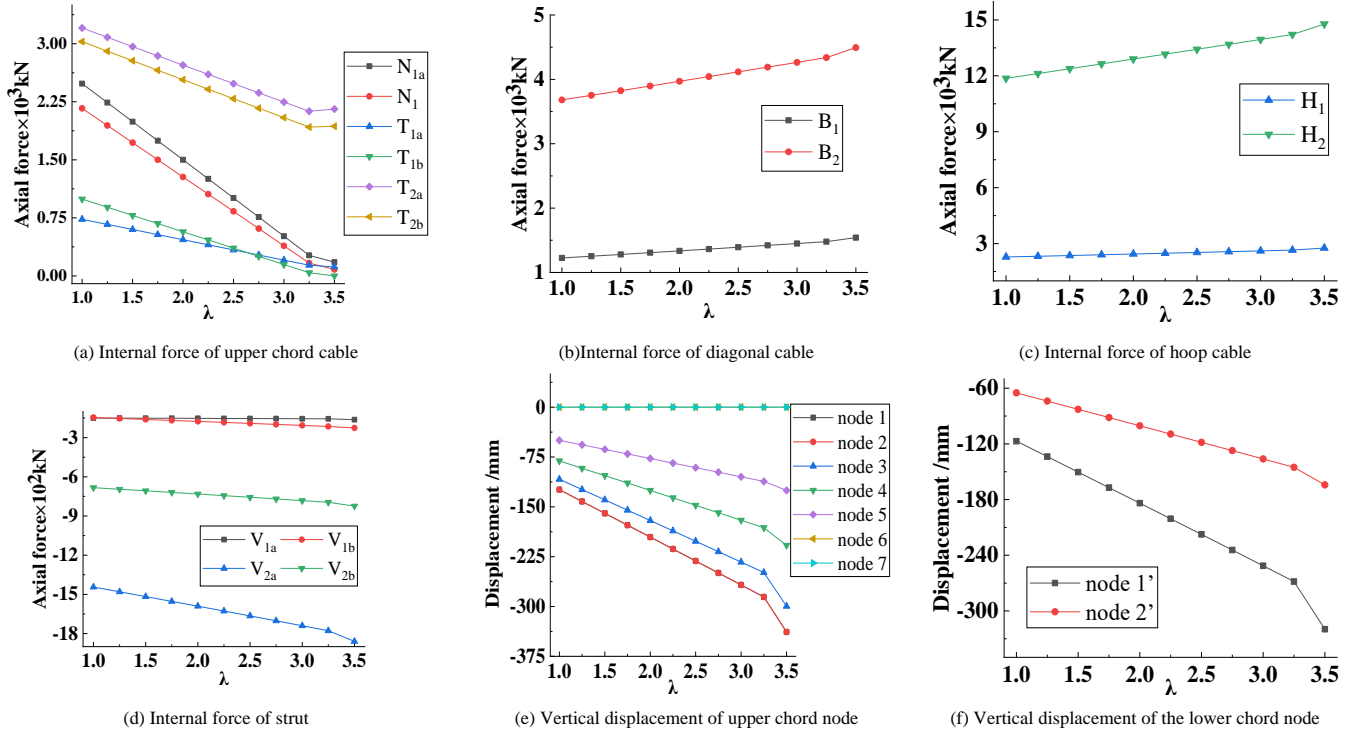


Fig. 3 Internal forces of components and nodal displacements under full-span uniform load

### 3.3. Half-span uniform live load

In Case 2, an asymmetric load analysis of the structure is carried out. The initial load comprises the dead load multiplied by 1.0 and the live load multiplied by 1.0. The live load is incrementally increased in steps (0.25 times per step). The changes in internal forces of components and nodal displacements are shown in Fig. 4 and 5. The results are summarized below.

- As shown in Fig. 4a and 5a, the internal forces of the upper chord hoop cables and ridge cables show a decreasing trend with the increase of vertical load. Particularly, the internal forces of upper chord hoop cables  $N_1$  and  $N_{1a}$  (span with live load) decrease significantly.
- As shown in Fig. 4b, 4c, 5b and 5c, in the span without live load, the internal

forces of both diagonal and hoop cables display a decreasing trend, while in the span with live load, the internal forces of diagonal and hoop cables display an increasing trend.

- As shown in Fig. 4e, 4f, 5e and 5f, the nodal displacements in the span with live load show an increasing trend with the increase of live load, while the nodal displacements in the span without live load show a decreasing trend. At a scale factor of  $\lambda=1.75$ , an arching phenomenon appears in the span without live load. When the structure is subjected to 3.25 times the initial live load, the maximum vertical displacement of the structure occurs at the upper chord node 1, measuring 544.878 mm. This value exceeds the limit of  $L/250$ , indicating that it does not meet the requirements of the standard.

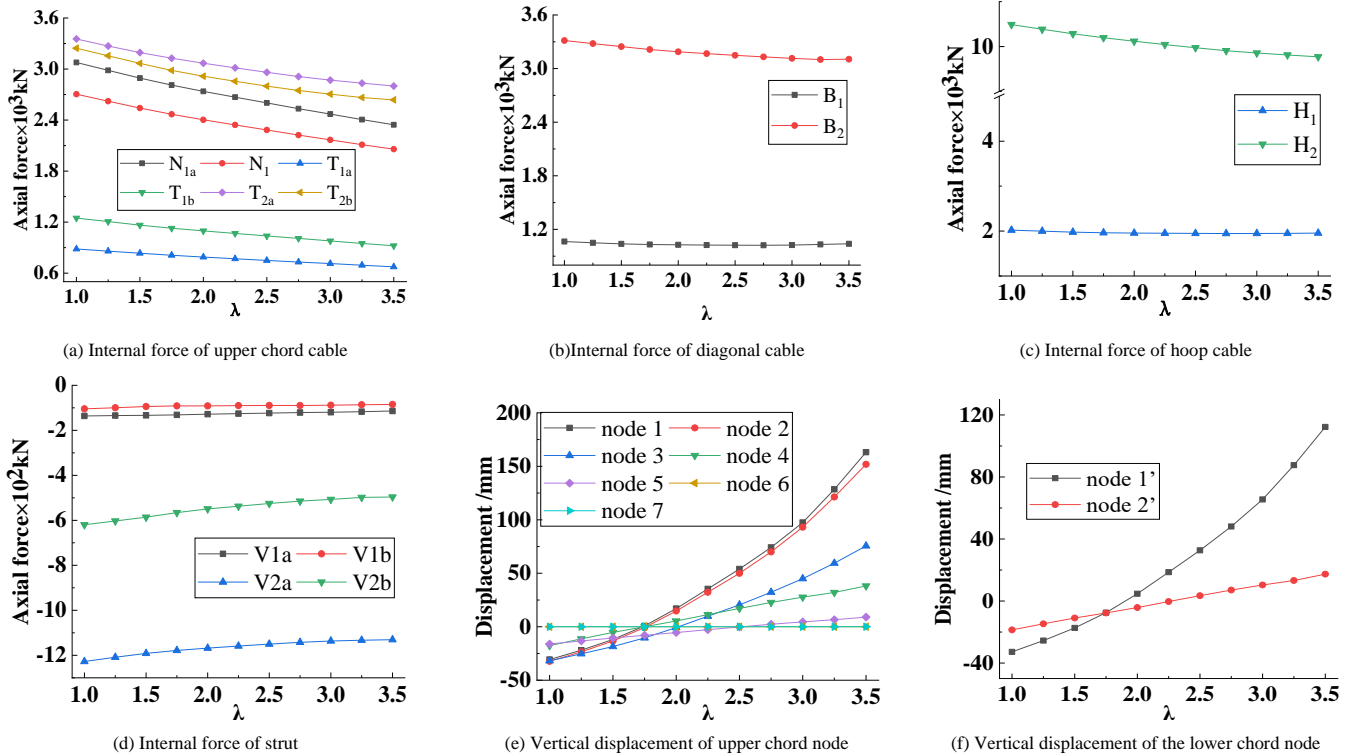


Fig. 4 Internal forces of components and nodal displacements under half-span load (span without live load)

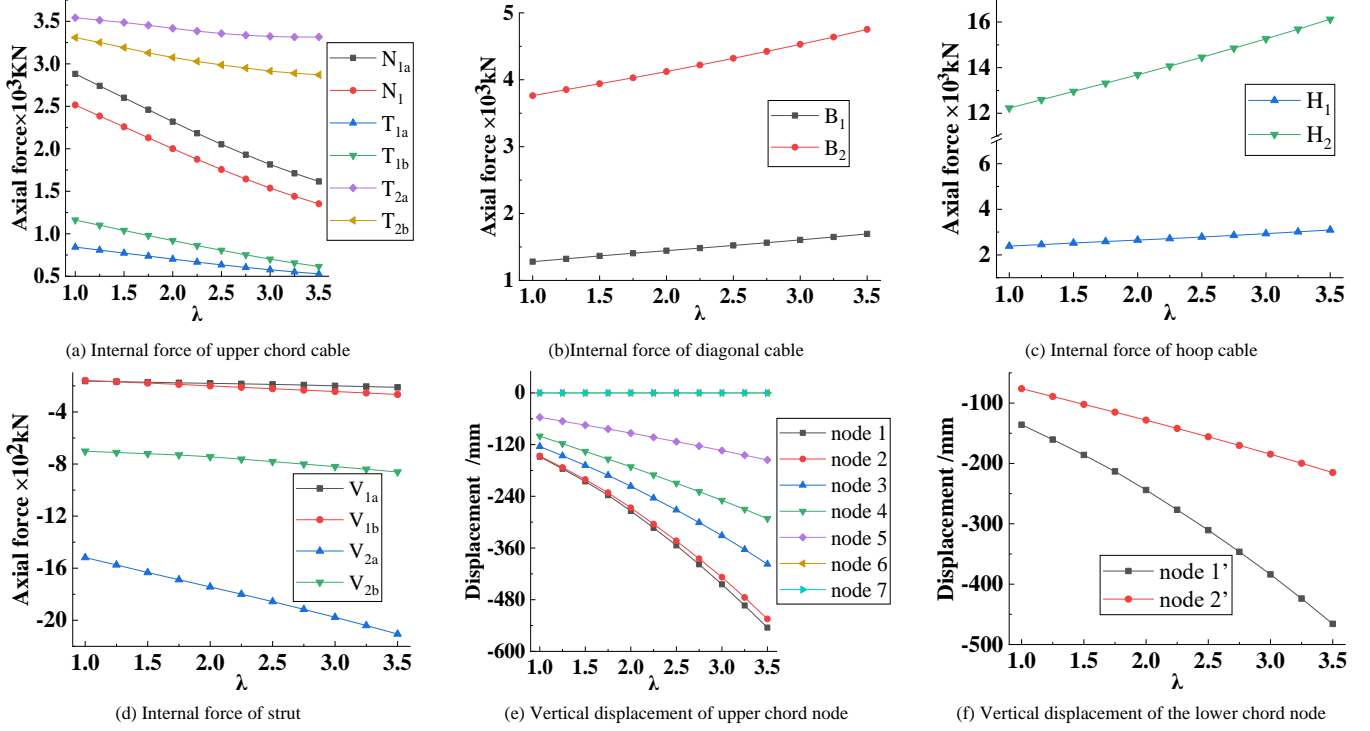


Fig. 5 Internal forces of components and nodal displacements under half-span load (span with live load)

A comparative analysis of Case 1 (Fig. 3) and Case 2 (Fig. 4) reveals that the deformation of the structure is uniform under full-span live load. However, when subjected to an asymmetric load, the deformation of the structure is undulating. In the case of half-span live load, the structure exhibits arching behavior. Under the full-span live load, the maximum vertical displacements appear at nodes 1 and 2. On the other hand, under the half-span live load, the maximum vertical displacement only occurs at node 1.

Ridge cable slackness was observed when the structure was subjected to 3.5 times the full span live load, indicating the significant influence of the pre-stress stiffness on the structure. Conversely, when the structure was subjected to 3.25 times the initial half-span live load, the deformation exceeded the limit of the standard, which indicates that the overall structural stiffness plays a dominant role at that point. The bearing capacity of the structure is reduced under asymmetric load conditions. Therefore, additional construction measures must be taken to mitigate the effect.

#### 3.4. Wind load

In large spatial structures, roof wind pressure and wind suction have a significant impact on the structural cable tension strain [28]. Therefore, it is of practical significance for structural design to study the mechanical response of the pentagonal three-four strut hybrid open-type cable dome under wind load. The equivalent static wind load is calculated according to the "GB 50009-2012 Load code for the design of building structures", using the formula  $\omega_k = \beta_z \mu_s \mu_z \omega_0$ . The wind-induced vibration coefficient  $\beta_z$  is determined as 1.0 based on wind tunnel test results and random vibration theory calculations for the flexible roof structure. The structural shape factor of wind load  $\mu_s$  is set to -1.0, considering the overall flexibility of the cable dome. For a building height of 40 m and a ground roughness class of C, the wind pressure coefficient  $\mu_z$  is assigned a value of -1.0. The reference wind pressure  $\omega_0$  is determined to be 0.45 kN/m<sup>2</sup>. The results of the comparative analysis between Case 3 and Case 4 are shown in Table 4.

**Table 4**  
Internal forces of components under two cases

Parameters	Case 3 (kN)	Case 4 (kN)	Parameters	Case 3 (kN)	Case 4 (kN)
$N_1$	1216.49	2470.07	$T_{2b}$	2142.77	2743.43
$N_{1a}$	1423.74	2811.65	$H_1$	2215.40	1965.92
$T_{1a}$	440.70	805.54	$H_2$	11961.27	10640.71
$T_{1b}$	547.07	1119.30	$V_{1a}$	-137.30	-132.01
$B_1$	1208.13	1042.57	$V_{1b}$	-153.21	-110.93
$B_2$	3392.99	3030.60	$V_{2a}$	-1433.61	-1237.29
$T_{2a}$	2507.29	3120.05	$V_{2b}$	-509.82	-463.74

Note:  $N_1, N_{1a}$ -Upper chord hoop cable;  $T_{1a}, T_{1b}$ -Ridge cable;  $B_i$ -Diagonal cable;  $H_i$ -Hoop cable;  $V_{1a}, V_{1b}$ -Strut.

The internal forces in the upper chord hoop cable and ridge cables nearly doubled under wind loads. Furthermore, when the structure is subjected to wind load, the maximum vertical displacement is -38.93 mm, whereas in the absence of wind load, the maximum vertical displacement is -134.58 mm. This substantial reduction in the maximum vertical displacement of the structure highlights the favorable impact of wind load on its structural behavior. The displacement is reduced by nearly 70%, which indicates that the structure is highly sensitive to wind load.

#### 3.5. Effect of temperature on the static performance of the structure

The effect of temperature loads on pre-stress large spatial structures should not be disregarded. In certain super-stationary structural systems, temperature stresses surpass the load stresses. Consequently, temperature loads have become the governing condition for determining the structural bearing capacity when considering load combinations. The fundamental impact of temperature on pre-stress structural systems is attributed to the thermal expansion and contraction of materials, causing the material to develop an inelastic shape. However, due to the presence of boundary constraints and mutual restraint between individual components, the free expansion or contraction are restricted, resulting in the generation of temperature stresses that ultimately affect the structural performance [29].

The annual mean temperature in China is 9.55°C, with a maximum temperature of 49.6°C and a minimum temperature of -52.3°C [30, 31]. The temperature of the component is closely influenced by the ambient temperature. In general, the surface temperature of steel tends to be 2-3°C higher than the surrounding air temperature [32]. If exposed to direct sunlight, the surface temperature of components can rise by 8-12°C compared to the ambient temperature. This study analyzes the effects of temperature on the structural performance within a temperature range of -60°C to 60°C. The structure under investigation is subjected to a uniformly distributed load of 0.7 kN due to gravity. Additionally, a pre-stress of 10,000 kN is applied to the outer hoop cable  $H_2$ . Fig. 6 shows the change in internal forces of the components and nodal displacements under different temperature loads. The conclusions are as follows:

1. With an increase in temperature, the internal forces of the struts consistently exhibit a decreasing trend (Fig. 6a-d). Notably, the outer hoop components are more sensitive to temperature variations compared to the inner loop components. The changes in internal forces in the components are significantly larger in the outer hoop than in the inner hoop.
2. When the temperature reaches 50°C, the ridge cable  $T_{1a}$  slacks, leading to a sudden change in the nodal displacement (Fig. 6a). To eliminate the



adverse effect of high temperature on the structural bearing capacity, it is recommended to appropriately increase the pre-stress level.

- When the temperature increases, the internal force of the components

decreases, and the vertical displacement decreases correspondingly (Fig. 6a-f). The reason is attributed to the diminishing contribution of pre-stress stiffness and the gradual dominance of structural stiffness.

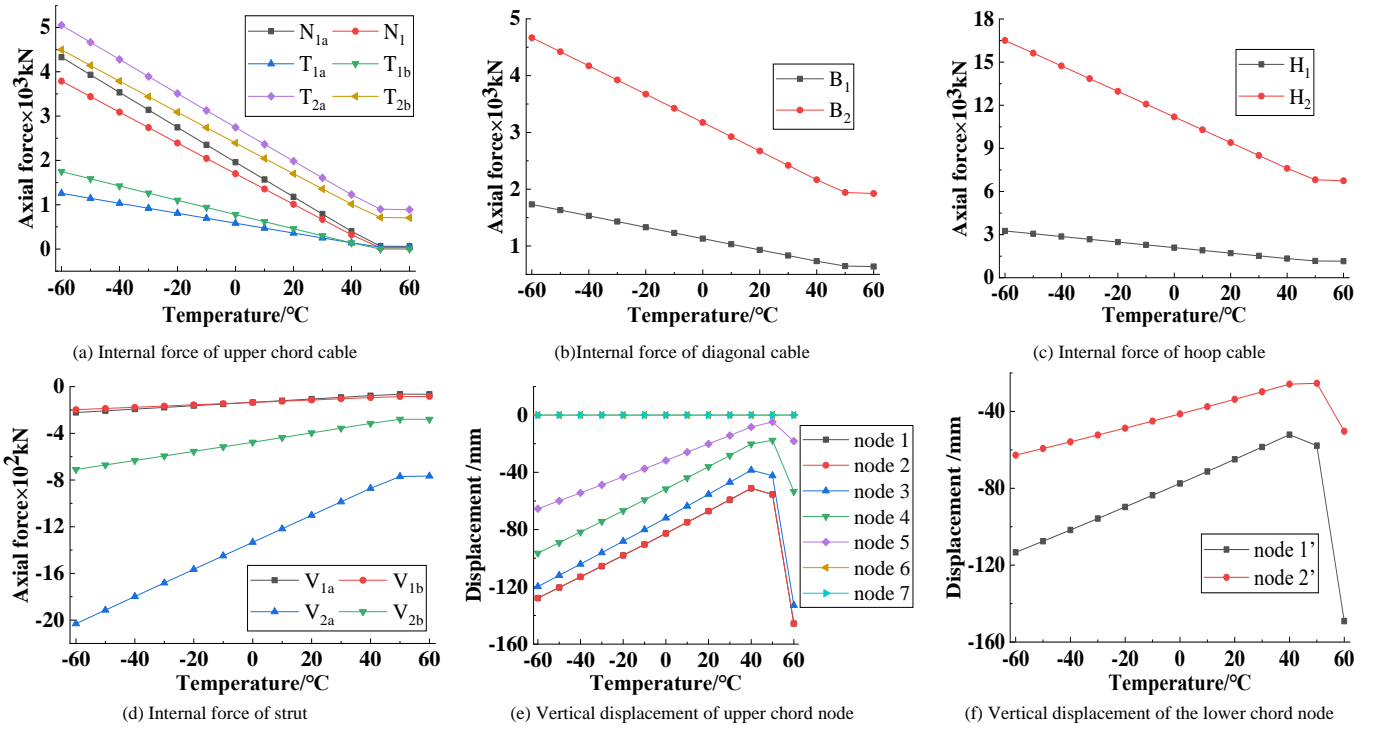


Fig. 6 Internal forces of components and nodal displacement response at different temperatures

#### 4. Parametric analysis

The performance of the cable dome structure is closely linked to its topological configuration, pre-stress distribution and pre-stress level. Therefore, it is indispensable to examine the influence of these parameters on the overall performance of the cable dome. To further explore the static characteristics of the novel cable dome, this study specifically focuses on analyzing the effects of three key parameters: rise-span ratio, thickness-span ratio and pre-stress level on the structural performance under the load conditions of case 1.

##### 4.1. Rise-span ratio

The effect of the structural rise-span ratio ( $f/L = 0.06, 0.07, 0.08, 0.09, 0.10$ ) on structural performance is discussed. The changes in internal forces of

the components are shown in Fig. 7a-d and the response of nodal displacements in Fig. 7e-f. The following conclusions can be drawn:

- As the rise-span ratio increases, the internal forces of all components decrease. The highest rate of change in internal force is observed in the upper chord hoop cable  $N_{1a}$ . Furthermore, the structural pre-stress distribution becomes more uniform.
- The larger the rise-span ratio, the smaller the structural deformation.
- With an increase in the rise-span ratio, the vertical nodal displacement becomes smaller, suggesting that appropriately increasing the rise-span ratio is beneficial to minimizing structural deformation.

However, as the rise-span ratio increases, the pre-stress of the upper chord cable decreases, resulting in a reduction in the stiffness of the structure. To prevent cable slackening, it is recommended to maintain the rise-span ratio within the range of 0.07 to 0.08.

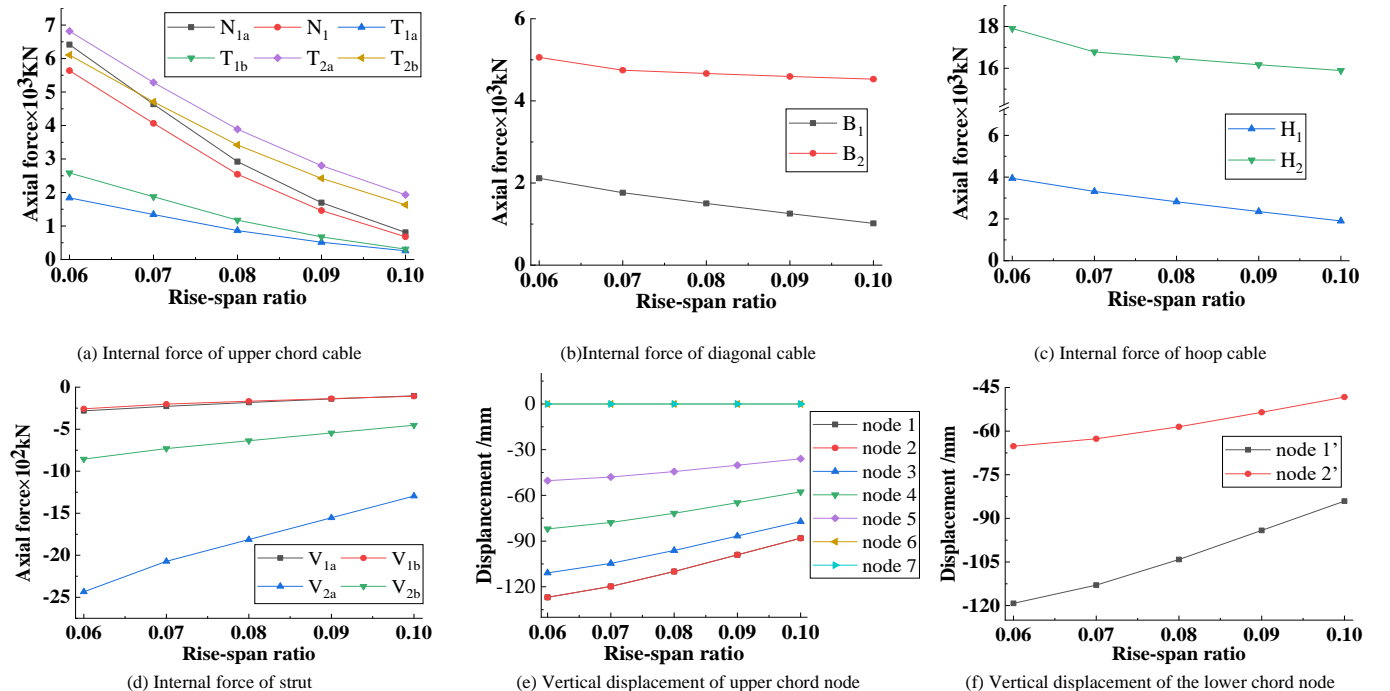


Fig. 7 Internal forces of components and nodal displacement response with the different rise-span ratios

#### 4.2. Thickness-span ratio

The response of internal forces of the components and the vertical nodal displacements as the thickness-span ratio increases is shown in Fig. 8. With an increase in thickness-span ratio, the internal forces of the upper chord cables increase. Specifically, the internal forces of  $N_1$  and  $N_{1a}$  are increased by 1600 kN and 1500 kN, respectively. Furthermore, it is observed that when the thickness-span ratio reaches 0.09, the internal force of  $N_1$  exceeds that of  $T_{2a}$ .

As the thickness-span ratio increases, the internal forces of the components generally increase. However, it is important to note that the internal force of the components does not increase uniformly with the increase in the thickness-span ratio. Specifically, in the case of the outer hoop cable  $H_2$ , its internal force exhibits an increasing trend initially and then a decreasing trend (Fig. 8b).

Increasing the thickness-span ratio can effectively reduce the vertical nodal displacement. As the thickness-span ratio increases, the vertical displacements of the upper and lower chord nodes decrease. Additionally, it is observed that the vertical displacements of the inner hoop nodes are significantly greater than those of the outer hoop nodes, indicating that the inner hoop components are more sensitive to changes in the thickness-span ratio (Fig. 8d, 8f). As the thickness-span ratio increases, the nodal displacements of the structure decrease and the internal forces of the ridge cables increase. This indicates that moderately increasing the thickness-span ratio can enhance the structural stiffness. Considering the structural cost and construction convenience, it is recommended to have a thickness-span ratio within the range of 0.06–0.08. At this range, the pre-stress forces are evenly distributed throughout the structure.

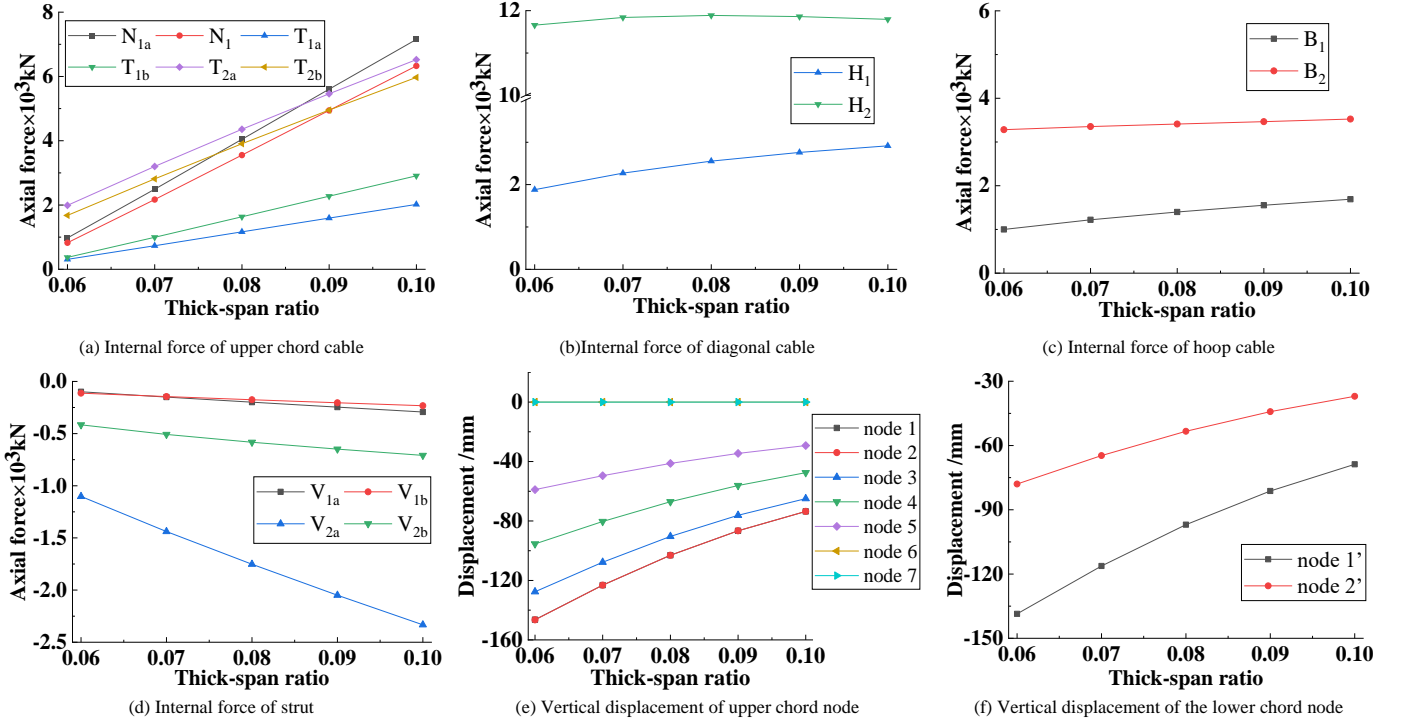


Fig. 8 Internal forces of components and nodal displacement response with the different thick-span ratios

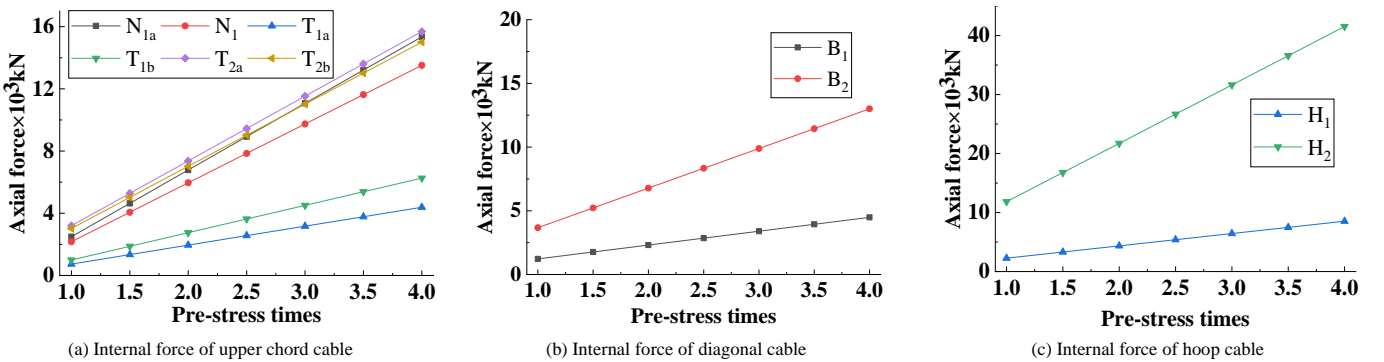
#### 4.3. Pre-stress Level

The change in internal forces of the structure and nodal displacements under different pre-stress levels is shown in Fig. 9.

1. It can be seen from Fig. 9a-d that as the initial pre-stress increases, the internal forces of all components continuously increase. The rate of change in the inner hoop ridge cables and struts is slower than that of the outer hoop ridge cables and struts.
2. From Fig. 9e-f, it is evident that the nodal displacement decreases as the

initial pre-stress increases, and the decreasing trend becomes gentler with each increment.

The vertical displacement of the structure decreases as the structural pre-stress level increases. This indicates that increasing the pre-stress level can improve the structural stiffness and prevent slackness in the ridge cables. However, it is vital to ensure that the pre-stress level does not exceed the breaking force of the cables. Additionally, increasing the pre-stress level will lead to higher construction costs.



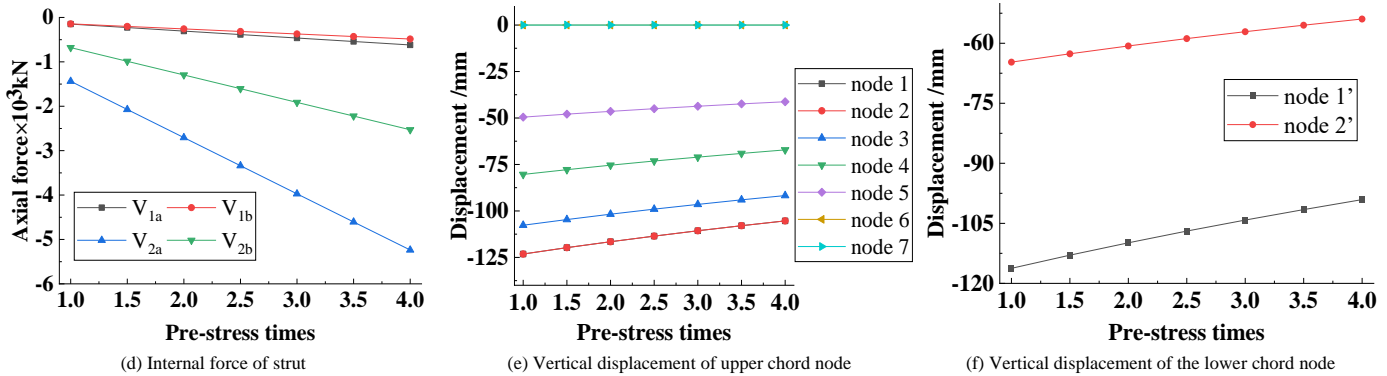


Fig. 9 Internal forces of components and nodal displacement response with different pre-stress multipliers

## 5. Conclusions

This study proposes a new cable dome design known as the pentagonal three-four strut hybrid open-type cable dome. The primary focus of the research is on conducting a topology analysis of this innovative cable dome structure. Based on the nodal equilibrium equations, the pre-stress state of the structure is determined. Furthermore, load state analysis and parametric analysis are conducted to evaluate the structural performance of the cable dome. The main conclusions of this paper are as follows:

Compared to the traditional cable dome, the structural performance of the new one is more advanced. Its strut-cable ratio is greater than that of the Levy-type cable dome and the Geiger-type cable dome. Under the same mass condition, the cost of the cable is 2.5 times higher than that of the steel pipe. Therefore, the new structure is more cost-effective.

The high-temperature load weakens the stiffness of the structure, while the low-temperature load strengthens it. The initial pre-stress design of the cable dome should consider the effect of temperature load on stiffness. To mitigate the impact of extreme weather, it is necessary to strengthen the pre-stress stiffness of the structure.

When subjected to significant asymmetric loads, the maximum nodal displacement exceeds the limit of the standard. Therefore, structural deformation should be monitored during the installation of the membrane. Engineers and workers can divide the cable dome into designated areas and install membranes simultaneously in symmetrical areas.

The structure is sensitive to wind load. Appearance design should be considered to reduce the adverse effect of wind loads.

Appropriate adjustment of the rise-span ratio, thickness-span ratio and pre-stress level can optimize the structural performance. Considering factors such as construction cost and convenience, this paper recommends a pre-stress level ranging from 1.2 to 1.5 times, a rise-span ratio ranging from 0.07 to 0.08 and a thickness-span ratio ranging from 0.06 to 0.08.

## Acknowledgments

The work was financially supported by the National Natural Science Foundation of China (No. 52268031), the Jiangxi Province University Humanities and Social Sciences Research Project (No. YS22113) and the Intelligent Building Engineering Research Center of Jiangxi Province Open Fund (No. HK20213005), which is gratefully acknowledged.

## References

- [1] Hui. Deng, M.R. Zhang, H.C. Liu, et al., "Numerical Analysis of the Pretension Deviations of a Novel Crescent-shaped Tensile Canopy Structural System", *Engineering Structures*, 119, 24-33, 2016.
- [2] T.N. Zhang, J.Y. Zhao, "Seismic Resilience Assessment of a Single-layer Reticulated Dome During Construction", *Advanced Steel Construction*, 19(1), 77-85, 2023.
- [3] X.Y. Fu, Y. Gao, C.Z. Xiao, et al., "Horizontal Skyscraper: Innovative Structural Design of Shenzhen VANKE Center", *Journal of Structural Engineering*, 138(6), 663-668, 2012.
- [4] S.J. Sun, K.H. Mei, Y.M. Sun, et al., "Structural Performance of Super-Long-Span Cable-Stayed Bridges with Steel and CFRP Hybrid Cables", *Arabian Journal for Science and Engineering*, 45(5), 3569-3579, 2019.
- [5] M.M. Ding, Bin. Luo, S.Y. Ding, et al., "Experimental Investigation and Numerical Simulation of a Levy Hinged-Beam Cable Dome", *Buildings*, 11(3), 2021.
- [6] H.H. Ma, Y.Y. Ma, Feng. Fan, et al., "Seismic performance of single-layer spherical reticulated shells considering joint stiffness and bearing capacity", *Advanced Steel Construction*, 18(2), 604-616, 2022.
- [7] Jian. Lu, S.D. Xue, X.Y. Li, et al., "Segmented Assembly Construction Forming Method Without Brackets of Spatial Cable-Truss Structure Without Inner Ring Cables", *Advanced Steel Construction*, 18(3), 687-698, 2022.
- [8] L.M. Tian, J.P. Wei, Q.X. Huang, et al., "Collapse-Resistant Performance of Long-Span Single-Layer Spatial Grid Structures Subjected to Equivalent Sudden Joint Loads", *Journal of Structural Engineering*, 147(1), 2021.

- [9] Jie. Wu, "Cable Force Characteristic Test of Bidirectional Beam String Structure after Cable Shape Optimization", *Journal of Tianjin University (Science and Technology)*, 49(1), 86-95, 2016.
- [10] Z.L. Zong, Z.X. Guo, F.W. Lv, "Experimental Research on A Composite Structure of Cable Dome and Rigid Shell", *Journal of Zhejiang University (Engineering Science)*, 29(7), 75-79, 2013.
- [11] Feng. Fan, Li. Cai, "Static Analysis of Inclined-strut System Cable Dome", *Journal of Harbin Institute of Technology*, 40(6), 841-845, 2008.
- [12] Yu. Fang, C.W. Huang, T.W. Zhou, et al., "Parameter Analysis of Rigid Kiwit Dome Structure", *Industrial Construction*, 46, 313-316, 2016.
- [13] Hui. Wu, D.Q. Cen, B.Q. Gao, "Approximate Optimization and Performance Analysis of Rigid Cable Dome Structure", *Journal of Zhejiang University (Engineering Science)*, 45(11), 1966-1971, 2011.
- [14] A.L. Zhang, C.Q. Wu, Y.X. Zhang, "Analysis on the Structure and Initial Prestress of T-Type Three Strut Cable Dome", *Journal of Beijing University of Civil Engineering and Architecture*, 37(1), 01-07, 2021.
- [15] S.L. Dong, W.G. Chen, Yuan. Tu, et al., "Configuration and Prestressing Distribution of the Honeycomb-type Cable Dome with Three Struts", *Engineering Mechanics*, 36(9), 128-135, 2019.
- [16] S.L. Dong, Y.D. Wang, H.C. Liu, "Structural Form Innovation and Initial Prestress Analysis on Drum-shaped Honeycomb-type Cable Domes with Multi-strut Layout", *Spatial Structures*, 28(3), 3-15, 2022.
- [17] A.L. Zhang, W.J. Yuan, Y.X. Zhang, et al., "Static Performance Analysis of Alternated Cable Dome with Single and Double Brace Struts", *Journal of Vibration and Shock*, 41(12), 321-330, 2022.
- [18] H.Z. Bao, S.L. Dong, "Analyses on Functions of Static Mechanic in Bird-nest Cable Dome", *Building Structure*, 38(11), 11-13+39, 2008.
- [19] S.L. Dong, W.G. Chen, Yuan. Tu, et al., "Analysis of Multi-parameter Sensitivity and Prestressing Force Distribution of Sunflower-type Cable Dome with Double struts", *Journal of Tongji University (Natural Science)*, 47(6), 739-746+801, 2019.
- [20] A.L. Zhang, L.N. Zhu, Y.X. Zhang, et al., "Configuration and Prestress Analysis Method of Star Shaped Tetrahedral Cable Dome", *Journal of Vibration and Shock*, 40(9), 84-91, 2021.
- [21] S. Kmet, M. Mojdis, "Adaptive Cable Dome", *Journal of Structural Engineering*, 141(9), 2015.
- [22] M.S. Chen, Ling. Yue, "Static Performance Analysis of Geiger-type Cable Dome", *Journal of Hunan Institute of Engineering (Natural Science Edition)*, 25(4), 73-77, 2015.
- [23] Shu. Yao, Fan. Feng, "Static Analysis of K6 Suspen-Dome Structure", *Building Structure*, 38(2), 43-46, 2008.
- [24] R.W. Tang, X.Z. Zhao, Z.Y. Shen, "Factor Analysis of Geiger Cable Dome", *Building Science*, 29(1), 11-14+10, 2013.
- [25] Yue. Feng, X.F. Yuan, A. Samy, "Analysis of New Wave-curved Tensegrity Dome", *Engineering Structures*, 250, 113408, 2022.
- [26] W.T. Yan, H.B. Zhang, "Analysis of Form-finding of Cable Dome Supporting Membrane Structures", *Steel Construction*, 23(4), 1-3, 2008.
- [27] L.L. Zhang, Chong. Ma, Yuan. Cao, et al., "Structural Stiffness of Tensioned Membrane Structure and Its Effect on the Structure Properties", *Building Structure*, 47(21), 25-29, 2017.
- [28] Yue. Yin, W.J. Chen, J.H. Hu, et al., "In-situ Measurement of Structural Performance of Large-span Air-supported Dome under Wind Loads", *Thin-Walled Structures*, 169, 108476, 2021.
- [29] Zhong. Fan, Zhe. Wang, Jie. Tang, "Analysis on Temperature Field and Determination of Temperature upon Healing of Large-span Steel Structure of the National Stadium", *Journal of Building Structures*, 28(2), 32-40, 2007.
- [30] C.H. Ye, J.Z. Lv, Z.G. Lin, "A Study on New Extreme Maximum Air Temperature in China", *Meteorological Monthly*, 34(11), 3-6, 2008.
- [31] Y.J. Zhao, Cheng. Chang, C.Y. Bai, et al., "Climate Characteristic and Change of Mohe Extreme Temperature", *Meteorological Monthly*, 35(3), 94-98, 2009.
- [32] A.L. Zhang, X.C. Liu, Shan. Feng, et al., "Temperature Response Analysis of Large-Span Cable Dome Structure", *Journal of Building Structures*, 33(4), 40-45, 2012.

# SECOND-ORDER ANALYSIS OF BEAM-COLUMNS BY MACHINE LEARNING-BASED STRUCTURAL ANALYSIS THROUGH PHYSICS-INFORMED NEURAL NETWORKS

Liang Chen <sup>1</sup>, Hao-Yi Zhang <sup>1</sup>, Si-Wei Liu <sup>1, \*</sup> and Siu-Lai Chan <sup>2</sup>

<sup>1</sup> Department of Civil and Environmental Engineering, The Hong Kong Polytechnic University, Hung Hom, Kowloon, Hong Kong, China

<sup>2</sup> NIDA Technology Company Limited, Science Park, Hong Kong, China

\* (Corresponding author: E-mail: si-wei.liu@polyu.edu.hk)

## ABSTRACT

The second-order analysis of slender steel members could be challenging, especially when large deflection is involved. This paper proposes a novel machine learning-based structural analysis (MLSA) method for second-order analysis of beam-columns, which could be a promising alternative to the prevailing solutions using over-simplified analytical equations or traditional finite-element-based methods. The effectiveness of the conventional machine learning method heavily depends on both the qualitative and the quantitative of the provided data. However, such data are typically scarce and expensive to obtain in structural engineering practices. To address this problem, a new and explainable machine learning-based method, named Physics-informed Neural Networks (PINN), is employed, where the physical information will be utilized to orientate the learning process to create a self-supervised learning procedure, making it possible to train the neural network with few or even no predefined datasets to achieve an accurate approximation. This research extends the PINN method to the problems of second-order analysis of steel beam-columns. Detailed derivations of the governing equations, as well as the essential physical information for the training process, are given. The PINN framework and the training procedure are provided, where an adaptive loss weight control algorithm and the transfer learning technique are adopted to improve numerical efficiency. The practicability and accuracy of which are validated by four sets of verification examples.

## ARTICLE HISTORY

Received: 9 November 2023  
Revised: 23 November 2023  
Accepted: 29 November 2023

## KEYWORDS

Beam-columns;  
Physics-informed neural networks;  
Second-order analysis;  
Machine learning

Copyright © 2023 by The Hong Kong Institute of Steel Construction. All rights reserved.

## 1. Introduction

Numerical solutions using machine learning have seen drastic development in recent years, largely due to the advancement in Artificial Intelligence (AI) chips, especially the advent of highly computationally efficient Graphical Processor Units (GPUs) with extensive parallel processing capacities. The application of machine learning-based (ML) methods for solving various structural engineering problems has been explored recently, such as structural analysis and design [1-5], structural health monitoring [6-10], structural optimization [11-16], and so on. The existing research mainly focuses on adopting the ML technique for regression problems. These methods are data-intensive to establish artificial neural networks (ANNs) to solve structural analysis problems through regressions. Among these methods, ANNs are used as a “black box” and the effectiveness highly relies on the qualitative and quantitative of the provided data. However, in structural engineering practice, data is often relatively scarce and costly to generate [17], which causes certain obstacles to adopting the emerging machine-learning techniques in the field of computational structural engineering.

Recently, a novel machine learning method, namely Physics-Informed Neural Networks (PINN), has been proposed by Raissi et al. [18], which is an unsupervised ML technique with the potentials for solving complex mechanical problems. PINN enriches the neural network with information from underlying physical laws, making it possible to train the neural network with few or even no pre-defined datasets while still achieving accurate approximations [19, 20]. PINN incorporates physical information into the learning process, thereby relaxing the requirements for training data. The physical information is used to guide the learning process to create a self-supervised learning procedure [21]. The features of this method are highlighted by: (1) the absence of a requirement for a pre-defined dataset, which facilitates its application to problems where the governing equations for the solution are known; (2) a potentially very fast and efficient solution process, once the network has been pre-trained using transfer learning [22-24]; and (3) a mesh-free method that does not require the division of domains.

Despite those promising features, there are still some issues with PINN. For instance, PINNs employ physics as a regularizing term in their objective function, which brings forth the challenge of manually adjusting the corresponding hyperparameters. Besides, the absence of validation data or prior knowledge of the solution to the Partial Differential Equation (PDE) can render

PINN impracticable for solving forward problems [25]. To address this, methods such as reducing the order of a given PDE, relaxing stringent smoothness requirements [25, 26], using pre-trained neural networks, and implementing transfer learning [22-24] have been proposed. Employing these techniques, PINN shows promising potential for solving various forward problems, especially in the structural engineering area, a variety of PINN-based models have been recently developed for a few mechanical problems, such as plate and shell structures [17, 27-29], solid mechanics [30, 31], beam-column members [21, 32, 33], and simple structures [34], among others. For example, Li et al. [27] established a PINN framework to characterize the finite deformation of elastic plates, where only a pseudo dataset was used. Haghighat and Juanes [31] illustrate the PINN to solve nonlinear solid mechanics, revealing that the stress distribution and displacement fields can be predicted accurately. Tao et al. [32] introduced the PINN approach for axial compression buckling analysis of thin-walled cylinders, and their research shows that the PINN model can provide satisfactory prediction only using a considerably reduced size of data. Katsikis et al. [21] illustrated the application of the PINN in static beam problems, where linear behaviors of the beams in different loading conditions can be predicted successfully. These research works confirm the feasibility of using PINN for some forward mechanical problems, suggesting that it could be an alternative solution with promising features to be the next-generation structural analysis method.

Second-order analysis is a simulation-based method and includes the effects of large deflection by establishing the equilibrium conditions on deformed shapes, which is originally proposed for stability analysis of steel members and is now used extensively in the design of steel structures [35-37] nowadays. The use of second-order analysis for the stability and large deflection problems has been extensively studied in recent decades, including stability function methods [38-40], Finite Element method (FEM) using shell elements [41-43], Line element method [44-47], Finite strip method [48-50] and so on. These methods are mostly simulation-based numerically and require trial-and-error procedures to obtain the solutions, which are usually time-consuming with extensive computational efforts. In contrast to the traditional matrix structural analysis (MSA) method, involving computational efforts of solving large sparse linear equations, the machine learning-based structural analysis (MLSA) method through PINN is proposed for the second-order analysis of steel members in this research. A schematic illustration of the traditional MSA and the proposed MLSA methods is given in Fig. 1.



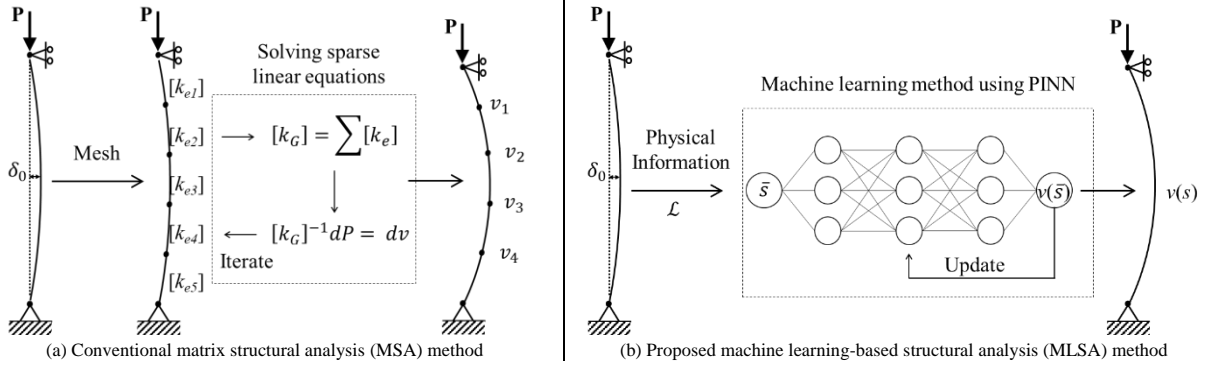


Fig. 1 An illustration of the conventional MSA method and the MLSA method

This paper extends the application of the machine learning-based method to the second-order analysis of steel beam-columns using PINN. The governing equations for the typical beam-columns under large deflection are derived and then incorporated into the physics-informed neural networks. The physical information derived from the governing equations and the boundary conditions is used to guide the training process to establish a self-supervised learning procedure. The derivation of the governing equations, the architecture of the PINN frameworks, and the training procedure are provided in detail. The practicability and accuracy of the proposed MLSA method are validated using four sets of verification examples.

## 2. Formulation

This paper proposed an innovative machine-learning-based method through PINN for the second-order analysis of steel members, where the accuracy of the embedded physical information in neural networks is the key to an accurate and reliable solution. The detailed derivation of the governing differential equations, which delineates the physical information, is given in the following section.

### 2.1. Assumptions

The following assumptions are adopted: (1) this research focuses on the geometric nonlinearity (second-order effect) of beam-columns; thus, material nonlinearity is not considered; (2) plane sections remain plane after deformation; (3) the applied loads are conservative; (4) all member connections are assumed to be either pinned or rigid, semi-rigid joints are not considered, and (5) member local buckling and distortional buckling are not considered. These assumptions are commonly accounted for in conventional structural engineering practices but can be revised and upgraded using the same concept discussed in this paper.

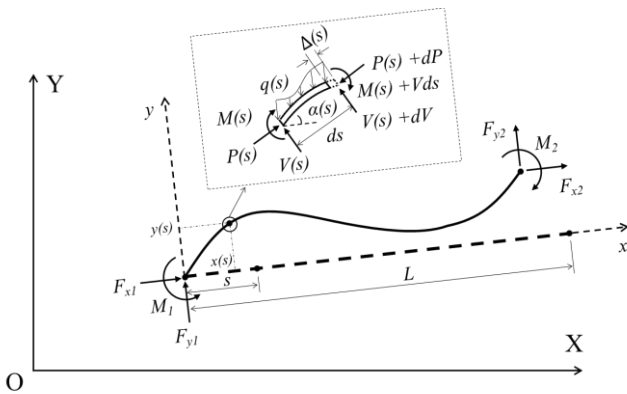


Fig. 2 Forces and deflections of a typical beam-column member

### 2.2. Mechanical model and problematic description

The basic forces versus displacements relations for a typical steel beam-column member are given in Fig. 2. The forces applied on the member ends can be summarized as follows:

$$\mathbf{F} = [F_{x1} \ F_{y1} \ M_1 \ F_{x2} \ F_{y2} \ M_2]^T \quad (1)$$

where the subscripts 1 and 2 indicate the left and right ends of the member. For a small length of the member with an original length of  $ds$  (Fig. 2), the forces acting on it can be calculated based on the equilibrium equations for the forces:

$$P(s) = F_{x1} \cos \alpha(s) + F_{y1} \sin \alpha(s) + \int_0^s q(s) \sin \alpha(s) ds \quad (2)$$

$$M(s) = -F_{x1} y(s) + F_{y1} x(s) - M_1 - \int_0^s q(s) x(s) ds \quad (3)$$

$$V(s) = -F_{x1} \sin \alpha(s) + F_{y1} \cos \alpha(s) - \int_0^s q(s) \cos \alpha(s) ds \quad (4)$$

in which,  $y(s)$  and  $x(s)$  are the local coordinates along the member after deformation, and  $q(s)$  is the distribution load applied on the member.

The displacements of any points on the member after deformation can be generated by,

$$u(s) = x(s) - s = \int_0^s \cos \alpha(s) (ds - \Delta(s)) - s; \quad 0 \leq s \leq L \quad (5)$$

$$v(s) = y(s) = \int_0^s \sin \alpha(s) (ds - \Delta(s)); \quad 0 \leq s \leq L \quad (6)$$

in which,  $\Delta(s)$  is the axial deformation as shown in Fig. 2 and  $\alpha(s)$  is the slope along the member, which can be obtained by solving the governing differential equations.

### 2.3. Governing differential equations

The governing differential equations of the beam-columns can be written as given below, based on the Hooke's law and the Euler-Bernoulli moment-curvature relationship,

$$\frac{\Delta(s)}{ds} = \frac{P(s)}{EA}, \quad \frac{d\alpha(s)}{ds} = -\frac{M(s)}{EI}, \quad \frac{d^2\alpha(s)}{ds^2} = -\frac{V(s)}{EI},$$

and  $\frac{d^3\alpha(s)}{ds^3} = -\frac{q(s)}{EI}$  (7)

where  $E$  is the material Young's modulus,  $A$  is the cross-section area, and  $I$  is the second moment of area.

### 2.4. Boundary conditions

As shown in Fig. 2, there are totally six boundary cases in a typical beam-column member. The boundary conditions and the corresponding governing equations are given in Table 1.

### 2.5. Solutions to the problem

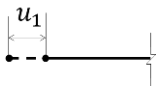
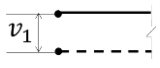
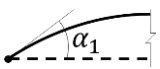
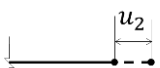
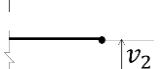
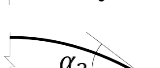
One conventional manner to solve the governing differential equations given above are to use the closed-form solutions like elliptic integral solutions [51-54]. However, in some cases, for example, when general boundary conditions are considered, the governing differential equations are notoriously difficult to solve using closed-form solutions [55]. Therefore, numerical

solutions like the FEM using line elements, also known as the frame analysis method, are often required [56]. However, the conventional FEM is based on variational principles rather than differential equations, where the primary physical law is the extremal principle, and the differential equations is only the

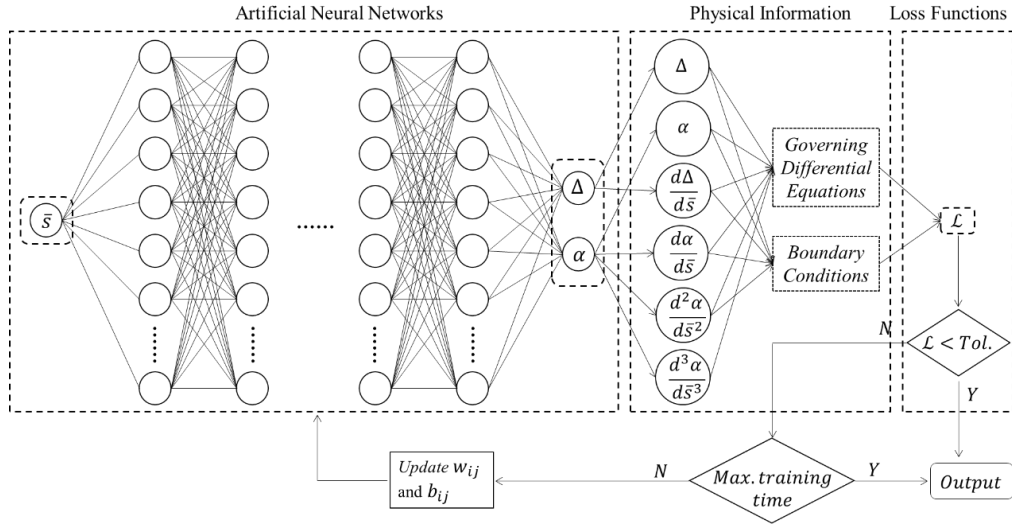
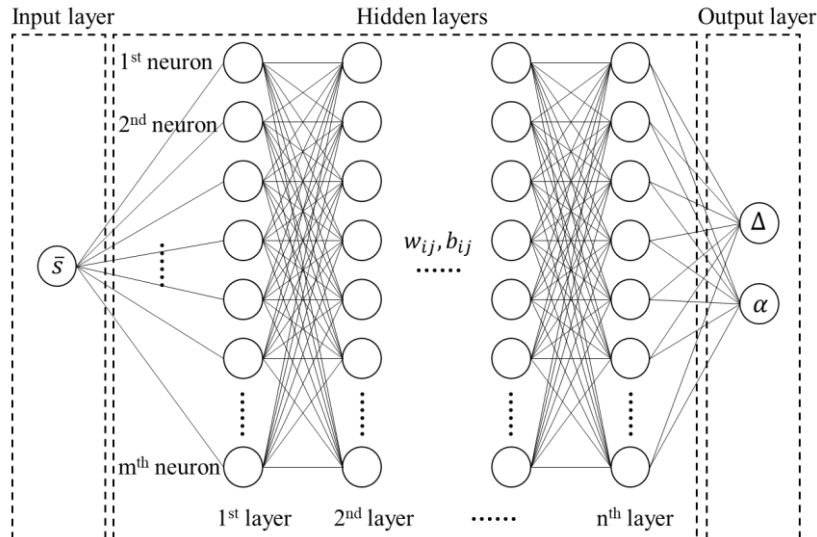
secondary consequence [57]. Therefore, a refined mesh is essentially required to get an accurate approximation, leading to extensive computational time and data-manipulation efforts.

**Table 1**

Governing equations for different boundary conditions

Boundary Condition	Fixed	Free
	$u(0) = 0$	$\frac{\Delta(s)}{ds} \Big _{s=0} = \frac{F_{x1}\cos\alpha(0) + F_{y1}\sin\alpha(0)}{EA}$
	$v(0) = 0$	$\frac{d^2\alpha(s)}{ds^2} \Big _{s=0} = \frac{F_{y1}\cos\alpha(0) - F_{x1}\sin\alpha(0)}{EI}$
	$\alpha(0) = 0$	$\frac{d\alpha(s)}{ds} \Big _{s=0} = \frac{M_1}{EI}$
	$u(L) = 0$	$\frac{\Delta(s)}{ds} \Big _{s=L} = \frac{F_{x2}\cos\alpha(L) + F_{y2}\sin\alpha(L)}{EA}$
	$v(L) = 0$	$\frac{d^2\alpha(s)}{ds^2} \Big _{s=L} = \frac{F_{y2}\cos\alpha(L) - F_{x2}\sin\alpha(L)}{EI}$
	$\alpha(L) = 0$	$\frac{d\alpha(s)}{ds} \Big _{s=L} = \frac{M_2}{EI}$

Note: the subscripts <sub>1</sub> and <sub>2</sub> indicates the left and right ends of the member

**Fig. 3** The proposed PINN framework**Fig. 4** Architecture of the neural network

### 3. Physics-informed neural networks (PINN) framework

A machine learning-based solution via physics-informed neural networks (PINN) for solving and discovering partial differential equations has been adopted in this research to solve the governing differential equations as derived above. The machine learning method using PINN to solve partial differential equations was first proposed by Raissi et al. [18] and later adopted by several researchers for different mechanical problems [19, 58-60].

Fig. 3 illustrates the framework of the PINN proposed for the present problem, which is composed of three parts: the ANNs (the approximation), the physical information (the target and correction for the approximation), and the loss functions (the evaluation of the differences). The details of each component of the PINN framework will be given in the succeeding sections. It should be noted that the proposed PINN is non-data-driven neural network; as such, pre-generated data is not required.

#### 3.1. Neural networks architecture

An essential technique required in the PINN is the architecture of the network that is formed by neurons in several layers. Neurons are expressed in an activation function used for the forward propagation that passes the information in the neural network. The neural network may comprise a large number of neurons with a complicated layer structure, which is crucial for machine-learning-based method. In this research, a fully connected feedforward neural network, as shown in Fig. 4, is used as the core of the training model. The neural network is composed of an input layer,  $n$  numbers of hidden layers, and an output layer, where the connection between layers can be written as,

$$\alpha_{ij} = f(w_{ij}\bar{s} + b_{ij}) \text{ for } j=1 \text{ (Input layer)} \quad (8)$$

**Table 2**

The number of neurons and the activation function for each layer

	Input layer	1 <sup>st</sup> hidden layer	2 <sup>nd</sup> hidden layer	3 <sup>rd</sup> hidden layer	Output layers
Number of neurons	1	10	10	10	2
Activation function	<i>Tanhshrink</i>	<i>Tanh</i>	<i>Tanh</i>	<i>Tanh</i>	<i>Tanhshrink</i>

#### 3.2. Physical information

In the traditional machine-learning methods, the ANNs are used as the “black-box” algorithms, the effectiveness of which is significantly dependent on the quality and quantity of the data provided [17]. The machine-learning methods using PINN integrate the governing equations into the learning process to essentially relax the requirements on training data. The physics-informed governing equations are used to orientate the learning process creating a self-

$$\alpha_{ij} = \sum_{i=1}^m f(w_{ij}\alpha_{ij-1} + b_{ij}) \text{ for } 2 \leq j \leq n \text{ (Hidden layer)} \quad (9)$$

$$\alpha(x) = \sum_{i=1}^m f(w_{ij}\alpha_{ij-1} + b_{ij}) \text{ for } j = n+1 \text{ (Output layer)} \quad (10)$$

in which,  $\bar{s} = s/L$  represents the normalized coordinate along the member;  $n$  and  $m$  are the numbers of hidden layers and the number of neurons at each layer, respectively, and  $n=3$  and  $m=10$  are used in the present study of being effective for most problems;  $w_{ij}$  are the internal weights;  $b_{ij}$  are the bias; and  $f$  stands for the activation function.

The activation functions were introduced by Candès [61] based on harmonic analysis, which decide whether a neuron should be activated or not based on the importance of the neuron’s input in the process of the prediction. In the present study, two types of activation functions, *Tanh* and *Tanhshrink*, are adopted in the hidden layers and input/output layers, respectively. (See Table 2).

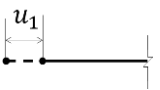
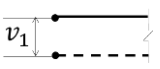
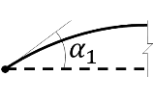
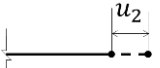
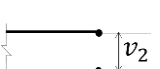
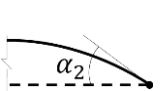
$$\text{Tanh}(x) = \frac{e^x - e^{-x}}{e^x + e^{-x}} \quad (11)$$

$$\text{Tanhshrink}(x) = x - \text{Tanh}(x) \quad (12)$$

supervised learning procedure, which is considered the unsupervised learning method. In summary, the PINN method is a machine learning-based computational method intended to provide an accurate prediction of problems via the ANNs with incorporation of the physical information. As shown in Fig. 3, the physical information incorporated in the proposed PINN method is provided by two parts: the governing differential equations and the boundary conditions.

**Table 3**

Governing equations for different boundary conditions

Boundary Conditions	Fixed	Free
	$\mathcal{L}_{BC1} = [0 - u(0)]^2$	$\mathcal{L}_{BC1} = \left[ \frac{F_{x1}\cos\theta(0) + F_{y1}\sin\theta(0)}{EA} - \frac{\Delta(s)}{ds} \right]_{s=0}^2$
	$\mathcal{L}_{BC2} = [0 - v(0)]^2$	$\mathcal{L}_{BC2} = \left[ \frac{F_{y1}\cos\theta(0) - F_{x1}\sin\theta(0)}{EI} - \frac{d^2\theta(s)}{ds^2} \right]_{s=0}^2$
	$\mathcal{L}_{BC3} = [0 - \theta(0)]^2$	$\mathcal{L}_{BC3} = \left[ \frac{M_1}{EI} - \frac{d\theta(s)}{ds} \right]_{s=0}^2$
	$\mathcal{L}_{BC4} = [0 - u(L)]^2$	$\mathcal{L}_{BC4} = \left[ \frac{F_{x2}\cos\theta(L) + F_{y2}\sin\theta(L)}{EA} - \frac{\Delta(s)}{ds} \right]_{s=L}^2$
	$\mathcal{L}_{BC5} = [0 - v(L)]^2$	$\mathcal{L}_{BC5} = \left[ \frac{F_{y2}\cos\theta(L) - F_{x2}\sin\theta(L)}{EI} - \frac{d^2\theta(s)}{ds^2} \right]_{s=L}^2$
	$\mathcal{L}_{BC6} = [0 - \theta(L)]^2$	$\mathcal{L}_{BC6} = \left[ \frac{M_2}{EI} - \frac{d\theta(s)}{ds} \right]_{s=L}^2$

Note: the subscripts 1 and 2 indicates the left and right ends of the member

### 3.3. Loss functions

The machine-learning solution via PINN requires the problem to be priorly described in a set of governing equations and the boundary conditions in the form of a series of partial differential equations. The training process is subsequently carried out to scrutinize the solution to the problem by assessing the errors, generally articulated in the form of loss functions, to verify its accuracy. The loss functions will provide a beneficial regularization effect on the training process by penalizing simulations that are not respectful of the given physical information. Based on the governing differential equations and the boundary conditions, the total loss function  $\mathcal{L}$  can be expressed by,

$$\mathcal{L} = \sum_{i=1}^4 \mathcal{L}_{Gi} + \sum_{j=1}^6 \mathcal{L}_{BCj} \quad (13)$$

where,  $\mathcal{L}_G$  is the loss function from the governing differential equations given by Equation (7):

$$\mathcal{L}_{g1} = \frac{1}{Nc} \sum_{i=1}^{Nc} \left[ \frac{P(s)}{EA} - \frac{\Delta}{ds} \right]_{s_i}^2 \quad (14)$$

$$\mathcal{L}_{g2} = \frac{1}{Nc} \sum_{i=1}^{Nc} \left[ \frac{M(s)}{EI} - \frac{d\theta}{ds} \right]_{s_i}^2 \quad (15)$$

$$\mathcal{L}_{g3} = \frac{1}{Nc} \sum_{i=1}^{Nc} \left[ \frac{V(s)}{EI} - \frac{d^2\theta}{ds^2} \right]_{s_i}^2 \quad (16)$$

$$\mathcal{L}_{g4} = \frac{1}{Nc} \sum_{i=1}^{Nc} \left[ \frac{q(s)}{EI} - \frac{d^3\theta}{ds^3} \right]_{s_i}^2 \quad (17)$$

in which,  $Nc$  is the number of the collocation points, which are randomly aligned along the member.  $\mathcal{L}_{BC}$  is the loss function from the boundary conditions that can be defined accordingly to Table 3.

### 4. Training details

The governing equations and boundary conditions of the beam-columns are defined in the form of a series of partial differential equations as given. Sequentially, the neural networks (see Fig. 4) are then established to provide an approximation solution to the problem. The training process, depicted in Fig. 5, is executed to examine the approximation of the problem by evaluating the errors - usually denoted in the form of loss functions - to validate its accuracy. During the training process, forward and back propagation operations are proceeded, wherein the internal weights  $w_{ij}$  and the bias  $b_{ij}$  connecting the neurons are updated continuously to minimize errors. The solution could be obtained once the value of the loss function is within the acceptable tolerance (usually 0.1%). This training process can be accelerated dramatically by introducing the adaptive loss function method [62], and the trained network can be inherited and later used for other problems by adopting the transfer learning method [22, 23].

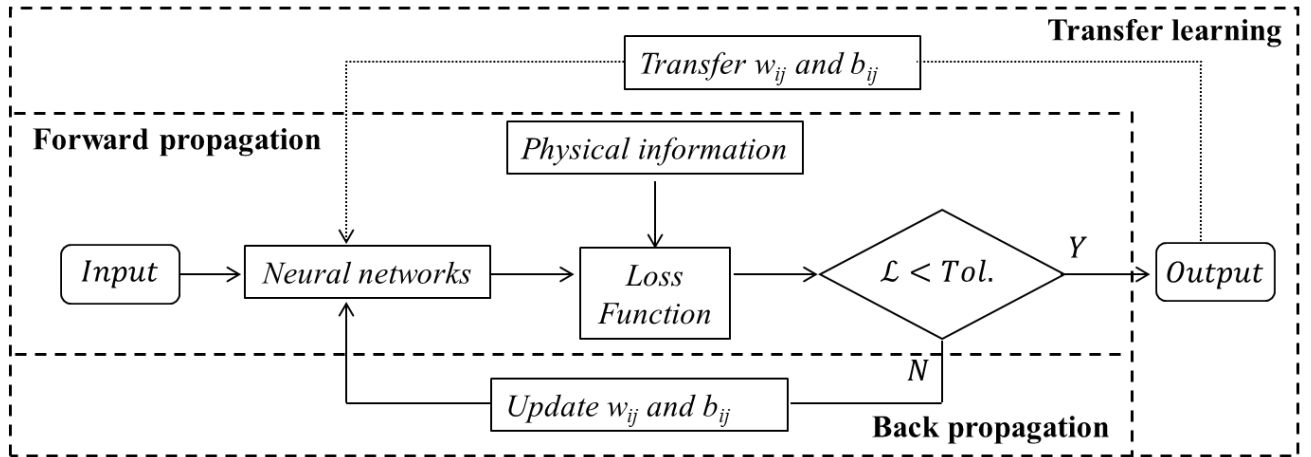


Fig. 5 The training procedure

#### 4.1. Self-supervised learning procedure

In this research, the underlying physical laws underpinning the second-order analysis of beam-columns encompassed within governing differential equations and the boundary conditions, based on which the loss functions are given to evaluate the differences between the approximation from the PINN-derived approximation and the established physical information. As shown in Fig. 5, during the learning procedure, the internal parameters of the neural network ( $w_{ij}$  and  $b_{ij}$ ) will be updated by optimization algorithms to minimize the loss functions given in Equation (13).

Several stochastic optimization algorithms have been proposed to minimize the loss function [63, 64], among which, the Adaptive Moment Estimation introduced by Kingma and Ba [65] is one of the most efficient and widely adopted optimization algorithms [66, 67]. In the present study, the learning rate of the Adam optimizer is set to 0.001 by default, and for the learning rate scheduler, we adjusted the hyperparameters used by the Adam optimizer. The exponential decay rate for the first-moment estimates (mean) is set to 0.9, and the decay rate for the second-moment estimates (uncentered variance) is set to 0.999. Integrating the Adaptive Moment Estimation as the optimization algorithm, the detailed backpropagation training procedure with six steps in total is elaborated as follows:

**Step 1:** Input the basic information for the structural analysis, such as the section properties, the boundary conditions, the geometric information, the loading conditions, etc.

**Step 2:** Assemble the neural network and initialize the internal parameters of the neural network.

**Step 3:** Randomly place  $Nc$  numbers of sampling points along the member and get an approximation from the output layer.

**Step 4:** Calculate the loss function using Equation (13)

**Step 5:** If the total loss is smaller than tolerance or the maximum training time has been achieved, terminate the training procedure, and output the approximation.

**Step 6:** Update the internal parameters of the neural network ( $w_{ij}$  and  $b_{ij}$ ) by optimization algorithms to minimize the loss functions and repeat Steps 3-5.

#### 4.2. Adaptive loss weight algorithm

In Equation (13), all the terms in the total loss function have the same weights, suggesting that the physical laws dictated by the governing differential equations and boundary conditions share the same significance. However, in real cases, one or several terms might be much more significant than the others. For example, for a simply supported beam under bending moment, the bending deformations are more significant than the axial shortening, which means that the loss function given by Equation (15) is more significant than the loss function expressed in Equation (14). Consequently, an adaptive loss weight algorithm proposed by Wang and Teng [62] is employed to improve the accuracy and efficiency of the training procedure. Equation (13) will be revised as,



$$\mathcal{L} = \sum_{i=1}^{NL} w_i \mathcal{L}_i \quad (18)$$

in which,  $NL$  stands for the number of terms from the governing differential equations and the boundary conditions in the total loss function, and the  $w_i$  are the weights for the terms in the loss function. The specific physical laws and boundary conditions, as given in Equation (7) and

Table 1, respectively, contribute to enhancing numerical stability when implementing the adaptive loss weight algorithm, which was previously reported for the instability issue in the literature [68]. Therefore, the potential instability issue is not significant in this research.

All the loss weights are set to be unity at the beginning of the training process. The update step for  $w_i$  in the training procedure can be expressed as follows,

$$w_i^t = \beta w_i^{t-1} + (1 - \beta) w_i^t \quad (19)$$

in which,

$$w_i^t = \frac{NL}{w_i^{t-1}} \frac{\max(|\mathcal{L}_i^t|)}{\sum_{i=1}^{NL} |\mathcal{L}_i^t|} \quad (20)$$

where, the superscript  $t$  denotes the  $t^{\text{th}}$  training time;  $\beta$  is a hyper-parameter and taken as 0.9 in this paper; and  $\mathcal{L}_i^t$  represents the gradient of the  $i^{\text{th}}$  loss term in the  $t^{\text{th}}$  training time.

#### 4.3. Transfer learning

Despite the proposed MLSA is a mesh-free solution with some intriguing features, the training process may be sometimes time-consuming. The neural network composes of enormous numbers of neurons with a complicated layer structure, and the optimization of the internal parameters of the neural network could take a certain long time. To enhance computational efficiency, the transfer learning technic can be adopted. Transfer learning is a well-established technique that has been widely used in machine learning methods [22-24]. The previously established neural network can be directly applied to similar problems, resulting in substantial savings in training time. Therefore, if a neural network can be properly established and well-trained through a range of problems, this network can be reutilized in subsequent applications with significantly enhanced computational efficiency, which may even achieve instant solutions faster than the traditional matrix-analysis-based structural analysis methods.

#### 5. Comparisons between traditional finite-element-based and proposed machine-learning-based analysis procedures

A comparison of the analysis procedures of the conventional finite-element-based analysis and the proposed MLSA methods is provided in Fig. 6. In the conventional FE-based methods [46-47, 69], after acquiring the basic information, for example, the geometric details, the material properties, and the boundary and loading conditions, the models will mesh into a series of fine-meshed elements. Sequentially, the derived element stiffness matrix formulations will be used to form the stiffness matrix, which will be further used for the generation of nodal displacements and forces.

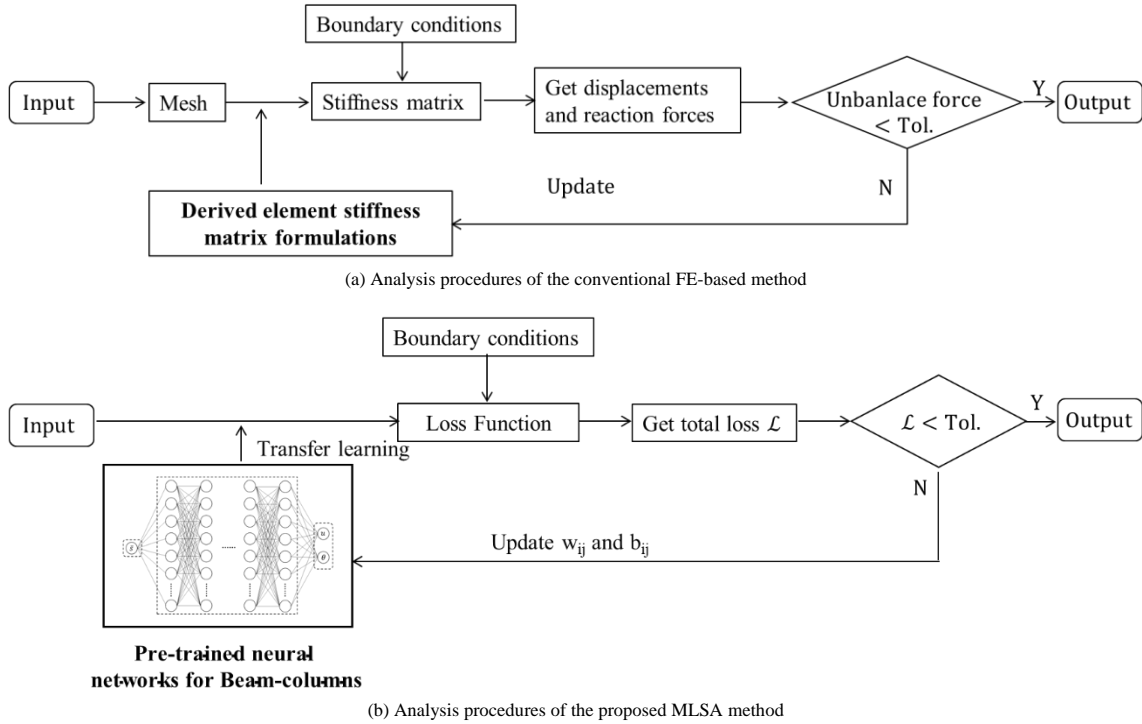


Fig. 6 Analysis procedure

In the proposed MLSA method, the derived element stiffness matrix formulations are not required; instead, the pre-trained neural networks are utilized. The pre-trained neural networks for beam-columns used in this paper were trained using some classic examples provided in the well-recognized textbook [70]. By leveraging the transfer learning method, these pre-trained neural networks will be used to enhance the computational efficiency of the proposed method.

#### 6. Verification examples

Four sets of verification examples are given to validate the practicability and accuracy of the proposed MLSA method. The second-order analysis of members under different boundary and loading conditions is conducted using the proposed method, and the results are compared with those from the closed-form solutions and FEM, where the high-order beam-column elements proposed

by Chan and Zhou [75] are used. The summaries of the analysis parameters and computational expenses for the following examples are provided in Table 4 and Table 5. All training processes and computations are performed on a computer equipped with an i9-12900h CPU and an NVIDIA GeForce 3090 GPU. The number of elements presented in Table 4 specifies the minimum quantity required for accurate analysis of problems exclusively associated with large deflections, as determined through the sensitivity study.

From Table 5, it can be observed that transfer learning is an effective method to reduce the computation time of the MLSA method; but the pre-training of the neural network is time-consuming. Nevertheless, unlike the modeling and mesh generation of the FE model, which is a case-to-case-based procedure, the pre-trained neural network can be a solution for general problems. In this research, the pre-trained neural networks for the second-order analysis of beam-columns are provided, and the practicability and accuracy of which are validated by the following examples.

**Table 4**

Summary of the analysis parameters for Examples 1 to 4

	FEM [75]			Proposed MLSA Method		
	Number of elements	Number of load steps	Numerical tolerance	Number of collocation points	Number of epochs for pre-training	Numerical tolerance
E.1	5	100	$1 \times 10^{-4}$	200	10000	$1 \times 10^{-4}$
E.2	Pin-pinned column	20		100	10000	
	Pin-fixed column	20		100	10000	
E.3	10	1		100	10000	
E.4	10	1		100	10000	

Notes: E. stands for Example

**Table 5**

Summary of the computational time for Examples 1 to 4

		FEM [75]	Proposed MLSA Method		
		Computational time	Pre-raining time	Computational time (with transfer learning)	Computational time (without transfer learning)
E.1	Pin-pinned column Pin-fixed column	31.2 s	About 20 minutes	13.32 s	21.66 s
E.2		8.35 s		24.66 s	48.81 s
		8.22 s		13.95 s	41.53 s
E.3		7.54 s		10.26 s	12.46 s
E.4		9.08 s		21.64 s	140.81 s

Notes: E. stands for Example

**6.1. Example 1 – Cantilever beams under end moment**

A cantilever beam subjected to end moment is studied and loaded to perform large deflection to show the accuracy and capability of the proposed MLSA method. The beam has a length of 4 meters, and the bending stiffness  $EI$  of the beam cross-section is assumed to be 1. The bending moments applied on the right end are up to  $4\pi$ , which can make the member wind twice around itself. This is a classical nonlinear structural analysis problem that has been investigated by several researchers [71-74] during the past decades. Recent studies tried to solve this large-rotation problem using the fine-meshed FEM, where the number of which ranges from three up to a hundred for a single member [71-72], showing the intensive computational expense.


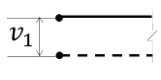
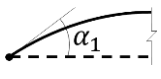

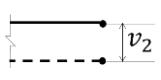
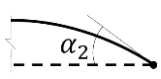
The detailed governing differential equations and boundary equations taken are given in Table 6 for demonstration. The deformed shapes of the members generated from the proposed MLSA method are plotted in Fig. 7, where the closed-form solutions to this problem (circular arcs with radius  $\rho = \frac{EI}{M}$ ) are

also given as the benchmarks. Besides, the results from the FEM using five high-order beam-column elements, proposed by Chan and Zhou [75], are also given for the comparisons.

The results given by the proposed MLSA method using PINN are perfectly in line with those from the closed-form solutions, indicating the proposed method can predict the nonlinear behaviors of the members under pure bending accurately. It should be noted that although the FEM using five beam-column elements can predict the displacements accurately, certain load steps with a number of iterations per step are required (as demonstrated in Table 7) to get accurate predictions leading to a long computational time. Besides, the FEM only gives the displacements at the element nodes, and the displacements between the element nodes need to be calculated approximately based on the assumed element shape functions with some small errors. However, the proposed MLSA method can get accurate member deformations along the whole length by a single attempt of analysis, accurate and efficient.

**Table 6**

Governing differential equations and boundary equations for Example 1

Governing differential equations		$\frac{\Delta(s)}{ds} = \frac{P(s)}{EA}$ , and $\frac{d\alpha(s)}{ds} = -\frac{M(s)}{EI}$	
Governing boundary equations		Fixed	$u(0) = 0$
		Fixed	$v(0) = 0$
		Fixed	$\alpha(0) = 0$
		Free	$\frac{\Delta(s)}{ds} \Big _{s=L} = \frac{F_{x2}\cos\alpha(L) + F_{y2}\sin\alpha(L)}{EA}$
		Free	$\frac{d^2\alpha(s)}{ds^2} \Big _{s=L} = \frac{F_{y2}\cos\alpha(L) - F_{x2}\sin\alpha(L)}{EI}$
		Free	$\frac{d\alpha(s)}{ds} \Big _{s=L} = \frac{M_2}{EI}$

Note:  $F_{x2} = 0$ ,  $F_{y2} = 0$ , and  $M_2 = M$  in this example

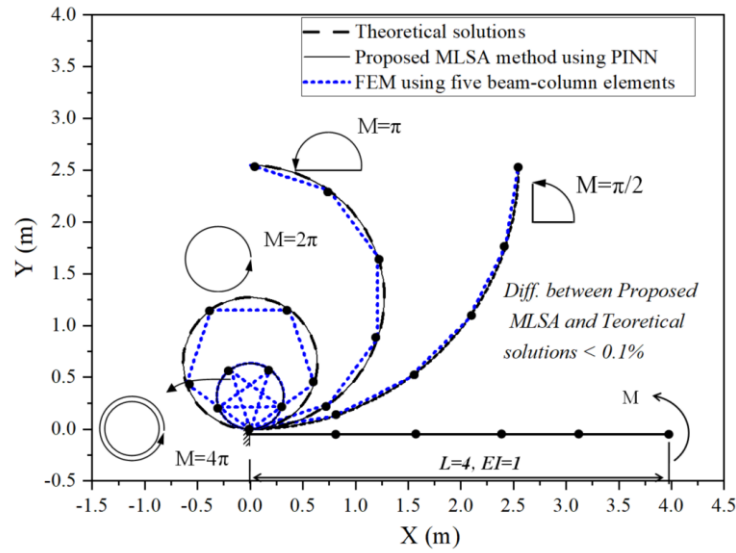


Fig. 7 Deformed shapes of the member under end moments

Table 7

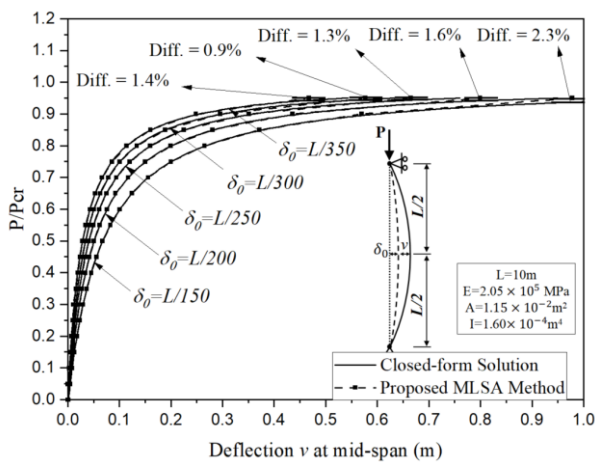
Numerical efficiency of the FEM when analysing the member winding twice around itself

FEM using five beam-column elements			FEM using ten beam-column elements		
Number of incremental load steps	Iterations per step	Total number of iterations	Number of incremental load steps	Iterations per step	Total number of iterations
1-23 steps	Divergent		1-23 steps	Divergent	
24 steps	7	168	24 steps	6	144
50 steps	4	200	50 steps	3	150
100 steps	2	200	100 steps	2	200

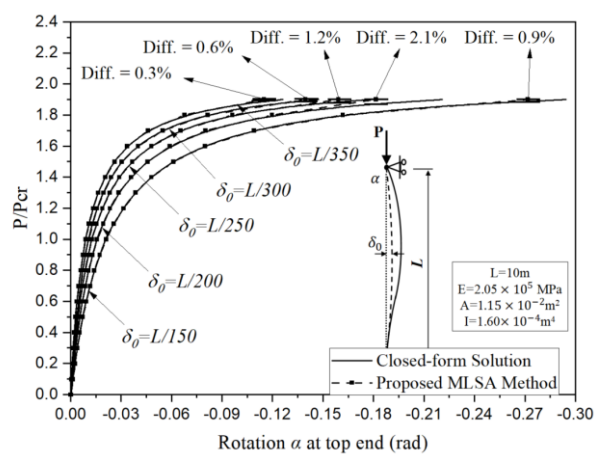
### 6.2. Example 2 – Imperfect columns under axial compression

This example studies the behaviours of imperfect members under axial compression. The columns with two different boundary conditions, such as the pin-pinned and the pin-fixed boundaries, are investigated. As shown in Fig. 8, the length of the column is 10 meters with the material Young's modulus equals to 205 GPa, and the cross-section area and the second moment of area equal to  $1.15 \times 10^{-2} \text{ m}^2$  and  $1.60 \times 10^{-4} \text{ m}^4$ , respectively. The shapes of member imperfections are all assumed as half sine-wave along the entire member length, and the magnitude of the initial curvature at mid-span  $\delta_0$  varies from  $L/350$  to  $L/150$ , as recommended in Eurocode-3 [36].

This example was formerly studied by Liu et al. [76], where an advanced beam-column element is used, and the detailed derivation of the closed-form solutions for this example is available in the reference [76]. The load-displacement curves prior to buckling are generated by the proposed MLSA method, and the comparison results are plotted in Fig. 8, where the results from the closed-form solutions are given as the benchmark. The results given by the proposed MLSA method closely matched those from the closed-form solutions. It confirms the applicability of the proposed MLSA method for accurately analyzing the imperfect column under axial compression.



(a) Pin-pinned column



(b) Pin-fixed column

Fig. 8 Load-displacement curve of the imperfect columns under axial compression

### 6.3. Example 3 – Cantilever beams under distributed loads

In this example, the behaviours of cantilever beams under distributed loads are investigated. As shown in Fig. 9, four different cases of uniformly and nonuniformly distributed loads are applied to the members to study the large deflection behaviors of the cantilever beams. The length of the beam is 4m, and the bending stiffness  $EI$  of the beam cross-section is  $1.006 \times 10^3 \text{ kNm}^2$ .

The deformed shapes of the cantilever beam under distribution loads are generated and plotted in Fig. 9, where results from the FEM using ten beam-column elements are introduced, serving as the benchmark solutions. From Fig. 9, the member deformations under uniformly and nonuniformly distribution load predicted by the proposed MLSA method using PINN are in line with those from the FEM, showing the accuracy and reliability of the proposed method.

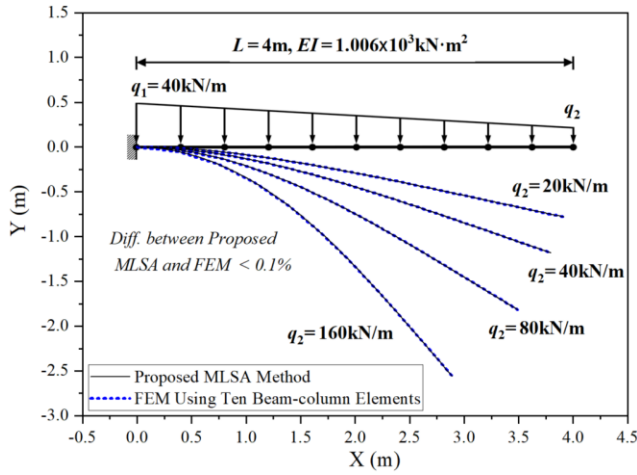


Fig. 9 Deformed shapes of the cantilever beam under distributed loads

#### 6.4. Example 4 - Columns under combined bending and axial loads

In this example, the members with relatively complex loading conditions are investigated, where columns under combined bending and axial loads are analyzed using the proposed MLSA method. Detailed loading and boundary conditions are given in Fig. 10, where the height of the column is 4m, and the bending moment varies from 0.02P to 0.1P. The material is steel with the Young's modulus of 205 GPa. The cross-section area is  $5.27 \times 10^{-3} \text{ m}^2$  and the second moment of area about both the principal axes is  $4.91 \times 10^{-8} \text{ m}^4$ .

The load-displacement curves of the members under combined bending and axial loads generated from the proposed MLSA method are given in Fig. 10, where the results from the FEM using ten beam-column elements are also given for comparison. The overall agreement is very satisfactory, indicating that the proposed MLSA method can predicate the nonlinear behaviors of the members under combined bending and axial loads accurately.

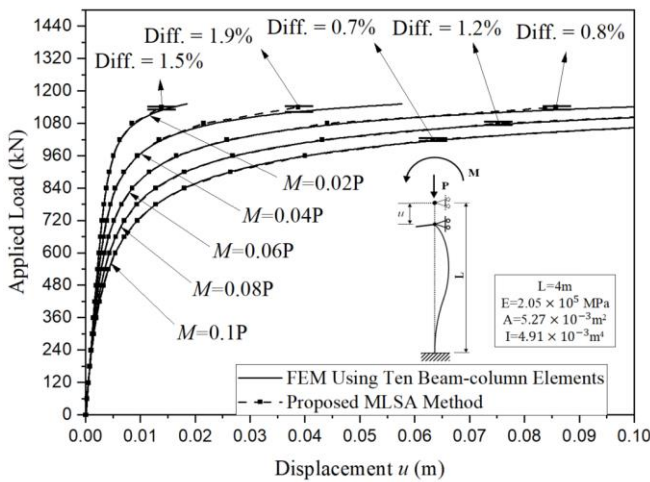


Fig. 10 Load-displacement curves of the column under combined bending and axial loads

## References

- [1] Hajela, P. and L. Berke, Neurobiological computational models in structural analysis and design. *Computers & Structures*, 1991. 41(4): p. 657-667.
- [2] Goh, A.T., Prediction of ultimate shear strength of deep beams using neural networks. *Structural Journal*, 1995. 92(1): p. 28-32.
- [3] Kasperkiewicz, J., J. Racz, and A. Dubrawski, HPC strength prediction using artificial neural network. *Journal of Computing in Civil Engineering*, 1995. 9(4): p. 279-284.
- [4] Luo, H. and S.G. Paal, Metaheuristic least squares support vector machine-based lateral strength modelling of reinforced concrete columns subjected to earthquake loads. *Structures*, 2021. 33: p. 748-758.
- [5] El-Kassas, E., R. Mackie, and A. El-Sheikh, Using neural networks in cold-formed steel design. *Computers & Structures*, 2001. 79(18): p. 1687-1696.
- [6] Wu, X., J. Ghaboussi, and J. Garrett Jr, Use of neural networks in detection of structural damage. *Computers & Structures*, 1992. 42(4): p. 649-659.
- [7] Stephens, J.E. and R.D. VanLuchene, Integrated assessment of seismic damage in structures. *Computer-Aided Civil and Infrastructure Engineering*, 1994. 9(2): p. 119-128.
- [8] Hakim, S.J.S. and H.A. Razak, Adaptive neuro fuzzy inference system (ANFIS) and artificial neural networks (ANNs) for structural damage identification. *Structural engineering and mechanics: An international journal*, 2013. 45(6): p. 779-802.
- [9] Huang, H. and H.V. Burton, Classification of in-plane failure modes for reinforced concrete frames with infills using machine learning. *Journal of Building Engineering*, 2019. 25: p. 100767.

## 7. Conclusion

Modern structural design methods are moving toward the rigorous design of structures through virtual simulations under critical scenarios, complying with physical laws and accounting for the imperfections in reality. The second-order analysis method has been developed in line with the same philosophy, continuously researched in scientific communities, and applied in designing numerous steel structures in engineering practices. The nonlinear finite-element method (FEM) using beam-column elements, also named line finite-elements, has been widely adopted in second-order analysis, which is a matrix analysis-based and computationally intensive method. When adopting the FEM for large deflection problems, numerical convergence is sometimes challenging as well as the long computational time of solving sparse linear equations. Although some research has been conducted during the past decades to improve numerical efficiency, the matrix-based algorithm is unstable when singularity occurs. It may hinder the development of emerging structural analysis methods to be more robust and efficient in satisfying highly demanded requirements in virtual simulations for modern structural design.

The computational efficiency of machine learning has been exceptionally improved in recent years, with the availability of fast AI processors tail-made for massive neural networks. To facilitate the adoption of new AI technology in structural engineering, this research proposes an innovative machine learning-based structural analysis (MLSA) method for the second-order analysis of beam-columns through Physics-Informed Neural Networks (PINN). The governing equations for the problems are discussed and incorporated into the physics-informed neural networks. The physical information provided by the governing equations and boundary conditions is used to orientate the training process creating a self-supervised learning procedure. The PINN framework and the training procedure are provided, where an adaptive loss weight control algorithm and the transfer learning technic are proposed to improve numerical efficiency. The pre-trained neural networks for the second-order analysis of beam-columns are provided.

The new method has been thoughtfully validated by well-established methods in terms of the analytical solutions and the FEM. Four verification examples are given, showing that the proposed MLSA method can obtain the results accurately and robustly. As the potential to be the next-generation structural analysis method, this research innovatively adopts the emerging computational technique based on machine learning to solve second-order analysis problems for single members that could be motivated for other engineering problems.

## Data availability

The input and output files for all examples, the computer source codes, and the trained neural networks are available at <https://github.com/zsulsw/mlsa>.

## Acknowledgment

The work described in this paper was partially supported by grants from the Research Grants Council of the Hong Kong Special Administrative Region, China (Project No. PolyU/21E/15203121), and a grant from the National Natural Science Foundation of China (No. 52008410). This work is also partially supported by a grant (BBTH) from Hong Kong Branch of National Rail Transit Electrification and Automation Engineering Technology Research Center.

- [10] Hakim, S.J.S., H.A. Razak, S.A. Ravanfar, and M. Mohammadhassani, Structural damage detection using soft computing method, *Structural Health Monitoring*, Volume 5: Proceedings of the 32nd IMAC, A Conference and Exposition on Structural Dynamics, 2014. Springer International Publishing. p. 143-151.
- [11] Berke, L., S.N. Patnaik, and P.L.N. Murthy, Optimum design of aerospace structural components using neural networks. *Computers & structures*, 1993. 48(6): p. 1001-1010.
- [12] Iranmanesh, A. and A. Kaveh, Structural optimization by gradient-based neural networks. *International journal for numerical methods in engineering*, 1999. 46(2): p. 297-311.
- [13] Kaveh, A., Y. Gholipour, and H. Rahami, Optimal design of transmission towers using genetic algorithm and neural networks. *International Journal of Space Structures*, 2008. 23(1): p. 1-19.
- [14] Tashakor, A. and H. Adeli, Optimum design of cold-formed steel space structures using neural dynamics model. *Journal of Constructional Steel Research*, 2002. 58(12): p. 1545-1566.
- [15] Šipoš, T.K., I. Miličević, and R. Siddique, Model for mix design of brick aggregate concrete based on neural network modelling. *Construction and building materials*, 2017. 148: p. 757-769.
- [16] Jeong, H., J. Bai, C.P. Batuwatta-Gamage, C. Rathnayaka, Y. Zhou, and Y. Gu, A Physics-Informed Neural Network-based Topology Optimization (PINNTO) framework for structural optimization. *Engineering Structures*, 2023. 278, p. 115484.
- [17] Yan, C.A., R. Vescovini, and L. Dozio, A framework based on physics-informed neural networks and extreme learning for the analysis of composite structures. *Computers & Structures*, 2022. 265: p. 106761.



- [18] Raissi, M., P. Perdikaris, and G.E. Karniadakis, Physics-informed neural networks: A deep learning framework for solving forward and inverse problems involving nonlinear partial differential equations. *Journal of Computational Physics*, 2019. 378: p. 686-707.
- [19] Yuan, L., Y.Q. Ni, X.Y. Deng, and S. Hao, A-PINN: Auxiliary physics informed neural networks for forward and inverse problems of nonlinear integro-differential equations. *Journal of Computational Physics*, 2022. 462: p. 111260.
- [20] Zhang, R., Y. Liu, and H. Sun, Physics-informed multi-LSTM networks for metamodeling of nonlinear structures. *Computer Methods in Applied Mechanics and Engineering*, 2020. 369: p. 113226.
- [21] Katsikis, D., A.D. Muradova, and G.E. Stavroulakis, A Gentle Introduction to Physics Informed Neural Networks, with Applications in Static Rod and Beam Problems. *Journal of Advances in Applied & Computational Mathematics*, 2022. 9: p. 103-128.
- [22] Chen, X., C. Gong, Q. Wan, L. Deng, Y. Wan, Y. Liu, B. Chen, and J. Liu, Transfer learning for deep neural network-based partial differential equations solving. *Advances in Aerodynamics*, 2021. 3(1): p. 1-14.
- [23] Goswami, S., C. Anitescu, S. Chakraborty, and T. Rabczuk, Transfer learning enhanced physics informed neural network for phase-field modeling of fracture. *Theoretical and Applied Fracture Mechanics*, 2020. 106: p. 102447.
- [24] Tang, H., H. Yang, Y. Liao, and L. Xie, A transfer learning enhanced the physics-informed neural network model for vortex-induced vibration. *arXiv preprint arXiv:2112.14448*, 2021.
- [25] Basir, S., Investigating and Mitigating Failure Modes in Physics-informed Neural Networks (PINNs). *arXiv preprint arXiv:2209.09988*, 2022.
- [26] Basir, S. and I. Senocak, Characterizing and Mitigating the Difficulty in Training Physics-informed Artificial Neural Networks under Pointwise Constraints. *arXiv preprint arXiv:2206.09321*, 2022.
- [27] Li, W., M.Z. Bazant, and J. Zhu, A physics-guided neural network framework for elastic plates: Comparison of governing equations-based and energy-based approaches. *Computer Methods in Applied Mechanics and Engineering*, 2021. 383: p. 113933.
- [28] Bastek, J.H. and D.M. Kochmann, Physics-Informed Neural Networks for Shell Structures. *European Journal of Mechanics-A/Solids*, 2022. 97: p. 104849.
- [29] Muradova, A.D. and G.E. Stavroulakis, Physics-informed neural networks for elastic plate problems with bending and Winkler-type contact effects. *Journal of the Serbian Society for Computational Mechanics*, 2021. 15(2): p. 45-54.
- [30] Haghighat, E., M. Raissi, A. Moure, H. Gomez, and R. Juanes, A deep learning framework for solution and discovery in solid mechanics. *arXiv preprint arXiv:2003.02751*, 2020.
- [31] Haghighat, E. and R. Juanes, SciANN: A Keras/TensorFlow wrapper for scientific computations and physics-informed deep learning using artificial neural networks. *Computer Methods in Applied Mechanics and Engineering*, 2021. 373: p. 113552.
- [32] Tao, F., X. Liu, H. Du, and W. Yu, Physics-informed artificial neural network approach for axial compression buckling analysis of thin-walled cylinder. *AIAA Journal*, 2020. 58(6): p. 2737-2747.
- [33] Wang, T., W.A. Altabay, M. Noori, and R. Ghiasi, A deep learning based approach for response prediction of beam-like structures. *Structural Durability & Health Monitoring*, 2020. 14(4): p. 315.
- [34] Yan, C., R. Vescovini, and L. Dozio, Analysis of Lightweight Structures Using Physics Informed Neural Networks. *Aerospace Europe Conference 2021 (AEC-21)*, 2021. p. 1-7.
- [35] AISI, ANSI/AISC 360-16: specification for structural steel buildings. 2016.
- [36] Standard, Eurocode 3-Design of steel structures. BS EN 1993-1, 2006. 1: p. 2005.
- [37] CoPHK, Code of practice for the structural use of steel 2011. 2011, Buildings Department Hong Kong SAR Government.
- [38] Chen, W.F., Structural stability: from theory to practice. *Engineering structures*, 2000. 22(2): p. 116-122.
- [39] Liew, J.R., H. Chen, N. E. Shanmugam, and W.F. Chen, Improved nonlinear plastic hinge analysis of space frame structures. *Engineering structures*, 2000. 22(10): p. 1324-1338.
- [40] Chen, W.F., Y. Goto, and J.R. Liew, Stability design of semi-rigid frames. 1995: John Wiley & Sons.
- [41] Schafer, B.W. and T. Peköz, Computational modeling of cold-formed steel: characterizing geometric imperfections and residual stresses. *Journal of constructional steel research*, 1998. 47(3): p. 193-210.
- [42] Yu, C. and B.W. Schafer, Simulation of cold-formed steel beams in local and distortional buckling with applications to the direct strength method. *Journal of Constructional Steel Research*, 2007. 63(5): p. 581-590.
- [43] Tang, Y., Y.P. Liu, and S.L. Chan, A co-rotational framework for quadrilateral shell elements based on the pure deformational method. *Advanced Steel Construction*, 2018. 14(1): p. 90-114.
- [44] Chan, S.L. and S. Cho, Second-order analysis and design of angle trusses Part I: Elastic analysis and design. *Engineering Structures*, 2008. 30(3): p. 616-625.
- [45] Du, Z.L., Y.P. Liu, and S.L. Chan, A second-order flexibility-based beam-column element with member imperfection. *Engineering Structures*, 2017. 143: p. 410-426.
- [46] Liu, S.W., R. D. Ziemian, L. Chen, and S.L. Chan, Bifurcation and large-deflection analyses of thin-walled beam-columns with non-symmetric open-sections. *Thin-Walled Structures*, 2018. 132: p. 287-301.
- [47] Chen, L., A.H.A. Abdelrahman, S.W. Liu, R.D. Ziemian, and S.L. Chan, Gaussian Beam-Column Element Formulation for Large-Deflection Analysis of Steel Members with Open Sections Subjected to Torsion. *Journal of Structural Engineering*, 2021. 147(12): p. 04021206.
- [48] Schafer, B.W., Local, distortional, and Euler buckling of thin-walled columns. *Journal of structural engineering*, 2002. 128(3): p. 289-299.
- [49] Ádány, S. and B.W. Schafer, Generalized constrained finite strip method for thin-walled members with arbitrary cross-section: Primary modes. *Thin-Walled Structures*, 2014. 84: p. 150-169.
- [50] Bian, G., K.D. Peterman, S. Torabian, and B.W. Schafer, Torsion of cold-formed steel lipped channels dominated by warping response. *Thin-Walled Structures*, 2016. 98: p. 565-577.
- [51] Howell, L.L. and A. Midha, Parametric deflection approximations for end-loaded, large-deflection beams in compliant mechanisms. 1995.
- [52] Saxena, A. and S.N. Kramer, A simple and accurate method for determining large deflections in compliant mechanisms subjected to end forces and moments. *Journal of Mechanical Design*, 1998. 120(3): p. 392-400.
- [53] Kimball, C. and L.W. Tsai, Modeling of flexural beams subjected to arbitrary end loads. *Journal of Mechanical Design*, 2002. 124(2): p. 223-235.
- [54] Banerjee, A., B. Bhattacharya, and A.K. Mallik, Large deflection of cantilever beams with geometric non-linearity: Analytical and numerical approaches. *International Journal of Non-Linear Mechanics*, 2008. 43(5): p. 366-376.
- [55] Cuomo, S., V.S. Di Cola, F. Giampaolo, G. Rozza, M. Raissi, and F. Piccialli, Scientific Machine Learning through Physics-Informed Neural Networks: where we are and what's next. *Journal of Scientific Computing*, 2022. 92(3): p. 88.
- [56] Katsikadelis, J.T. and G.C. Tsiatas, Large deflection analysis of beams with variable stiffness. *Acta Mechanica*, 2003. 164(1): p. 1-13.
- [57] Strang, G., Piecewise polynomials and the finite element method. *Bulletin of the American Mathematical Society*, 1973. 79(6): p. 1128-1137.
- [58] Pan, S. and K. Duraisamy, Physics-informed probabilistic learning of linear embeddings of nonlinear dynamics with guaranteed stability. *SIAM Journal on Applied Dynamical Systems*, 2020. 19(1): p. 480-509.
- [59] Nascimento, R.G., K. Fricke, and F.A. Viana, A tutorial on solving ordinary differential equations using Python and hybrid physics-informed neural network. *Engineering Applications of Artificial Intelligence*, 2020. 96: p. 103996.
- [60] Pang, G. and G.E. Karniadakis, Physics-informed learning machines for partial differential equations: Gaussian processes versus neural networks, *Emerging Frontiers in Nonlinear Science*. 2020, Springer. p. 323-343.
- [61] Candès, E.J., Harmonic analysis of neural networks. *Applied and Computational Harmonic Analysis*, 1999. 6(2): p. 197-218.
- [62] Wang, S., Y. Teng, and P. Perdikaris, Understanding and mitigating gradient flow pathologies in physics-informed neural networks. *SIAM Journal on Scientific Computing*, 2021. 43(5): p. A3055-A3081.
- [63] Bottou, L., Stochastic gradient descent tricks, *Neural networks: Tricks of the trade*. 2012, Springer. p. 421-436.
- [64] Johnson, R. and T. Zhang, Accelerating stochastic gradient descent using predictive variance reduction. *Advances in neural information processing systems*, 2013. 26.
- [65] Kingma, D.P. and J. Ba, Adam: A method for stochastic optimization. *arXiv preprint arXiv:1412.6980*, 2014.
- [66] Paszke, A., S. Gross, F. Massa, A. Lerer, J. Bradbury, G. Chanan, T. Killeen, Z. Lin, N. Gimelshein, L. Antiga, and A. Desmaison, Pytorch: An imperative style, high-performance deep learning library. *Advances in neural information processing systems*, 2019. 32.
- [67] Abadi, M., P. Barham, J. Chen, Z. Chen, A. Davis, J. Dean, M. Devin, S. Ghemawat, G. Irving, M. Isard, and M. Kudlur, TensorFlow: a system for Large-Scale machine learning. 12th USENIX symposium on operating systems design and implementation (OSDI 16), 2016. 16: p. 265-283.
- [68] Basir, S. and I. Senocak, Physics and equality constrained artificial neural networks: application to forward and inverse problems with multi-fidelity data fusion. *Journal of Computational Physics*, 2022. 463: p. 111301.
- [69] Chen, L., W.L. Gao, S. W. Liu, R.D. Ziemian, and S.L. Chan, Geometric and material nonlinear analysis of steel members with nonsymmetric sections. *Journal of Constructional Steel Research*, 2022. 198: p. 107537.
- [70] Chen, W.F. and T. Atsuta, Theory of beam-columns, volume 2: space behavior and design. Vol. 2. 2007, J. Ross Publishing.
- [71] Zhang, P., J. Ma, M. Duan, Y. Yuan, and J. Wang, A high-precision curvature constrained Bernoulli-Euler planar beam element for geometrically nonlinear analysis. *Applied Mathematics and Computation*, 2021. 397: p. 125986.
- [72] Dadgar-Rad, F. and S. Sahraee, Large deformation analysis of fully incompressible hyperelastic curved beams. *Applied Mathematical Modelling*, 2021. 93: p. 89-100.
- [73] Schulz, M. and F.C. Filippou, Non-linear spatial Timoshenko beam element with curvature interpolation. *International Journal for Numerical Methods in Engineering*, 2001. 50(4): p. 761-785.
- [74] Jirásek, M., E. La Malfa Ribolla, and M. Horák, Efficient finite difference formulation of a geometrically nonlinear beam element. *International Journal for Numerical Methods in Engineering*, 2021. 122(23): p. 7013-7053.
- [75] Chan, S.L. and Z.H. Zhou, Pointwise equilibrating polynomial element for nonlinear analysis of frames. *Journal of structural engineering*, 1994. 120(6): p. 1703-1717.
- [76] Liu, S.W., Y.P. Liu, and S.L. Chan, Direct analysis by an arbitrarily-located-plastic-hinge element—Part 1: Planar analysis. *Journal of Constructional Steel Research*, 2014. 103: p. 303-315.